Molecular Tribology

A thesis submitted in partial fulfillment of the requirements for the degree of Doctor of Philosophy

in the University of Durham

by

Kaustav Guha

Department of Chemistry and Ustinov College

Durham University

July 2011

ABSTRACT

Surface-active agents play an important role in lubrication technology and are often used as additives in liquid lubricants films to reduce the friction and wear. Under high loads, in asperity contacts or when there is no relative motion between two surfaces, fluid lubrication breaks down and boundary lubricants are essential to prevent wear and seizure. In other applications where the use of 'thick' films of liquid lubricants is not possible or desirable (i.e. micromotors, hard disk drives), lubrication between contacting surfaces is exclusively in the boundary regime. Despite the use of boundary lubricants in engineering applications for centuries, our understanding of how boundary lubricants work at the molecular level remains unclear. My thesis describes the use of total internal reflection (TIR) Raman scattering to characterise model boundary lubricants both *ex situ* and *in situ*, under realistic conditions of pressure and shear.

The model systems comprise either Langmuir-Blodgett (LB) monolayers of long chain fatty acids (e.g. Zn arachidate) and phospholipids (e.g. DPPC) deposited on silica and SF10 glass, or phospholipid bilayers (e.g. DMPC) fused to silica and SF10 glass surfaces in water. TIR Raman scattering is a form of vibrational spectroscopy with sub-nanometer sensitivity and spatial resolution of a few microns. Control of the polarisation of the incoming and scattered light allows us to probe the orientation of adsorbed molecules and how that orientation changes under pressure and shear. The resonant frequency and intensity of different molecular vibrations is also sensitive to the packing and conformational order in the lubricant film. LB monolayers of Zn arachidate and DPPC are first characterised *ex situ* and then subjected to increasing load (upto ~750 MPa) in a contact between a fused silica ball and the flat surface of an SF10 hemisphere. A better packing or a higher orderliness of the molecules are observed at higher pressure without the monolayers being squeezed out. In contrast, application of load to the DMPC bilayer appears to squeeze some of the lipid materials out of contact. The designs of two Raman tribometers are described that allow Raman measurements in a sheared contact with simultaneous measurements of friction and load. Elasto-hydrodynamic and boundary lubrication regimes are studied with the tribometers overcoming the engineering difficulties up to a significant extent.

Acknowledgements

I would like to say a thank you to all those who were with me during my PhD and made my stay at Durham such an enjoyable experience. My special thanks to my supervisor Prof. Colin Bain, for all his intellectual input into this project and support throughout my PhD tenure which was not very easy-going always. I thank Dr. Eric Tyrode who actively worked with me during the early stages of my doctoral research and his contributions and guidance were invaluable. I thank Dr. James Day for his technical support with the Raman Spectrometer during my early PhD days. At the later stages of my doctoral research, a part of the tribometer project for studying insitu lubricants under sliding confinement was carried out in close collaboration with Prof. S.K. Biswas and Praveena Manimunda from Mechanical Engineering Department, Indian Institute of Science (IISc) Bangalore. I would like to thank Prof. Biswas for useful discussions while his visit to Durham and also thank Praveena for his contributions in development of the tribometer during his three month stay at Durham. My thanks to the rest of the Bain group, Dan, Phil, Andy, David, John, Yan, Lisong, Alex, Mario for being fun to work alongside and also for their support, particularly towards the closing stages of my doctoral research. I would like to thank the BP-EPSRC Dorothy Hodgkin Postgraduate Award and UK-India Education and Research Initiatives (UKIERI) for providing me with the research funding.

Away from the laboratory, I acknowledge all the support I received from my parents whose lifetime sacrifices enabled me to be a Doctorate from Durham University, and I thank my younger brother Kaunteya for all the mental support. I am extremely indebted to Ramakrishna Mission, Narendrapur for their contributions in grooming me up from my school days till graduation and making me capable enough to be an IIT KGPian, and to find a PhD position at a 5* rated Chemistry Department in the UK.

List of Abbreviations

AFM	.....	atomic force microscopy
AOI	.....	angle of incidence
ATR	.....	attenuated total reflection
BAM	.....	Brewster angle microscopy
Bp	.....	boiling point
CCD	.....	charge-coupled device
CPP	……..	critical packing parameter
DC	.....	direct current
DLN	.....	diamond like nanocomposite
DMPC	.....	1,2-dimyristoyl-sn-glycero-3-phosphocholine
DPPC	.....	1,2-dipalmitoyl-sn-glycero-3-phosphocholine
EHD	.....	elasto-hydrodynamic lubrication
FFM	.....	friction force microscopy
FTIR	.....	Fourier transform infrared spectroscopy
FWHM	.....	full width at half maxima
IR	.....	Infrared
LB	.....	Langmuir-Blodgett
LC	.....	liquid condensed phase
LE	.....	liquid expanded phase
LFM	.....	lateral force microscopy
MD	.....	molecular dynamics
MP	.....	magnification power
Mp	.....	melting point

List of Abbreviations

NA	.....	numerical aperture
PAO	.....	poly-alpha olefin
PTFE	.....	Poly-tetrafluoro-ethane
QCM	.....	quartz-crystal microbalance
rpm	.....	rotations per minute
SAM	.....	self-assembled monolayer
SERS	.....	surface enhanced Raman spectroscopy
SFA	.....	surface force apparatus
SFG	.....	sum-frequency generation
SFS	.....	sum-frequency spectroscopy
TDC	.....	top dead centre
TIR	.....	total internal reflection
ULWD	.....	ultra-long working distance
UV	.....	Ultraviolet
XPS	.....	X-ray photoelectron spectroscopy
ZDDP	.....	zinc dialkyldithiophosphate

Table of Contents

1. Introduction

Tribology is the science and technology of friction, lubrication, and wear, derived from the Greek tribo meaning "I rub". It is formally defined as the science and technology of interactive surfaces in relative motion and all practices related to it. It is a well-established fact that lubricants reduce friction and wear, but a clear understanding of the mechanism and functioning of the lubricants at the molecular level is still lacking. Thin organic films confined between two solid surfaces are of immense significance in lubrication science. My PhD thesis is aimed at studying the molecular basis of lubrication, to find out what exactly happens to organic/lubricant films confined at solid-solid interface under applied pressure and shear.

1.1 Regimes of lubrication

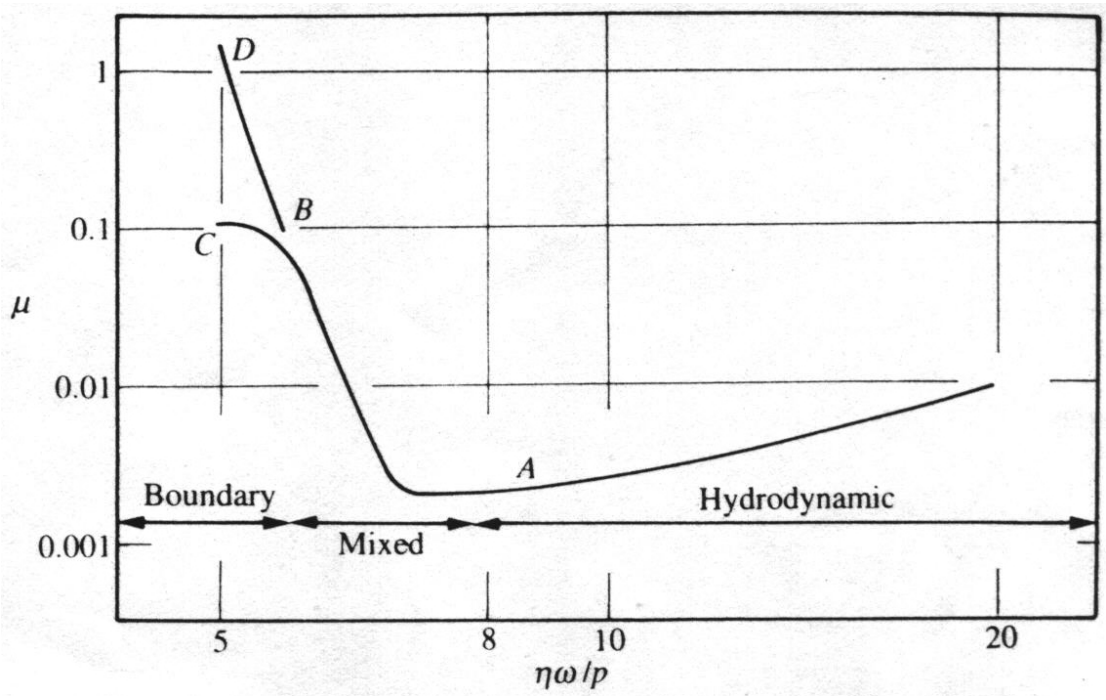

Figure 1.1.1 The Stribeck diagram for a journal bearing. μ is the friction coefficient, η is the lubricant viscosity, ω the rate of rotation, and p the nominal bearing pressure. Diagram from "Engineering Tribology" by J.A. Williams [1].

As the applied pressure/load is increased on the surfaces in contact, three distinct situations arise with respect to the properties of lubrication, which are called regimes of lubrication.

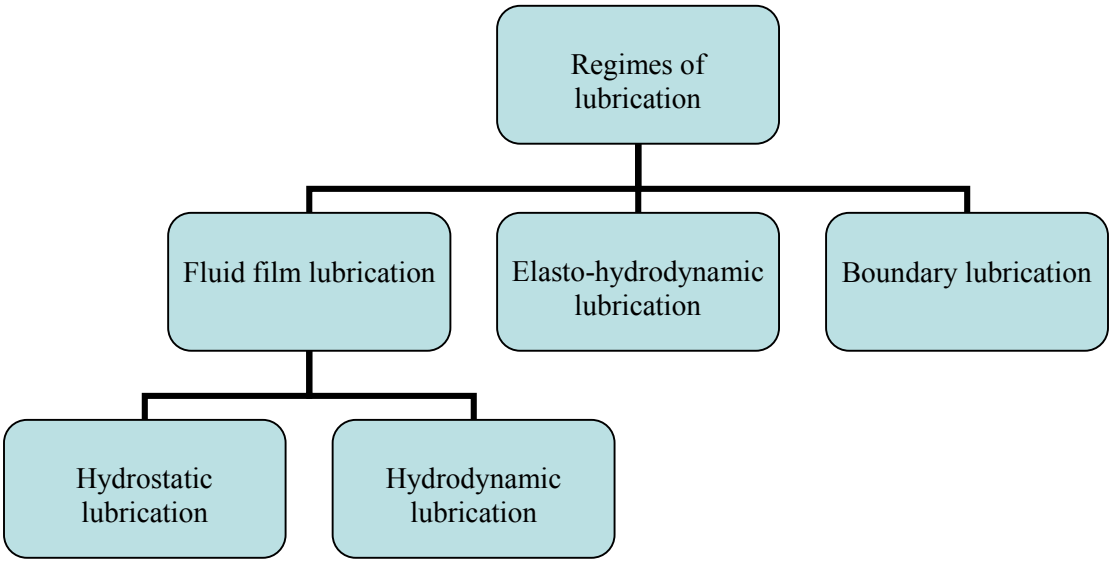

Figure 1.1.2 Organisation chart showing different regimes of lubrication

- **Fluid film lubrication:** In this lubrication regime, the solid-solid contact is avoided by the load being completely supported by the viscous forces of the lubricant in the lubricated junction. The fluid bearings are often used in high load, high speed or high precision applications where ordinary ball bearings have short life or high noise and vibration. This form of lubrication was established by Osborne Reynolds [2], and has been very well studied since then.
  - **Hydrostatic lubrication:** In this form of lubrication, an external pressure is applied to the lubricant in a bearing to prevent the fluid lubricant film being squeezed out of the solid-solid contact. In a hydrostatic bearing, the fluid is generally oil, water or air, and the pressurisation is done by a pump. For example in many gas or air bearings, the fluid is pumped in through an orifice or through a porous material.
  - **Hydrodynamic lubrication:** This form of lubrication involves a relative motion between the contacting surfaces, and a suitable bearing design to

pump the lubricant film between the contacting surfaces. The film of lubricant breaks or is squeezed out of the solid-solid contact when the relative motion ceases, causing wear and damage to the contacting surfaces. In fluid-dynamic bearings, the rotation sucks the fluid onto the inner surface of the bearing forming a lubricating wedge under/ around the shaft. For example in a computer hard disk, heads are supported by hydrodynamic lubrication where the fluid is the atmosphere.

- **Elasto-hydrodynamic lubrication (EHD):** In EHD lubrication, the liquid lubricant lies in the conjunction of the solid surfaces, but one of the solids is elastically deformed in forming the contact. In fact some interaction occurs between the raised solid features called asperities, and the elastic deformation of the contacting surface enlarges the load bearing area, thereby reducing the effective pressure, and the load is supported by the viscous resistance of the lubricant. As an example of EHD, the contact of a rubber blade of a windscreen wiper and a glass windscreen in the presence of rain can be cited, where the rain water acts as a lubricant and the rubber blade deforms elastically at the contact with the lubricated glass windscreen.
- **Boundary lubrication:** With slow sliding speed and high applied load, the lubricated conjunction are separated just by a boundary layer of lubricant film (<10 nm) and as the thickness of the film approaches molecular dimensions, the functioning of the lubrication is governed by the molecular properties rather than the bulk lubricant properties such as viscosity. When the solids come closer to asperity contacts, the heat developed by local pressures give rise to a condition called stick-slip motion, and some asperities break off. At this high temperature and pressure, the chemically reactive components of the lubricants form highly stable boundary films on the solid surfaces which in turn support the load and avoid severe damage due to wear. It can be said that in this mode of lubrication, the load is carried by the asperities rather than the lubricant [3]. The boundary lubrication or 'dry' lubrication is widely used where use of 'wet' or fluid film lubrication is not suitable e.g. in outer space, in hard disk of computers and in microdevices. It may be noted here that boundary lubrication can also arise in wet

lubrication when the relative motion ceases e.g. at the top dead centre (TDC) of a piston.

1.2 Types of boundary lubricants and their applications in real systems

A short history of research developments of different regimes of lubrication has been included in the DPhil thesis of Sarah Amanda Haydock (University of Oxford, 2002). In this thesis we will be mainly examining monolayers and bilayers in molecular confinement at solid-solid interface under applied pressure and shear to study the tribological response, the type of lubrication which is catagorised as 'boundary lubrication'. Hence the common types and examples of boundary lubricants and their applications in real systems are worth a discussion.

Friction coefficients of alcohols and acids on glass, steel, and bismuth surface were investigated by Hardy in 1922, which is the first report on boundary lubrication studies [4]. The boundary lubricants reduce interactions between two sliding surfaces and thereby reduce friction and wear. The long chain hydrocarbon molecules with active head groups e.g. alcohols, ammonium salts and fatty acids are found to be good boundary lubricants.

The active head groups are strongly bound to the solid surface thereby forming a boundary layer. Alcohols are non-ionic boundary lubricants (fig. 1.2.1 (a)) which are commonly used as hair and fabric conditioners, which when coated to the hair or fabric enable the fibres to slide smoothly over one another. The alcoholic boundary lubricants are also used to lubricate silicon nitride ceramic surfaces. Quaternary ammonium salts are cationic boundary lubricants (fig. 1.2.1 (b)) which are also used in hair and fabric conditioners. The long chain fatty acids are anionic surfactants (fig. 1.2.1 (c)) which are commonly used in soaps and detergents. The fatty acids are also used as boundary lubricants in car engines [5]. The action of boundary lubricants can be described in general but scientifically very little is understood about the film strength and the molecular contribution to the anti-friction properties.

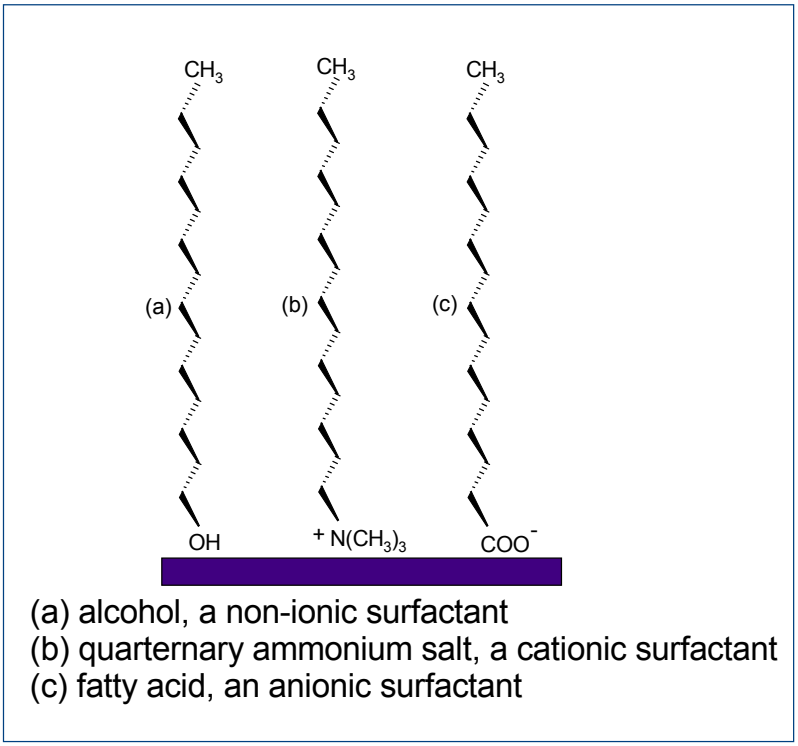

Figure 1.2.1 Examples of boundary lubricants on solid surfaces

Boundary lubricants are not necessarily formed by adsorbed monolayers on solid surfaces, but can also be formed by micellar adsorption (aggregate of surfactant molecules in definite geometries) on the surfaces from a solution of surfactants. Typical packing adaptations of the surfactant molecules on the surfaces are explained by the 'critical packing parameter' (CPP), which is the ratio of the effective volume, v to the product of the the head group area, S_0 and the chain length, l_c of the surfactant molecules.

$$\mathrm{CPP} = \frac{v}{S_0 l_c} \qquad (1.2.1)$$

The CPP determines the preferred association structures assumed for each molecular shape [6]. The general pattern is that spherical micelles are formed at low CPP values (~ 0.3) and the aggregate structure is shifted to hexagonal and, in turn, to lamellar phases as the CPP increases. If the surfactant hydrocarbon chains are very flexible, the lamellar phase is replaced by a bicontinuous microemulsion phase. In solution, alterations that increase the CPP of an ionic surfactant system are:

a) Increasing the hydrocarbon chain length of the surfactant

b) Changing the hydrocarbon chain to two chains
c) Changing from a linear to a branched hydrocarbon chain
d) Adding a solubilizate e.g. long chain alcohol
e) Adding a nonionic surfactant
f) Adding salt
g) Adding a small amount of ionic surfactant with opposite charges

For nonionic surfactant systems with ethylene oxide as polar part, the same dependence on the hydrocarbon chain is observed. Besides, an increase in the CPP is observed with the following alterations:

a) Changing the ethylene oxide chains to shorter ones
b) Increasing the temperature
c) Adding salt
h) Adding a solubilizate e.g. long chain alcohol
d) Adding a shorter ethylene oxide chain nonionic surfactant

In real systems, the engine oil, which is used for lubrication of various internal combustion engines, is composed of a cocktail of chemicals. Although the main function of engine oils is to lubricate moving parts, the engine oils also clean, inhibit corrosion, improve sealing and cool the engine by conducting away heat from the moving parts. The engine oils are blended from base oils, which are either mineral oils or synthetic oils e.g poly-alpha olefin (PAO). The base oil of some high performance motor oils can contain up to 20 wt. % of esters. The base oils usually operate in the hydrodynamic regime. With an increasing demand for low viscosity base oils in the hunt for increased fuel efficiency, these base oils can reach the boundary regime very quickly compared to high viscosity base oils. As a result, critical contacts can experience more severe boundary lubrication conditions.

Different additives, including surfactants, are therefore mixed with the base oils. The surfactant can adsorb to the moving surfaces and reduce friction. These friction modifiers are effective under engine conditions of temperature and pressure. Hence the mechanism

of this tribo-film formation, its molecular structure and its relation to reduction of friction needs in-depth research. Anti-wear agents are also added to the base oils, which bind to the moving surface and provide high protection against wear damage during boundary lubrication. For last few decades the most commonly used anti-wear agent has been zinc dialkyldithiophosphate (ZDDP) and lot of research has been carried out on the mechanical properties and structures of these substances in the recent past [7-12]. However, the poisoning of the exhaust catalysts due to the ZDDPs lead to concerns over emissions of sulphur, phosphorous and zinc. Due to these environmental concerns the usage of ZDDPs as anti-wear additives has been restricted within limits in certain motor oil products. Therefore it is important to carry out further research to develop alternative anti-wear additives.

The other components of the engine oil comprise detergents to keep the deposits in suspension and thereby the engine cleaner, anti-oxidants, anti-foaming agent etc. It is important to note that around 20% of the power is lost due to frictional losses in the car engines; therefore reducing friction in the engines can lead a few steps to the goal of manufacturing low emission vehicles.

1.3 Commonly used techniques to study lubricated surfaces

Today boundary lubrication is very widely studied and is of immense importance because of the fact that metallic friction reduces by a factor of 10 and wear by factor of >10000 [13, 14]. In applications where the use of ‘thick’ films of liquid lubricants is not possible or desirable (i.e. micromotors, hard disk drives), lubrication between contacting surfaces is exclusively in the boundary regime. However, in spite of various state of the art research being carried out in this field, very little is known about the mechanism of boundary lubrication in the molecular scale. Scanning probe microscopes such as AFM [15-18] and FFM [19] etc are commonly used to study friction and wear in a small area. AFM exploits the forces existing between atoms and molecules. A sharp AFM tip is mounted over a cantilever with a known spring constant, and is passed over the surface

under examination (fig. 1.3.1). The deflection of the cantilever holding the tip is monitored by a photodiode sensitive to laser light reflected at the backside of the tip. While scanning across the surface, the tip interacts with the atoms/molecules at the surface and deflects according to the interaction: for an attractive interaction between the tip and the surface, the tip deflects towards the surface and for a repulsive tip-surface interaction the tip deflects away from the surface. These deflections in the cantilever are converted into an image of surface topography. AFM can also provide information on film thickness, frictional properties and elastic compliances of thin films.

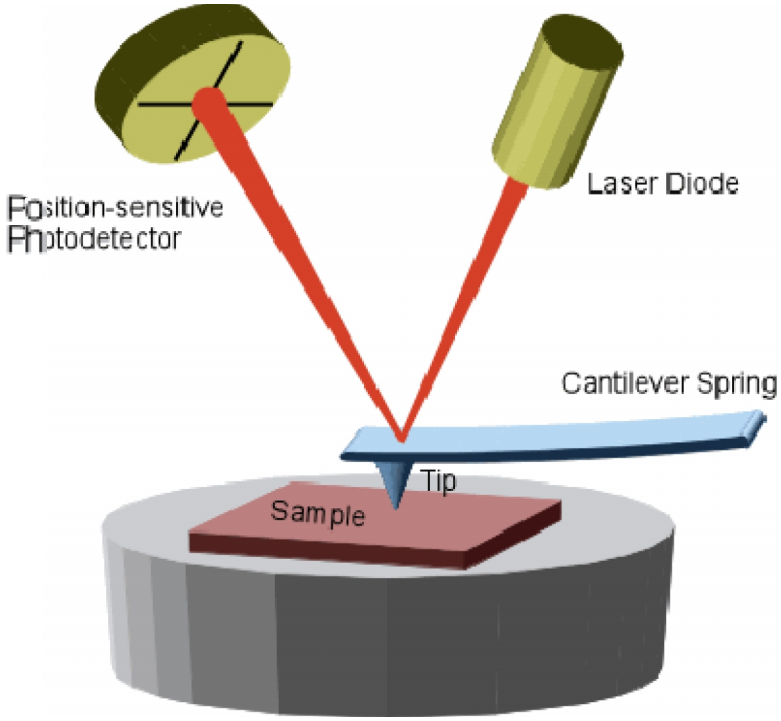

Figure 1.3.1 Mechanism of Atomic Force Microscopy (AFM)

Friction force microscopy (FFM) is a technique based upon scanning force microscopy and is a powerful tool for the quantitative analysis of nanometer scale chemistry [20]. FFM can measure both the vertical (normal) force as well as the lateral (friction) force in contact mode imaging. Similar to the AFM setup, beam deflection systems with quadrant photodiode detectors are employed for these kinds of experiments [21]. Friction

measurements are performed by imaging in contact mode, usually with constant force, and recording the lateral deflection in the direction of the scanning motion of the cantilever to obtain the "friction image". A topographic image can be recorded simultaneously, by measuring the required feedback signal to maintain constant force, so that the topographical features of the sample can be compared with the tribological features appearing in the friction image.

To mention a few out of many advantages of this scanning probe technique, it is capable of extremely high resolution imaging (atomic level in certain favourable cases) without sample treatment of coating, can be run under vacuum, air or liquid environment, with possibility of quantitative measurements of sample form, distribution, roughness over a large range of magnifications, friction, adhesion, wear etc. Some of the results obtained by AFM, FFM studies most relevant to my topic of research have been included in section 1.5. At most solid-solid interfaces contact occurs at many asperities and a sharp AFM/FFM tip sliding over a solid surface simulates one such contact. However, asperities can be of many shapes and sizes and using tips of different radii, the effect of a particular asperity on a sliding surface can be studied. Typical shear rates in engine bearings are in the order of 10^7 s^{-1} [22] while the shear rates in the AFM/FFM friction studies are in the order of 10^5 s^{-1} (typical relative velocity 200 μm/s and pressure ~ 1 GPa).

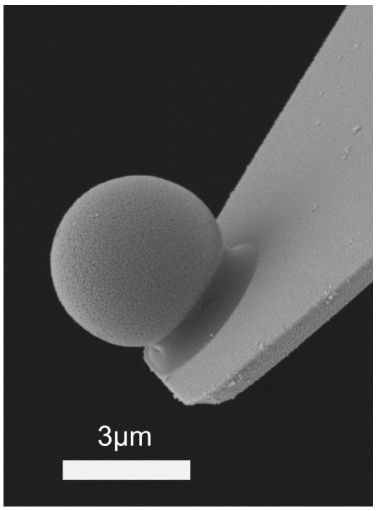

Figure 1.3.2 Colloidal Probe Microscopy: a colloid particle attached to AFM tip [23]

In colloidal probe technique, an individual colloidal particle is attached to the tip, and its interaction with a flat surface or another particle is studied e.g. the particle-surface (or particle-particle) interaction, adhesion, friction. The material chosen for the attached colloidal particle can be chosen rather freely. Colloidal probe microscopy has been used to study sliding friction between model cellulose surfaces in aqueous solutions [24], adhesion and interfacial surface interactions in cellulose/gypsum interface [25], etc. Unlike AFM, in colloidal probe microscopy it is possible to investigate the interactions between two surfaces with desired molecular coatings; however we are still limited to the study of frictional responses between a sliding surface and a surface of a sphere of colloidal dimension i.e. a particle of a very small radius.

Surface Force Apparatus (SFA) is an instrument that can measure the forces occurring between two curved surfaces and is more suited for measuring surface-surface interactions and is capable of measuring longer range forces more accurately [26-28] than AFM/FFM.

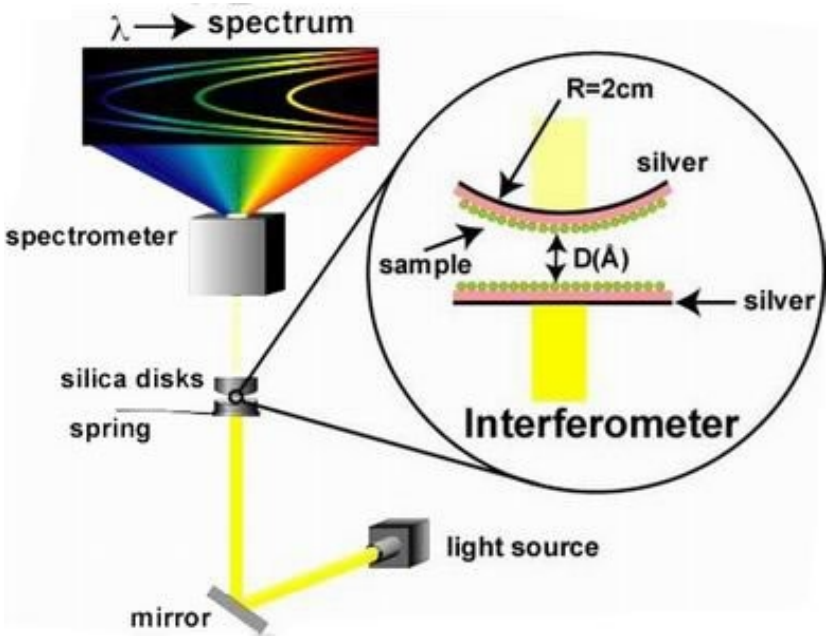

Figure 1.3.3 Working mechanism of Surface Force Apparatus (SFA) [29].

In an SFA, two smooth back-silvered cylindrically curved surfaces (usually of mica) are mounted in a crossed-cylinder configuration (cylindrical axes are positioned 90° to each

other), and are made to approach each other in a direction normal to the axes (fig. 1.3.3). The first surface is mounted on a mechanical spring and the measurement of its deflection allows the force between the two surfaces to be determined. The second surface is rigidly held on a piezoelectric cylinder that varies the separation between the surfaces. White light (use of laser is also possible) is then passed through the mica surfaces and is reflected from the silver, and the wavelengths of the discrete fringes that are transmitted can be used to give the surface separation to accuracy of 0.1 nm. The force-measuring spring can be replaced with a more rigid support, and an organic liquid can be confined between the two mica surfaces. Any other molecule or material of interest can be coated or adsorbed to the mica surface. The white light is used to obtain the surface separation can also be used to obtain the refractive index of the confined organic film. Friction measurements can be performed sliding one cylinder over the other in an SFA. Normal pressure (0–5 MPa) and tangential velocity (~40 μm/s) can be applied and the corresponding forces can be measured by a system of leaf springs to study the film properties of the confined material under varied pressure. The contact radius in these experiments is up to 50 μm [30].

Although the different scanning techniques are well equipped to provide enough physical tribological information about film thickness, film degradation and wear, and frictional resistance offered in sliding contacts, these techniques completely fail to provide any kind of chemically specific or molecular information about the thin films in solid-solid confinement. Different spectroscopic techniques such as synchrotron IR absorption [12] have been applied so far to study the tribological contacts and diamond anvil cells have been used to reach higher compressions (~25 GPa) [12]. Vibrational spectroscopy [31-35] is a useful tool to obtain molecular information about these thin films in confinement which can enable a study of molecular orientations and structural changes under applied pressure and shear, possible defects in molecular packing arising out of conformational changes, phase changes in the films (if any) and film degradation. FTIR spectroscopy [36-38], Raman spectroscopy [31, 33, 39-42], and sum-frequency spectroscopy (SFG) [31, 34, 35, 43] are the common forms of vibrational spectroscopy used to study boundary lubrication and molecular confinements. However with the higher wavelength

of IR radiation (~3.0–3.5 μm for the CH stretching region), it is difficult to focus the IR beam to a very small area, therefore studying a very small contact area (~50–200 μm across) becomes difficult; on the other hand the use of focused lasers increases the power per unit area at the sample in Raman spectroscopy. The other concern of using IR spectroscopy to study solid-solid interface is the issue of sensitivity, as most of the commonly used solid materials for tribology experiments are not IR transparent and we are limited to a choice of materials like some types of sapphire, calcium fluoride (CaF_2) and zinc selenide (ZnSe).

In Raman spectroscopy for most vibrational transitions, the Stokes radiation lies in the visible region when the incident radiation is in the range 400–600 nm (a more detailed description of Raman spectroscopy will be presented in Chapter 2). Therefore, only one dispersing system and one detector are required for the study of all vibrational modes, the sample cell (or optics as in case of our tribology studies) can be made of glass, and the laser can be polarised to allow polarisation experiments to be carried out. Raman spectroscopy and sum-frequency spectroscopy are better equipped to study smaller contact areas. In FTIR spectroscopy, however, Fourier transform is applied and no dispersing system is required although an additional detector is required to detect signals in the mid-IR region.

In SFG, a vibration has to be both Raman-active and IR-active to generate a sum-frequency signal, therefore centrosymmetric molecules are SF-inactive [34].

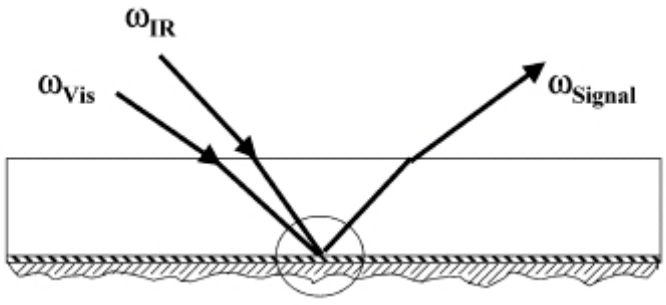

Figure 1.3.4 SFG experimental setup [44].

In SFG, two photons, one in the visible ($\boldsymbol{\omega}_{vis}$) and one in the infrared ($\boldsymbol{\omega}_{IR}$) overlap on a surface in space and time to emit a photon whose frequency is their sum ($\boldsymbol{\omega}_{SF} = \boldsymbol{\omega}_{vis} + \boldsymbol{\omega}_{IR}$). This is accomplished by overlapping pulsed laser beams from an IR and a visible laser (fig. 1.3.4). The resultant, or sum-frequency beam, is emitted at a specific angle from the surface normal, $\boldsymbol{\omega}_{SF}$, to conserve momentum. Generally, the IR laser has tunable frequency (nowadays the IR lasers are often broadband which allows whole spectrum at once) while the visible laser has fixed frequency. When the frequency of the IR laser is in resonance with a vibrational mode of the surface molecules, the intensity of the sum-frequency (SF) beam is enhanced (figure 1.3.4) [44-46].

While studying Zn arachidate as a model boundary lubricant, only the terminal methyl (CH_3) groups will produce SF signal for all-trans chains, as local inversion symmetry makes the methylene groups ($-CH_2$) SF inactive. However, the presence of gauche defects in the molecular packing breaks the symmetry and some SF signal from $-CH_2$ vibrations is visible. Sum frequency spectroscopy experiments pressing zinc arachidate monolayer in between a sapphire prism and silica lens revealed that the monolayer was resistant to pressure and shear induced conformational disorders, however a transfer of monolayer material was observed between the surfaces [34]. Beattie *et al.* [47] used total internal reflection (TIR) Raman spectroscopy to study octamethylcyclotetrasiloxane (OMCTS) and hexadecane molecules squeezed (~40 MPa) between a prism lens system, and observed that the liquids do not form any boundary layer under such conditions, rather they were squeezed out under modest applied pressures.

1.4 Difficulties in studying solid-solid contacts and possible solution

There are certain potential difficulties in studying these solid-solid contacts by spectroscopic techniques.

a) Accessing the contact region with light
b) Destruction of the sample/molecularly thin film under investigation from laser heating

c) Inadequate sensitivity of the techniques when small amounts of lubricant materials are studied (in our experiments ~ 5 $\times 10^9$ molecules of Zn arachidate were trapped between the two solid surfaces in a contact area of around 0.03 mm^2)
d) Difficulty of obtaining a reference beam for a background to be subtracted from the original spectrum

To access the contact region with light, one of the solids under investigation should be transparent. The chances of destruction of the sample or the film under investigation from laser heating can be reduced using total internal reflection (TIR) geometry, where the film sample is probed by an evanescent wave rather than a transmitted laser beam. The details of the TIR Raman spectroscopic setup and the ways the aforesaid difficulties have been overcome in our project will be discussed in chapter 3.

1.5 A literature study and a background for molecular tribology

The term 'tribology' was coined in the 1960s, however these ideas have been pursued for centuries [48]. With the advent of small devices, partly by the rapid development of silicon microfabrication techniques [49], novel problems appear that require knowledge of lubrication at the nanometer scale e.g. computer hard disks with coatings and lubricants [50] which protect the stored information, micrometer sized actuators, sensors and motors. Knowledge for performance optimisation is now an urgent need, which can be achieved by studying the molecular basis of lubrication [51].

Although the art of lubrication has been practiced since ancient times, and despite the voluminous works performed so far [5, 52-55], the absence of a fundamental understanding of the mechanism of friction and tribology still challenges the scientists. The main reason behind this lack of understanding is the difficulty in probing the molecules and the atomic processes taking place at the buried interface. A comprehensive review of boundary lubrication at solid-solid interfaces was included by Sarah Haydock

in her D.Phil thesis, 2002, Oxford University. Here I focus on some comparatively recent advancement in the field of tribology.

A few fundamental questions where we require a better understanding includes whether the motion between two bodies in contact is continuous (smooth sliding) or discontinuous (stick-slip), whether friction depends on the actual area of contact between a pair of materials, whether friction is related to adhesion [56], what are the behaviours of lubricant molecules at the interface, and how they are compressed and displaced during loading and shear, what is the mechanism of energy dissipation during sliding and of course the most important question that forms the basis for my PhD project, that how does the behaviour of lubricant depend upon their molecular structure and chemical identity. However, advancement of analytical techniques that allow us to probe the properties of thin molecular films at interfaces has created a lot of excitement in the recent years because now we have started to understand and answer a few of these fundamental questions. Appreciable advancements in the applications of quartz-crystal microbalance (QCM) [57-59] and extensions of surface force apparatus (SFA) [60, 61], and of course atomic force microscopy (AFM) [60-67] have brought new dimensions to the study of tribology, to measure frictional forces [68, 69] at the nano level. The developments in computational methods [70-72] have also contributed a lot in studying complex sophisticated atomistic models.

Molecular lubrication under confinement differs from usual lubrication of macroscopic bodies [73]. The variation of friction forces between two sliding surfaces with a variable gap is described by the Stribeck curve (Fig. 1.1.1) [52, 74]. This curve consists of three major regimes: hydrodynamic regime for thick lubrication film (combined with high velocities), mixed regime, and boundary lubrication regime at very small film thickness (less than 5 nm). The hydrodynamic regime possesses an extremely low friction coefficient, μ, defined as the ratio of lateral forces to a given normal load, and is in the range 10^{-4}–10^{-3}. Reducing the film thickness to a few-nanometer range results in a sharp (several orders of magnitude) increase of the friction coefficient to 10^{-1} – 1. Reduction of the friction coefficient to more reasonable values ($\sim 10^{-2}$) that allow sustainable sliding of

two surfaces in virtually intimate contact and a simultaneous resistance to wear damage is a challenging task.

The coefficient of friction, μ, is defined as the ratio of the force that maintains contact between an object and a surface and the frictional force that resists the motion of the object. Amonton's Law of Friction states that the amount of force needed to overcome friction between two surfaces only depends on the types of surfaces being pushed together and the amount of force pressing them together. The actual surface of contact between the two surfaces is not related to the friction force at all; the amount of force between the two surfaces and not the size of the sliding surfaces affects the friction. Practical engineering materials, however, are not perfectly flat: there are many millions of imperfections, crags, teeth and ridges at a microscopic level. When two surfaces come into contact, these tiny geographies do not match up correctly. The mountains on one side will not fit into the valleys on the other. The actual surface of contact is much smaller than what we estimate superficially. So the force needed to overcome friction is indeed proportional to the contact area measured accurately.

Classically, the friction forces are caused by junction shearing and plowing with first contribution being the most important for non-damaging regime of sliding [52, 74, 75]. The force, F, required to shear the junctions at the point of contact is defined as:

$$F = A.s \qquad (1.5.1)$$

where A is the actual contact area and s is the shear strength of the interface per unit area. Reduction in the friction forces and thereby the friction coefficient can be achieved by reducing the area of contact and shear strength. Reduction of the actual contact area can be achieved by surface engineering approaches. However, for the nanoscale contact areas in the microdevices, the only apparent way to reduce friction forces is the reduction of the interfacial shear strength. Logically, the application of organic and polymeric monolayers with low shear strength as boundary or molecular lubricants can reduce friction. However, lower shear strength means lower compression modulus, E, and thus, increasing contact area according to $A \sim E^{-2/3}$ (in Hertzian approximation) [76]. This results in a concurrent increase of friction and adhesive forces for surfaces in contact. In

addition, at the nanoscale contact area, when only tens of molecules are directly involved in direct surface-surface interaction, energy dissipation occurs along different paths. In this situation, to reduce friction forces, the amount of energy dissipated in the nanoscale contact area should be diminished by applying principles represented by Equation (1.5.1).

Confinement of ordered molecular films at the solid-solid interface is one of the procedures that reduce the energy dissipation in nanoscale contact, thereby reducing the friction. Ordered molecular films are generally obtained in six different mechanisms; (a) Langmuir- Blodgett (LB) films, (b) self-assembled monolayers (SAM), (c) molecular deposition (MD) film, (d) molecular beam epitaxial growth film, (e) vesicle fusion bilayer film and (f) shear-induced ordered film [77]. The following sections are focused primarily on the LB films and its properties (along with some important results obtained and conclusions drawn from study of SAMs), as this thesis mainly comprises of experiments with the LB monolayers as model boundary lubricants.

1.5.1 Effect of velocity

Studying the tribological properties of decane on steel surfaces, Bowden and Lenben [78] were able to show that the phenomenon of stick–slip is obvious at low speed. In stick stage, the friction coefficient decreases rapidly with increasing speed; however, in the slip stage, the friction coefficient decreases more gradually as the velocity increases. Moreover, as the velocity increases further, the variation in friction coefficient over the stick–slip cycle becomes almost constant and the fluctuations in the friction coefficient decrease. But van der Vegte *et al.* from their scanning force microscopy studies of unsymmetrical dialkyl sulphide SAMs formed on gold surface came up with a somewhat contrasting conclusion. They found that the friction-velocity relationship is such that the friction force initially increases with increasing velocity, reaches a maximum, and then tends to decrease. They also noted that the maxima of the friction forces shift to lower velocities (critical velocity) with increasing load and shift to higher velocities with increasing chain lengths [79]. Two explanations were proposed for this friction-velocity relationship but the nature of the friction maxima was not fully understood. The first

explanation was based on local phase transition in the layers which are induced by flow, although the nature of these phase transitions was unclear. The second proposal was based on a characteristic relaxation time for molecular interdigitation or entanglement. Van der Vegte and coworkers described their system by two characteristic times. One of them was the interdigitation (relaxation) time, τ_r which is connected with attainment of the equilibrium between two monolayers after the tip and surface come into contact and is generally dependent on the chain length, specific interactions and external pressure. The second was the time of contact between the tip and the surface, τ_{cont} which depend on the linear area of contact, *d* and get reduced with the increasing sliding velocity, *u*. τ_{cont} was expressed by the equation $\tau_{cont} = d/u$, and they concluded that the friction force maximum occurred when $\tau_{cont} = \tau_r$.

Wang Xinkuan *et al.* studied the frictional properties of perfluoro and non-perfluoro alkylsilane monolayers (SAM) by a ball-on-disk tribometer [80] and found that the friction coefficient increases with the increasing sliding velocity.

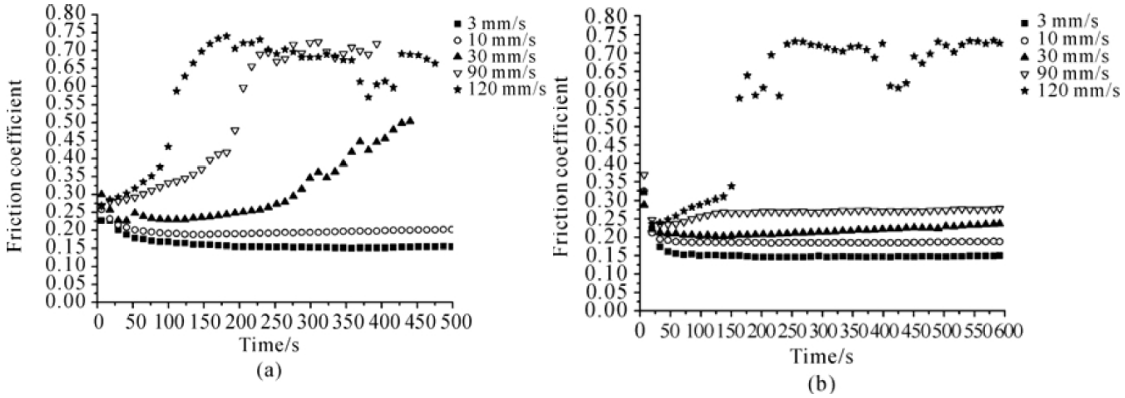

Figure 1.5.1: Effect of sliding velocity of a steel ball on frictional coefficient; Normal load= 40 gm; (a) Octyltrichlorosilane ($C_8H_{17}Cl_3Si$)/Si (b) 1H,1H,2H,2H-perfluorooctyltrichlorosilane ($C_8H_4Cl_3F1_3Si$)/Si [80].

AFM studies have been performed to find the correlation of friction and wear to sliding speed for the arachidic acid LB films deposited on pre-treated oxidised silicon (100) substrate at pH 9.3 with poly(dimethyl-diallyl-ammonium chloride) (PDAA) as counterion polymer [62]. Overney and coworkers found that, at low scan speeds (1.25–10

μm/s) and under conditions of constant normal pressure (ranging between 10–40 nN) and temperature, both the friction and wear of ultrathin organic films are functions of scanning speed and that the friction force decreases with increasing scanning speed. The behaviour of friction in this range could roughly be described with a power law of a negative exponent of –0.6.

Bhusan and Jahsman [81, 82] reported that the strength of many metals and nonmetals are greater at higher shear strains, and as a result posses a lower real contact area and therefore a lower friction coefficient at dry contacts. At high loads and sliding speeds, high interface temperatures can significantly reduce the strength of most materials [83]. However, localized surface melting can reduce the shear strength and friction coefficient drops to a lower value. According to Fridmen and Levesque [84] this reduction in friction is partly due to the negative slope of the dependence of the friction force with sliding velocity. At higher sliding speeds the time during which the opposite surface asperities press each other is reduced and this increases the separation between the two surfaces and reduces the real area of the sliding contact resulting in a reduction in friction force. In other way, with increased rotational speed, the momentum is transferred in the upward normal direction resulting in the separation of the two sliding surfaces.

1.5.2 Effect of Load

Bowden and Lenben observed that the friction force of LB films increases with increasing load [78]. However, some results obtained by Kohno *et al.* [85] showed that if the LB film is thicker than a monolayer, the friction coefficient is essentially independent of the load over the range of loads investigated in agreement with Amonton's second law. Meyer *et al.* reported an independence of frictional force on loads at loads below certain thresholds [86] from their FFM studies on LB films. They noted that on increasing the load from 1–10 nN only small changes in frictional force on the LB films were measured, which they considered to be constant as a first approximation (figure 1.5.2).

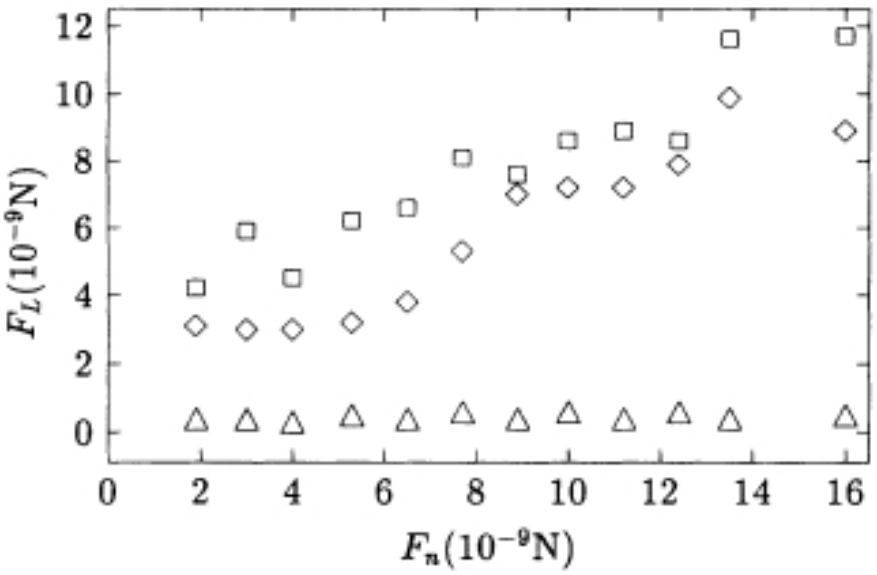

Figure 1.5.2: Lateral forces F_L between probing tip and sample as a function of normal forces, F_n. Data points were measured on the flat, film-covered areas (Δ), at the step edges (□), and on the substrate (◊). The lateral forces at the step edges and on the substrate increased with load whereas these forces remained constant on the flat areas of the film [86]

Meyer *et al.* explained this observation at low loads (1−10 nN) by Eyring's model of boundary lubrication, where a friction is a function of the form

$$F_L = F_0 + \alpha F_n \qquad (1.5.2)$$

Here F_L is the lateral (friction) force, F_0 is a constant force, F_n is the applied normal force and α is proportionality constant. A small value of α as measured for monolayers of fatty acids [87] resulted in a constant frictional force within the load range 1−10 nN.

Friction force microscopy (FFM) studies carried out by Fujiwara *et al.* [88] showed the microscopic frictional properties of two kinds of LB films (a) 2-docosylamino- 5-nitropyridine, (b) barium arachidate. They found that if the normal load is small, the friction force is directly proportional to the normal load. When the normal load is relatively large, the friction force increases as the 2/3 power of the normal load. Moreover, the friction coefficient of the LB film is decreased if the alkyl chains are tilted. This can be explained by an increase in the limiting area of the adhering molecule. Also it was found that the load dependence of the frictional responses of the LB films is

simultaneously dependent on film forming material and its thickness. Recently Wang *et al.* arrived at a somewhat different conclusion from their ball-on-disk tribometer experiments on perfluoro and non-perfluoro alkylsilane coated silicon surfaces [80]. They found that the friction coefficient first decreases with increase in normal load and then increases with increasing normal load beyond a critical normal load. They believed that as the normal load increased the molecular films were more compliant to endure shear force, and consequently less energy was required and the friction coefficient decreased gradually. However the friction force increased with loads in sliding at higher loads as very high normal loads induced failures of the molecular films.

1.5.3 Effect of number of layers

There is a threshold in the number of layers of LB film, for a given environment and substrate, for effective lubrication [52]. Below this threshold, the greater the number of layers, the better the lubrication performance of LB film. On the other hand, above this threshold, the number of layers in the LB film has no effect on its frictional properties. The frictional studies of ω-tricosenoic acid LB films of different layers deposited on Cr surface by AFM and FFM [89] showed that the friction coefficient of a five-layer LB film is approximately same as that of the three-layer LB film but for the monolayer LB film, the value is lower. Hence we can consider that the number of layers in LB film could affect the lubricity of film if it is below a threshold value. The top two bilayers of a 5 layered LB film was scratched with an AFM tip and the etching time of the layers suggested that the interaction between the hydrophobic tails were weaker than the interaction between the hydrophilic heads and between the first monolayer and the Cr substrate. The ambient and warm/wet contact start-stop experiment carried out by Fengqiu Fan *et al.* on LB multilayers of a fluorinated polymer, poly(*N*-1H,1H-pentadecafluorooctylacrylamide) deposited on hard disk confirmed that a 3-layered LB film of the polymer on a hard disk is durable enough for practical use [90] as they formed stable and uniform polymer film. Fan *et al.* suggested that in order to increase the durability of LB films, it may be a good way to have an LB film with stronger interaction with the disk overcoat.

1.5.4 Effect of chain lengths

Levine *et al.* observed that friction coefficient of carboxylic acid films of chains with 6–14 carbon atoms decreased with increasing number of carbon atoms. However, no significant change in the friction coefficient was observed for chains with over fourteen carbon atoms [91]. Dominguez *et al.* [92] investigated the frictional properties of long-chain carboxylic acid monolayers with 12–26 carbon atoms deposited on glass and steel surfaces. That the friction coefficient is independent of the chain length can be explained as a consequence of the fact that all monolayers have surface densities equal to or greater than a threshold of surface density (5 molecules/nm^2). However, the durability of these monolayers is dependent on the hydrocarbon chain length, surface density of the film, film thickness, and substrate material, but independent of the slider material. SFM studies of n-alkanethiolates chemisorbed at Au(111) to function as boundary lubricant, carried out by McDermott *et al.* [93] revealed similar results, that longer chain monolayers exhibit a markedly lower friction and a reduced likelihood to wear than shorter chain monolayers. More extensive cohesive interactions exist between the chains in case of longer chain alkyl groups and hence their ability to retain molecular scale order during shear, which leads to a lower order friction. Lio *et al.* [61] performed a comparative study of frictional properties of alkanethiols and alkylsilanes as a function of chain length on monolayers produced on Au(111) and mica, respectively, by AFM. They showed that with more than 8–11 carbons in the chain, the frictional property was quite similar, and independent of long range order and head group linkages. However for the chains below 8 carbons, they observed a strong dependence of chain lengths on frictional properties. For shorter chain alkyl groups, the silanes exhibited higher friction than the thiols. Arguably in going from thiols to silanes, the disorder increased, that supported the number and type of low-energy modes (kinks, bendings, and distortions) that were available for excitation and energy dissipation. Fan *et al.* [94] found that the friction coefficient of the fluorinated polymer LB films decreases with increasing fluoroalkyl chain length. They suggested that the surface with lower critical surface energy could give smooth surface with lower friction coefficient in the fluorinated polymer LB films.

1.5.5 Effect of substrates

The physical and chemical properties of the substrates determine the nature of adsorption and strength of LB films formed on it and this can influence the tribological properties. For example, adsorption of carboxylic acid on glass is better than that on steel and the friction coefficient on glass is approximately half of that on a steel surface [92]. Thiolipids are covalently bound on gold surfaces but physisorbed on mica, as an outcome the tribological properties of the former are better than the latter [95].

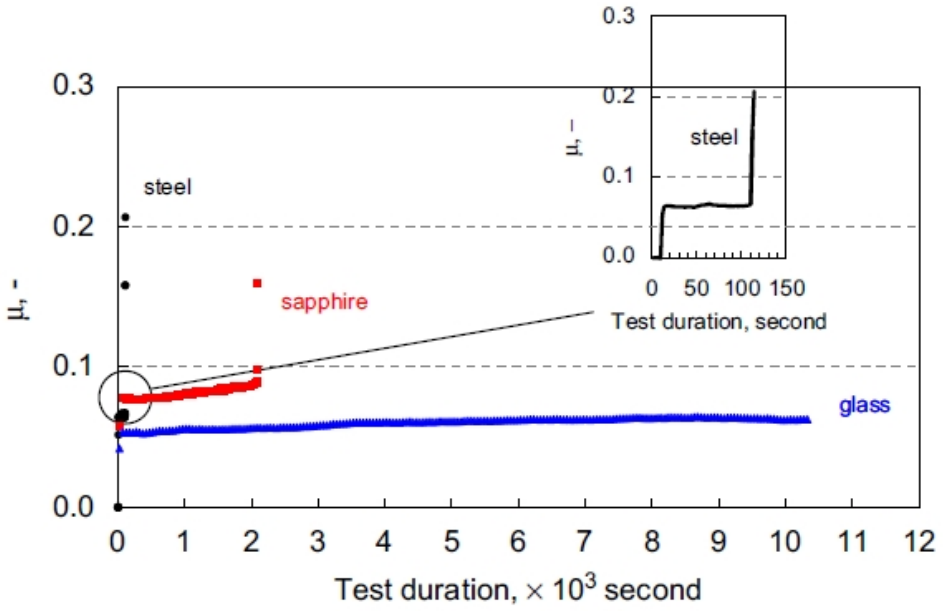

Figure 1.5.3: Effect of ball material on the durability of monomolecular film [96]

Recently Minami *et al.* examined the influence of ball material on the tribological properties [96], by sliding steel, sapphire and glass balls against a flat silicon surface coated in an LB monolayer of stearic acid ($C_{17}H_{35}COOH$). 40 mN loads were applied on all the balls while sliding with a reciprocating frequency of 20 Hz and amplitude 1.5 mm. The influences of the ball material on the lifetime of the monolayer films are shown in fig. 1.5.3. The friction force of the steel ball increased within the test duration of 100 s (2000 cycles), a sapphire ball provided a longer lifetime of 2100 s, and the glass ball provided an excellent lifetime of more than 10,000 s. The glass ball also provided low friction coefficient (approximately 0.06) throughout the tribo-test which can be explained

by low contact pressure (470 MPa) for the ball material and better affinity for carboxylic acid. The steel ball (applied pressure = 670 MPa) also provided a low friction coefficient of 0.06 at steady state but the duration was short. The sapphire ball gave a higher friction coefficient on the range 0.07–0.09 which can be attributed to the higher contact pressure (710 MPa) for the same applied load. From their observations, Minami *et al.* proposed a mechanism of durability of monolayer films (figure 1.5.4) where due to mechanical stress the monomolecular films were removed from the flat Si surface and a better transfer of film to the ball surface reduced friction and enhanced durability in the sapphire and glass balls. This affinity of carboxylic acid for the ball material influenced the transfer phenomenon.

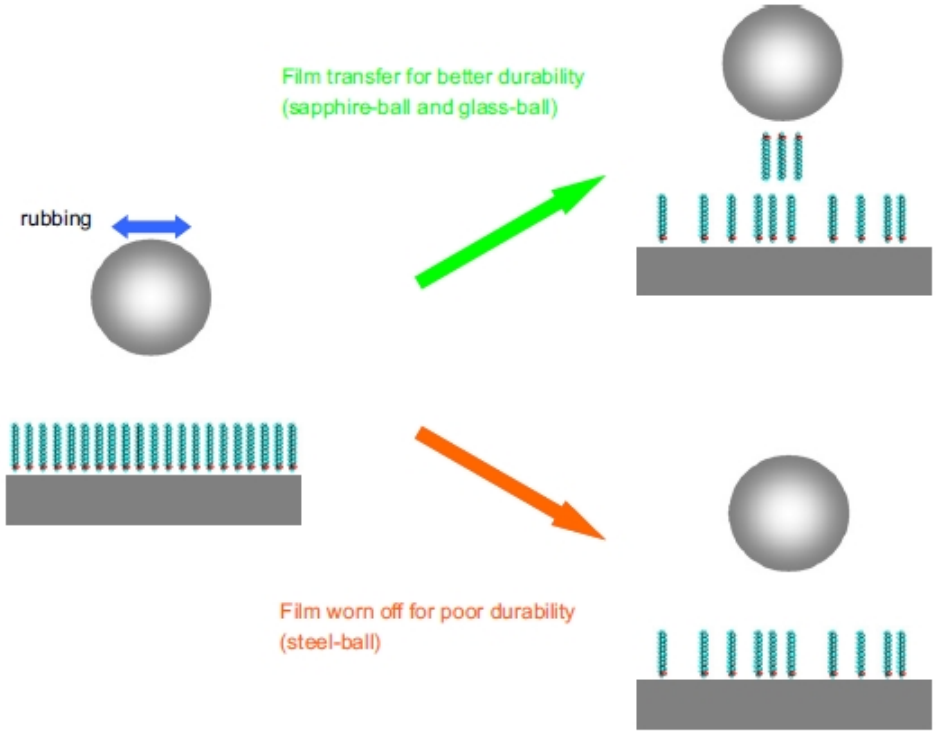

Figure 1.5.4: A proposed mechanism for durability of monomolecular film [96].

Friction converts kinetic energy into lattice vibrations. In order to study its mechanism, Robert Carpick and coworkers carried out AFM measurments by changing the mass of the terminating atoms on a surface and hence their vibrational frequencies [97] which affected to nanoscale friction significantly. They compared hydrogen and deuterium

terminated single-crystal diamond and silicon surfaces and in both the cases hydrogenated surface exhibited higher friction which implied that the lower natural frequency of the chemisorbed deuterium reduced the rate at which the tip's kinetic energy was dissipated.

1.5.6 Effect of subphase

Both the Young's modulus and the frictional force decrease on increase of the pH of the subphase of a monolayer film composed of a mixture of behenic acid and partially fluorinated carboxylic acid ether [98]. This is partly due to that the pH of the subphase of the LB film influences the film forming density as well as the order and roughness of the film.

1.5.7 Effect of electric field

SFM studies of the microtribological properties of LB monolayers of arachidic acid in AC and DC electric fields revealed that the friction and wear characteristics of LB films can be controlled and improved by an external electric field [99]. In a DC field, the frictional force increased with the DC voltage, and the wear-life was significantly shortened. However, in an AC field at 130 V and 19 kHz, the frictional force was nearly zero, and the wear-life of the LB film was highly extended. Liu and coworkers [99] suggested that this may be related to the surface charge and mechanical vibration of the cantilever, induced by the external AC electric field. In an AC field, the material difference between the tip and the films caused the surface charges on them to exhibit phase-differences, i.e. they showed time-lag properties. Therefore, at certain frequency, such as 19 kHz, both the tip and the cantilever may have had the same surface charge, which in turn lead to the transient repulsive force. The repulsive force reduced the normal load and the friction force was reduced.

1.5.8 Effect of film forming material

LB films of fatty acids, e.g. stearic acid, arachidic acid and behenic acid, and of MoS_2 nanoparticles modified with diakyldithiophosphate (DDP) were deposited on a glass substrate [36, 100] and the tribological properties of the LB films were studied by Zhang *et al.* They found that the LB films of fatty acids and surface-modified MoS_2 nanoparticles all decrease the friction coefficient of a glass/steel pair. Compared to the fatty acid LB films, the surface modified MoS_2 nanoparticles–DDP LB film has a larger antiwear life and load-carry capacity. This can be attributed to the load-carrying capacity of the MoS_2 nanoparticles. Reich and Der [101] investigated the influence of polymerization on the mechanisms of lubrication of polymeric and monomeric LB films of the cadmium salt of 10,12-tricosadiynoic acid and found that the pin-on-disk wear rate of the LB film increases when the film is polymerized by ultraviolet light, and also the friction coefficient of a surface can decrease from 0.6 to 0.1 when a polymer monolayer is deposited on a surface. Mohammod Aminuzzaman *et al.* have recently attempted to improve the tribological properties of a fluorinated polymer nanosheet by chemical immobilisation. Langmuir-Blodgett monolayer of N-(1H,1H-Pentadecafluorooctylmethacrylamide) copolymers containing carboxyl group as a reactive moiety form a highly ordered reactive fluorinated polymer nanosheet which was immobilised onto solid substrates through chemical binding with an aminosilane coupling agent [102].

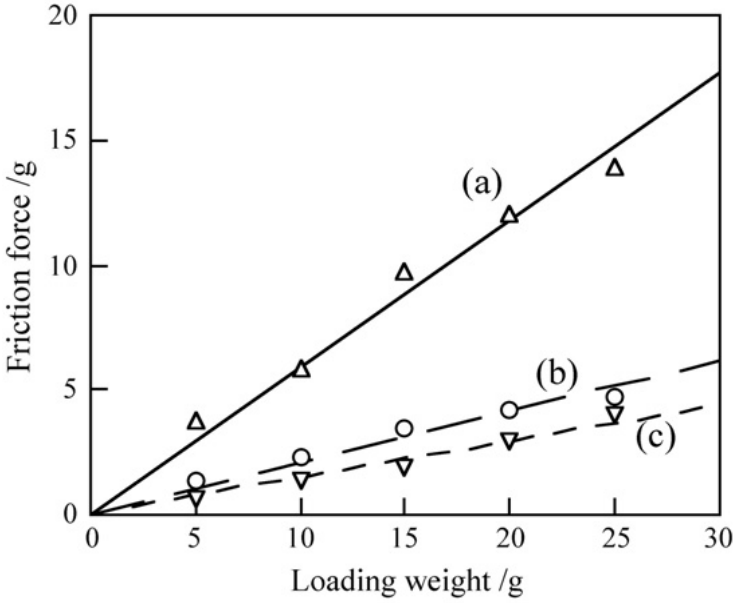

Figure 1.5.5: Friction force vs loading weight for (a) glass substrate, (b) uncoupled nanosheet onto glass substrate and (c) immobilised nanosheet onto aminosilane modified surface [102].

Figure 1.5.5 shows the plot of friction force against loading weight for glass substrate, uncoupled nanosheet onto glass surface and immobilised nanosheet onto aminosilane modified surface as obtained by Aminuzzaman and coworkers. The plot indicated the lowest friction force was obtained for chemically immobilised polymer nanosheet against applied loads. Surface roughness affects the friction characteristics of ultrathin films on micro/nanoscale [94, 103], and the reduction in friction with chemical immobilisation of the nanosheet can be attributed to the reduced surface roughness compared to the uncoupled polymer nanosheet as confirmed by AFM images.

1.5.9 Effect of conformational order of organic thin films

Perry *et al.* [104] studied the variation of interfacial friction properties with molecular packing on the surface and related conformational order in a series of SAMs. The degree of order was varied by varying both the chain lengths and chain densities by adsorption of a series of spiroalkanedithiols and a single structurally related normal alkanethiol onto gold surface. X-ray photoelectron spectroscopy revealed that the films varied widely in interfacial structures and conformational orders. AFM studies revealed that the

correlation between measured frictional properties and conformational order of the films are defined by the mechanisms of energy dissipation in organic films, involving a number of factors, such as the effective area of contact, the local elastic modulus, and the presence of conformational defects at sliding interfaces. They also concluded that the organic structures that inherently posses a greater number of conformational defects at room temperature, also posses less resistance to defect creation under action of a contacting surface, hence exhibit higher frictional properties. Khatri *et al.* recently showed from their nanotribometer studies on alkyl silane SAMs on rough Al surfaces, that the friction coefficient, $\mu_{0,}$ at the commencement of sliding is independent of the normal load, but is correlated to the initial conformational order of the SAM, which they varied by changing the alkyl chain lengths and treatment of heat on the monolayer [38].

1.5.10 Effect of end groups

The connection between chemical nature, adhesion and friction was established by Frisbie *et al.* [105] in 1994. They demonstrated different adhesive forces between surfaces (tip and substrate) coated with molecules exposing a variety of end groups: CH_3/CH_3, CH_3/COOH, and COOH/COOH. The adhesive forces were found to decrease in the order COOH/COOH>CH_3/CH_3>COOH/CH_3 with the corresponding friction forces following exactly same order. The interaction between hydrophilic groups forming hydrogen bonds is stronger than that between hydrophobic groups, whereas the hydrophobic–hydrophilic interaction will be the weakest. Similar results were attained by Brewer *et al.* [106] using friction force microscopy (FFM). AFM was used by Kim *et al.* [107] to study the frictional properties of SAMs formed by the adsorption of methyl-, isopropyl-, and trifluoromethyl- terminated alkanethiols on Au(111) surfaces. They also studied the mixed monolayers of varying concentrations of methyl- and trifluoromethyl-terminated thiols. They observed a substantial increase in the frictional response for films with isopropyl- and trifluoromethyl- terminating groups, and also for mixed monolayers which contained small concentrations of trifluoromethyl- terminated component, where the films only differed in their outermost chemical reactivity, characterised by a well packed backbone structure. There results prominently support that the difference in

frictional forces here were due to difference in terminal group sizes, and that the larger terminal groups in the films which have same lattice spacing gives rise to increased steric interactions that allow better energy dissipation during sliding, hence a higher friction.

Frictional forces are also dependent on the functional groups at the solid/air interface [108]. The terminal functional group can affect the wettability of the surface. Under conditions of high humidity, the frictional force for hydrophilic surfaces is decreased due to the lubricating effect of water, whereas for hydrophobic surfaces, the friction force is increased by increased adhesion in the contact zone. Recently good methods were reported to improve the tribological properties of polymer films by chemisorption of molecules with lower surface energy. Ren *et al.* [109] generated heptafluorobutyric anhydrite (HFBA) derivatised film on polyethyleneimine (PEI) surface in presence of a chemical amide bond, where the HFBA derivatised film possessed good friction reducing and adhesion-resistant property due to hydrophobicity and low surface energy.

1.5.11 Results from Molecular dynamics (MD) simulations

MD simulations were used to simulate the sliding of a model bilayer LB film in order to investigate the friction between two-LB monolayers of model alkane chains [110]. Glosli *et al.* found that there are two kinds of energy dissipation mechanisms; one is continuous, known as viscous mechanism, similar to the energy dissipation of liquid viscosity, and the other is discontinuous, known as plucking mechanism, describing a simple thermal activation model in which stored strain potential energy is converted into thermal energy.

MD simulation results of sliding friction for LB monolayers of perfluorocarboxylic and hydrocarboxylic acid on SiO_2 obtained by Koike and Yoneya [111] revealed that the friction coefficient of the former is about three times as large as that of the latter which supports the existing experimental results. They suggested that the difference in the friction coefficient was mainly due to the differences in the 1–4 van der Waals interaction and that the friction coefficient was roughly proportional to the difference in the potential energy fluctuation between the shear and equilibrium conditions. In spite of the fact that

perfluoro polymers greatly reduce the friction coefficient of a surface, both the experimental and simulation results show a high friction coefficient for the fluorocarbon LB films. It is suggested that the friction mechanisms for small molecular films and polymeric films are quite different. For polymers, a long-ranged repulsive interaction caused by the excluded volume plays a more important role than the intramolecular interactions. Therefore an increase in configurational entropy contributes to the reduction in friction. However, this is not true for dense polymer films in absence of a solvent.

Tutein *et al.* [72] performed classical molecular dynamics simulations to examine the compression and friction of monolayers composed of linear hydrocarbon chains of 8, 13 and 22 carbon atoms, which were chemically bound to diamond(111) surface. They confirmed that the structural defects play an important role in compression friction and energy dissipation processes. They found that the number of defects increase with increasing load, reaching a plateau at a specified load. Similar MD simulations performed by Mikulski *et al.* [71] on a model system of 18 carbon alkane chain covalently bound to diamond (111) surface with (a) a tightly packed (2×2) arrangement and (b) a loosely packed system with ~30% fewer chains. They found that under high loads, the tightly packed monolayer exhibited lower friction than the loosely packed monolayer. They supported this observation by the argument that sliding initiates larger bond length fluctuations in loosely packed systems, causing more energy dissipation via vibration, and hence more friction. Mikulski *et al.* also studied the friction between an amorphous carbon tip and two n-alkane thiol SAMs deposited on Au(111) and found that the monolayers composed of C_{13} chains (or odd numbered C atoms in the alkyl chain) had higher friction than those composed of C_{14} chains (or even numbered C atoms in the alkyl chain) [112] while sliding in the direction of the chain tilt. This difference in friction became more pronounced on application of higher loads. Difference in contact forces between the chains and the tip together with the differences in conformations between the two types of chains as shown in the simulation snapshot in figure 1.5.6 resulted in the difference in friction forces.

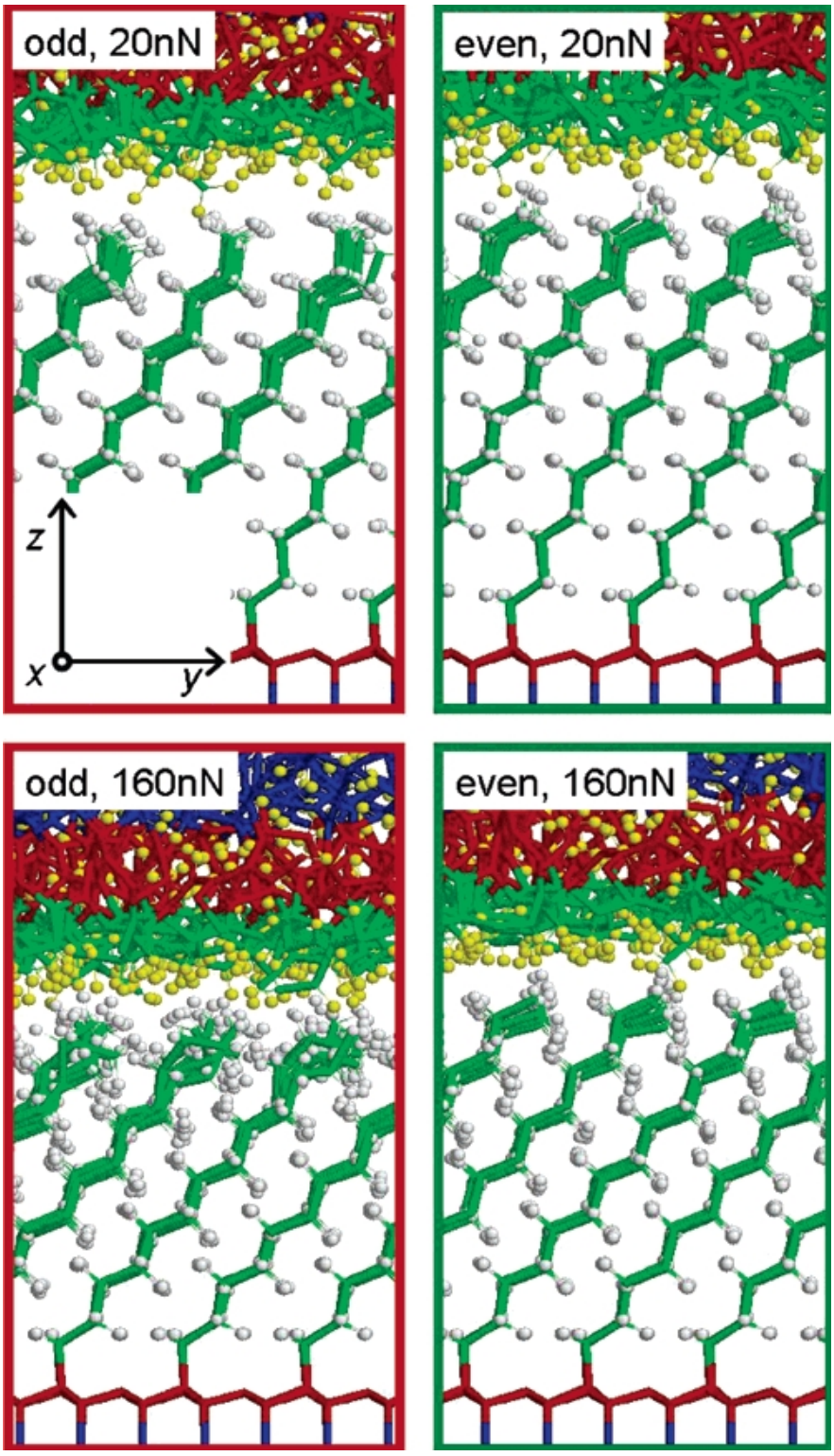

Figure 1.5.6: Snapshots of model system under investigation performed by Mikulski and coworkers [112] for different monolayer types and loads. Atoms in the blue and red regions were held rigid and thermostated, respectively. Wireframe format represented carbon atoms. Hydrogen atoms of the monolayers and tip were represented in white and yellow, respectively. Sliding is in the *y*-direction.

1.5.12 Our approach to studying molecular tribology

From the above discussions, it is quite evident that information about the frictional forces, adhesion and cohesion at the solid-solid interface can be obtained successfully by use of AFM, FFM, SFA, nanotribometer etc. But to correlate to what exactly happens in a tribological contact in a molecular scale in a lubricant film, with respect to angle of alkyl chain tilt, origin of defects in packing of the monolayer films, to the macroscopic friction with the increase/decrease of pressure and sliding velocity, vibrational spectroscopy appears to the potentially best approach. Thompson and Pemberton [113] used Raman spectroscopy to characterise octadecylsilane and stearic acid layers on Al_2O_3 surfaces *ex situ*. Sum frequency spectroscopy (SFS) and Raman spectroscopy have been used by our group in the past to characterise the Langmuir-Blodgett (LB) monolayers of Zn arachidate in the solid-solid interface e.g. CaF_2/MgF_2 [31], sapphire/silica [34] and found that the high conformational order is retained even at pressures as high as ~600 MPa. The relative intensity of the Raman signal in the Zn arachidate monolayer at the solid-solid interface have been explained in terms of the relative interfacial electric field strengths [31]. This was the first report of an unenhanced Raman spectra obtained successfully from a solid-solid interface. In continuation with these findings, in order to examine the molecular changes which accompany the different frictional responses in the macroscopic scale, developments were continued in the total internal reflection (TIR) experimental geometry/setup where Raman spectroscopy has been extensively used as a tool for the study of molecular tribology of model boundary lubricants, and will be discussed in the following chapters. The following chapter 2 contains the theory that forms the basis of the experiments included in this thesis where the behaviour of electric fields at the interface and the theories associated with linear optics and Raman spectroscopy have been discussed. In chapter 3, the development of total internal reflection (TIR) Raman spectroscopy experiments has been described. Langmuir-Blodgett (LB) films of fatty acids and lipid monolayers form the model boundary lubricants studies in this thesis and a brief study of monolayer history together with the LB deposition techniques used in this project and LB isotherms have been discussed in chapter 4. Chapter 5 comprises of the TIR Raman spectra of the model boundary

lubricants obtained at static contacts at different pressures from solid-solid interfaces and their characterisations. In chapter 6, the development of two multi-purpose Raman tribometers for the purpose of performing sliding contact experiments at applied pressures and shears in presence of desired lubricants have been discussed. The results obtained from different experiments performed in the elasto-hydrodynamic lubrication regime and boundary lubrication regime with the designed Raman tribometers are described in chapter 7. In chapter 8, the study of tribology of supported lipid bilayers have been attempted which includes a brief literature review of lipid bilayer/phospholipid tribology, their applications in biology and the experiments carried out and results obtained with our TIR Raman set up.

References:

1. Williams, J.A., *Engineering Tribology.* 1994(Oxford: Oxford University Press).
2. Reynolds, O., Phil. Trans. Roy. Society, 1886. **177**: p. 157.
3. Bosman, R., and Schipper, D.J., *Microscopic Mild Wear in the Boundary Lubrication regime.*
4. Hardy, W.B., Proceedings of the Royal Society of London Series a-Containing Papers of a Mathematical and Physical Character, 1922. **100**(707): p. 550-574.
5. Bhusan, B., Handbook of Micro/nanotribology, Chemical Rubber 1995(Boca Rotan).
6. Kronberg, B., *Surfactants in Tribology* Vol. 1: CRC Press 2008.
7. Gauvin, M., Dassenoy, F., Minfray, C., Martin, J. M., Montagnac, G., and Reynard, B., Journal of Applied Physics, 2007. **101**(6).
8. Li, Y.R., et al., Tribology Letters, 2007. **28**: p. 319-328.
9. Li, Y.R., et al., Tribology Letters, 2008. **29**(3): p. 201-211.
10. Nicholls, M.A., et al., Tribology International, 2005. **38**(1): p. 15-39.
11. Onodera, T., et al., Applied Surface Science, 2009. **256**(4): p. 976-979.
12. Shakhvorostov, D., Muser, M. H., Song, Y., and Norton, P. R., Journal of Chemical Physics, 2009. **131**(4).

13. Bailey, A.I., and Courtney-Pratt, J.S., Proceedings of Royal Society London A, 1954. **227**: p. 501.
14. Rabinowitz, E., and Tabor, D., Proceedings of Royal Society London A 1951. **208**: p. 455.
15. Nicholls, M.A., et al., Tribology Letters, 2004. **17**(2): p. 205-216.
16. Singh, R.A., et al., Wear, 2008. **265**(1-2): p. 42-48.
17. Tanahashi, K., Y. Laboratory, and T. Yamamoto, Surface & Coatings Technology, 1998. **100**(1-3): p. 260-263.
18. Jarzabek, D., Z. Rymuza, and N. Ohmae, International Journal of Materials Research, 2009. **100**(7): p. 973-977.
19. Meyer, E., Overney, D., Bordbeck, L., Howald, R., Luthi, R., Frommer, J., and Guntherodt, H.-J., Physical Review Letters, 1992. **69**(12): p. 1777.
20. Leggett, G.J., Nicholas J. Brewer and Karen S. L. Chong Physical Chemistry Chemical Physics, 2005. **7**: p. 1107-1120.
21. Burke, S.A. [cited; Available from: http://www.physics.mcgill.ca/~burkes/coursework/FFM/FFMreview.pdf.
22. Bhusan, B., *Handbook of Nanotechnology*. 2nd ed: Springer.
23. Butt, H.-J., Biophysical Journal, 1991. **60**: p. 1438.
24. Zauscher, S., and Klingenberg, D.J., Colloids and Surfaces A: Physicochemical and Engineering Aspects, 2001. **178**: p. 213-229.
25. Bastidas, J.C., Pawlak, J.J., Venditti, R.A., Heitmann, J.A. Hubbe, M.A., and Kadla, J.F., Materials Characterisation, 2008. **59**: p. 144-150.
26. Drummond, C., M. In, and P. Richetti, European Physical Journal E, 2004. **15**(2): p. 159-165.
27. Zhao, B.X., et al., Langmuir, 2008. **24**(4): p. 1517-1524.
28. Zhu, Y.X., et al., Tribology Letters, 2003. **15**(2): p. 127-134.
29. Leckband, D.E. *http://www.scs.illinois.edu/leckband/pmwiki.php/Research/SurfaceForceApparatus*. [cited.
30. Johnson, K.L., Proceedings of the Institution of Mechanical Engineers, Part C: Journal of Mechanical Engineering Science, 2000. **214**: p. 11.

31. Beattie, D.A., S. Haydock, and C.D. Bain, Vibrational Spectroscopy, 2000. **24**(1): p. 109-123.
32. Street, K.W., Analytical Letters, 2008. **41**(3): p. 351-376.
33. Beattie, D.A., Winget, S.A., and Bain, C.D., Tribology Letters, 2007. **27**: p. 159-167.
34. Beattie, D.A., Fraenkel, R., Winget, S.A., Peterson, A., and Bain, C.D., Journal of Physical Chemistry B, 2006. **110**: p. 2278-2292.
35. Du, Q., Xiao, X.-d., Charych, D.,Wolf, F., Frantz, P., Shen, Y.R., and Salmeron, M., Physical Review B, 1995. **51**(12): p. 7456-7463.
36. Zhang, P., Xue, QJ., Du, ZL., Zhang, ZJ., Wear, 2000. **242**: p. 147-151.
37. Khatri, O.P., and Biswas, S.K., Surface Science, 2006. **600**: p. 4399-4404.
38. Khatri, O.P., Colin D. Bain and Sanjay K. Biswas, Journal of Physical Chemistry B, 2005. **109**: p. 23405-23414.
39. Greene, P.R., and Bain, C.D., Spectroscopy Europe, 2004. **16**: p. 8-15.
40. Jaoul, C., Jarry, O., Tristant, P., Merle-Mejean, T., Colas, M., Dublanche-Tixier, C., and Jacquet, J. M., Thin Solid Films, 2009. **518**(5): p. 1475-1479.
41. Sahoo, R.R. and S.K. Biswas, Thin Solid Films. **518**(21): p. 5995-6005.
42. Jiang, S., S.C. Bae, and S. Granick, Langmuir, 2008. **24**(4): p. 1489-1494.
43. Berg, O. and D. Klenerman, Journal of the American Chemical Society, 2003. **125**(18): p. 5493-5500.
44. Chen, C., Wang, J., Even, M., and Chen, Z., Macromolecules, 2002. **35**: p. 8093-8097.
45. Bain, C.D., Journal of the Chemical Society Faraday Transactions, 1995. **91**: p. 1281-1296.
46. Lambert, A.G., Davies, P.B., and Neivandt, David J., Applied Spectroscopy Reviews, 2005. **40**: p. 103-145.
47. Beattie, D.A., Winget, S.A., and Bain, C.D., Tribology Letters, 2007. **27**: p. 159.
48. Dowson, D., *History of Tribology.* Longman, 1979(London).
49. Howe, R.T., Muller, R.S., Gabriel, K.J., Trimmer, W.S.N., *IEEE Spectrum.* 1990. **27**: p. 29.
50. Grochowski, E., Hoyt, R.F., IEEE Transactions on Magnetics, 1995. **32**: p. 1850.

51. Maboudian, R., Howe, R.T., Journal of Vacuum Science & Technology B, 1997. **15**: p. 1.
52. Bowden, F.P., Tabor, D., *Friction and lubrication of solids: Part 1.* 1950(Oxford University Press).
53. Bowden, F.P., Tabor, D., *Friction and lubrication of Solids: Part 2.* 1964(Oxford University Press).
54. Hutchings, I.M., *Tribology.* 1992(CRC Press: Boca Raton).
55. Singer, I.L., Pollock, H.M., Eds, *Fundamentals of Friction: Microscopic and Macroscopic processes.* Kluwer, Dordrecht, 1992.
56. Yoshizawa, H., You-Lung Chen, and Israelachvili, J., Journal of Physical Chemistry, 1993. **97**: p. 4128-4140.
57. Daly, C., Krim, J., Physical Review Letters, 1996. **76**: p. 803.
58. Krim, J., Solina, D.H., Chiarello, R., Physical Review Letters, 1991. **66**: p. 181.
59. Watts, E.T., Krim, J., Wisdom, A., Physical Review B, 1990. **41**: p. 3466.
60. Fujihira, M., Kawate, H., Journal of Vacuum Science & Technology B, 1994. **12**(3): p. 1604-1608.
61. Lio, A., Charych, D.H., and Salmeron, M., Journal of Physical Chemistry B, 1997. **101**: p. 3800-3805.
62. Overney, R.M., Takano, H., Fujuhira, M., Mayer, E, Guntheradt, H.J., Thin solid films, 1994. **240**: p. 105-109.
63. Yang, X., Perry, S.S., Langmuir, 2003. **19**: p. 6135-6139.
64. Zhang, Q., Lynden A. Archer, Journal of Physical Chemistry B 2003. **107**: p. 13123-13132.
65. Shon, Y.-S., Lee, S., Colorado, R, Jr., Perry, S.S., and T. Randall Lee, Journal of American Chemical Society, 2000. **122**: p. 7556-7563.
66. Barrena, E., Ocal, C., and Salmeron, M., Journal of Chemical Physics, 2000. **113 No. 6**: p. 2413-2418.
67. Wang, Y., Lieberman, M., Langmuir, 2003. **19**: p. 1159-1167.
68. Israelachvili, J.N., McGuiggan, P.M., Homola, A.M.,, Science, 1988. **240**: p. 189.
69. Peachey, J., Van Alsten, J., Granick, S., S. Rev. Sci. Instrum., 1991. **62**: p. 463.

70. Harrison, J.A., Brenner, D.W., Handbook of Micro/nanotribology, Bhusan, B. Ed; CRC Press; Boca Raton, 1995: p. 397.
71. Mikulski, P.T., Harrison, J.A., Journal of American Chemical Society, 2001. **123**: p. 6873-6881.
72. Tutein, A.B., Stuart, S.J. and Harrison, J.A., Langmuir, 2000. **16**: p. 291-296.
73. Tsukruk, V.V., Advanced Materials, 2001. **13**(No. 2): p. 95-108.
74. Rabinowicz, E., *Friction and Wear of Materials*. Wiley, New York, 1995: p. 1965.
75. Persson, B., Surface Science Reports, 1999. **33**: p. 83.
76. Kluwer, D., *Fundamentals of Friction.* (Eds: E. Singer, H. Pollack), 1998(The Netherlands).
77. Zhang, S.-W., Hui-qing Lan, Tribology International, 2002. **35** p. 321-327.
78. Bowden, F.P., Lenben, L., Philosophical Transactions of Royal Society A, 1939. **239**: p. 1-27.
79. van der Vegte, E.W., Subbotin, A., and Hadziioannou, G., Langmuir, 2000. **16** p. 3249-3256.
80. Wang, X., et al., Journal of Wuhan University of Technology--Materials Science Edition, 2009. **24**(4): p. 588-593.
81. Bhusan, B., and Jahsman, W.E., International Journal of Solids and Structures, 1978. **14**: p. 39-51.
82. Bhusan, B., and Jahsman, W.E., International Journal of Solids and Structures, 1978. **14**: p. 739-753.
83. Bhusan, B. in *Proc. Seventh Leeds-Lyon Symposium on Tribology*. 1981: IPC Business Press, Guildford, UK.
84. Fridman, H.D., and P. Levesque, Journal of Applied Physics , 1959. **30**: p. 1572-1575.
85. Kohno, A., Sugiura, M., Mori, M., Journal of Japanese Society of Lubrication Engineers, 1987. **32**: p. 225.
86. Meyer, E., et al., Physical Review Letters, 1992. **69**(12): p. 1777.
87. Briscoe, B.J., and Evans, D.C.B., Proceedings of Royal Society London A, 1981. **380**: p. 389.

88. Fujiwara, I., Kamei, T., Seto, J., Japanese Journal of Applied Physics, 1995. **34**: p. 4932.
89. Fujihira, M., and Takano, H., Journal of Vacuum Science & Technology B, 1994. **12**(3): p. 1860-1865.
90. Fan, F.Q. and Miyashita, T., Thin Solid Films, 2003. **434**(1-2): p. 239-243.
91. Levine, O., Zisman, WA., Journal of Physical Chemistry, 1957. **61**: p. 1068-1077.
92. Dominguez, D., Mowery, RL., Turner, NH., Tribology Transactions, 1994. **37**(1): p. 59-66.
93. McDermott, M.T., John-Bruce D. Green and Marc D. Porter, Langmuir, 1997. **13**: p. 2504-2510.
94. Fan, F., Li, XD., Miyashita, T., Thin solid films, 1999. **348**: p. 238-241.
95. Santesson, L., Wong, TMH., Taborelli, M., Journal of Physical Chemistry, 1995. **99**: p. 1038-45.
96. Minami, I., et al., Tribology International, 2008. **41**(11): p. 1056-1062.
97. Cannara, R.J., Brukman, M.J., Cimatu, K., Sumant, A.V., Baldelli, S., and Carpick, R.W., Science, 2007. **318**: p. 780.
98. Overney, R., Meyer, E., Frommer, J., Guntherodt, HJ.,Fujihira, M., Takano, H., Gotoh, Y., Langmuir, 1994. **10**(4): p. 1281-1286.
99. Liu, H., Fujisawa, S., Tanaka, A., Thin solid films, 2000. **368**: p. 152-155.
100. Xue, Q., Zhang, PY., Zhang ZJ., Liu, WM.,Du, ZL., Ma, GH., Thin Solid films, 1999. **346**: p. 234-237.
101. Reich, R., Der, DS., Tribology Transactions, 1990. **33**: p. 463-469.
102. Aminuzzaman, M., et al., Thin Solid Films, 2007. **516**(1): p. 67-71.
103. Bhusan, B., Kasai, T., Kulik, G., Barbieri, L., and Hoffman, P., Ultramicroscopy, 2005. **105**: p. 176.
104. Perry, S.S., Lee, S., Shon, Y-S., Ramon Colorado, Jr., T. Randall Lee, Tribology Letters, 2001. **10**(1-2): p. 81.
105. Frisbie, C., Rozanyal, LF., Noy, A., Wrightton, MS., Lieber, CM., Science, 1994. **265**: p. 2071-3.
106. Brewer, N.J., Ben D. Beake and Graham J. Leggett, Langmuir 2001. **17**: p. 1970-1974.

107. Kim, H., Graupe, M., Oloba, O., Koini, T., Imaduddin, S., Lee, TR., Perry, SS., Langmuir, 1999. **15**: p. 3179-3185.

108. Liu, Y., Evans, DF., Song, Q., Grainger, DW., Langmuir, 1996. **12**: p. 1235-44.

109. Ren, S.L., S.R. Yanga, Y.P. Zhao, Applied Surface Science, 2004. **227**: p. 293-299.

110. Glosli, J., McClelland, GM., Physical Review Letters, 1993. **70**(13): p. 1960-1963.

111. Koike, A., Yoneya, M., Journal of Chemical Physics, 1996. **105**(14): p. 6060-7.

112. Mikulski, P.T., Herman, L.A., and Harrison, J. , Langmuir, 2005. **21**: p. 12197-12206.

113. Thompson, W.R., Pemberton, J.E., Langmuir, 1995. **11**: p. 1720-1725

2. Theory

2.1 Light and Matter

Total Internal Reflection (TIR) Raman spectroscopy has been extensively used in my research project. To understand the underlying theory behind the working of TIR Raman spectroscopy (hence, Raman spectroscopy in general), the study of the interactions of the conducting material or a dielectric substance with an external electric field is essential.

2.1.1 Linear optics

The most common optical effects we experience day-to-day, like using light from the sun or from electric bulbs, are examples of linear optics in action. When a molecule is exposed to an electric field, a force is exerted on the negatively charged electrons. This induces a charge separation in the molecule by displacing the equilibrium position of the bonded electrons, and the induced dipole oscillates with the same frequency as the applied electric field (in linear optics). The resulting dipole moment can be expressed as a power series in the electric field (bold indicates a vector quantity, or a matrix, or a tensor).

$$\boldsymbol{\mu} = \boldsymbol{\mu}^{(0)} + \boldsymbol{\mu}^{(1)} + \boldsymbol{\mu}^{(2)} + \boldsymbol{\mu}^{(3)} + \ldots, \qquad (2.1.1)$$

where $\boldsymbol{\mu}^{(0)}$ is the static dipole moment and

$$\boldsymbol{\mu}^{(1)} = \boldsymbol{\alpha}\mathbf{E} \qquad (2.1.2)$$

$$\boldsymbol{\mu}^{(2)} = 1/2\,\boldsymbol{\beta}\mathbf{E}\mathbf{E} \qquad (2.1.3)$$

$$\boldsymbol{\mu}^{(3)} = 1/6\,\boldsymbol{\gamma}\mathbf{E}\mathbf{E}\mathbf{E} \qquad (2.1.4)$$

where $\boldsymbol{\alpha}$ is a polarisability tensor of second rank, $\boldsymbol{\beta}$ is a hyperpolarisabilty tensor of third rank, $\boldsymbol{\gamma}$ is the hyperpolarisability tensor of fourth rank. Polarisability is related to refractive index, and gives an estimate of how easily the valence electrons are displaced from the equilibrium position. $\boldsymbol{\mu}^{(0)}$ and $\boldsymbol{\beta}$ are zero in case of centro-symmetric molecules. In weak electric fields, as in case of our TIR Raman (off-resonance) scattering experiments, only equation (2.1.2) is important and all the other non-linear terms can be neglected. Hence equation (2.1.1) turns out to be

$$\mu = \mu^{(0)} + \alpha \mathbf{E} \qquad (2.1.5)$$

It is evident in the equation (2.1.5) that the magnitude of an induced dipole in a molecule is directly proportional to the applied electric field.

For a dielectric substance, or in a condensed media, the macroscopic polarisation, **P** given by the dipole moment per unit volume, is a more relevant term. So, in a condensed media the analogous equation for the induced polarisation stands as

$$\mathbf{P} = \mathbf{P}^{(0)} + \mathbf{P}^{(1)} + \mathbf{P}^{(2)} + \mathbf{P}^{(3)} + ..., \qquad (2.1.6)$$

where $\mathbf{P}^{(0)}$ is the static polarisation and is zero for most materials, and

$$\mathbf{P}^{(1)} = \varepsilon_0 \chi^{(1)} \mathbf{E} \qquad (2.1.7)$$

$$\mathbf{P}^{(2)} = \varepsilon_0 \chi^{(2)} \mathbf{E}\mathbf{E} \qquad (2.1.8)$$

$$\mathbf{P}^{(3)} = \varepsilon_0 \chi^{(3)} \mathbf{E}\mathbf{E}\mathbf{E} \qquad (2.1.9)$$

where ε_0 is the vacuum permittivity, $\chi^{(1)}$ is the first order, or linear susceptibility and is a tensor of second rank, $\chi^{(2)}, \chi^{(3)}, \ldots$ are the second order and third order non-linear susceptibilities and tensors of third rank and fourth rank respectively. Due to these non-linear susceptibilities $\chi^{(2)}, \chi^{(3)}, \ldots$ the induced polarisation, **P**, oscillates at frequencies different to the frequency of the applied electric field, **E**. Light emitted at these different frequencies is a non-linear effect and forms the basis of difference frequency generation (DFG) and sum frequency generation (SFG). However, these non-linear effects were not used to study my systems presented in this thesis.

Once again, in case of weak applied electric fields, the higher order or non-linear terms are negligibly small and only the first order or linear term in equation (2.1.7) is important. Hence in case of weak electric fields, equation (2.1.6) stands as

$$\mathbf{P} = \varepsilon_0 \chi^{(1)} \mathbf{E} \qquad (2.1.10)$$

The induced polarisation, **P** is not necessarily in the same direction as the applied electric field since $\chi^{(1)}$ is a second rank tensor, but its magnitude is directly proportional to the electric field strength. Neglecting local field effects, the macroscopic susceptibility $\chi^{(1)}$

is given by multiplying the molecular polarisability, α averaged over all orientations of molecules in the material by the number of molecules per unit volume, *N*. Therefore

$$\chi^{(1)} = N\langle\alpha\rangle / \varepsilon_0 \qquad (2.1.11)$$

The induced polarisation, **P**, gives rise to an electric field which opposes the electric field from the incident radiation. Therefore the electric field, **E** is reduced and the term electric displacement, **D**, becomes relevant where **D** is given by

$$\mathbf{D} = \varepsilon_0\mathbf{E} + \mathbf{P} \qquad (2.1.12)$$

It may be noted here, that in SI units, permittivity is measured in farads per meter (F/m or $A^2{\cdot}s^4{\cdot}kg^{-1}{\cdot}m^{-3}$). The displacement field **D** is measured in units of coulombs per square meter (C/m^2), while the electric field **E** is measured in volts per meter (V/m). **D** and **E** describe the interaction between charged objects. **D** is related to the charge densities associated with this interaction, while **E** is related to the forces and potential differences.

Combining equation (2.1.12) with equation (2.1.10) we obtain

$$\mathbf{D} = \varepsilon_0\mathbf{E} + \varepsilon_0\chi^{(1)}\mathbf{E} \qquad (2.1.13)$$

which can also be expressed as

$$\mathbf{D} = \varepsilon_0(1+\chi^{(1)})\mathbf{E} \qquad (2.1.14)$$

From equation (2.1.14) it is evident that the electric displacement, **D** is directly proportional to the electric field, **E** where the proportionality constant is the electric permittivity of the substance, denoted as ε_p. Therefore

$$\varepsilon_p = \varepsilon_0(1+\chi^{(1)}) \qquad (2.1.15)$$

The ratio $\varepsilon_p/\varepsilon_0$ gives the relative electric permittivity, or dielectric constant of the substance, denoted as ε. Therefore

$$\varepsilon_p/\varepsilon_0 = \varepsilon \qquad (2.1.16)$$

From equations (2.1.15) and (2.1.16), we find that $\chi^{(1)}$ is related to the dielectric constant, ε of the material, and hence its complex refractive index, $\tilde{n}$:

$$\tilde{n}^2 = \varepsilon = 1+\chi^{(1)} \qquad (2.1.17)$$

where $\tilde{n}$ is given by

$$\tilde{n} = n + ik \qquad (2.1.18)$$

Here n forms the real part of the complex refractive index, $\tilde{n}$ and is related to the speed of light in the medium, while the imaginary part k is related to the absorption losses in the medium.

As mentioned in the beginning of this section, when an applied electric field induces a polarisation in a dielectric substance, the induced polarisation oscillates at the same frequency as the applied field, provided the electric field is not too strong. This oscillating induced polarisation emits radiation (light) which is scattered, reflected and refracted at the frequency of the incident light. However, the intensity and angle of the scattered light is dependent upon the optical properties of the medium.

2.2 Electric fields at interface

The experiments set out in this project probes molecules at interfaces with laser light, and an understanding of the theory of light at interfaces is needed to design experiments and interpret results.

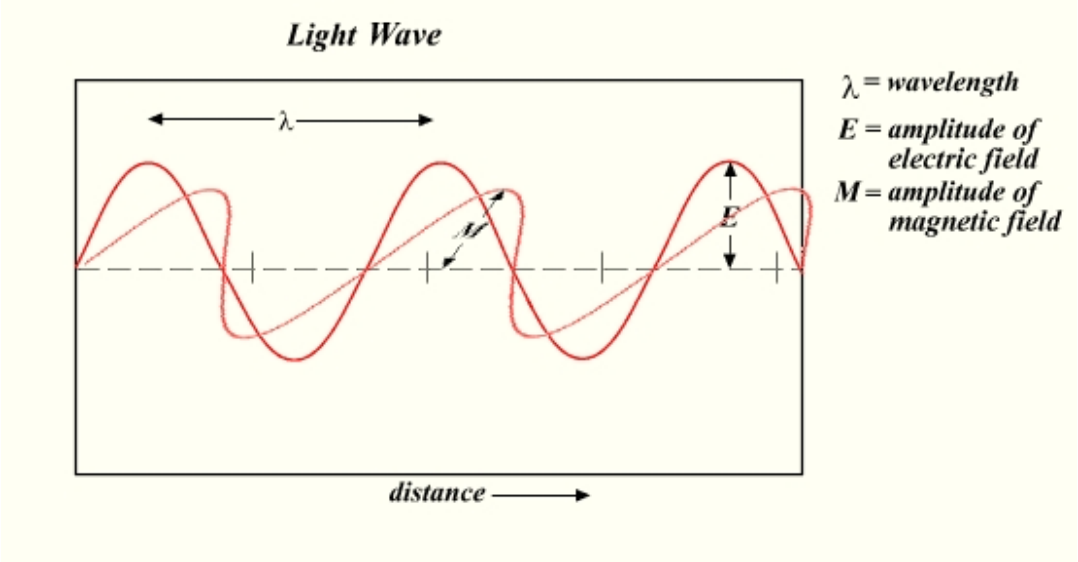

Figure 2.2.1: Schematic illustration of an electromagnetic wave/ light wave

2.2.1 Reflection and Refraction

When light travels through a medium of refractive index n_i and meets a boundary with a medium of refractive index n_t, this light is both reflected and refracted as shown in figure 2.2.2. The incident, reflected and refracted rays all lie in the plane of incidence, and the relationship between the angles of incidence (θ_i), reflection (θ_r) and refraction (θ_t) is given by

$$\theta_r = \theta_i \qquad (2.2.1)$$

and Snell's law $$n_t \sin\theta_t = n_i \sin\theta_i \qquad (2.2.2)$$

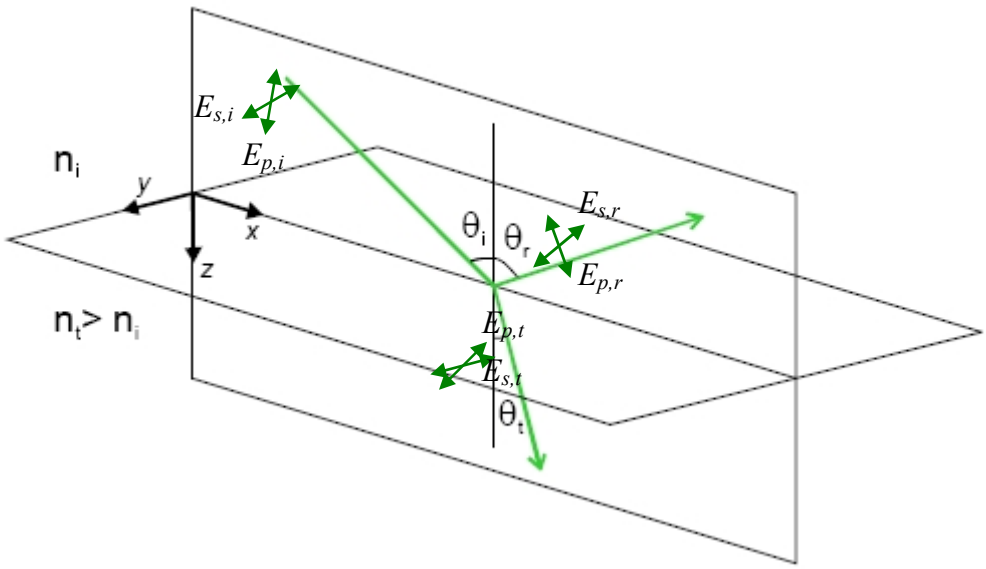

Figure 2.2.2: Schematic illustration of reflection and refraction at an interface

It should be noted here that the same equations (2.2.1 & 2.2.2) apply to substrates with complex refractive indices, $\tilde{n}$, e.g. steel and other conducting materials. However, in this section we are only considering dielectric media with real refractive indices, n.

If the light is incident through the medium of higher refractive index, then there is a critical angle of incidence (θ_c) at which $\theta_t = 90^o$. When light is incident above θ_c it is wholly reflected back into the incident medium and the process is termed as total internal reflection (TIR). The critical angle is given by

$$\theta_c = \sin^{-1}\frac{n_t}{n_i} = \sin^{-1} n_{ti} \qquad (2.2.3)$$

$$\text{where,} \quad n_{ti} = \frac{n_t}{n_i} \qquad (2.2.4)$$

Even though no energy is transferred across the interface, there must be a transmitted field to satisfy the boundary conditions so that across the boundary the tangential components of electric field, E & magnetic field, B are continuous [1]. This field propagates along the surface in the plane of incidence, and the electric field, E exponentially fades with distance, z away from the interface – hence known as an evanescent ('quickly fading') wave, and is expressed by the equation (2.2.5).

$$\frac{E}{E_0} = \exp(-\beta z) \qquad (2.2.5)$$

$$\text{where,} \quad \beta = \frac{2\pi n_{ti}}{\lambda}\left(\frac{\sin^2\theta_i}{n_{ti}^2} - 1\right)^{\frac{1}{2}} \qquad (2.2.6)$$

β is the electric field amplitude decay coefficient, θ_i is the angle of incidence, λ is the wavelength of incident light in the incident medium and E_0 is the electric field at $z = 0$. The penetration depth, d_p , of the electric field into the optically rarer medium is given by equation (2.2.7).

$$d_p = 1/\beta \qquad (2.2.7)$$

Typically, d_p is of the order of λ , and the electric field becomes negligible at a distance of only a few wavelengths into the second medium.

In Raman spectroscopy, the signal is proportional to the intensity of the incident light, I and

$$I \propto E^2 \qquad (2.2.8)$$

hence the Raman signal drops twice as fast as the electric field, E. In fact 98% of the Raman signal originates from a distance $<2\,d_p$ from the interface. Therefore combining equations (2.2.5) and (2.2.8), the mathematically relevant intensity decay equation for Raman scattering is

$$\frac{I}{I_0} = \left(\frac{E}{E_0}\right)^2 = \exp(-2\beta z) \qquad (2.2.9)$$

and the penetration depth, $d_p(E^2)$, of the electric field into the optically rarer medium for a squared electric field is given by

$$d_p(E^2) = 1/2\beta \qquad (2.2.10)$$

When the angle to incidence (θ_i) is equal to the critical angle (θ_c), the penetration depth (d_p) is infinite, where 'infinite' means macroscopic. The evanescent wave is inhomogeneous: the wavefronts (surfaces of constant phase) are perpendicular to the surfaces of constant amplitude.

Figure 2.2.3 shows the variation of the penetration depth as a function of squared electric field with angle of incidence, for silica/monolayer/air interface using 532 nm light; figure 2.2.4 shows the decay of Raman signal intensity with distance, z from interface at an angle of incidence of 45°. The evanescent electric field can be used to investigate material lying close to an interface, by observation of either absorption or scattering phenomena.

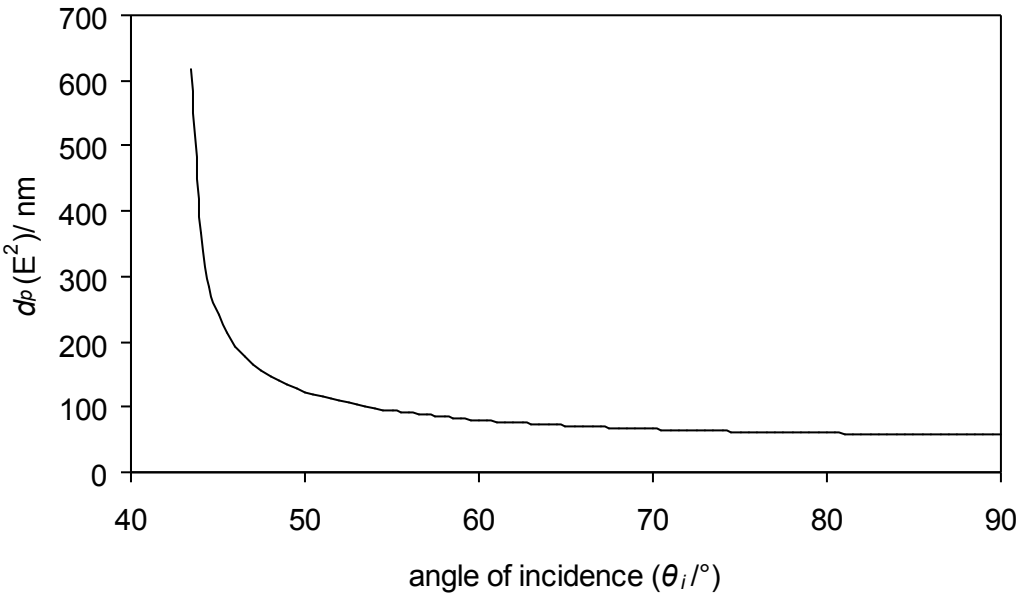

Figure 2.2.3: Variation of penetration depth with angle of incidence for silica/monolayer/air interface probed with 532 nm light; θ_c = 43.2°.

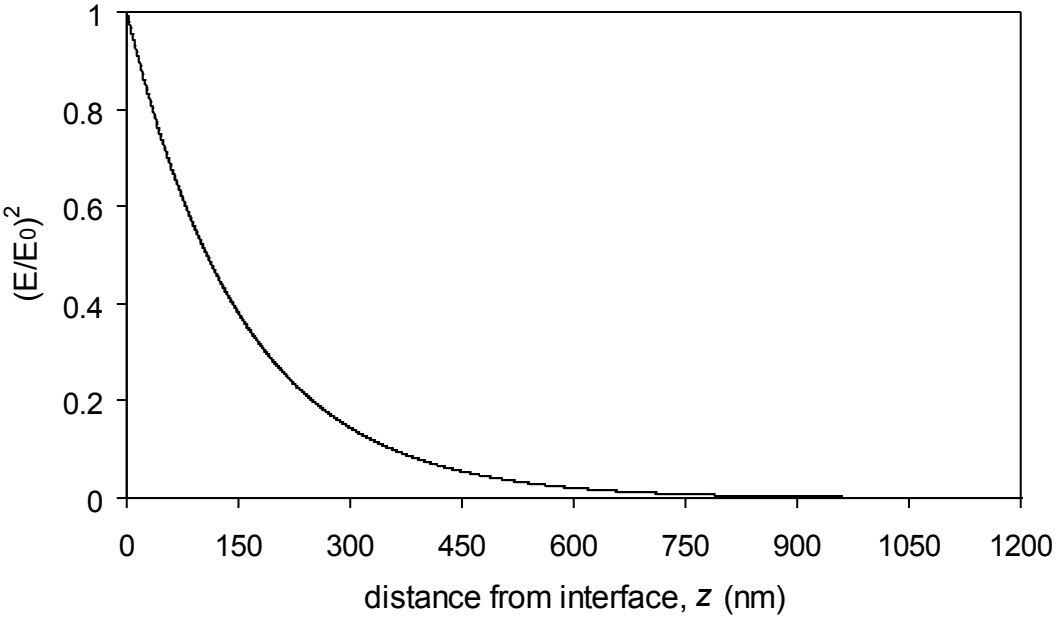

Figure 2.2.4: Plot of Raman intensity decay with distance from the interface, z for silica/monolayer/air interface probed with 532 nm laser at angle of incidence = 45°

2.2.2 Fresnel's equations

In general, when a wave reaches a boundary between two different dielectric constants, part of the wave is reflected and part is transmitted, and the sum of the energies in these two waves equal to that of the original wave. In 1823, Augustine Fresnel derived equations that relate the amplitudes of the electric field of the transmitted and reflected electric field vectors to the amplitude of the incident electric field, E, when an electromagnetic radiation is incident on an interface of two homogeneous isotropic media. P-polarised light with electric field vector in the plane of incidence behaves independently to light with the electric field vector perpendicular to the plane of incidence (S-polarised light). For a pair of non-magnetic media (magnetic permeability, μ = 1), considering the continuity conditions of electric field, E across the interface [1] (section 2.2.3), the amplitude reflection coefficient of S-polarised light, r_s and amplitude reflection coefficient of P-polarised light, r_p are given by the Fresnel's equations as

$$r_s = \frac{n_i \cos\theta_i - n_t \cos\theta_t}{n_i \cos\theta_i + n_t \cos\theta_t} \qquad (2.2.11)$$

and $$r_p = \frac{n_t \cos\theta_i - n_i \cos\theta_t}{n_i \cos\theta_t + n_t \cos\theta_i} \qquad (2.2.12)$$

which on application of Snell's law (2.2.2) can be modified respectively as

$$r_s = -\frac{\sin(\theta_i - \theta_t)}{\sin(\theta_i + \theta_t)} \qquad (2.2.13)$$

$$r_p = \frac{\tan(\theta_i - \theta_t)}{\tan(\theta_i + \theta_t)} \qquad (2.2.14)$$

where the amplitude reflection coefficient, r is defined as the ratio of the amplitude of the reflected electric field, E_r to the amplitude of the incident electric field, E_i.

$$r = \frac{E_r}{E_i} \qquad (2.2.15)$$

Similarly the amplitude transmission coefficient, t is defined as the ratio of the amplitude of the transmitted electric field, E_t to the amplitude of the incident electric field, E_i,

$$t = \frac{E_t}{E_i} \qquad (2.2.16)$$

and the amplitude transmission coefficient of S-polarised light, t_s and amplitude transmission coefficient of P-polarised light, t_p is given by the Fresnel's equations as

$$t_s = \frac{2n_i \cos\theta_i}{n_i \cos\theta_i + n_t \cos\theta_t} \qquad (2.2.17)$$

$$t_p = \frac{2n_i \cos\theta_i}{n_i \cos\theta_t + n_t \cos\theta_i} \qquad (2.2.18)$$

The reflectance (intensity reflection coefficient), R is the square of the amplitude reflection coefficient, r.

$$R = r^2 \qquad (2.2.19)$$

Combining equation (2.2.19) with equations (2.2.13) and (2.2.14) we obtain the reflectance of S-polarised light, R_s and reflectance of P-polarised light, R_p and are given by the equations (2.2.20) and (2.2.21) respectively.

$$R_s = \frac{\sin^2(\theta_i - \theta_t)}{\sin^2(\theta_i + \theta_t)} \qquad (2.2.20)$$

$$R_p = \frac{\tan^2(\theta_i - \theta_t)}{\tan^2(\theta_i + \theta_t)} \qquad (2.2.21)$$

If light travelling in a rarer medium is incident on a denser medium i.e. if $n_i < n_t$ (e.g. air/glass interface), the transmitted or refracted light always moves closer to the surface normal i.e. $\theta_i > \theta_t$. In such instances, $\theta_i - \theta_t > 0$. However, the right hand side of equation (2.2.21) vanishes if $\theta_i + \theta_t = \frac{\pi}{2}$ in which case the denominator becomes infinite. Under such circumstances, all the P-polarised light is transmitted to the denser media. The value of θ_i at which this occurs is known as Brewster's angle (named after Sir David Brewster in 1814) and is denoted as θ_B. Applying Snell's law (2.2.2) at Brewster's angle we obtain

$$n_i \sin\theta_B = n_t \sin\theta_t = n_t \sin(\frac{\pi}{2} - \theta_B) = n_t \cos\theta_B \qquad (2.2.22)$$

$$\text{or,} \qquad \tan\theta_B = \frac{n_t}{n_i} = n_{ti} \qquad (2.2.23)$$

Equation (2.2.23) is known as Brewster's law, and has often been used in the experiments covered in this thesis to determine the refractive indices of different materials by ellipsometry. Unlike the perfect interfaces where the refractive index changes as a step function, in real interfaces where the refractive index gradually changes the reflectivity of P-polarised light incident at θ_B is not zero but attains a minima. Therefore, the Fresnel's equations laid the foundation for ellipsometry (where the complex relationship between the amplitude reflection coefficients of S-polarised light and P-polarised light are studied), Brewster Angle Microscopy (BAM) etc.

2.2.3 Interfacial electric fields: Fresnel K-factors

The macroscopic electric field, **E** at the interface is different from the electric field in the incident medium, and Fresnel's equations relate the field at the interface to that in the bulk. The electric field experienced by the molecules at the interface is subject to an additional effect arising from the induced dipoles of adjacent molecules in addition to that of the macroscopic electric field. Inclusion of local field corrections can however be readily calculated for isotropic systems: the well-known Clausius-Mossotti equation is

one example [2-4]. Local field corrections are complicated in anisotropic systems and it is not clear how to treat the molecular effects correctly for a monolayer at the solid-solid interface. A full treatment, however, is not expected to modify the equations except that **E** would be replaced by $\mathbf{E}_{local}$, a locally-corrected electric field. Local field corrections are therefore neglected in the subsequent discussions.

Fresnel's equations are derived from a consideration of the total electric field at the interface: the field at the interface in the incident medium is the sum of the incident and reflected fields; the field in the interface in the transmitting medium is the electric field of the transmitted beam. In the systems discussed in this project there is an organic film at the interface between the incident medium and the second medium, which is thin in comparison with the wavelength of the incident laser beam. Consequently, the refraction or reflection by the film can be neglected in calculating the amplitude of reflected and transmitted beams. The electric fields in the film are then calculated from continuity of **E** parallel to the surface (E_x and E_y along x-axis and y-axis respectively) and continuity of $\varepsilon\mathbf{E}$ perpendicular to the interface (εE_z along z-axis), where the optical permittivity, $\varepsilon = n^2$.

The incident laser beam can either be S-polarised with the electric field perpendicular to the plane of incidence or P-polarised with the electric field parallel to the plane of incidence, where the plane of incidence is the plane containing the incident ray and the refracted ray or the totally reflected ray. The fields at the interface in the incident medium along the x-, y- and z- axes (Fig 2.2.2), therefore, are related to the incident P- and S-polarised electric fields by

$$E_x = -(E_p - r_p E_p)\cos\theta_i \qquad (2.2.24)$$

$$E_y = E_s + r_s E_s \qquad (2.2.25)$$

$$\text{and } E_z = (E_p + r_p E_p), \qquad (2.2.26)$$

where r_s and r_p are the Fresnel amplitude reflection coefficients. Parallel and perpendicular polarisations operate independently in the absence of any anisotropy in the media, so the incident light selectively induces electric field oscillations in its own plane. Thus, P-polarised incident light in general gives rise to E_x and E_z oscillations, and S-polarised light gives E_y oscillations. From the laws of electromagnetic theory [5], the total

tangential component of **E** on one side of the surface must equal that on the other, i.e. this component is continuous across the boundary, as is the case for the normal component of the magnetic field **B**; the normal component of **E** and the tangential component of **B** are not continuous across the interface, but the tangential component of $\mu^{-1}\mathbf{B}$ and the normal component of ε**E** are, where, μ (μ=1 for nonmagnetic media) and ε are the permeability and the dielectric constant of the medium, respectively. From the equations (2.2.24), (2.2.25) and (2.2.26), and the knowledge that $\hat{\mathbf{k}} \times \mathbf{E} = v\mathbf{B}$ and $\hat{\mathbf{k}} \bullet \mathbf{E} = 0$, where *v* is the speed of light through the medium and $\hat{\mathbf{k}}$ is the unit propagation vector of the light, the following equations can be derived for the ratio of the electric field in the interfacial film to the electric field of the incident beam in the incident bulk medium [5]

$$K_{sy} = \frac{2n_i \cos\theta_i}{n_i \cos\theta_i + n_t \cos\theta_t} \qquad (2.2.27)$$

$$K_{px} = \frac{2n_i \cos\theta_i \cos\theta_t}{n_i \cos\theta_t + n_t \cos\theta_i} \qquad (2.2.28)$$

$$K_{pz} = \left(\frac{n_t}{n'}\right)^2 \frac{2n_i \cos\theta_i \sin\theta_t}{n_i \cos\theta_t + n_t \cos\theta_i} \qquad (2.2.29)$$

where n_t, n_i and n' are the refractive indices of the incident medium, the second medium and the monolayer, respectively. K_{sy} is the ratio of electric field in the *y*-direction at the interface to the electric field of the s-polarised beam in the incident medium and so on. The factor $\left(\frac{n_t}{n'}\right)^2$ in equation (2.2.29) arises from the continuity of εE_z across the interface. The K-factors become complex when the pump beams (as in most of my experiments) are incident at the solid-solid or the solid-air interface through the material of greater refractive index above θ_c, so that total internal reflection (TIR) occurs. Conveniently, these K-factors are split into their real and imaginary parts

$$\mathrm{Re}\left(K_{px}\right) = \frac{2\cos\theta_i \left(\sin^2\theta_i - n_{ti}^2\right)}{n_{ti}^4 \cos^2\theta_i + \sin^2\theta_i - n_{ti}^2} \qquad (2.2.30)$$

$$\mathrm{Im}\left(K_{px}\right)=\frac{2n_{ti}^2\cos^2\theta_i\left(\sin^2\theta_i-n_{ti}^2\right)^{1/2}}{n_{ti}^4\cos^2\theta_i+\sin^2\theta_i-n_{ti}^2} \tag{2.2.31}$$

$$\mathrm{Re}\left(K_{sy}\right)=\frac{2\cos^2\theta_i}{1-n_{ti}^2} \tag{2.2.32}$$

$$\mathrm{Im}\left(K_{sy}\right)=\frac{-2\cos\theta_i\left(\sin^2\theta_i-n_{ti}^2\right)^{1/2}}{1-n_{ti}^2} \tag{2.2.33}$$

$$\mathrm{Re}\left(K_{pz}\right)=\left(\frac{n_t}{n'}\right)^2\frac{2n_{ti}^2\cos^2\theta_i\sin\theta_i}{n_{ti}^4\cos^2\theta_i+\sin^2\theta_i-n_{ti}^2} \tag{2.2.34}$$

$$\mathrm{Im}\left(K_{pz}\right)=\left(\frac{n_t}{n'}\right)^2\frac{-2\cos\theta_i\sin\theta_i\left(\sin^2\theta_i-n_{ti}^2\right)^{1/2}}{n_{ti}^4\cos^2\theta_i+\sin^2\theta_i-n_{ti}^2} \tag{2.2.35}$$

where $n_{ti} = n_t / n_i$.

In figures 2.2.6 and 2.2.7 values of the K-factors are plotted against angle of incidences for a laser beam of wavelength 532 nm incident at the silica/monolayer/air and SF10/monolayer/slica interfaces, respectively, the two most commonly used interfaces in my tribology experiments. As the molecular layers at both the interfaces are very thin compared to the wavelength of the incident radiation, the critical angle, θ_c at the interface is calculated taking the refractive indices of the pair of dielectric media into consideration. Therefore the critical angles, θ_c at silica/monolayer/air interface and SF10/monolayer/silica interface are effectively the θ_c at the silica/air and SF10/silica interfaces respectively. The θ_c at the silica/monolayer/air interface is 43.2^o (fig. 2.2.6) and θ_c at the SF10/monolayer/silica interface is 57.2^o (fig. 2.2.7). As evident from both the plots of Fresnel K-factors, at the critical angle there are not only the maximum interfacial fields (as K_{sy} and K_{pz} attain maximum values) and therefore the strongest spectra, but the spectra are also simplified because a P-polarised incident beam will give only a *z*-component in the field at the interface (K_{px} reduces to 0 at θ_c).

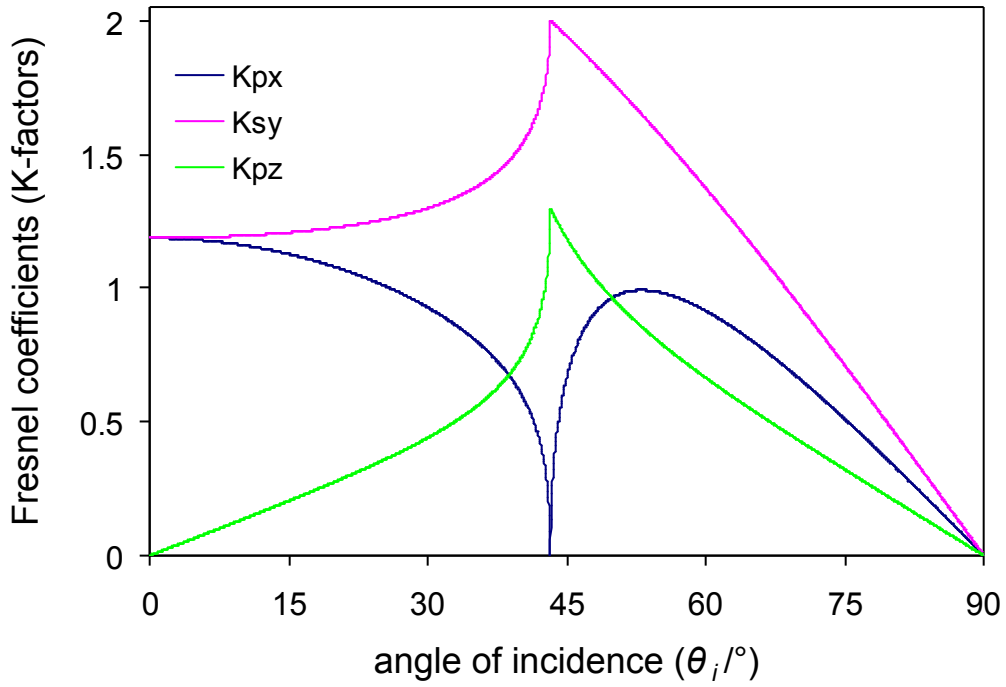

Figure 2.2.6: Plots of K-factors vs angle of incidence for electromagnetic radiation (λ = 532 nm) at silica/monolayer/air interface; n_{silica} = 1.461 and $n_{monolayer}$ ~ 1.5.

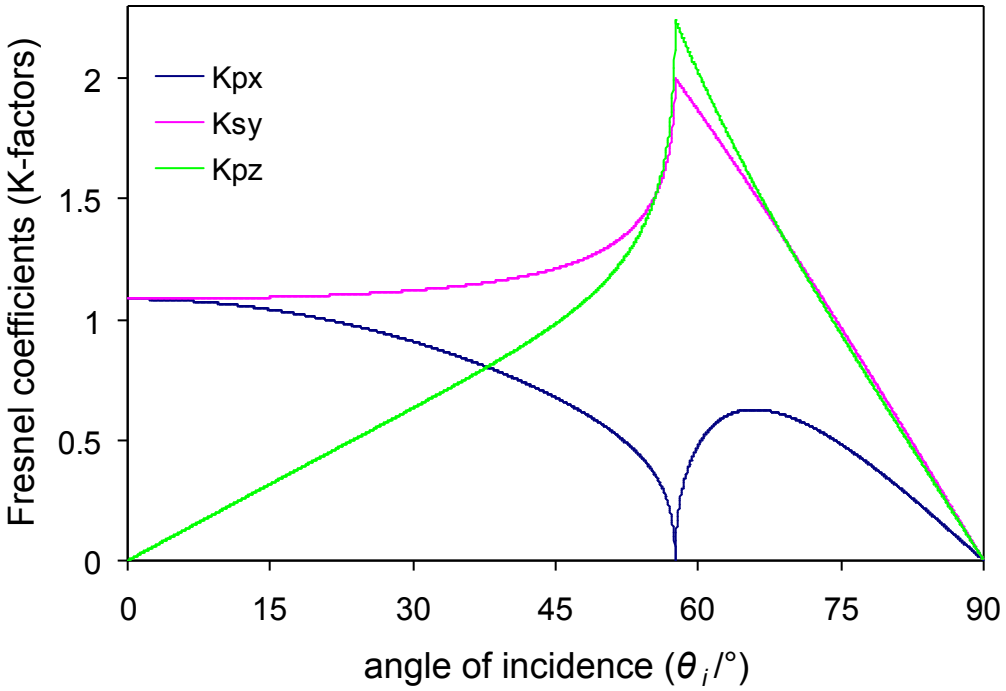

Figure 2.2.7: Plots of K-factors vs angle of incidence for electromagnetic radiation (λ = 532 nm) at SF10/monolayer/silica interface; n_{SF10} = 1.737, $n_{monolayer}$ ~ 1.5 and n_{silica} = 1.461.

2.3 Raman Scattering

When light is scattered from a molecule most photons are elastically scattered. The scattered photons have the same energy (and therefore same frequency and wavelength) as the incident photons. However, a small fraction of the scattered light (approximately 1 in 10^7 photons) is at optical frequencies different from, and usually lower than, the frequency of the incident photons. The process leading to this inelastic scattering is termed the Raman effect. Predicted theoretically in 1923 by Smekal [6], and first observed in liquids in 1928 by Chandrasekhara Venkata Raman & K.S. Krishnan [7], the Raman effect was quickly followed by reports of Raman scattering in many other systems. By 1934, G. Placzek [8] had predicted almost all of the phenomenon now observed. Raman scattering can occur with a change in vibrational, rotational or electronic energy of a molecule. We are concerned primarily with the vibrational Raman effect and will use the term Raman effect to mean only vibrational Raman spectroscopy in this thesis.

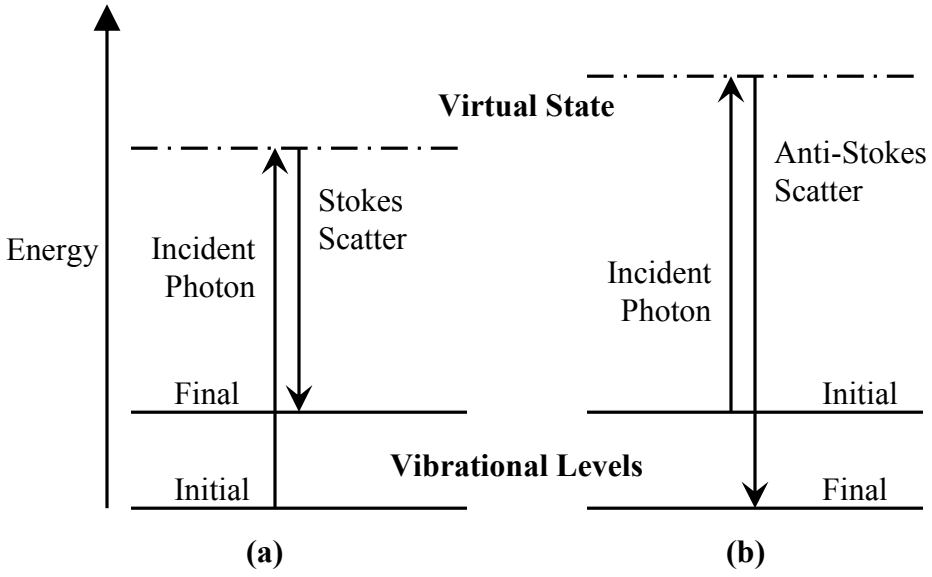

Figure 2.3.1. Energy level diagram for Raman scattering; (a) Stokes Raman scattering (b) anti-Stokes Raman scattering.

Raman scattering can be thought of formally as a two-photon absorption-emission process [9]. The difference in energy between the incident photon and the Raman scattered photon is equal to the energy of a vibration of the scattering molecule. A plot of intensity of scattered light versus energy difference is a Raman spectrum. The Raman effect arises when a photon is incident on a molecule and interacts with the electric dipole of the molecule. It is a form of electronic (more accurately, vibronic) spectroscopy, although the spectrum contains vibrational frequencies. In classical terms, the interaction can be viewed as a perturbation of the molecule's electric field [10]. In quantum mechanics the scattering is described as an excitation to a virtual state lower in energy than a real electronic transition with nearly coincident de-excitation and a change in vibrational energy. The virtual state description of scattering is shown in Figure 2.3.1.

The energy difference between the incident and scattered photons is represented by the arrows of different lengths in Figure 2.3.1. Numerically, the energy difference between the initial and final vibrational levels, $\bar{\nu}$, or Raman shift in wave numbers (cm^{-1}), is calculated through equation

$$\bar{\nu} = 1/\lambda_{incident} - 1/\lambda_{scattered} \qquad (2.3.1)$$

where $\lambda_{incident}$ and $\lambda_{scattered}$ are the wavelengths (in cm) of the incident and Raman scattered photons, respectively. The vibrational energy is ultimately dissipated as heat. Because of the low intensity of Raman scattering, the heat dissipation does not cause a measurable temperature rise in a material.

At room temperature the thermal population of excited vibrational states is low, although not zero. Therefore, the initial state is usually the ground state, and the scattered photon will have lower energy (longer wavelength) than the exciting photon. This Stokes shifted scatter is what is usually observed in Raman spectroscopy. Figure 2.3.1a depicts Raman Stokes scattering. A small fraction of the molecules are in vibrationally excited states. Raman scattering from these vibrationally excited molecules leaves the molecule in the ground state where the scattered photon appears at higher energy, as shown in Figure 2.3.1b. This anti-Stokes-shifted Raman spectrum is always weaker than the Stokes-

shifted spectrum, but at room temperature it is strong enough to be useful for vibrational frequencies less than about 1000 cm^{-1}. The Stokes and anti-Stokes spectra contain the same frequency information. The ratio of anti-Stokes to Stokes intensity at any vibrational frequency is a measure of temperature. Anti-Stokes Raman scattering is used for contactless thermometry. The anti-Stokes spectrum is also used when the Stokes spectrum is not directly observable, for example because of fluorescence, poor detector response or spectrograph efficiency.

2.3.1 Classical Discussion

The frequencies at which Raman scattering occurs can be described classically as beat frequencies arising from the interaction of induced dipoles with incident radiations. The origin of the anti-Stokes and Stokes scattered light can be understood from a simple classical model of a diatomic molecule. Classically, the magnitude of the applied electric field, **E**, which fluctuates with time, *t*, can be written as

$$\mathbf{E} = \mathbf{E}_0 \cos w_p t \qquad (2.3.2)$$

where $\mathbf{E}_0$ is the amplitude and w_p is the angular frequency of the incident pump laser radiation. The induced dipole moment in the molecule, $\boldsymbol{\mu}$, is given by the equation

$$\boldsymbol{\mu} = \boldsymbol{\alpha}\mathbf{E}_0 \cos w_p t \qquad (2.3.3)$$

If the molecule is vibrating with a angular frequency w_{vib}, the magnitude of the polarisability varies with the vibration as

$$\boldsymbol{\alpha} = \boldsymbol{\alpha}_0 + \boldsymbol{\alpha}_1 \cos w_{vib} t \qquad (2.3.4)$$

where $\boldsymbol{\alpha}_0$ is the average equilibrium polarisability and $\boldsymbol{\alpha}_1$ is the first derivative of the polarisability with respect to the normal mode co-ordinate. Combining equations (2.3.3) and (2.3.4) we obtain an expression for the induced dipole moment varying with time during the vibration

$$\boldsymbol{\mu} = \boldsymbol{\alpha}_0\mathbf{E}_0 \cos w_p t + \frac{1}{2}\boldsymbol{\alpha}_1\mathbf{E}_0 \cos\left(w_p + w_{vib}\right)t + \frac{1}{2}\boldsymbol{\alpha}_1\mathbf{E}_0 \cos(w_p - w_{vib})t \qquad (2.3.5)$$

We can observe in equation (2.3.5) that the first term represents oscillation of induced dipole at an angular frequency of w_p, the second term corresponds to induced dipole

oscillations at angular frequency of $w_p + w_{vib}$ and the third term corresponds to induced dipole oscillations at angular frequency $w_p - w_{vib}$. Light is radiated at these frequencies; the scattering radiation frequency $w_p + w_{vib}$ is responsible for the anti-Stokes line and scattering radiation frequency $w_p - w_{vib}$ is responsible for the Stokes line.

2.3.2 The Polarisability Tensor

The polarisability of a molecule determines the scattering cross-section. Since the incident radiation is usually in the visible or near-ultraviolet region the polarisability is a measure of the degree to which the electrons in the molecule can be displaced relative to the nuclei. The relationship between the vectors $\boldsymbol{\mu}$ and **E** and the tensor $\boldsymbol{\alpha}$ can be expressed in matrix form, where $\boldsymbol{\alpha_{ij}}$ are the components of $\boldsymbol{\alpha}$.

$$\begin{bmatrix} \boldsymbol{\mu}_a \\ \boldsymbol{\mu}_b \\ \boldsymbol{\mu}_c \end{bmatrix} = \begin{bmatrix} \boldsymbol{\alpha}_{aa}\boldsymbol{\alpha}_{ab}\boldsymbol{\alpha}_{ac} \\ \boldsymbol{\alpha}_{ba}\boldsymbol{\alpha}_{bb}\boldsymbol{\alpha}_{bc} \\ \boldsymbol{\alpha}_{ca}\boldsymbol{\alpha}_{cb}\boldsymbol{\alpha}_{cc} \end{bmatrix} \begin{bmatrix} \mathbf{E}_a \\ \mathbf{E}_b \\ \mathbf{E}_c \end{bmatrix} \qquad (2.3.6)$$

$\boldsymbol{\alpha}_{aa,}$ $\boldsymbol{\alpha}_{bb}$ and $\boldsymbol{\alpha}_{cc}$ are the values of $\boldsymbol{\alpha}$ along the a, b and c axes of the molecule. It is clear from this matrix that $\boldsymbol{\mu}$ can have contributions from all three components of **E**, and so the direction of the induced dipole is usually different from the direction of the incident electric field. The polarisability tensor can be expressed as an ellipsoid. The polarisability ellipsoid shown in figure 2.3.2 is obtained by drawing a surface so that the distance from the origin to any point on the surface has a length $\boldsymbol{\alpha}^{-1/2}$, where $\boldsymbol{\alpha}$ is the polarisability in that direction.

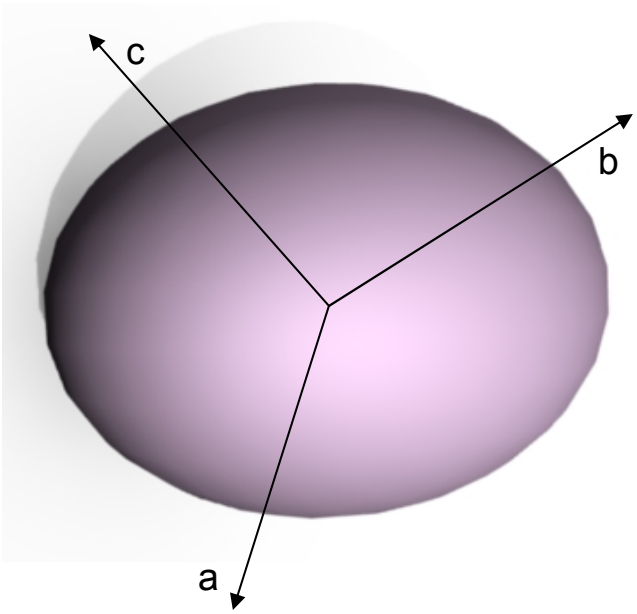

Figure 2.3.2 Graphical representation of the polarisability tensor. The distance from the origin to a point on the surface has a length $\alpha^{-1/2}$, where α is the polarisability in that direction

The Raman tensor, $\boldsymbol{\alpha}'_k$ is a second rank tensor, and is the polarisability tensor, $\boldsymbol{\alpha}_0$ differentiated with respect to the normal coordinate, Q_k of the kth vibration with an angular frequency w_k. The Raman tensor elements are given by

$$\left(\frac{\delta\boldsymbol{\alpha}_{lm}}{\delta Q_k}\right)_0 = \left(\boldsymbol{\alpha}'_{lm}\right)_k \qquad (2.3.7)$$

Using this relationship (2.3.7) and the assumption that the time dependence of Q_k follows simple harmonic motion, equation (2.3.5) may be rewritten as

$$\boldsymbol{\mu} = \boldsymbol{\alpha}_0\mathbf{E}_0\cos w_p t + \frac{1}{2}\boldsymbol{\alpha}'_k\mathbf{E}_0 Q_{k0}\cos\left[\left(w_p + w_k\right)t + \delta k\right] + \frac{1}{2}\boldsymbol{\alpha}'_k\mathbf{E}_0 Q_{k0}\cos\left[\left(w_p - w_k\right)t + \delta k\right] \qquad (2.3.8)$$

where δk is the phase difference between the normal mode of the vibration and the electric field and is different for different molecules. In Stokes scattering a dipole is therefore induced at the Stokes angular frequency, w_s. The amplitude of this dipole is given by

$$\boldsymbol{\mu}\left(w_s\right) = \frac{1}{2}\boldsymbol{\alpha}'_k\mathbf{E}_0 Q_{k0} \qquad (2.3.9)$$

There are two prominent differences between the two polarisability tensors. The axes of the $\boldsymbol{\alpha}'$ ellipsoid may not necessarily coincide with the axes of the $\boldsymbol{\alpha}_0$ ellipsoid; and the components of $\boldsymbol{\alpha}'$ can be positive or negative whereas those of $\boldsymbol{\alpha}_0$ can only be positive. It should be noted that since the components of $\boldsymbol{\alpha}'$ can be negative, $\boldsymbol{\alpha}'$ cannot always be represented by a real ellipsoid.

2.3.3 Raman Scattering Intensity

In general, an assembly of molecules do not vibrate in phase (i.e. δk varies between 0 and 2π randomly) and hence light scattered by different molecules is incoherent and does not exhibit interference effects. Therefore Raman scattered light does not have a single well-defined direction. Scattering from individual centres is always additive so that the intensity of the Raman signal scales with the number of emitters. The dipole radiation law gives the radiant intensity of the dipole in a given direction (intensity per solid angle),

$$I = \frac{w^4 \mu^2 \sin^2 \theta}{32\pi^2 \varepsilon_0 c^3} \qquad (2.3.10)$$

where μ is the magnitude of the oscillating dipole, w is the angular frequency of the oscillating dipole and θ is the angle made between the vector of the induced dipole and the Poynting vector (the vector denoting the direction of propagation of the scattered radiation). There is no dependence on the angle of the incident beam, but greatest radiant intensity occurs for $\theta = 90^{\circ}$. Thus most radiated intensity is scattered perpendicular to the direction of the induced dipole, and when studying induced dipoles parallel to the surface, axial collection geometry will maximise the Raman signal. However, this geometry will give very weak Raman signals for dipoles induced in the direction normal to the surface (section 2.4).

The K-factors expressed in the section 2.2.3 apply to Raman scattering from an interface. Since I is proportional to the second power of the induced dipole, it is also proportional to the second power of the electric field at the interface and therefore also to the second

power of the K-factors. However, a fully quantitative treatment of the intensity of Raman scattering would have to incorporate the local field effects mentioned in section 2.2.3 and also the consequence of image dipoles, where the induced dipoles in molecules interact with induced dipoles in adjacent molecules (section 6.4 in chapter 6).

2.3.4 Total internal Reflection Raman (TIR) Spectroscopy

Total internal reflection (TIR) Raman spectroscopy has been extensively used in the tribology experiments discussed in this thesis. In TIR Raman spectroscopy we deal with the scattered radiation that the evanescent wave produces while probing the sample in total internal reflection geometry i.e. when a laser beam travelling through a denser medium is incident on an interface to a rarer medium above the critical angle of incidence, θ_c. Applicability of TIR Raman spectroscopy was first hinted by Harrick and Loeb [11] and the first TIR Raman spectra was obtained by Ikeshoji *et al.* [12]. The Raman signals they measured were, however, very weak and their results suggested that this technique may not be promising enough for practical use unless the Raman signals could be intensified. Right choice of materials, and working at an optimum angle of incidence ($\theta_c \leq \theta_i$) depending on the experimental requirements can significantly increase the TIR Raman signal. Detailed description of the TIR experimental setup will be discussed in Chapter 3, here we briefly describe some other commonly used techniques to enhance the Raman signal.

2.3.5 Resonance-enhanced Raman scattering

Raman spectroscopy is conventionally performed with green, red or near-infrared lasers. The wavelengths are below the first electronic transitions of most molecules, as assumed by scattering theory (section 2.3). The situation changes if the wavelength of the exciting laser lies within the electronic spectrum of a molecule. In such cases the intensity of some Raman-active vibrations increases by a factor of 10^2–10^4. This resonance enhancement or resonance Raman effect can be quite useful.

Resonance Raman spectroscopy is a major probe of the chemistry of fullerenes, polydiacetylenes and other "exotic" molecules which strongly absorb in the visible region of light. Although many more molecules absorb in the ultraviolet, the high cost of lasers and optics for this spectral region have limited UV resonance Raman spectroscopy to a small number of specialists [13, 14]**.** The Bain group is presently engaged in building an UV resonance Raman spectrometer at Durham University, UK. Resonance enhancement does not begin at a sharply defined wavelength. In fact, enhancement of 5×-10× is commonly observed if the exciting laser is even within a few hundred wave numbers below the electronic transition of a molecule [15, 16]. This pre-resonance enhancement can be experimentally useful because in this case we have less absorption and less damage to the sample.

2.3.6 Surface Enhanced Raman Scattering (SERS)

The Raman scattering from a compound (or ion) adsorbed on or even within a few ångstroms of a structured metal surface can be 10^3–10^6 × greater than in solution [17-19].This surface-enhanced Raman scattering is strongest on silver, but is observable on gold and copper as well. At practical excitation wavelengths, enhancement on other metals is unimportant. Surface-enhanced Raman scattering (SERS) arises from two mechanisms.

The first and most important mechanism is an enhanced electromagnetic field produced at the surface of the metal. When the wavelength of the incident light is close to the plasma wavelength of the metal, conduction electrons in the metal surface are excited into an extended surface electronic excited state called a surface plasmon resonance. Molecules adsorbed or in close proximity to the surface experience an exceptionally large electromagnetic field. Vibrational modes normal to the surface are most strongly enhanced. The second mode of enhancement is by the formation of a charge-transfer complex between the surface and analyte molecule. The electronic transitions of many charge transfer complexes are in the visible, so that resonance enhancement occurs.

Molecules with lone pair electrons or pi clouds show the strongest SERS. The effect was first discovered with pyridine. Other aromatic nitrogen or oxygen containing compounds,

such as aromatic amines or phenols, are strongly SERS active. The effect can also been seen with other electron-rich functionalities such as carboxylic acids.

SERS can give single molecule sensitivity [17-19] and is used to study monolayers of materials adsorbed on metals, including electrodes. Many formats other than electrodes can be used. The most popular formats include colloids, metal films on dielectric substrates and, recently, arrays of metal particles bound to metal or dielectric colloids through short linkages.

2.4 Orientational analysis based on Raman tensors and symmetry considerations in TIR geometry

The Raman tensor α' is a second rank tensor. Each vibrational mode in a molecular film has a particular symmetry, and α' being a property of the molecular vibration, it shares the symmetry. The number of independent elements in a tensor can be reduced by symmetry considerations, since many elements are zero for a given vibration. In the following experiments described, the *z*-axis is chosen to be normal to the plane of the interface and the *xy*-plane is the plane of the interface (fig. 2.4.2).

In the laboratory frame (*x*,*y*,*z*), six out the nine Raman tensor elements are independent, which are $\langle\alpha'_{xx}\rangle$, $\langle\alpha'_{yx}\rangle = \langle\alpha'_{xy}\rangle$, $\langle\alpha'_{yy}\rangle$, $\langle\alpha'_{zx}\rangle = \langle\alpha'_{xz}\rangle$, $\langle\alpha'_{zy}\rangle = \langle\alpha'_{yz}\rangle$ and $\langle\alpha'_{zz}\rangle$. Since the LB monolayer is considered to have uniaxial symmetry, showing in-plane isotropy [20] only four out the six Raman tensors are independent which are $\langle\alpha'_{yx}\rangle$, $\langle\alpha'_{xx}\rangle = \langle\alpha'_{yy}\rangle$, $\langle\alpha'_{zx}\rangle = \langle\alpha'_{zy}\rangle$ and $\langle\alpha'_{zz}\rangle$. With our TIR experimental geometry, $\langle\alpha'_{yx}\rangle$, $\langle\alpha'_{yy}\rangle$ and $\langle\alpha'_{zx}\rangle = \langle\alpha'_{zy}\rangle$ can all be determined independently, since at the critical angle the electric field, *E* arising from S-polarised and P-polarised incident light oscillates in the *y*-direction and *z*-direction, respectively (fig. 2.2.6 and fig. 2.2.7). Scattered light with *E* in either the *x*- or the *y*-direction can then be selected for analysis. $\langle\alpha'_{zz}\rangle$ is difficult to measure because of the poor collection efficiency of the microscope objective (the Olympus 50× objective had a numerical aperture, NA= 0.55 and collected a cone of

scattered light with half angle = $\sin^{-1}0.55$ = 33.37°) as Raman scattered light with E in the z-direction is predominantly horizontal (fig. 2.4.2). If the incident pump laser is S-polarised, the elements of Raman tensors probed are $\langle\alpha'_{xy}\rangle$, $\langle\alpha'_{yy}\rangle$, and $\langle\alpha'_{zy}\rangle$. Selecting the direction of collection of the scattered radiation along x-axis, a spectrum due to the Raman tensors $\langle\alpha'_{xy}\rangle$ and $\langle\alpha'_{zy}\rangle$ can be collected and if the direction of collection of scattered radiation is along y-axis, a spectrum due to the Raman tensors $\langle\alpha'_{yy}\rangle$ and $\langle\alpha'_{zy}\rangle$ can be collected. Due to the poor collection efficiency of the microscope objective for light emitted by dipoles oscillating in the z-direction, the scattered radiation from $\langle\alpha'_{zy}\rangle$ is weakly collected (fig. 2.4.2), hence effectively the Sx spectrum (incident radiation S-polarised, collection along x-axis) is due to probing of the element $\langle\alpha'_{xy}\rangle$ and the Sy spectrum (incident radiation S-polarised, collection along y-axis) is due to probing of the element $\langle\alpha'_{yy}\rangle$. If the incident pump laser is P-polarised and incident at an angle higher or lower than the critical angle, θ_c the elements of Raman tensors probed are $\langle\alpha'_{xz}\rangle$, $\langle\alpha'_{yz}\rangle$, $\langle\alpha'_{zz}\rangle$, $\langle\alpha'_{xx}\rangle$, $\langle\alpha'_{yx}\rangle$, and $\langle\alpha'_{zx}\rangle$. Again $\langle\alpha'_{zz}\rangle$ and $\langle\alpha'_{zx}\rangle$ can be ignored because these signals are weakly collected by the objective (fig. 2.4.2). If the direction of collection of scattered radiation is chosen along x axis, the signal obtained in the Px spectrum is due to the Raman tensor elements $\langle\alpha'_{xx}\rangle$=$\langle\alpha'_{yy}\rangle$ and $\langle\alpha'_{xz}\rangle$. Similarly, if the direction of collection of scattered radiation is chosen along y-axis, the signal obtained in the Py spectrum is due to the Raman tensor elements $\langle\alpha'_{yx}\rangle$=$\langle\alpha'_{xy}\rangle$ and $\langle\alpha'_{yz}\rangle$. It is due to this reason that above and below the critical angle, the Py spectra resemble to the Sx spectra and Px spectra resemble to the Sy spectra. However if the P-polarised pump laser beam is incident at the critical angle, θ_c, the electric field at the interface has a z-component only and has no x-component (fig. 2.2.6 & fig. 2.2.7). Therefore at the critical angle, in the Px and Py spectra, the signal obtained is only due to the Raman tensor element $\langle\alpha'_{xz}\rangle$ and $\langle\alpha'_{yz}\rangle$ respectively. Because of the in-plane isotropy of the LB monolayer of Zn arachidate, $\langle\alpha'_{xz}\rangle$= $\langle\alpha'_{yz}\rangle$, the reason due to which at the critical angle

the Px and Py spectra should appear identical. Conversely the shear alignment could be detected in differences between Px and Py spectra at the critical angle.

For an upright aliphatic hydrocarbon chain, for both symmetric C-H stretching, d^+, and antisymmetric C-H stretching, d^- , the vibrations occur in the *xy*-plane and have no component along the *z*-axis (fig.2.4.1). Therefore $\langle \alpha'_{xz} \rangle = \langle \alpha'_{yz} \rangle = 0$ for both d^+ and d^- vibrations. However, though $\langle \alpha'_{zz} \rangle$ is zero for d^-, it is nonzero for d^+. Therefore for an upright hydrocarbon chain, at the critical angle of incidence of the pump laser beam, the Px and Py spectrum should minimize to very close to zero, with some weak signals due to the element $\langle \alpha'_{zz} \rangle$ for the d^+.

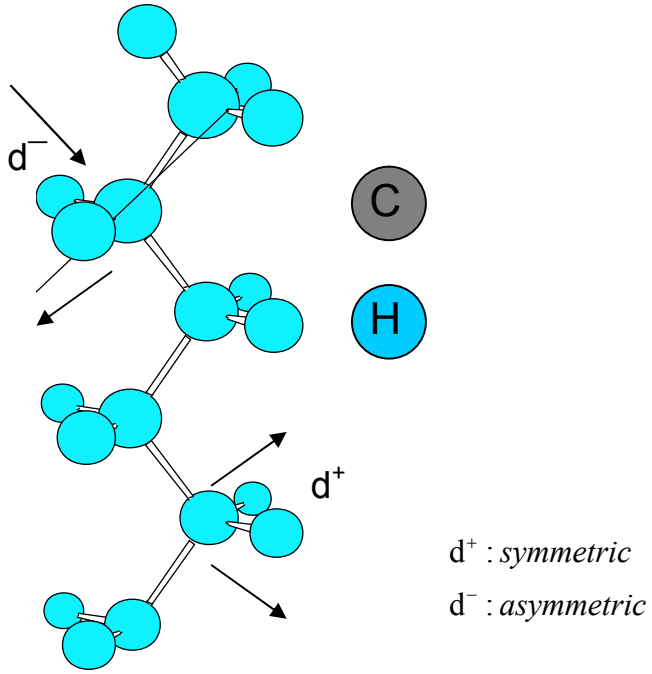

Figure 2.4.1: Symmetric, d^+ and asymmetric, d^- C-H stretching in an aliphatic hydrocarbon chain

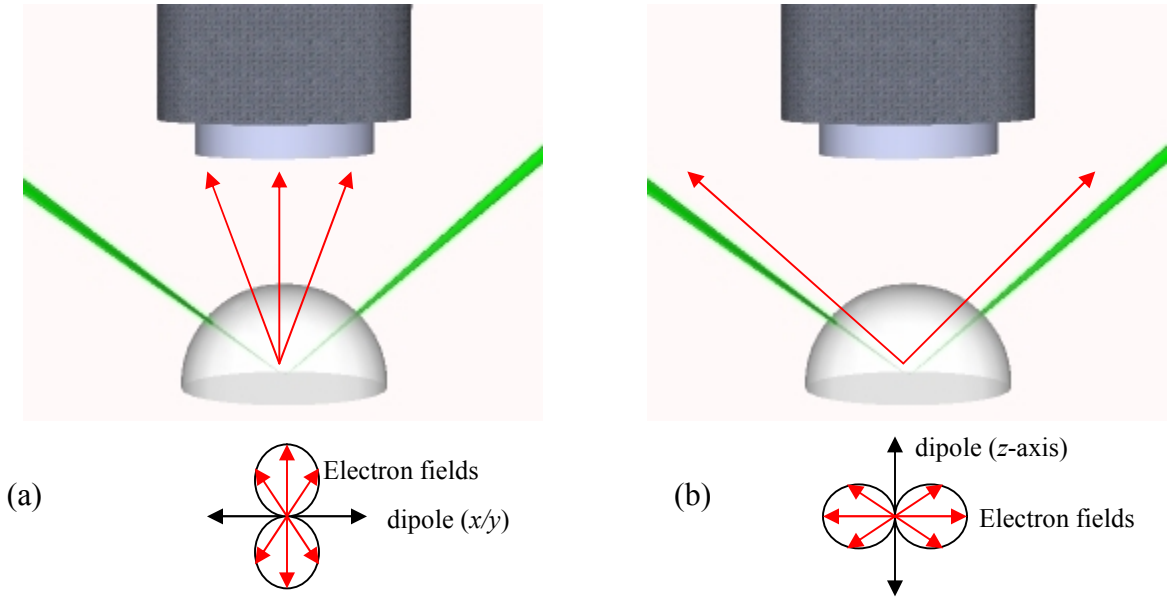

Fig. 2.4.2: A schematic representation of (a) The collection of scattered light from an induced dipole in the *xy*- plane and (b) the problem associated with the collection of scattered light from an induced dipole in the *z*-axis

2.5 Contact Mechanics

In the experiments in this project, a curved surface (sphere) is brought into contact with a flat surface (hemisphere) and a circular area of contact is formed. Hertzian theory is then used to calculate the pressures a thin organic film/lubricant experiences when it is sandwiched between these two solid surfaces.

Figure 2.5.1 Newton's rings observed at SF10 hemisphere/silica ball interface with a 5× objective on back-illumination of the contact interface with white light through the SF10 hemisphere.

2.5.1 Newton's Rings

A series of circular bright and dark bands appear surrounding the point of contact between a flat glass surface (hemisphere) and a curved surface (sphere) which is pressed against it and illuminated with monochromatic light. When the top of the hemisphere is illuminated with white light and a microscope objective is focussed onto the curved sphere surface in contact with the flat hemisphere surface, Newton's rings are seen, as presented in figure 2.5.1. The white light is reflected from both the sphere (curved surface) and the hemisphere (flat surface) surfaces, causing wedge fringes with radial symmetry to occur. This process is illustrated in figure 2.5.2. The dark area in the centre of the Newton's rings appears if there is true contact between the sphere and the hemisphere, as a significant amount of light passes straight through this area of contact without reflection. Measuring the radius of the dark central area gives an approximate value for the radius of the contact spot.

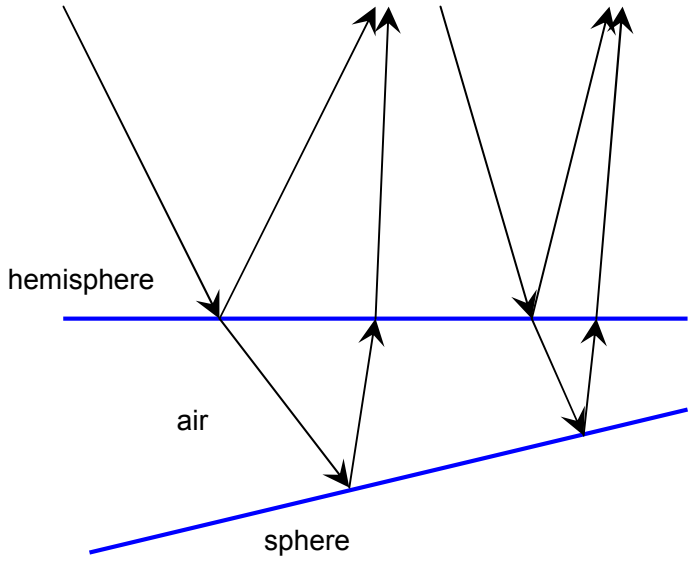

Figure 2.5.2 Ray diagram of the light path in the wedge formed between the hemisphere and sphere surfaces around the circular area of contact when white light is incident onto the back of the hemisphere.

2.5.2 Hertz's Equations

The standard Hertzian theory [21] describes the elastic deformation and stress distribution in a contact area between and flat surface and a spherical surface. The radius of the contact area, a is given by

$$a = \left[\frac{3FR}{4E} \right]^{1/3} \qquad (2.5.1)$$

where F denotes the total force exerted, R denotes the radius of curvature of the sphere, and E denotes the reduced Young's modulus of the pair of substrates. E is given by

$$E = \left[\frac{\left(1 - v_1^{\,2}\right)}{E_1} + \frac{\left(1 - v_2^{\,2}\right)}{E_2} \right]^{-1} \qquad (2.5.2)$$

where v_i and E_i are the Poisson ratio and the Young's modulus respectively of material i. The Poisson ratio is a ratio of transverse strain to axial strain. The values for v_i and E_i for each of the materials presented in this thesis are give in table 2.5.1 below.

	Fused Silica	Calcium Fluoride	SF10	Steel
Young's Modulus, E_i	75.8 GPa	72.1 GPa	64 GPa	207 GPa
Poisson Ratio, v_i	0.26	0.179	0.232	0.3

Table 2.5.1 Table of values for the Poisson Ratio (*v*) and the Young's modulus (*E*).

The average pressure, P_m in the contact area is given by

$$P_m = \frac{F}{\pi a^2} = \frac{1}{\pi}\left[\frac{16FE^2}{9R^2} \right]^{1/3} \qquad (2.5.3)$$

The pressure depends on 1/3 power of the force, so to vary the pressure by a factor of 10, the force has to be varied by a factor of 1000. The possibility of damage of the SF10 and silica optics used in our experiments limits us to attain very high forces. Therefore a more efficient way was chosen for varying the pressure by changing the radius of curvature of the sphere. Combination of equations (2.5.1) and (2.5.3) gives:

$$P_m = \frac{4Ea}{3\pi R} \qquad (2.5.4)$$

The maximum pressure, P_0 at the centre of the contact area is given by

$$P_0 = 1.5P_m = \frac{3}{2}\left(\frac{4Ea}{3\pi R}\right) \qquad (2.5.5)$$

The focal spot of the pump laser beam is smaller (30–40 μm diameter) compared to the contact spot area (50–300 μm depending on the pressure exerted) and is positioned at the centre of the contact area, therefore the pressure experienced by the model boundary lubricants/lubricating fluids sampled in our TIR Raman experiments is close to the maximum pressure P_0 (for higher pressures). The radius of the contact spot a can be determined from the central dark spot of the Newton's rings formed at SF10/silica interface when the interface is back-illuminated with white light [22] and using equation (2.5.5) the maximum pressure, P_0 can be calculated to find out the pressure acting on the organic lubricant molecules sandwiched at the interface.

In our static contact experiments, a force sensor capable of providing direct force readings was also used and using equation (2.5.1) the maximum pressure P_0 can be calculated by

$$P_0 = 1.5P_m = \frac{1.5}{\pi}\left[\frac{16FE^2}{9R^2}\right]^{1/3} \qquad (2.5.6)$$

References:

1. Born, M., Wolf, E and Bhatia, A.B., *Principles of Optics: electromagnetic theory of propagation, interference and diffraction of light.* Cambridge University Press, 1999.
2. Castle, P.J., and Lekner, J., Physika, 1980. **101A**: p. 99.
3. Jackson, J.D., *Classical Electrodynamics.* New York: John Wiley, 1975.
4. Ye, P., and Shen, Y.R., Physical Review B, 1983. **28**(8): p. 4288-4294.
5. Hecht, E., *Optics.* Reading, Massachusetts: Addison-Wesley, 1987.

6. Smekal, A., Naturwiss, 1923. **11**: p. 873.
7. Raman, C.V., and Krishnan, K.S., Nature, 1928. **121**: p. 501.
8. Landau, L., and Placzek, G., Phys. Z. der Sowjetunion, 1934. **5**: p. 172.
9. Williams, K.P.J., et al., Journal of Raman Spectroscopy, 1994. **25**: p. 131.
10. Hédoux, A., Guinet, Y., and Descamps, M., International Journal of Pharmaceutics, 2011. **In Press, Corrected Proof**.
11. Harrick, N.J., and Loeb, G.I., Analitical Chemistry, 1973. **45**: p. 687.
12. Ikeshoji, T., Ono, Y., and Mizuno, T., Applied Optics, 1973. **12**: p. 2236.
13. Addison, C.J., Konorov, S. O., Schulze, H. G., Turner, R. F. B., and Blades, M. W., Journal of Raman Spectroscopy, 2011. **42**(3): p. 349-354.
14. Sharma, B., and Asher, S. A., Journal of Physical Chemistry B, 2011. **115**(18): p. 5659-5664.
15. Johnson, C.R., and Asher, S.A., Journal of Raman Spectroscopy, 1987. **18**: p. 345-349.
16. Barham, B.P. and P.J. Reid, Chemical Physics Letters, 2002. **361**(1-2): p. 49-56.
17. Hou, X.M., et al., Journal of Nanoparticle Research, 2011. **13**(5): p. 1929-1936.
18. Sreeprasad, T.S. and Pradeep, T., Langmuir, 2011. **27**(7): p. 3381-3390.
19. Terekhov, S.N., et al., Journal of Raman Spectroscopy, 2011. **42**(1): p. 12-20.
20. Cholett, P., Thin Solid Films, 1978. **52**: p. 343.
21. Johnson, K.L., Contact Mechanics, (Cambridge University Press, Cambridge, England, 1985).
22. Heavens, O., and Ditchburn, R., Insight into optics, (Wiley: Chichester, 1991).

3. Total Internal Reflection (TIR) Raman Experimental Setup

In this chapter the development of the total internal reflection (TIR) Raman experiments, setup of the Raman optical bench, TIR geometry for the *ex-situ* (solid/air interface) and *in-situ* (solid/solid interface) experiments, choice of materials followed for most of the experiments are described. A slightly different experimental setup was employed for the rotating ball experiments to study the lubricant properties under simultaneous pressure and shear, which involved development of a multipurpose tribometer, and will be discussed later in chapter 6.

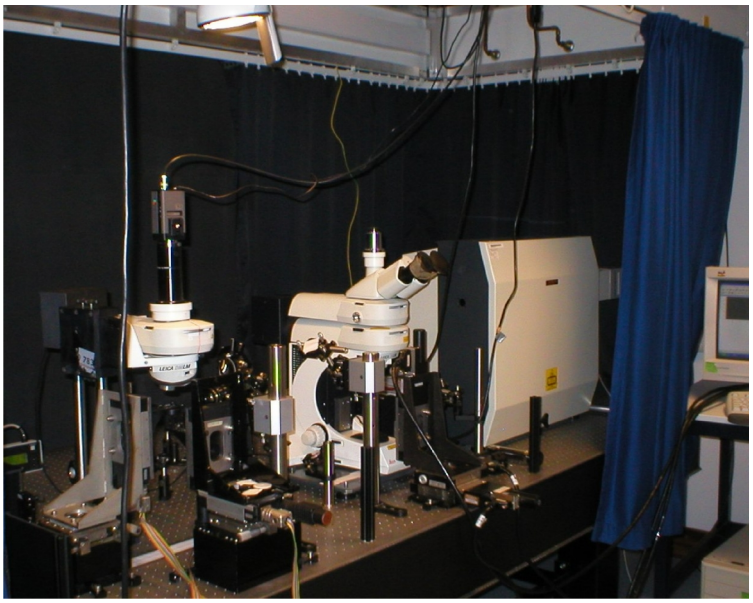

Figure 3.1: Photograph of the Raman optical bench used for the tribology experiments

3.1 The Raman optical bench

3.1.1 The Raman spectrometer

The Raman spectrometer was based on a commercial Raman microscope (Ramascope 1000, Renishaw) equipped with a 50× ULWD, 0.55 NA objective (Olympus). The scattered light is collected by a Leica DMLM microscope and directed into the Renishaw spectrometer, where it passes through long-pass edge filters that remove Rayleigh scattering. A removable polariser and a removable half-wave plate are in the path of the

collected light, allowing the polarisation of Raman scattering sent to the detector to be selected along *x*/*y*- axis. The transmitted radiation is then focused by a lens through a slit, re-collimated by another lens and directed onto a diffraction grating. The slit controls the depth and lateral resolution so that collected scattering can be restricted to a small depth and a small area at the point of focus of the microscope objective (fig. 3.1.1). Our Raman spectrometer has a maximum depth resolution of 2 μm and a lateral resolution of 2 μm. However, in my experiments the slit was open to a width of 200 μm to allow signal collection from a larger area and thereby increasing the effective field view.

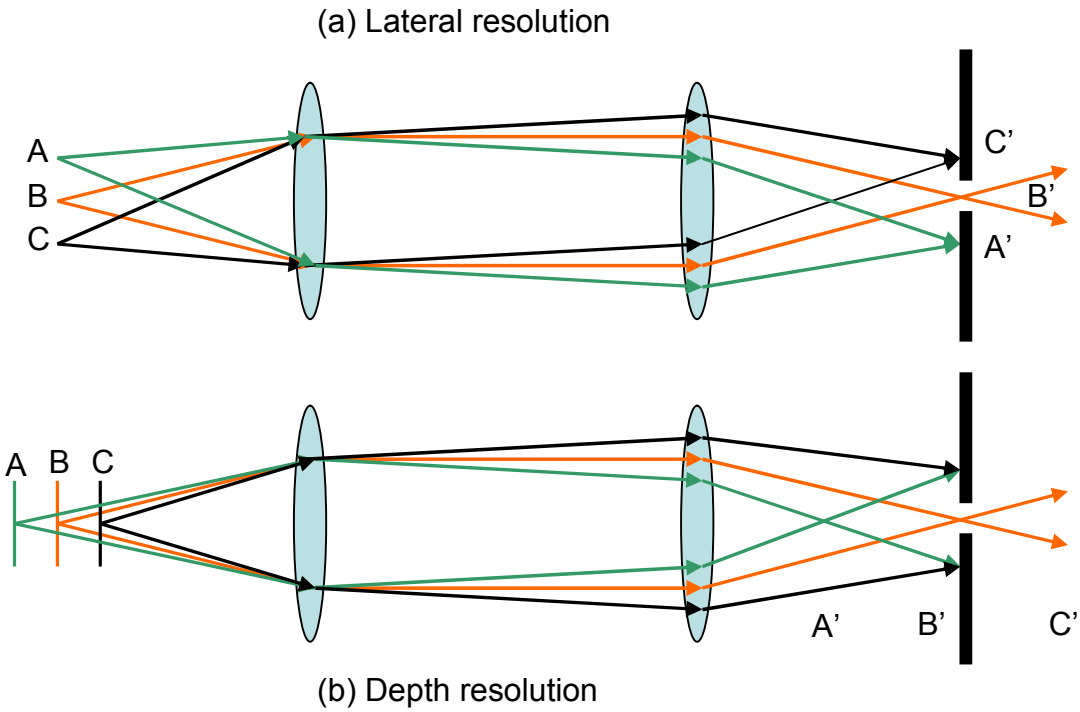

Figure 3.1.1: A ray tracing diagram showing the action of a pinhole to improve spatial resolution; (a) lateral resolution and (b) depth resolution.

The diffraction grating then disperses the scattering onto a Peltier cooled (-70 °C) CCD (charge-coupled device) detector. The area of the CCD that is read out can also be reduced which in turn reduces noise. In our experiments, the full length of the CCD was used in the spectral direction, and roughly 12 pixels (adjusted slightly according to the laser alignment in individual experiments) were used in a perpendicular direction. All

Raman spectral acquisitions were carried out in a dark room. A WiRE (Windows Raman Environment, from Renishaw plc.) software package controls the spectrometer.

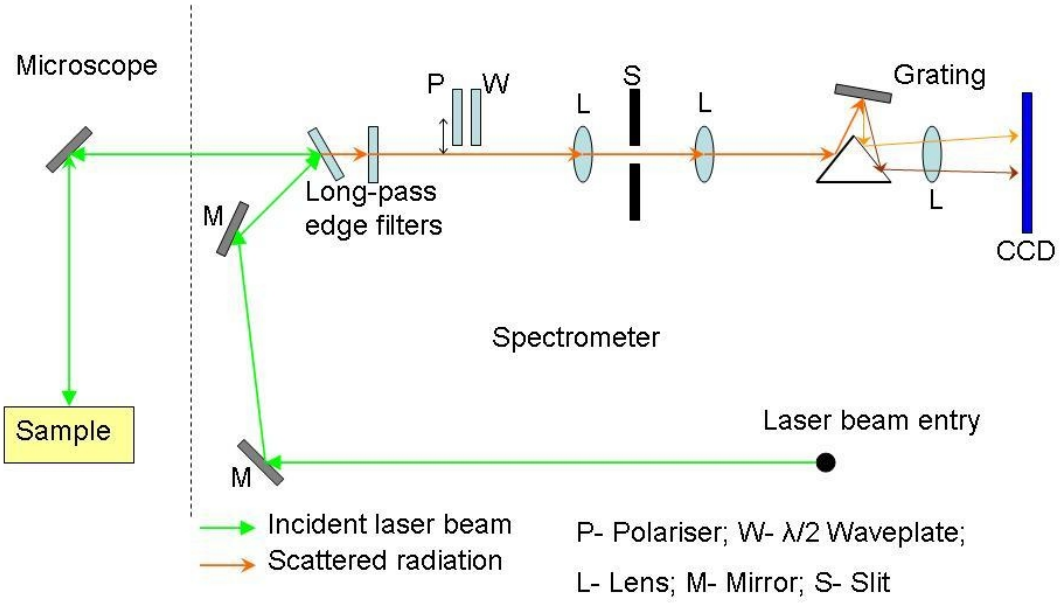

Figure 3.1.2: Ray tracing diagram showing the "internal" beam path in the Raman Spectrometer

3.1.2 Pump laser

In the early stages of our Raman experiment developments, a frequency-doubled continuous-wave Nd:YVO_4 laser was used as a light source, which emitted green vertically polarised light at a wavelength of 532 nm (Spectra-Physics Millennia II). This was later replaced by a diode-pumped solid-state laser (Opus 532, Laser Quantum), which emitted horizontally polarised light, also at 532 nm, and was used for acquiring most of the spectral data presented in this thesis. When the Spectra-Physics Millennia II laser was in action, 10% of the laser beam was split off for use along the "internal" beam path using a beam-splitter [1]. The "internal" beam path is the path of the laser in which the laser enters the back of the spectrometer, is reflected by a long-pass edge filter and travels down the Raman microscope, where it is focussed onto the sample (fig. 3.1.2). The remaining 90% of the laser beam travelled along the "external" beam path, the optical path I used in my TIR experiments, which does not involve passing the pump

laser through the internal optics of the spectrometer. A modified beam path was used for the "internal" beam along the Raman optical bench when the Opus 532, Laser Quantum was brought into action (fig. 3.1.3) and a polarising cube, which selectively allowed the horizontally polarised light to pass through, was placed in the beam path instead of the beam-splitter. The mirrors had to be rearranged in this case to shift to "external" beam path for TIR experiments. The laser power used in our experiments varied between 50 mW to 400 mW at the source.

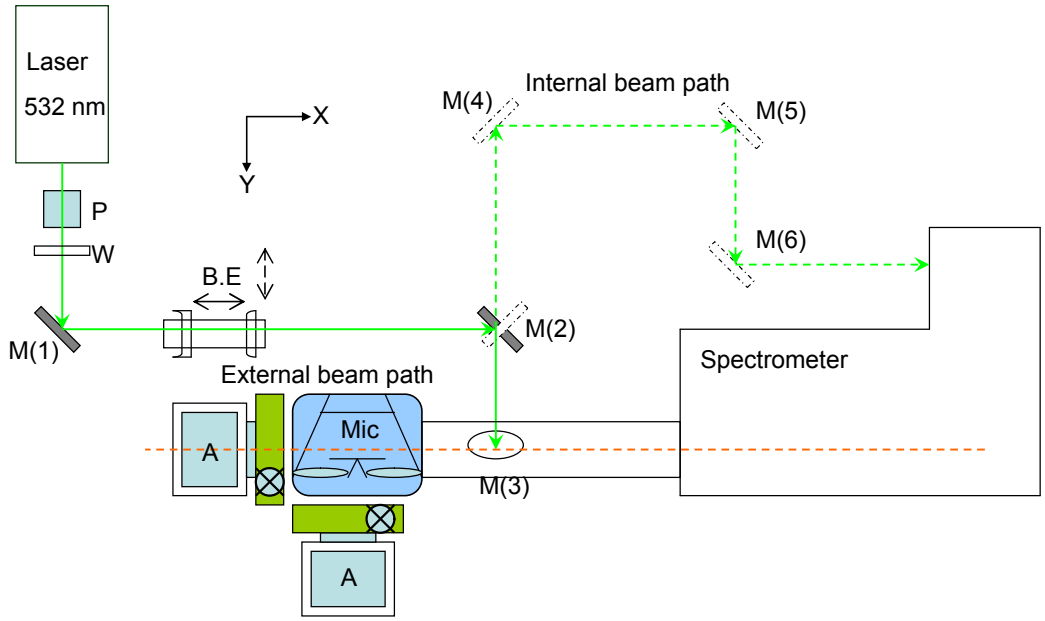

P- Polarising cube; W- λ/2 waveplate; B.E- Beam expander (removed for internal beam path); Mic- Microscope; A- Assembly of micromotion stages; M(1-6)- Mirrors. M(2) can be adjusted for internal and external beam paths; M(3) gives a periscopic elevation to the laser beam to focus at a desired angle of incidence, θ_i .

Figure 3.1.3: Schematic diagram of the Raman optical bench viewed from above

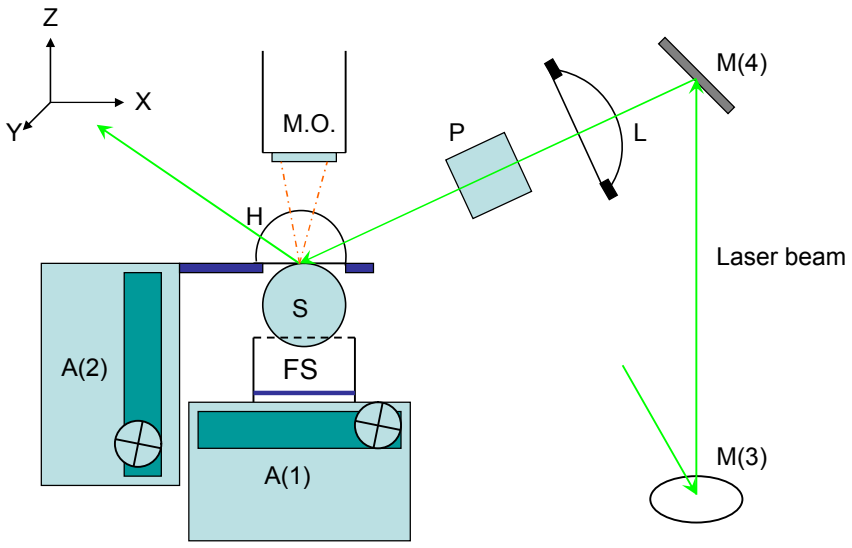

M.O.- Microscope objective; H- Hemisphere; S- Sphere; P- Polarising cube; L- focussing lens; M(3)- Periscopic mirror; M(4)- mirror guiding the laser beam at desired angle of incidence; A(1)- assembly of micromotion stages with the sphere holder; A(2)- assembly of micromotion stages with the hemisphere holder; FS- Force Sensor

Figure 3.1.4: Schematic diagram of the experimental geometry showing the mechanism of control of angle of incidence to focus the laser beam at the solid-solid contact area.

3.1.3 External beam path

Figure 3.1.3 is a schematic picture of the Raman optical bench from above. The laser travelled along this "external" beam path and was focused by a BK7 plano-convex lens (f = 100 mm) onto the solid-solid interface, just above critical angle, θ_c for the interface studied (fig. 3.1.4). The angles were chosen in such a way so that the total internal reflection (TIR) and the enhancement of the electric fields in the thin organic films are ensured at the interface.

Horizontally polarised light was emitted from the laser Opus 532- Laser Quantum, which was selectively polarised by a half-wave plate placed in the beam path after it passed through a polarising cube. The polarising cube was placed in the beam path to ensure that

only horizontally polarised light could pass through and the laser beam of any other polarisation was blocked. A fixed 5× beam expander expanded the laser beam to ~ 9 mm diameter ($1/e^2$ point in the intensity), so that a small spot size could be achieved on focussing into the solid-solid contact. However, for certain experiments e.g. obtaining TIR Raman spectra from Zn arachidate monolayers sandwiched at SF10/silica interface where getting the angle of incidence, $\theta_i \cong \theta_c$ is of significant importance, the beam expander was removed from the beam path. The advantages and disadvantages of using a beam expander in the external beam path will be described in section 3.2. The mirror, M(4) that directed the laser onto the sample, the focussing lens, L and the polarising cube, P (fig. 3.1.4) were all mounted on a single manual micrometer motion stage to allow changes in the height, and lateral direction, keeping the angle of incidence unchanged.

3.1.4 Experimental geometry

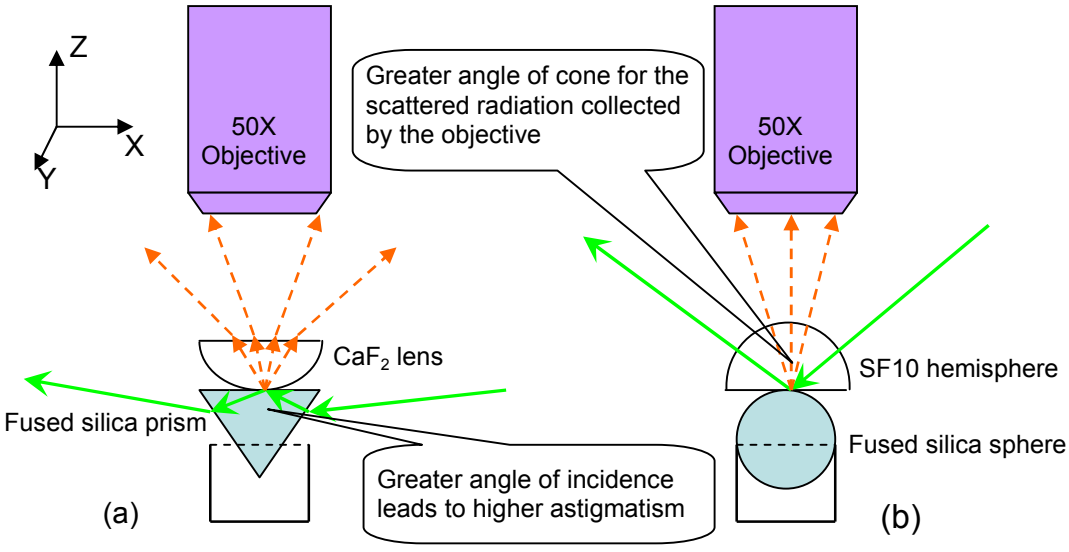

Figure 3.1.5: Schematic diagram of the experimental geometry (a) prism-lens system and (b) hemisphere-sphere system, showing the advantages of hemisphere-sphere system over the prism-lens system for tribology studies.

During the early days of our tribology experiments, we started with a prism-lens system (fig. 3.1.5(a)) where a CaF_2 lens (Crystran) was brought in contact from the top of a fused silica prism (Specac). The laser beam was focussed at the point of contact through the fused silica prism. This experimental setup was used by Sarah Haydock during her D.Phil. research at Oxford University and a detailed report of these experiments are included in her thesis [1]. Gradually we found it to be more advantage to use the hemisphere-sphere system, where the laser is focussed from the top of the hemisphere to the point of contact (fig. 3.1.5(b)). Therefore we moved on to using SF10 hemisphere of diameter 10 mm (ISP Optics) and fused silica (Global Optics, UK) sphere of 10 mm diameter for static experiments and 8 mm diameter for tribometer experiments to be described in a separate chapter.

The advantages of using the SF10 hemisphere/silica sphere system over silica prism/CaF_2 lens system are as follows:

(1) The critical angle, θ_c for silica (n = 1.46)/ CaF_2 (n = 1.437) system is 79.8° while the θ_c for SF10 (n = 1.74)/silica (n = 1.46) system is 57.2°. To obtain TIR, the angle of incidence, $\theta_i \geq \theta_c$, and higher angle of incidence leads to higher astigmatism, therefore an elliptical laser spot is formed at the focus. Hence using the SF10 hemisphere/silica sphere system the astigmatism can be eliminated, a less elliptical spot with a smaller diameter can be obtained at the focus, and a higher laser power per unit area of the contact spot can yield more intense Raman signals.

(2) In the prism/lens system, the scattered radiation is collected by the objective from top of the lens, and in the hemisphere/sphere system, the scattered radiation is collected by the objective from the top of the hemisphere as shown in figure 3.1.5(a) and 3.1.5(b) respectively. In case of prism/lens system, the numerical aperture, NA of the objective is reduced by refraction at the lens as shown in the figure.

(3) It is much simpler to align the laser beam for hemisphere/sphere system than the prism/lens system.

The advantage of using the prism/lens system over the hemisphere/sphere system is that it is easy to introduce shear in the experiments if the prism is translated along the *y*-axis in a micromotion stage keeping the position of lens fixed. In this case neither the laser alignment nor the contact spot moves and spectra can be acquired under sliding contact. Introducing shear in the hemisphere/sphere system is much more complex and involves rotation of the ball in a tribometer.

3.1.5 Formation of the solid-solid contact

The cleaned and monolayer-coated SF10 hemisphere and silica sphere were mounted into respective holders. The hemisphere holder was mounted onto a computer-controlled motion stage (controller: Newport MotionMaster 2000) with 0.1-μm resolution (Newport model UTMCC.1DD), which moved the hemisphere in and out of contact from the sphere surface. This stage was in turn mounted onto a set of manual micrometer motion stages, which allowed movement of the hemisphere in all directions parallel to the Raman optical bench (*xy*-plane). The sphere holder was mounted onto a force sensor (Omegadyne Inc., LC204-25) which was in turn mounted onto two motion stages with 1-μm resolution (Newport model UTMCC1DD), which moved the prism along the axis of the hemisphere (*z*-axis) and the *y*-axis (fig- 3.1.4(b)). The two computer controlled stages were mounted on a manual micrometer motion stage, which allowed controlled movement of the sphere in the *x*-axis if required. The three computer-controlled stages were equipped with DC servo drives, built-in tachometers, and linear encoders for position information, ensuring accurate and precise motion.

The focal point of the 5× microscope objective (Leica objective, NA 0.12) and that of 50× long working distance microscope objective (Olympus ULWD objective, WD = 8 mm, NA = 0.55) used in my Raman experiments were not exactly the same. The 50× objective was focused onto the upper surface (highest point) of the sphere and slid in the 5× objective which nearly focussed at the same point. Then the plane surface of the hemisphere was slowly brought down into contact with the sphere surface, at a speed of < 10 μm s^{-1}. When contact had been made Newton's rings were clearly visible around the

area of contact (figure 2.5.1). The 50× microscope objective was then slid back in place of the 5× objective to focus at the point of solid-solid contact and with minor adjustments in the positioning of the micromotion stages the central dark spot of the Newton's rings was centred exactly at the focus of the 50× objective.

3.1.6 Alignment

The contact area was estimated from the dark area inside the Newton's rings, with the 5× objective focussed. Throughout the Raman experiments spheres with radius of curvature (ROC) = 5 mm were used for in-situ static tribology experiments (without shear) and lipid bilayer squeezing experiments in aqueous environment, and spheres with ROC = 4 mm were used for tribometer experiments under applied pressure and shear. Contact regions of 0.05 – 0.3 mm diameter were observed at different applied pressures. The pressures applied to the molecules under solid-solid confinement were calculated from Hertz's equations [2] and were also matched with the reading from the digital force sensor placed under the sphere holder for all static experiments. In all Raman experiments, the maximum pressure in the centre of the contact area was calculated, and pressures achieved ranged from 150 MPa to 800 MPa. The laser spot was then focused to a minimum size (area ~ 2500 μm^2 when the beam expander is not used and area ~ 100 μm^2 in presence of beam expander in the external beam path), using the image on the video screen for guidance (section 3.2).

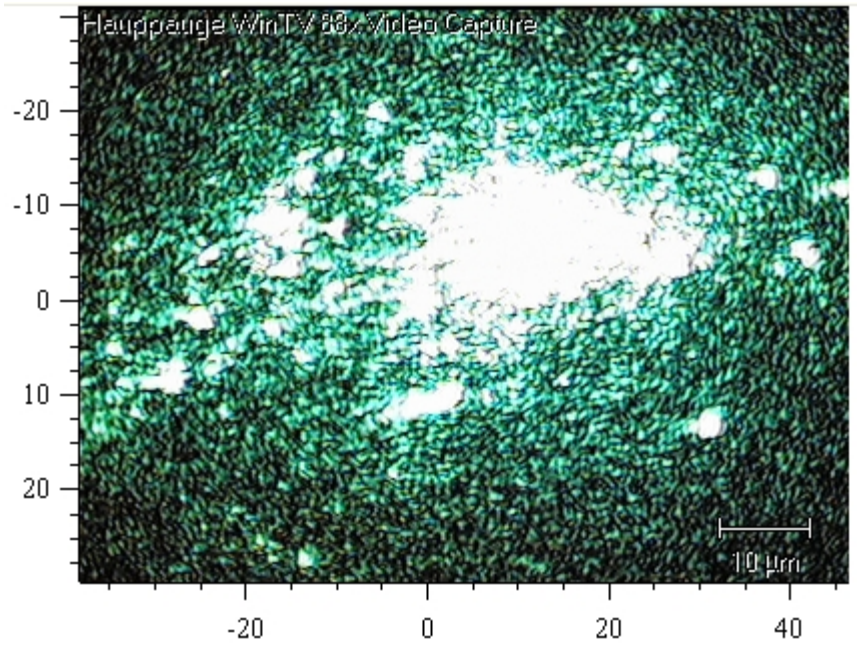

Figure 3.1.6: Laser spot recorded by a CCD camera, observed by 50× objective; a beam expander was used in the external beam path to obtain a focal spot of this dimension.

Focussing was achieved by altering the position of the focussing lens with the manual micrometer stages. During focussing regular spectra of 5 s acquisitions were obtained from the film at the solid-solid interface, since at optimal focus the Raman signal will be of optimal strength.

3.1.7 Shearing

In order to investigate the effects of shear forces on thin films, shearing experiments were carried out using in-situ Raman tribometers described in chapters 6 & 7. In the past shearing experiments were carried out in a prism-lens system by Sarah Haydock [1], where the prism can be moved along the shear axis (*y*-axis), against the lens at a very slow speed (~ 0.5 mm/s), without changing the angle of incidence throughout the movement. Raman spectra can then be obtained exactly as they would be from a stationary interface. However this scheme was not going to work when we shifted to hemispherical optics as a movement of the hemisphere along the *y*-axis would result in change in the angle of incidence with a fixed laser alignment. Hence a Raman tribometer was developed where a DC motor rotates a glass or a metal sphere at a controlled speed

while in contact with the plane surface of the hemisphere at a definite pressure. In this scheme, the hemisphere is kept fixed, and as the laser beam is focussed through the static hemisphere the alignment of the laser beam in principle does not change during the shearing process. However, there were associated difficulties in alignment of the optics in the tribometer, which will be discussed in a separate chapter, along with gradual development of the tribometer and possible remedies of the persisting problems.

3.1.8 Acquisition of spectra

The incident laser beam can be S- or P-polarised by using the half-wave plate in the beam path and the scattered radiation can be collected selectively along the *x*-axis or the *y*-axis using a polariser and another half-wave plate in the spectrometer giving rise to different set of spectra e.g. Sx, Sy, Px and Py. The spectra were acquired with acquisition times ranging from 30 s to 10 min, depending on the strength of the Raman signal. The spectra acquired were of two types; (a) a fixed-window scan centred about a particular wavenumber to look at the signals from a particular region of interest (e.g. spectra centred around 2900 cm^{-1} to look at the C-H stretching region), and (b) an extended scan over a wider range of wavenumbers as required for looking at the C-D stretching region (~ 2200 cm^{-1}) or water bands (~ 3400 cm^{-1}).

3.2 Working of a beam expander in the laser beam path

When a collimated laser beam of diameter, d (at $1/e^2$ point in the intensity) is focused by a converging lens of focal length, f the diameter of a laser focal spot is limited by (a) diffraction and (b) spherical aberration. The focal spot diameter, d_{diff} due to diffraction is

$$d_{diff} = \frac{4\lambda M^2 f}{\pi d} \qquad (3.2.1)$$

where λ is the wavelength of the laser beam and M^2 is the beam mode parameter (generally obtained from manufacturer's specifications). The focal spot diameter, d_{blur} due to spherical aberration, known as the blur circle is

$$d_{blur} = \frac{kd^3}{f^2} \qquad (3.2.2)$$

where k is an index of refraction function.

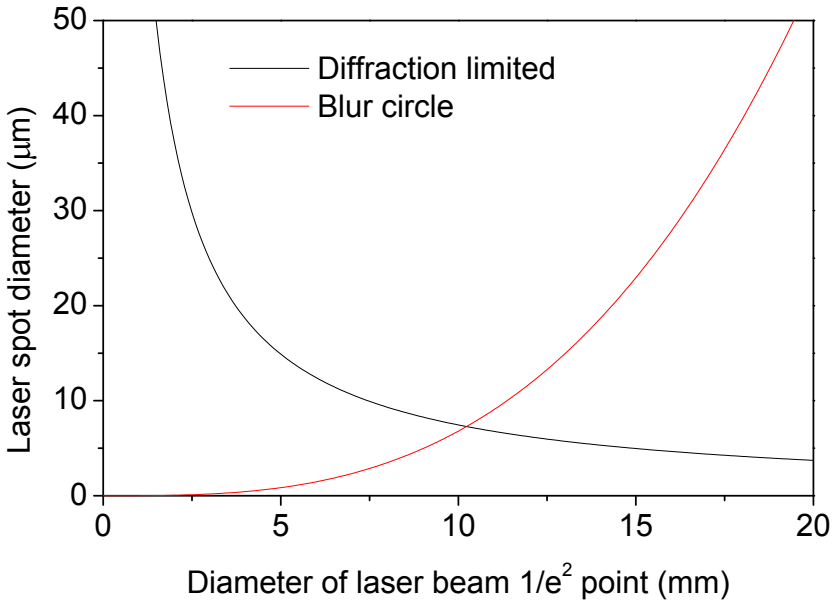

Figure 3.2.1: Plot of variation of laser spot size with increasing laser beam diameter ($1/e^2$ point in the intensity) when focused with a plano-convex BK7 lens (f = 100 mm)

If for a certain input diameter of a laser beam, d, the focal spot diameters $d_{diff} > d_{blur}$, then the focal spot is diffraction limited and if $d_{diff} < d_{blur}$, the focal spot is spherical aberration limited. In our experiments, the Opus 532 laser from Laser Quantum emitted laser at λ = 532 nm with a beam diameter ~1.8 mm (at $1/e^2$ point in the intensity) and $M^2 < 1.1$ as obtained from the manufacturer specifications, and a plano-convex BK7 lens with focal length, f = 100 mm was used to focus the laser spot at the solid-solid interface. The value of k for the BK7 plano-convex lens is 0.068. The variation of the diffraction limited and spherical aberration limited focal spot size was plotted against increasing diameters of the input laser beam in figure 3.2.1. The figure shows that the focal spot size is the smallest (~ 7.3 μm) if the incident laser beam has a diameter 10.2 mm (at $1/e^2$ point in the intensity). If the laser beam has a diameter less than 10.2 mm the focal spot size is diffraction limited and if the laser beam diameter is above 10.2 mm the focal spot size is spherical aberration limited. For a laser beam diameter 1.8 mm emitted from our laser source, the focal spot size was diffraction limited to a diameter 41.4 μm.

A simple Galilean beam expander [3] used in our Raman experiments consisted of a plano-concave lens or diverging lens of focal length, f = –25 mm (objective lens) followed by a plano-convex lens or converging lens of focal length, f = +125 mm (image lens) where the distance separating the two lenses is the sum of the focal lengths of the two lenses. Since the concave lens has a negative focal length and the convex lens has a positive focal length, the effective distance of separation (100 mm) between the two lenses is shorter than the focal length of the convex lens (image lens). The magnification power (M.P.) of the beam expander is the ratio of the output laser beam diameter to the input laser beam diameter. The beam expander used in our Raman bench has a M.P. = (–) focal length of the image lens/focal length of the objective lens = 5.

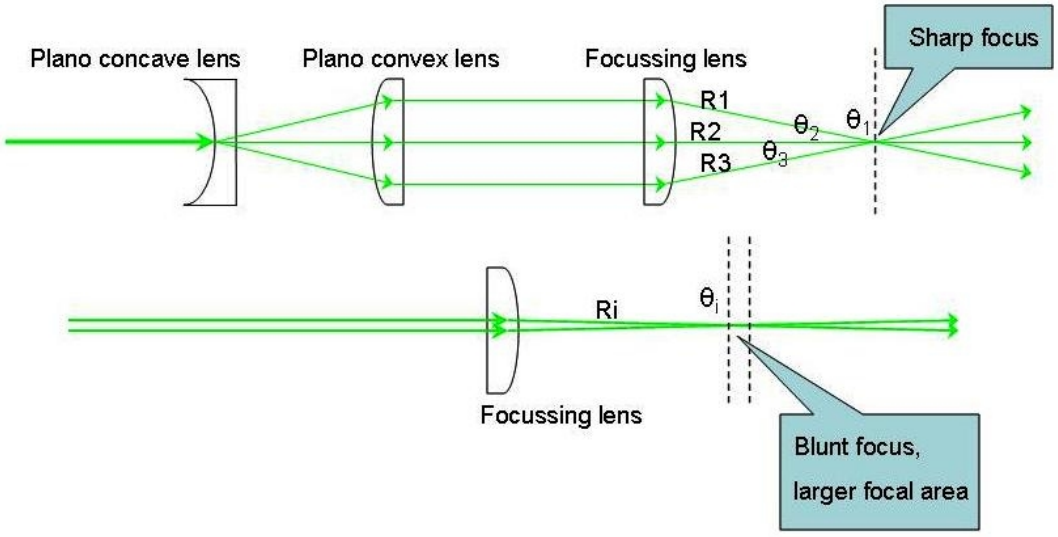

Figure 3.2.2: Working action of a beam expander in the path of laser beam in the Raman optical bench (rays R1, R2, R3 are incident at angles θ_1 , θ_2, θ_3 where $\theta_1 < \theta_2 < \theta_3$.

By using a beam expander in the external beam path a laser beam of diameter ~ 9 mm was obtained from an input laser beam diameter ($1/e^2$ point in the intensity) ~ 1.8 mm. A laser beam of wider diameter can be focused to a smaller area by the plano-convex BK7 lens at the solid-solid contact area (figure 3.2.2) thereby increasing the laser power per unit area of the focal spot resulting in more intense Raman signals. Figure 3.2.1 shows that the minimum focal spot size that can be obtained by focusing a laser beam of

diameter ~ 9 mm is diffraction limited to 8.3 μm. However, in the experiments like studying the molecular orientations of Zn arachidate monolayer molecules under solid-solid confinement, where working at the critical angle of incidence is of utmost importance due to reasons discussed in chapter 2, it is preferable to avoid using the beam expander in the external beam path. The reason is when a beam of larger diameter is focused at the interface, even though the laser beam is initially aligned at the critical angle for the pair of optics concerned, the cone of angles produced while focusing the expanded beam ranges from below to above the critical angle ($\pm 3.7°$).Therefore only a fraction of the incident laser beam undergoes total internal reflection (TIR), and for the rest of the beam which undergoes TIR, it is difficult to perform the orientational analysis on the probed monolayers due to nonzero value of K_{px} above and below the critical angle of incidence (section 2.2.3). Therefore for all the static experiments on Zn arachidate monolayers and DPPC monolayers at solid/air or solid/solid interface under applied pressure discussed in chapter 5, the beam expander was not used in the external beam path. However, for the lipid bilayer experiments in aqueous environment (chapter 6) where any observable phase change or squeezing of lipid material was the centre of interest rather than orientation of the molecules, we used the beam expander to obtain a smaller focal spot and therefore obtained better Raman signals even while working at an angle of incidence higher than the critical angle by a safe margin. Similarly for the tribometer experiments (chapter 7 & 8) particularly while working with fluid lubricants (hexadecane, PAO etc), the angle of incidence (θ_i = 60°) used for the laser beam was higher than the critical angle for the pair of solids to account for the run out issues of the rotating ball and the beam expander was used to obtain a better focus and more intense Raman signal.

It may be noted here that as the laser beam was focused at the solid-solid interface with an angle of incidence, θ_i greater than the critical angle, θ_c the focused spot was elliptical and the major axis, b of the elliptical spot is related to the minor axis, a by the equation

$$b = \frac{a}{\cos\theta_i} \qquad (3.2.3)$$

where the minor axis, a of the elliptical focal spot is the d_{diff} or d_{blur} diameters calculated using equation 3.2.1 and 3.2.2. The area, A of the elliptical focal spot can therefore be calculated as

$$A = \pi \frac{ab}{4} \qquad (3.2.4)$$

The laser spot was focused to an area of approximately 2500 μm^2 at the interface without the beam expander in the external beam path, while the focal spot was reduced to an area of around 100 μm^2 (fig. 3.1.6) using a beam expander in the external beam path.

3.3 Comparison of normal incidence Raman spectroscopy with TIR Raman spectroscopy

While studying model boundary lubricants under pressure and shear, I was interested in studying the monolayer films of zinc arachidate (less than 6 nm thick for two monolayers deposited on each solid surface at the solid-solid interface), where achieving sufficient sensitivity was a big problem. Adding to the problem, there was a very small number of molecules (~ 3×10^{11}) trapped between the two solid surfaces at a contact area of around 0.03 mm^2, which gave rise to the scattering. Hence the TIR geometry was employed in our experiments, which was expected on theoretical grounds, to sufficiently enhance the Raman scattering sensitivity at the interface allowing the detection of such thin films.

Experiments were carried out at Oxford University by Sarah Haydock [1], to illustrate the advantages of the TIR approach over normal incidence in studying ultra-thin organic films. The outcome of the comparison between normal incidence Raman spectroscopy and TIR Raman spectroscopy can be summarised as follows:

(1) Ratio of signal to background for the TIR configuration (4:1 for long chain fatty acids) is nearly two orders of magnitude better than for normal incidence method (1:14 for long chain fatty acids).

(2) Signal per unit time in the TIR spectrum is an order of magnitude greater than in the normal incidence spectrum.

(3) The power density in TIR configuration is an order of magnitude lower than in normal incidence configuration.

This significant improvement in signal to background ratio on using the TIR geometry can be due to the following reasons:

a) The background fluorescence from the sample is reduced, since the incident radiation does not penetrate the substrates e.g. prism (in prism-lens system)/ sphere (in hemisphere-sphere system) to a great depth directly below the microscope objective (the evanescent wave penetrates only a few hundred nanometers below the interface).

b) The excitation laser does not pass through the collection optics prior to reaching the sample, giving a reduction in fluorescence and Raman scattering from these optics.

The reasons for a significantly larger TIR signal with respect to power density are as follows:

a) The signal can be collected from a larger area without background fluorescence increasing prohibitively,

b) In the TIR configuration the electric field in the monolayer is enhanced giving greater Raman Scattering.

However, the main advantage of using a TIR configuration in Raman spectroscopy over the normal incidence mode is the fact that the TIR Raman spectroscopy has a sub-micron surface sensitivity. This is why TIR Raman spectroscopy has been used in depth profiling of polymer laminates [4]. Additionally, at critical angle of incidence and selecting the incident beam to be S- or P-polarised and choosing the direction of collection of scattered radiation along the *x*- or *y*-axes, the acquired spectra can be subjected to orientational analysis (section 2.4).

3.4 Choice of materials/optics in the TIR Raman experiments

For the solid-solid contact region to be accessible to light, at least one of the solids must be optically transparent. The laser beam can be delivered to the contact area and the

scattered light can be collected through the optically transparent solid. Therefore, the plane surface of SF10 hemisphere can be pressed against and sheared on model lubricants on a rotating steel ball (a useful configuration for the tribometer experiments). However, in most of my experiments, both the solids used for the solid-solid contact, were required to be optically transparent to obtain a total internal reflection (TIR) and therefore to obtain a surface enhancement of Raman signals. To obtain TIR at the solid-solid interface, the essential criterion remains that the solid through which the laser beam is delivered should have a higher refractive index, n. The other factors that influenced the choice of materials can be summarised as follows:

a) Availability and cost
b) Possibility to deposit high-quality Langmuir-Blodgett (LB) monolayers of zinc arachidate (or other fatty acids and their salts under examination) and DPPC (or any other lipids under examination) onto their surfaces (chapter 4).
c) Minimized fluorescence when pumped with 532 nm laser light, to avoid the possibility that the background swamps the signal (section 3.5).
d) Absence of substrate peaks (preferred) in regions of the Raman spectrum where hydrocarbon peaks from the organic films appear (section 3.5).
e) Ease of cleaning, as daily removal of the organic material will be required (section 3.6).
f) Smoothness of the solid surface to ensure a uniform contact between the surfaces. Additionally, this ensures that all the molecules at the point of contact are aligned in similar fashion on the surface of the substrate (when not in contact).

Guided by the aforesaid factors, I performed preliminary investigations choosing both solids to be optics (a) fused silica prism, n = 1.46 and (b) CaF_2 lens, n = 1.437 where the laser beam was delivered to the contact area through the silica prism at an angle of incidence higher than the critical angle ($\theta_c = 79.8°$) to obtain TIR. However, due to the advantages of using a hemisphere-sphere system over a prism-lens system described in section 3.1.4, we moved on to using SF10 hemisphere, n =1.74 and fused silica sphere, n =1.46 as the pair of solids forming the contact, where the both the laser light delivery and collection of the scattered light was through the SF10 hemisphere (fig. 3.1.5). Both the

hemispherical and spherical optics were chosen to have reasonably good surface quality (scratch/dig: 40/20) as provided by the supplier on the basis of a cost-quality compromise.

3.5 Raman bands from substrates

To check for fluorescing background (if any) from the substrates when pumped with 532 nm laser and to find out the presence/absence of substrate peaks in the Raman spectra where the hydrocarbon peaks from the organic films appear, cleaned uncoated optics were subjected to TIR Raman spectroscopy. The TIR spectra from CaF_2 hemisphere (Crystran) and fused silica hemisphere (ISP Optics) were carried out with 200 mW, S polarised incident laser beam with $\theta_i = 45.2^o$ and with acquisition times of 200 seconds. The TIR spectrum from SF10 hemisphere (ISP Optics) was carried out with a 20 mW, S-polarised incident laser beam with $\theta_i = 44.2^o$ and 200 seconds acquisition time. The lower power of incident laser beam was used for SF10 hemisphere to avoid saturation of the detector.

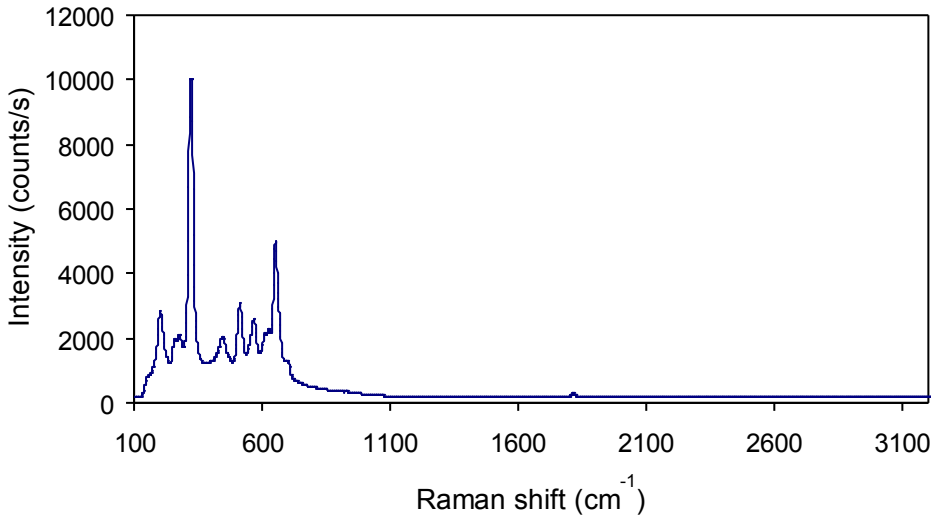

Fig. 3.5.1: TIR Raman spectrum at CaF_2/air interface from a CaF_2 hemisphere; S-pol. incident radiation, 200 mW laser power, 200 secs. acquisition, $\theta_i = 45.2^o$ ($\theta_c = 44.1^o$)

From fig. 3.5.1 it is evident that CaF_2, as a substrate is well suited for the Raman experiments as it does not show any significant peaks in the fingerprint region (700 cm^{-1}-

1500 cm^{-1}), neither any peaks in the 2900 cm^{-1} region where the hydrocarbon peaks from the organic molecules appear.

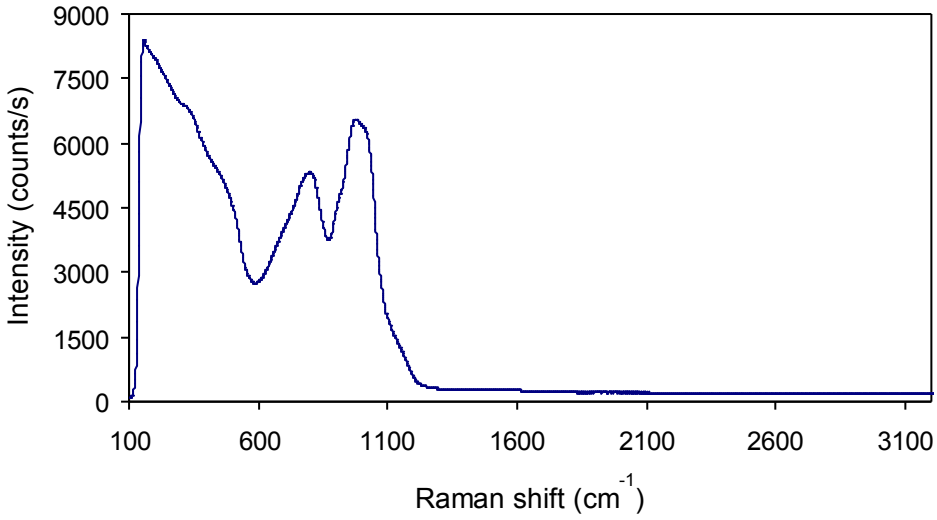

Fig. 3.5.2: TIR Raman spectrum at SF10/air interface from a SF10 hemisphere; S-pol. incident radiation, 20 mW laser power, 200 secs. acquisition, $\theta_i = 44.2^o$ ($\theta_c = 35.2^o$)

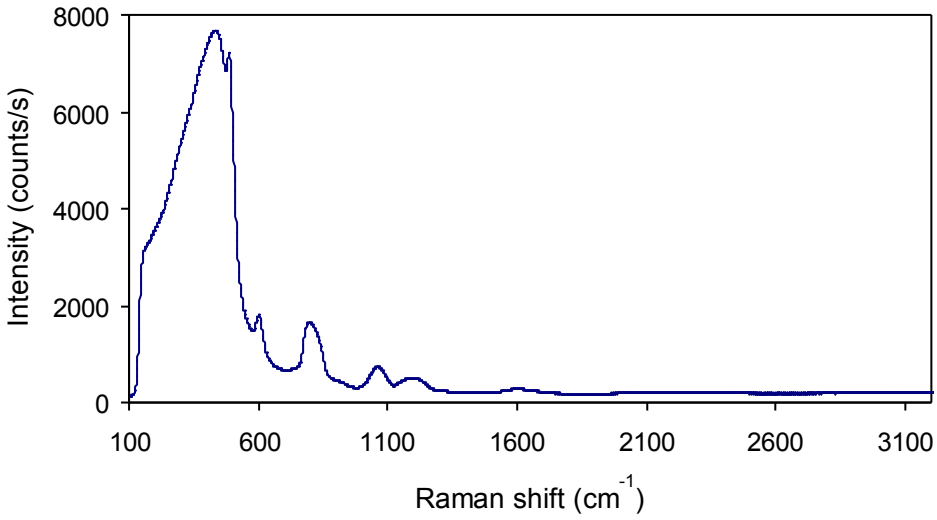

Fig. 3.5.3: TIR Raman spectrum at silica/air interface from a fused silica hemisphere; S-pol. incident radiation, 200 mW laser power, 200 secs. acquisition, $\theta_i = 45.2^o$ ($\theta_c = 43.23^o$)

Figure 3.5.2 and 3.5.3 shows that SF10 and fused silica can be good substrates for the Raman experiments as well, as we were mostly interested in the C-H stretching region (~2900 cm^{-1}) and to some extent C-D stretching region (~ 2180 cm^{-1}) in the Raman

spectra of organic molecules, surfactants and lipids, where there are no significant substrate contributions in the Raman signal. However, to work in the fingerprint region, SF10 and fused silica are not the best choice of materials as the substrate bands from SF10 and fused silica continue till midway and full length into the fingerprint region respectively.

Overall, due to the ease of cleaning of SF10 and fused silica optics, and due to greater instability of CaF_2 optics to sharp temperature changes and higher susceptibility to damage, SF10 and fused silica optics combination were preferred in our TIR experiments.

3.6 Cleaning of the optics

Cleanliness is of significant importance in surface science. To ensure a high level of cleanliness, a procedure was followed for the systematic cleaning of the optics used in forming the solid-solid contact, prior to the preparation of each experimental sample.

For fused silica and SF10 optics, which are insoluble soluble in water, the following procedure was followed:

(1) The optics were briefly washed with deionised water (Milli-Q, Gradient A10) and suspended in a clean teflon beaker containing analytical grade ethanol. It was sonicated for 15 mins to remove traces of polar organic materials (if any).

(2) The optics were rinsed briefly with deionised water (Milli-Q, Gradient A10) and immersed in chromosulphuric acid (composition 2-5% $Na_2Cr_2O_7$ in 90% H_2SO_4, abbreviated as BIC) in a clean Teflon beaker for 2 hours.

(3) The optics were rinsed briefly and then sonicated for 10 minutes suspended in deionised water (Milli-Q, Gradient A10).

(4) The optics were placed in the teflon-made optics holders, designed for coating Langmuir-Blodgett films, and suspended in BIC solution for another 20 minutes.

(5) The optics holder together with the optics attached to it were rinsed under the tap with deionised water (Milli-Q, Gradient A10) until it is completely free of Cr^{3+}

ions (the water dripping from the optics/holder was completely colourless), and fastened to the dipper in the LB trough for coating.

It may be noted here that due to safety reasons the Teflon beaker containing the BIC solution and the immersed optics were kept in a fume hood covered with a glass slide to avoid the absorption of moisture in the air by the BIC solution (strongly hygroscopic) and thereby getting diluted. A pair of hand gloves was used to carry out all the operations with the BIC solution as it is highly corrosive and harmful to skin. After the optics were immersed in BIC solution for 2 hours (step 2), the excess BIC solution in the Teflon beaker was transferred back to the original container for future use, and the remaining BIC solution adhered to the optics and the Teflon beaker. The Teflon beaker was then filled up with water twice and the yellowish green solution containing Cr^{3+} and $Cr_2O_7^{2-}$ ions was disposed off to the 'heavy metal waste' bottle for recycling. The steps 3, 4, and 5 were then carried out as described above.

For materials that are sparingly soluble in water, i.e. the CaF_2 lenses/hemispheres, the above procedure of suspending the optics in BIC was not followed, instead it was dried in a stream of N_2 and the optics were put in the plasma cleaner and plasma treated for 10 minutes to remove traces of non-polar organic materials and surfactants.

3.7 Deposition of Langmuir-Blodgett (LB) films on the substrates

The description of the experimental procedure remains incomplete without the description of the sample preparation methods, which involved Langmuir-Blodgett (LB) deposition of the Zn arachidate as model boundary lubricants, or deposition of DPPC lipid monolayer onto SF10 hemispheres and silica spheres, to be used in the tribology experiments *ex-situ* and *in-situ*. A detailed description this LB deposition technique used in the experiments along with characterisation of these monolayers by TIR Raman spectroscopy is included in chapter 4.

References:

1. Haydock, S.A., in *D.Phil thesis, Oxford University*. 2002.
2. Johnson, K.L., *Contact Mechanics.* Cambridge University Press, 1985.
3. Hecht, E., *Optics.* Reading, Massachusetts: Addison-Wesley, 1987.
4. Greene, P.R., and Bain, C.D., Spectroscopy Europe, 2004. **16**: p. 8-15.

4. Langmuir-Blodgett monolayer and organic films

Throughout my PhD project thin films under solid-solid confinement have been characterised by Total Internal Reflection (TIR) Raman Spectroscopy, under varied conditions of pressure and shear. To understand the properties of these thin films under applied pressure and shear presented in the later chapters of this thesis, it is important to understand the structure and properties of these films in absence of any applied forces. This chapter begins with a brief history of monolayers and then moves on to discuss the Langmuir-Blodgett (LB) deposition, pressure-area isotherms and characterisation of deposited films by TIR Raman spectroscopy.

4.1 A brief history of Langmuir-Blodgett (LB) monolayers

The history of monolayers began with Benjamin Franklin, an American statesman, who spent many years travelling on ships and during that time it is likely he became aware of the effect of oil in calming the waves, a phenomenon that was well known to the sailors. During one such journey in a convoy of ships, Franklin noticed that the water behind his ship was smoother than the water behind other ships, and a sailor explained to him that the greasy water from the kitchen had just been discarded. After a few months, in the pond at Clapham Common in London, Franklin did an experiment by pouring a teaspoonful of oil on to the pond surface [1]. Although the observation by sailors about the calming effect of ripples on the water surface caused by spreading oil was reported even before by Plutarch (46 – 120 AD) and Aristotle (384 – 322 BC) [2], Franklin's report to the British Royal Society in 1774 on his observation at Clapham Common can be stated as the first scientific report of a monolayer [3].

"At length at Clapham where there is, on the common, a large pond, which I observed to be one day very rough with the wind, I fetched out a cruet of oil, and dropped a little of it on the water. I saw it spread itself with surprising swiftness upon the surface... the oil, though not more than a teaspoonful, produced an instant calm over a space several yards square, which spread amazingly and extended itself gradually until it reached the leeside, making all that quarter of the pond, perhaps half an acre, as smooth as a looking glass."

A simple calculation reveals that if one teaspoon (5 ml) of oil is spread over half an acre of area, the thickness of the oil film must be ~2.5 nm, which corresponds to one molecule thick layer. Molecular dimensions were not known in those days, which prevented Franklin from investigating monolayer films any further.

After over a hundred years later Lord Rayleigh found out that the maximum extension of an oil film on water surface represents a molecularly thick layer [4, 5]. Around the same time a German woman named Agnes Pockels laid the foundation of characterising monolayers at air-water interface. Around 1882, she started her experiments on monolayers in her kitchen sink. She used a tin tray as a water container and a small disc suspended from a balance with a slide weight to measure the surface tension. With this rudimentary surface balance she could determine water surface contamination as a function of the area for different oils confining the water surfaces to different areas using waxed tin strips. Pockels' work was published in Nature in 1891 [6], on recommendation of Lord Rayleigh which laid the foundation for Langmuir's quantitative work on fatty acid, ester and alcohol monolayers.

Irving Langmuir was an industrial research scientist employed by US General Electric Company in Schenectady, New York and was the first to perform systematic studies on floating monolayers on water in the late 1910's and early 1920's. He was the first person to give the modern understanding of the structure of monolayer systems at the molecular level, particularly the fact that the molecules at air-water interface show preferential orientation [7]. In early 1920's he reported that molecular layers of fatty acids can be transferred from the air-water interface to solid substrates [8]. In 1932 Irving Langmuir was awarded the Nobel Prize for his contribution to surface chemistry. However, the first report of sequential monolayer transfer on a solid substrate was first given by Katherine Blodgett, who was an assistant working with Irving Langmuir at General Electric [9]. She found that multilayer films of custom thickness can be built up by repeating the deposition process more than once [10]. Therefore these built-up monolayer assemblies are now referred to as 'Langmuir-Blodgett (LB) films', while the term 'Langmuir film' is generally used for a floating monolayer. Blodgett published a paper in 1939 [11, 12]

reporting the use of LB films to cause deconstructive interference of light being reflected from coated glass surfaces.

There was a relatively quiet period in the research of LB films after Langmuir and Blodgett, when in the 1960s George Gaines, who was also a research chemist at GE started publishing his work on insoluble monolayers at liquid-gas interfaces and also wrote a book on the history of LB film research [13, 14]. This revived the research interest of Kuhn and Möbius in LB films and around 1970s, they found the importance of molecular orientation and multilayer structure in the fluorescing and quenching of the films of dye molecules [15]. The first international conference on Langmuir-Blodgett (LB) films was held in 1979, and since then this technique has been used increasingly by scientists on various fields of research. Despite the production of ultrathin organic films with LB- technique for possible practical applications in many fields [16] e.g. artificial membranes, patterning materials, thin film optical devices, displays etc., LB films are still mostly used for research purpose to model biomembranes and multilayer coatings.

4.2 LB monolayers as model boundary lubricants

Langmuir-Blodgett (LB) monolayers are model boundary lubricants. Preliminary investigations have been carried out in Bain's group with sum-frequency spectroscopy (SFS) of LB monolayers of zinc arachidate at the sapphire/silica interface [17], and comparative investigations with Raman scattering [18]. During my PhD research, the investigations on the LB monolayers confined at the solid-solid interfaces (e.g. SF10/silica interface) by Raman scattering have been extended.

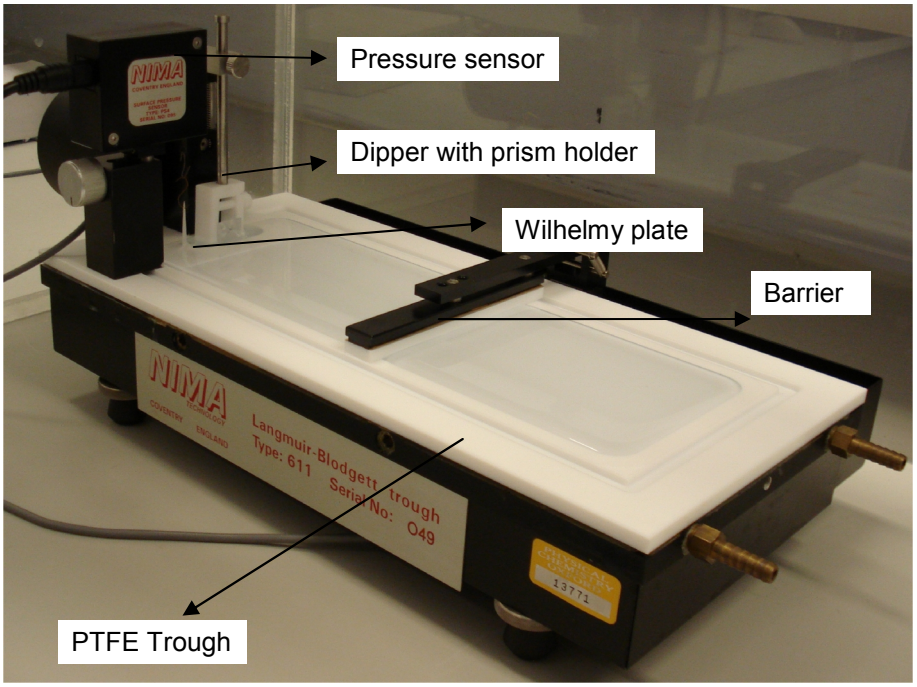

Figure: 4.2.1: Picture of the LB trough (NIMA) used for deposition of the monolayers

LB monolayers used in this project contain the following molecules:

- Zinc stearate $Zn^{2+}\,[CH_3(CH_2)_{16}CO_2^-]_2$
- Zinc arachidate $Zn^{2+}\,[CH_3(CH_2)_{18}CO_2^-]_2$
- Zinc behenate $Zn^{2+}\,[CH_3(CH_2)_{20}CO_2^-]_2$
- Dipalmitoyl-phosphatidylcholine (DPPC) $C_{40}H_{80}NO_8P$

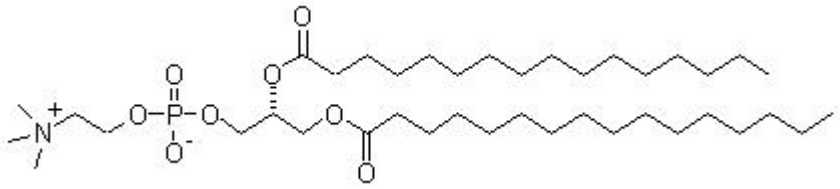

Figure 4.2.2: Molecular structure of DPPC

Zinc salts of fatty acids are used rather than cadmium salts, because previous investigations carried out in this laboratory discovered that good LB monolayers of zinc salts could be formed. Zinc is much less toxic than cadmium, and so is preferable for use in the laboratory on a daily basis. For the substrates to be used in my research e.g. hydrophilic surfaces of SF10, fused silica optics etc., it is the polar head group of the

surfactant molecule that binds to the substrate surfaces. SF10 and fused silica surfaces are negatively charged at pH 7, and Zn^{2+} acts to bridge between the $-SiO^-$ at the optics surfaces and $-CO_2^-$ of the head group of fatty acids.

4.2.1 The Langmuir-Blodgett trough

A computer-controlled LB trough was used (NIMA Technology 611M), which is made from inert and hydrophobic polytetrafluoroethane (PTFE). The trough measures roughly 10 cm x 27 cm. A computer-controlled PTFE barrier moves across the trough in order to compress the surface area of the solution (known as the sub-phase) in the trough, and this barrier is operated by a D.C. motor for smoothness (fig. 4.2.1). A Wilhelmy plate made of filter paper is partially immersed in the sub-phase, in order that indirect measurements of the surface pressure can be given by the computer interface. The plate experiences a downward force, F from the sub-phase, which is measured by a counter-balance.

[Force on plate] = [Weight of plate] + [Surface tension force] – [Buoyant force]

$$F = (m_p g) + 2(t_p + w_p)\sigma \cos\theta - \rho V_p g \qquad (4.2.1)$$

where m_p = mass of the plate, g = acceleration due to gravitation, t_p = thickness of the plate, w_p = width of the plate, σ = surface tension, θ = contact angle, ρ = density of liquid, V_p = volume of the immersed plate, or volume of the displaced liquid. The weight of the plate can be determined beforehand and set to zero on the electrobalance, and the effect of buoyancy can be removed by extrapolating the force back to the zero depth of immersion. The remaining component of force is only the wetting force. Assuming that perfect wetting of the plate occurs, contact angle, $\theta = 0$ and $\cos\theta = 1$. Dividing the force experienced by the Wilhelmy plate, F by the perimeter of the filter paper gives a value of the surface tension, σ.

Surface pressure, π can be calculated as

$$\pi = \sigma_0 - \sigma \qquad (4.2.2)$$

where σ_0 is the surface tension of pure water. The computer interface allows control of the barrier speed and produces plots of π *vs* surface area on the trough.

4.2.2 Deposition of LB monolayers

Deposition was carried out by standard LB techniques [9, 10] . An aqueous solution of $ZnSO_4$ (10^{-4} M $ZnSO_4$ in Milli-Q water) was prepared as the sub-phase for deposition of zinc stearate, zinc arachidate and zinc behenate. For deposition of DPPC pure deionised Milli-Q water was used as a subphase. The subphase was poured into the trough such that the upper meniscus/surface of the subphase lies ~2 mm above the level of the trough. The barrier was opened to a large surface area and a clean substrate (e.g. an SF10 or fused silica optics) was attached to a dipper rod, and was lowered vertically into the well at the end of the trough. The surface of the sub-phase was then cleaned by repeated closing of the barrier and suction of the surface impurities.

Solutions of surfactant in chloroform (approx 1 mg/ml) were prepared, concentration was exactly noted, and ~ 40 μl were dropped onto the centre of the trough surface with a micro-syringe. The primary surfactants used in my experiments were arachidic acid (Aldrich) and Dipalmitoyl-phosphatidylcholine (DPPC). Other surfactants e.g. stearic acid (Aldrich) and behenic acid (Aldrich) was also used to examine the nature of the pressure-area isotherms. The chloroform was allowed to evaporate and the barrier was slowly closed under computerised pressure control menu. When a surface pressure of 35 mNm^{-1} was reached, and the molecules in the floating surface layer were in a solid phase for zinc arachidate and liquid condensed phase for DPPC, deposition was carried out. The substrate was slowly drawn vertically out of the well in the trough with the computer controlled dipper rod (at 2 mm/min), through the floating surface layer of surfactant molecules. The pressure was held at 35 mNm^{-1} by the computer interface (the barrier position was altered as necessary to achieve this), therefore a highly ordered layer of surfactant molecules was always present on the trough surface. As the substrate was drawn through this surface floating layer, the surfactant molecules were transferred from the trough to the substrate surface, and a monolayer was deposited. Since the substrates were hydrophilic, the head-groups of the monolayer oriented towards to the solid surface, whereas the hydrophobic alkyl chains were exposed to the air.

The trough had provisions for thermal control; where water-cooled/heated could be circulated through a channel below the trough throughout the deposition in order to keep the temperature constant at 20°C. However the room temperature for our experiments was almost fixed to 20°C by the room heater, so we did not use the water circulation. Figure 4.2.3 shows a schematic diagram of LB deposition in process.

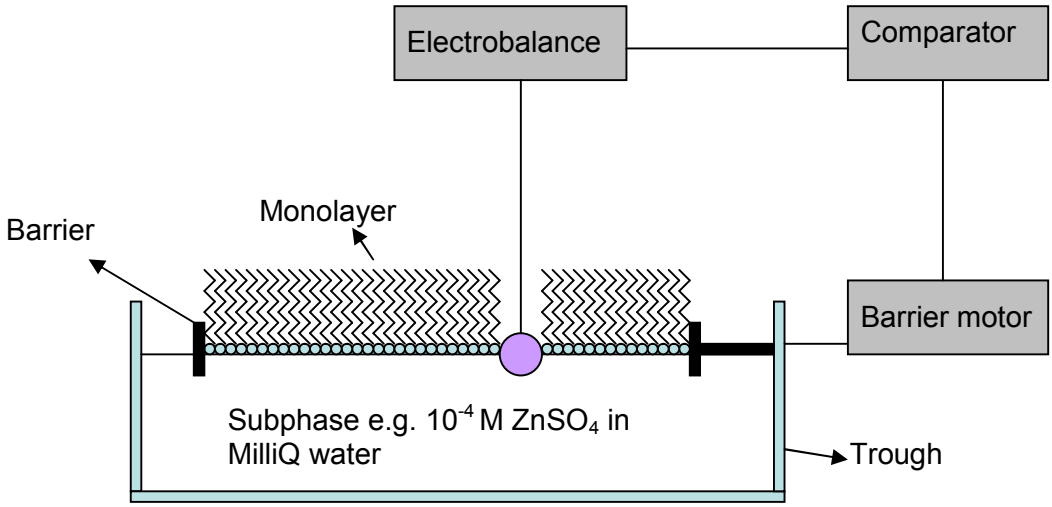

Figure 4.2.3: A diagram of an LB deposition in progress. The substrate is drawn through the Langmuir film whilst the barrier position is altered to maintain an ordered film on the surface of the subphase. An LB film is therefore transferred onto the substrate surface.

4.2.3 Pressure-Area isotherms

Pressure-area isotherms are presented for zinc stearate, zinc arachidate, and zinc behenate in figure 4.2.4 and that of DPPC in figure 4.2.5. All isotherms were obtained at ~ 20°C. For all the stearate, arachidate and behenate salts the surface area was decreased until collapse of the surfactant film was observed. There are 4 distinct regions in the pressure-area isotherms of zinc salts of straight-chain fatty acids, which are labelled a–d in figure 4.2.4. Initially, at large surface area, the plot is horizontal (region a), which corresponds to a floating layer consisting of "islands" of tilted molecules that move towards each other as the surface area is decreased. The first phase change occurs when the tilted molecules occupy the whole surface area of the Langmuir trough; this phase is fairly

compressible due to the untilting of the hydrocarbon chains (region b). The second phase change occurs as the hydrocarbon chains of the molecules become upright, but this phase is comparatively incompressible (region c). The phase transition is second-order, as evidenced by the absence of a plateau in the pressure-area isotherm. Decreasing the surface area further eventually causes the monolayer to collapse. Collapse occurs when the surface pressure becomes so high that the surfactant molecules become dissolved in the subphase, or the monolayer breaks and one layer of molecules slides over another layer to form a bilayer or multilayer (region d). The second-order phase transition occurred at a surface pressure between 20 and 25 mNm^{-1} for each fatty acid and so LB depositions were carried out at 35 mNm^{-1} (marked in black in fig 4.2.4) and 20 ^{o}C to ensure that a highly ordered LB monolayer was obtained for use in my experiments. The area per molecule in the solid phase for the all the three fatty acids were around 18.8 $Å^2$ [19].

There are 4 distinct regions in the pressure-area isotherm of DPPC as well (figure 4.2.5), however the phase changes accompanied with compression of the DPPC monolayer are somewhat different from that of the straight chain fatty acids [20]. At high molecular areas the monolayer exhibits a quasi two-dimensional gas state (region a). For molecular areas between ~98 $Å^2$/molecule to ~78 $Å^2$/molecule the region represents the liquid-expanded (LE) phase (region b), where the amphiphiles are in contact without molecular ordering. At molecular area ~78 $Å^2$/molecule, with further film compression the isotherm shows a co-existence between the liquid-expanded (LE) phase and liquid-condensed (LC) phase (region c). At the LE-LC co-existence region the surface pressure forms a plateau starting at π = 4 mN/m and ending at 5.2 mN/m with a corresponding molecular area ~53 $Å^2$/molecule, from where the single liquid-condensed (LC) phase begins. In the LC-phase (region d) DPPC exhibit a short-range translational order of the headgroup positions. Simultaneously, the alkyl chains of the hydrophobic molecular part show a long-range order in their orientation. The LB depositions of DPPC monolayers were carried out at 35 mN/m (marked in black in fig 4.2.5).

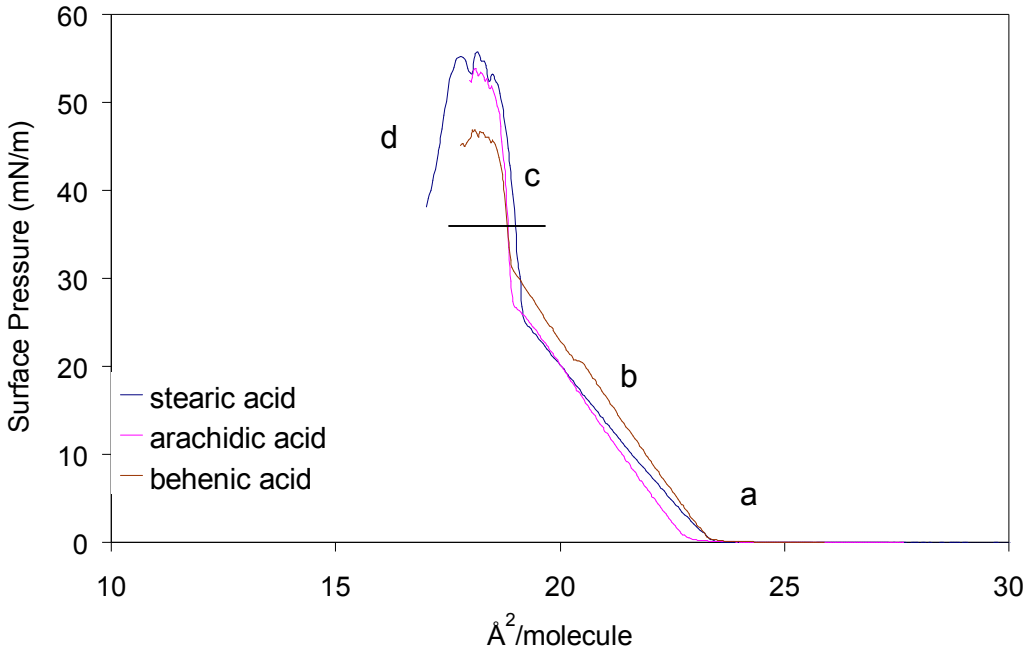

Figure 4.2.4: Pressure-area isotherms of zinc stearate, zinc arachidate and zinc behenate monolayers at ~20°C obtained by compressing the respective fatty acids spread on a sub-phase of 10^{-4} M $ZnSO_4$ solution.

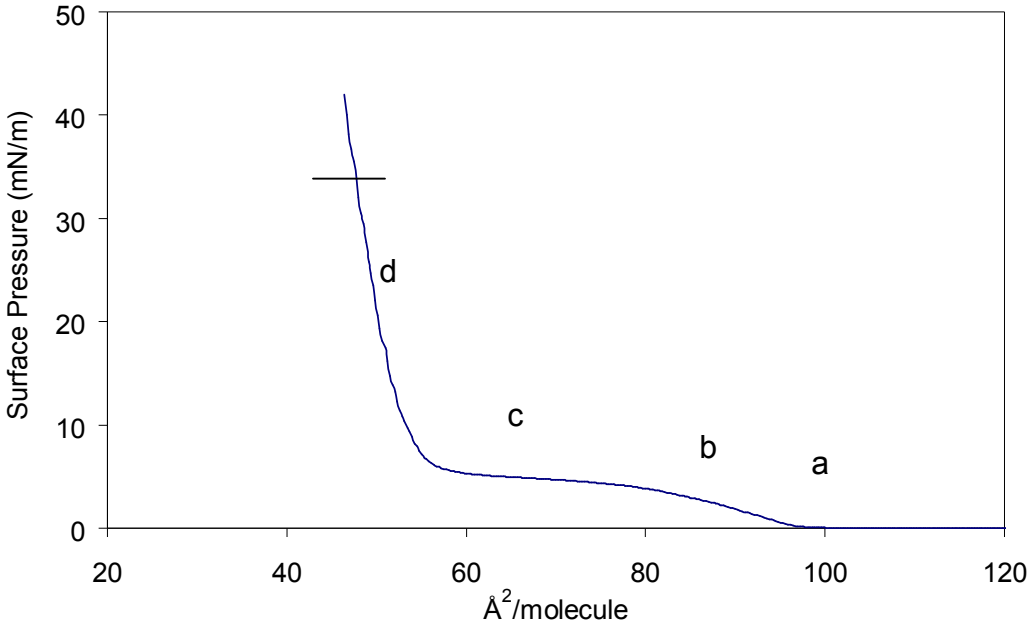

Figure 4.2.5: Pressure-area isotherm of DPPC monolayer; subphase MilliQ water; temp. ~20 °C.

4.3 TIR Raman spectra from LB monolayers

TIR Raman spectra were obtained from LB monolayers of Zn arachidate and DPPC deposited on silica, SF10 and CaF_2 surfaces in order to study the appearance of the spectra prior to application of the pressure and thereby study the quality of the deposited monolayer. Figure 4.3.1 shows the TIR Raman spectra collected form Zn arachidate monolayers deposited on clean fused silica prism and CaF_2 prism. The angle of incidence was set to be 45^o which is above the critical angle for both silica and CaF_2 in air (θ_c for the CaF_2/air interface is 44.1^o, and silica/air interface is 43.2^o).

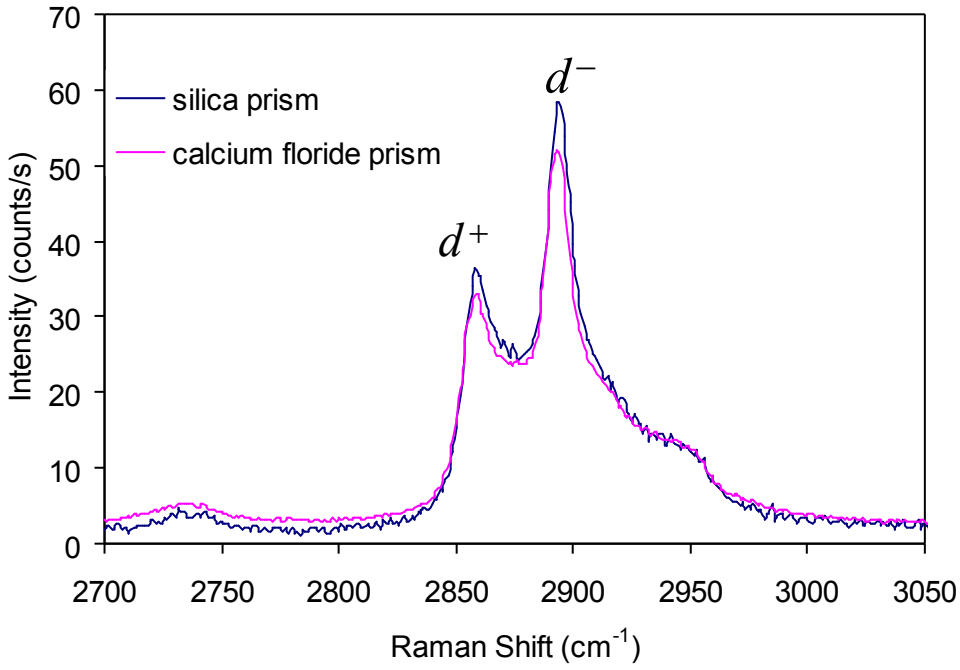

Fig 4.3.1: TIR Raman spectra obtained with S-polarised incident radiation from an LB monolayer of Zn arachidate on the surface of clean silica prism and clean CaF_2 prism, both in air; 400 mW, 532 nm, 300 s acquisition, $\theta_i \sim 45^o$.

Raman vibrational mode	Position (cm^{-1})
Fermi resonance of the CH_2 symmetric stretch with an overtone of the CH_2 scissors mode.	2931
Antisymmetric CH_2 stretch (d^-)	2881
Symmetric CH_2 stretch (d^+)	2846

Table 4.3.1: Table showing major Raman bands arising from the hydrocarbon chains at the C-H stretching region

The C-H stretching region of the spectrum obtained with S-polarised light in figure 4.3.1 is typical of a spectrum obtained from an ordered LB film. In both the substrates, the intensity ratio of the peaks due to asymmetric C-H stretching to symmetric C-H stretching, denoted as $I(d^-)/I(d^+)$ or d^-/d^+ is ~ 1.7 (as obtained from the curve-fitting data of the spectra in figure 4.3.1, refer chapter 5, section 5.3 for curve fitting parameters), which is indicative of a film containing mainly all-*trans* hydrocarbon chains with very few gauche defect. According to Ho and Pemberton [21], intensity ratio, d^-/d^+ value ranging from 1.6-2 indicates solid well ordered material, while d^-/d^+ value less than 0.9 indicates disordered liquid material. The intensity ratio, d^-/d^+ is found to increase with increasing structural order of hydrocarbon chains. This spectra of a highly ordered monolayer suggested that good quality of Zn arachidate monolayer formation was possible on both silica and CaF_2 surfaces and are possible choices of materials for the solid-solid contact experiments.

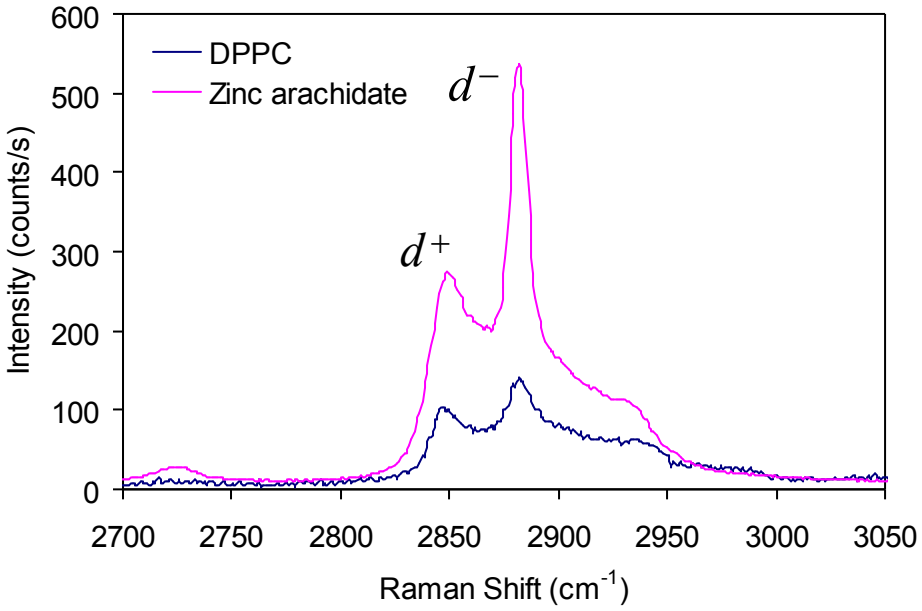

Fig 4.3.2: TIR Raman spectra obtained with S-polarised incident radiation from an LB monolayer of Zn arachidate and DPPC on the surface of clean fused silica hemisphere in air; 300 mW, 532 nm, 300 s acquisition, $\theta_i \sim 44.1^o$

However, due to issues like difficulty in cleaning, and greater susceptibility to damage due to sharp temperature change, a substitute of CaF_2 was sought after. As we moved on to the hemisphere-sphere system from prism-lens system to simplify the alignment, and attain smaller laser spot by focusing closer to the critical angle of incidence, SF10 hemisphere was chosen as one of the solids to press on fused a silica sphere – the other solid.

Figure 4.3.2 shows the TIR Raman spectra of zinc arachidate and DPPC monolayers deposited on fused silica hemispheres, and in comparison to figure 4.3.1 it is clearly evident that the Raman signal from zinc arachidate deposited on fused silica hemisphere was much more intense than that deposited on fused silica prism, even for a lower power of incident radiation used. In figure 4.3.2, the d^-/d^+ ratio for the spectra from zinc arachidate monolayer is ~1.9 (as obtained from the curve-fitting data of the spectra in figure 4.3.2, refer chapter 5, section 5.3 for curve fitting parameters) which reconfirmed the transfer of highly ordered monolayer onto fused silica surface by LB technique.

However, the DPPC monolayer on fused silica hemisphere produced a much weaker Raman signal. This can be related back to the pressure-area isotherms (fig. 4.2.4 & fig. 4.2.5) where during the deposition process the area per molecule for zinc arachidate was ~18.8 $Å^2$/molecule and that of DPPC was ~49 $Å^2$/molecule. So the Raman scattering is from fewer number of molecules in case of DPPC monolayer. Although DPPC has total 28 $–CH_2$ groups in two alkyl chains, while zinc arachidate has 18 $–CH_2$ groups in one alkyl chain (excluding the terminal $–CH_3$ groups in both the molecules), the integrated intensity of the spectra from DPPC is expected to be weaker than the integrated intensity of zinc arachidate spectra by a factor of ~1.7. Additionally, the d^-/d^+ ratio for DPPC is ~1.25 (calculated from curve-fitting data) which indicates that the DPPC monolayers are not as well ordered as the zinc arachidate monolayers, with more gauche defects in the hydrocarbon chains.

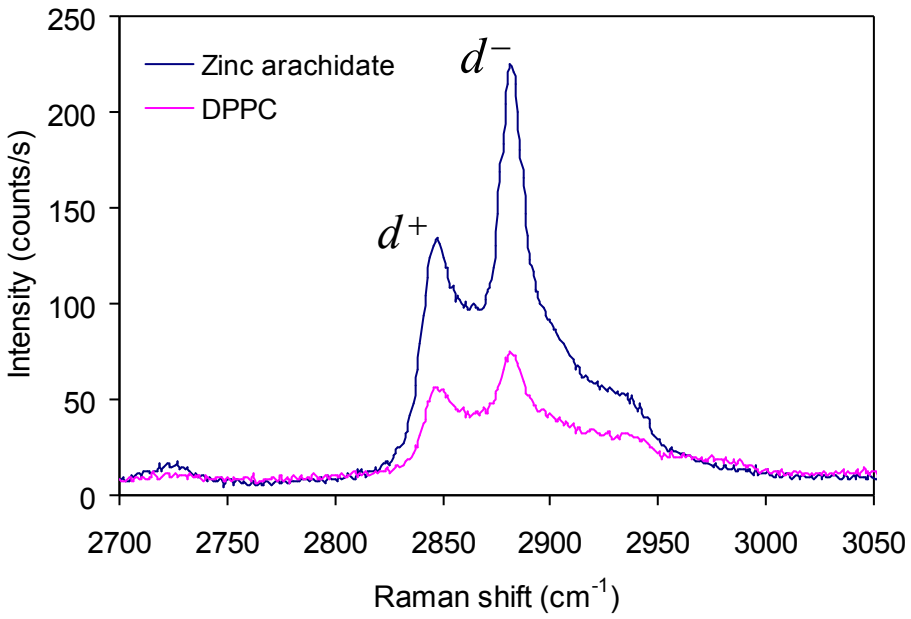

Fig 4.3.3: TIR Raman spectra obtained with S-polarised incident radiation from an LB monolayer of Zn arachidate and DPPC on the surface of clean SF10 hemisphere in air; 300 mW, 532 nm, 300 s acquisition, $\theta_i \sim 57.4^o$

Figure 4.3.3 shows the TIR Raman spectra from zinc arachidate and DPPC monolayers deposited on cleaned SF10 hemispheres. The relative intensity of the zinc arachidate and

DPPC spectra ~ 2.7 was obtained which can be either due to lower coverage of DPPC on SF10 surface (due to poorer transfer) or greater tilt of the DPPC molecules on the SF10 surface as compared to the zinc arachidate molecules. The d^-/d^+ ratio for DPPC spectra ~1.26 (obtained from curve-fitting data) indicated lower orderliness and higher gauche defects. The big drop in Raman intensity from both zinc arachidate and DPPC monolayers on fused silica hemisphere (fig. 4.3.2) to SF10 hemisphere (fig. 4.3.3) was because the angle of incidence, $\theta_i \sim 44.1^o$ was closer to the critical angle, $\theta_c \sim 43.2^o$ for the silica/air interface, while the angle of incidence, $\theta_i \sim 57.4^o$ for SF10/air interface was far away from the critical angle, $\theta_c \sim 35.2^o$. As the incident laser beam used was S-polarised, so a stronger electric field was probing the monolayers at the silica/air interface closer to the critical angle of incidence (ref. Chapter 2).

References:

1. Smith, E., ed. *Clapham Saints and Sinners*. 1987, The Clapham Press, London.
2. Fulford, G.D., *Pouring holy oil on troubled water.* Isis, 1968. **59**(2): p. 198-199.
3. Franklin, B., Philosophical Transactions of the Reyal Society (London), 1774. **64**: p. 445.
4. Rayleigh, L., Proceedings of the Royal Society Series A, 1890. **47**: p. 364.
5. Rayleigh, L., Philosophical Magazine, 1899. **48**: p. 321.
6. Pockels, A., Nature (London), 1891. **43**: p. 437.
7. Langmuir, I., Journal of the American Chemical Society, 1917. **39**: p. 1848-1906.
8. Langmuir, I., Transactions of the Faraday Society, 1920. **15**(3): p. 0062-0074.
9. Blodgett, K.B., Journal of American Chemical Society, 1935. **57**: p. 1007-1022.
10. Blodgett, K.B. and Langmuir, I., Physical Review, 1937. **51**(11): p. 0964-0982.
11. Blodgett, K.B., Science, 1939. **89**: p. 60-61.
12. Blodgett, K.B., Physical Review, 1939. **55**(4): p. 0391-0404.
13. Gaines, G.L., *Insoluble monolayers at liquid-gas interfaces*. Interscience (New York), 1966.
14. Gaines, G.L., Thin Solid Films, 1983. **99**: p. ix-xiii.

15. Kuhn, H., Mobius, D., Buchner, H., in: A. Weissberger, B. Rossiter (Eds.), *Physical Methods of Chemistry.* 1972. **1**(Wiley, New York).
16. Zhavnerko, G., and Marletta, G., Materials Science and Engineering B-Advanced Functional Solid-State Materials, 2010. **169**(1-3): p. 43-48.
17. Fraenkel, R., Butterworth, G.E., and Bain, C.D., Journal of American Chemical Society, 1998. **120**: p. 203-204.
18. Beattie, D., Haydock, S., and Bain, CD., Vibrational Spectroscopy, 2000. **24**(1): p. 109-123.
19. Oncins, G., Torrent-Burgués, J., and Sanz, F, Journal of Physical Chemistry C, 2008. **112**(6): p. 1967–1974.
20. Li, J.B., et al., Colloid and Polymer Science, 1996. **274**(10): p. 995-999.
21. Ho, M., & J.E. Pemberton, Analytical Chemistry, 1998. **70**: p. 4915.

5. TIR Raman Spectra of Model Boundary Lubricants

LB monolayers are good model boundary lubricants and their behaviour under pressure and shear is of immense interest to tribologists. The lubricant monolayers bound to the sliding surface reduce friction in the macroscopic level, however as discussed in chapter 1, the perturbations at the molecular level that induce the reduction in friction at the macroscopic level are not clearly understood. Observations in sliding surfaces such as 'stick-slip motion', where the two surfaces move by making small rapid jumps separated by longer periods of rest, could be due to transition between phases in the lubricant monolayers. The mechanism of 'stick-slip motion', which causes more damage to the lubricated surface than smooth sliding is not clearly understood [1, 2], while it is known that smooth sliding occurs only above a critical sliding velocity [3]. In this chapter I will describe the molecular changes in the LB monolayers with respect to molecular conformations, molecular tilting to the surface normal of the sliding surface, molecular packing and/or defects induced with applied pressure at solid-solid interface as observed with total internal reflection (TIR) Raman spectroscopy. For this study LB monolayers of zinc arachidate and DPPC were chosen, where the zinc arachidate monolayers have a greater packing density and fewer gauche defects than DPPC monolayers as described in Chapter 4. LB monolayers at solid surfaces *ex-situ* i.e. at solid/air interface were investigated first and then *in-situ* studies at solid/solid interfaces under higher applied pressures were carried out.

5.1 *Ex-situ* experiments to probe monolayers at solid/air interface

The *ex-situ* experiments as shown in figure 5.1.1**,** comprise polarisation resolved Raman spectra from the LB monolayers of Zn arachidate and DPPC at the silica/air interface.

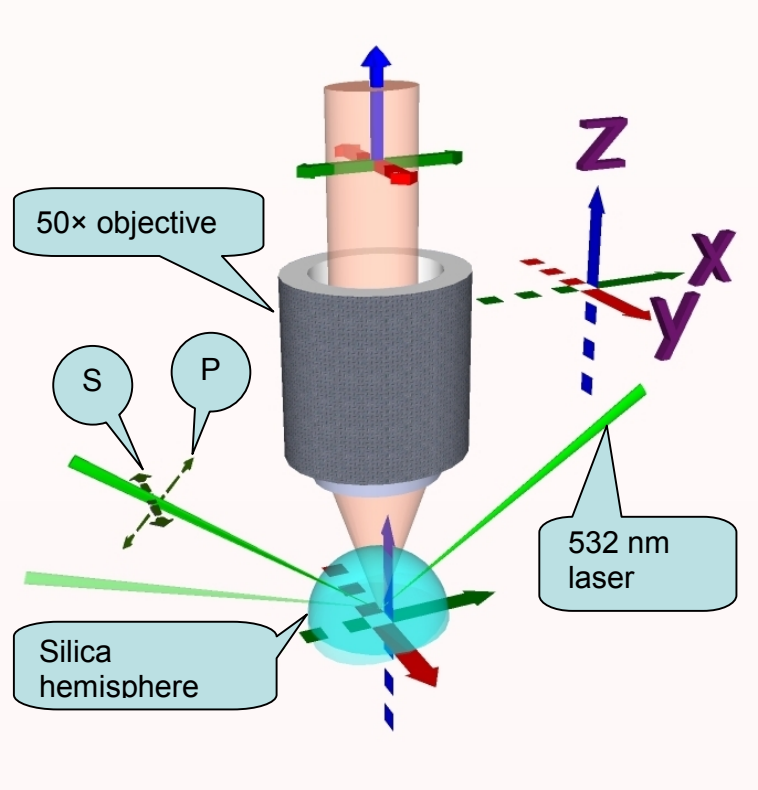

Figure 5.1.1: 3D schematic diagram of TIR geometry for *ex-situ* studies of LB monolayers

The LB monolayers at the silica/air interface were probed for a wide range of angles of incidence from below the critical angle to high above the critical angle ($\theta_c = 43.23°$), and the changes in the electric field with the angle of incidence were calculated for the same set of spectra. The laser beam was aligned for 44.3º (+/– 0.1º) angle of incidence and then the hemisphere was rotated by small amounts (+/– 3° in both directions) to obtain the other angles of incidence. The numerical aperture (NA) of the collection objective being 0.55, the full cone angle of collection of scattered light was $2\sin^{-1} 0.55 = 66.7°$, therefore the centre of cone of collection for the collection optics varied up to +/– 4.5% for the different angle of incidence spectrum. The angle of incidence was accurately determined by placing a vertical ruler equidistant (15 cm) on both sides of the hemisphere in the path of the beam, and comparing the heights of the incoming beam (fixed) and the outgoing beams (variable).

5.1.1 Zn arachidate monolayer at silica/air interface

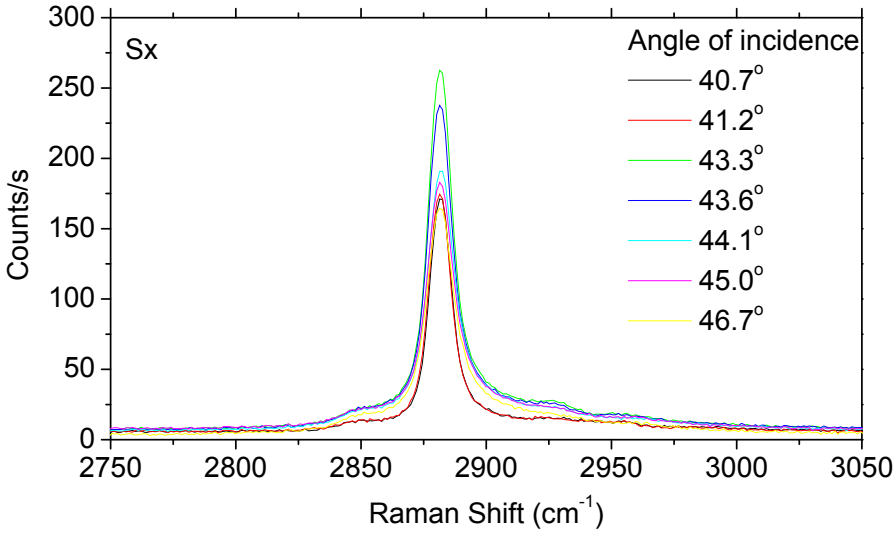

Figure 5.1.2a: Sx polarisation-resolved TIR Raman spectra from Zn arachidate monolayer at silica/air interface; 532 nm laser; power 200 mW; acquisition time 5 mins.

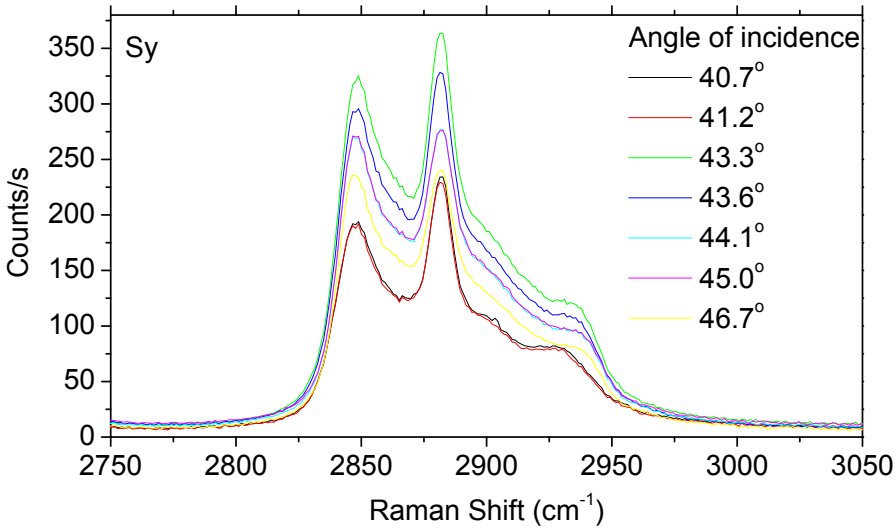

Figure 5.1.2b: Sy polarisation-resolved TIR Raman spectra from Zn arachidate monolayer at silica/air interface; 532 nm laser; power 200 mW; acquisition time 5 mins.

Figures 5.1.2a, 5.1.2b, 5.1.2c and 5.1.2d show polarisation-resolved Raman spectra obtained from the Zn arachidate monolayer on a silica hemisphere at atmospheric pressure at different angles of incidences (both below and above the critical angle ~43.2º)

using S- and P-polarised incident laser beam, respectively. The spectra from S-polarised light were of 5 minutes acquisition, and those of P-polarised light were of 10 minutes acquisition and all the spectra were scaled to intensity in counts/s. The laser power used to obtain the spectra was 200 mW.

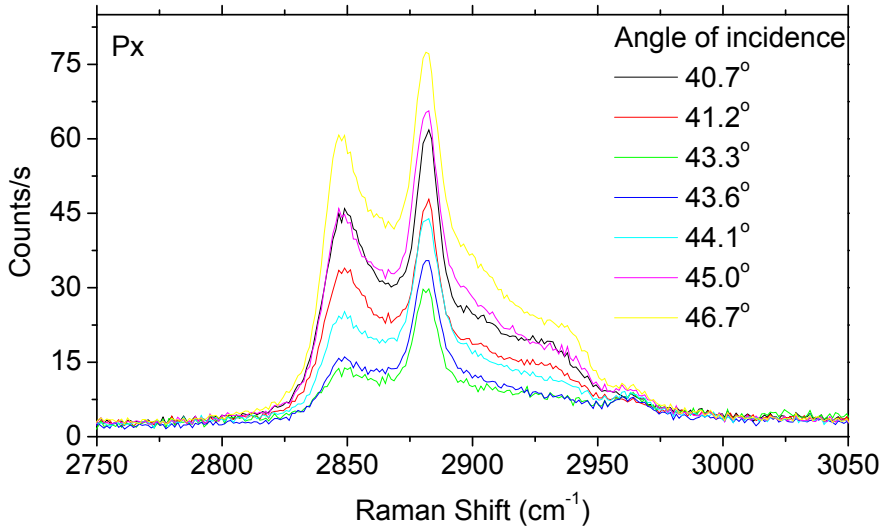

Figure 5.1.2c: Px polarisation-resolved TIR Raman spectra from Zn arachidate monolayer at silica/air interface; 532 nm laser; power 200 mW; acquisition time 10 mins.

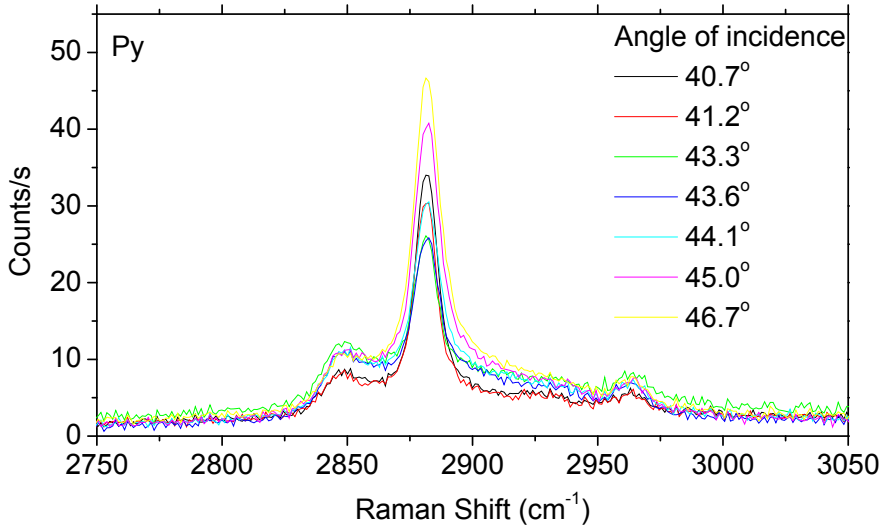

Figure 5.1.2d: Py polarisation-resolved TIR Raman spectra from Zn arachidate monolayer at silica/air interface; 532 nm laser; power 200 mW; acquisition time 10 mins.

The spectra show that the intensities of the Sx and Sy spectra attain maxima and the Px and Py spectra attain minima very close to the critical angle (~43.2º) which can be explained by the Fresnel coefficient plots in figure 2.2.6 in chapter 2. The signal obtained at the critical angle from Px and Py spectra is primarily due to the Raman tensor elements $\langle \alpha'_{xz} \rangle$ and $\langle \alpha'_{yz} \rangle$ respectively since the collection efficiency of $\langle \alpha'_{zz} \rangle$ is much lower than for either of these components. From the spectra it is also evident that at the critical angle the Px and Py spectra appear identical which is possible if the Raman tensor elements $\langle \alpha'_{xz} \rangle = \langle \alpha'_{yz} \rangle$, which confirms the isotropic nature of the LB monolayer of Zn arachidate. In addition to that, the Py spectra began to resemble the Sx spectra and the Px spectra began to resemble the Sy spectra above and below the critical angle, which is expected from the symmetry considerations. Away from the critical angle, the signal obtained from Px spectrum is due to the Raman tensor elements $\langle \alpha'_{xx} \rangle = \langle \alpha'_{yy} \rangle$ and $\langle \alpha'_{xz} \rangle$ and the Sy spectrum is due to probing of the element $\langle \alpha'_{yy} \rangle$. Similarly the signal obtained in the Py spectrum is due to the Raman tensor elements $\langle \alpha'_{yx} \rangle = \langle \alpha'_{xy} \rangle$ and $\langle \alpha'_{yz} \rangle$ while the Sx spectrum is due to probing of the element $\langle \alpha'_{xy} \rangle$.

The fact that the Px and Py spectra does not go to zero at the critical angle suggests that the Zn arachidate molecules in the monolayers are tilted from the surface normal. Recently Oncins *et al.* have employed an indirect method to determine molecular chain tilt angle by AFM scratching and height of monolayer determination [4]. They found the aliphatic hydrocarbon chains of an LB monolayer of arachidic acid coated on mica surface at 1, 15 and 35 mN/m surface pressures are tilted to the surface normal by 48°, 32°, and 22° respectively.

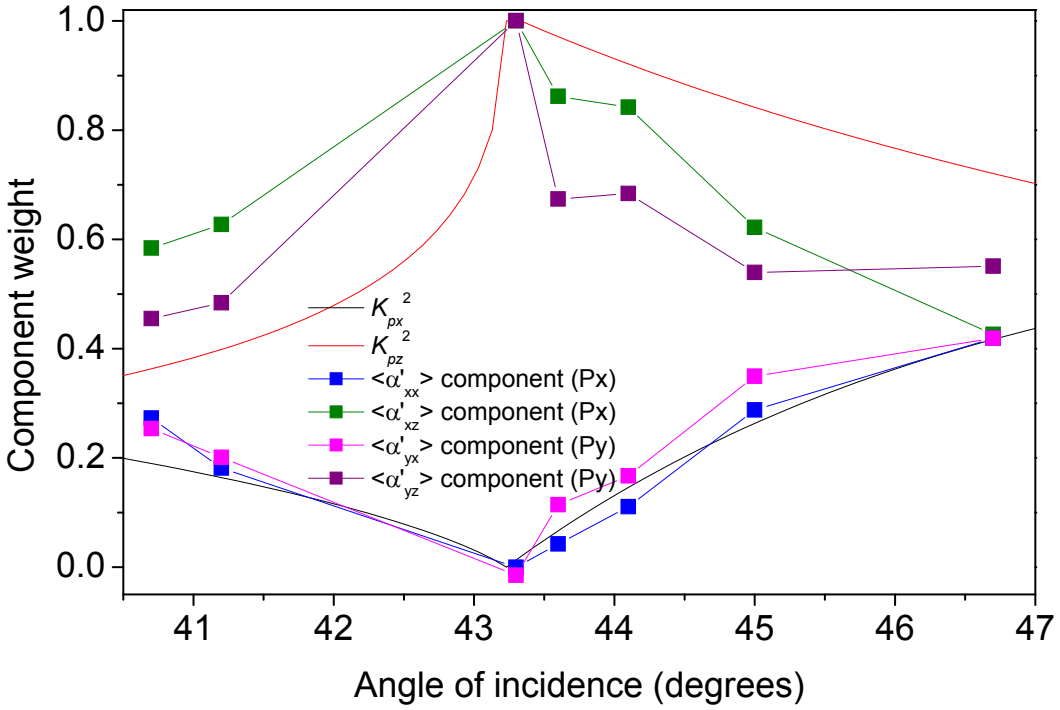

Figure 5.1.3: Component weights in Px and Py spectra shown in Fig 5.1.2. *z*-component weights are scaled to K_{pz}^2 value at 43.3° and *x*-component weights are scaled to K_{px}^2 value at 46.7°. The solid black and red lines show the squared Frensel coefficients, K_{px}^2 and K_{pz}^2.

Application of factor analysis technique (carried out by Dr. Eric Tyrode) yielded the component weights in the Py and the Px spectra figure 5.1.3 which closely resembled the squared Fresnel co-efficient plots K_{px}^2 and K_{pz}^2 for silica/air interface (Raman intensity is directly proportional to the squared Fresnel coefficients). In this plot the component weights in Px and Py spectra were scaled such that the *z*-components ($\langle \alpha'_{xz} \rangle$ and $\langle \alpha'_{yz} \rangle$) matched with the K_{pz}^2 at 43.3° angle if incidence and the *x*-components ($\langle \alpha'_{xx} \rangle$ and $\langle \alpha'_{yx} \rangle$) matched with the K_{px}^2 at 46.7° angle of incidence (as K_{px}^2 = 0 at critical angle of incidence, 43.23°).

5.1.2 DPPC monolayer at silica/air interface

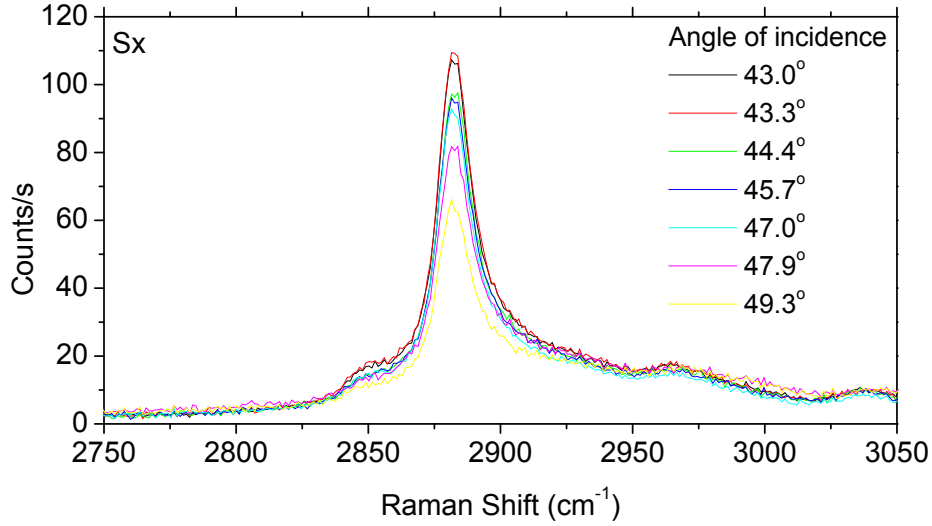

Figure 5.1.4a: Sx polarisation-resolved TIR Raman spectra from DPPC monolayer at silica/air interface; 532 nm laser; power 300 mW; acquisition time 5 mins.

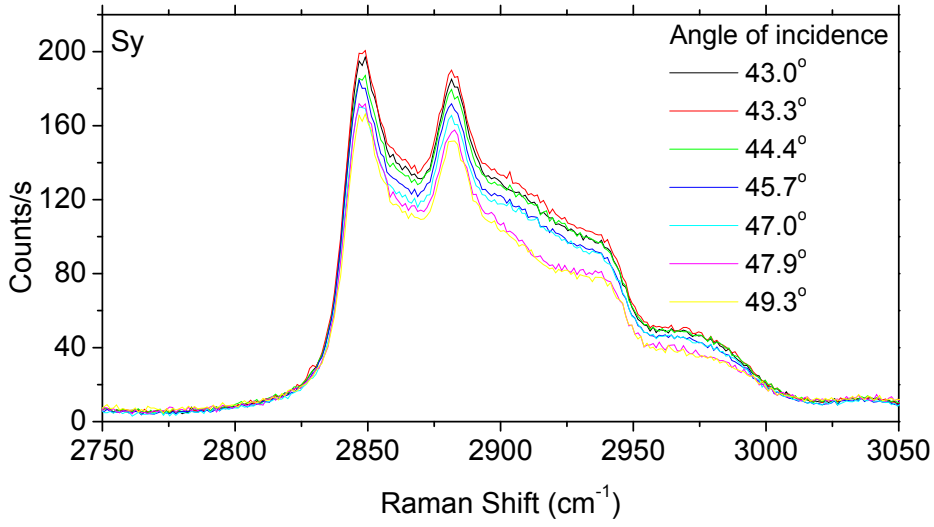

Figure 5.1.4b: Sy polarisation-resolved TIR Raman spectra from DPPC monolayer at silica/air interface; 532 nm laser; power 300 mW; acquisition time 5 mins.

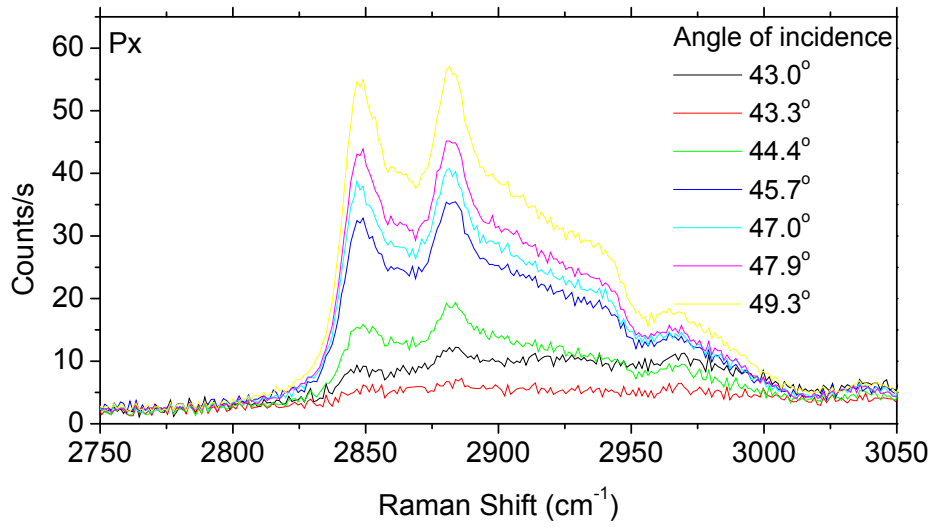

Figure 5.1.4c: Px polarisation-resolved TIR Raman spectra from DPPC monolayer at silica/air interface; 532 nm laser; power 300 mW; acquisition time 10 mins.

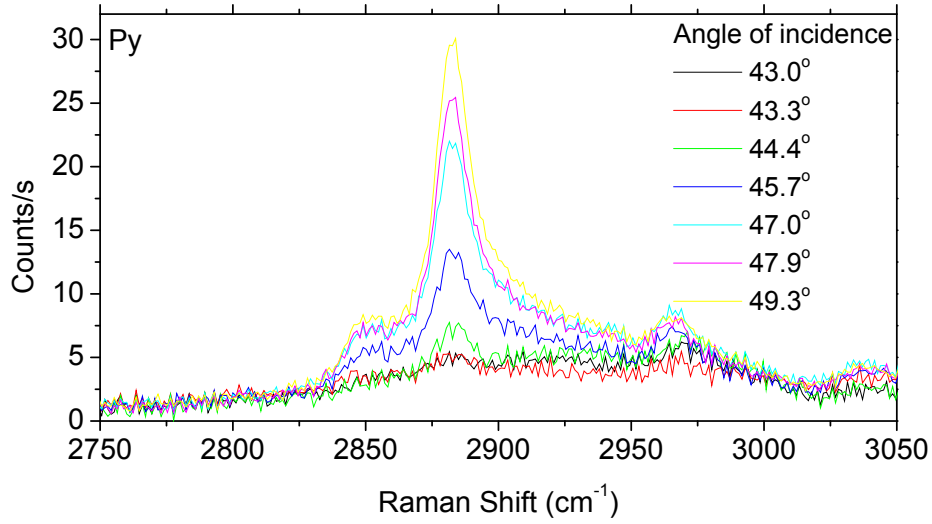

Figure 5.1.4d: Py polarisation-resolved TIR Raman spectra from DPPC monolayer at silica/air interface; 532 nm laser; power 300 mW; acquisition time 10 mins.

Figures 5.1.4a, 5.1.4b, 5.1.4c and 5.1.4d show polarisation-resolved Raman spectra obtained from the DPPC monolayer on a silica hemisphere at atmospheric pressure at different angles of incidences (both below and above the critical angle ~43.2º) using S- and P-polarised incident laser beam respectively. The spectra from S-polarised light were

of 5 minutes acquisition, and those of P-polarised light were of 10 minutes acquisition and all the spectra were scaled to intensity in counts/s. The laser power used to obtain the spectra was 300 mW. The intensity in the spectra in scaled in terms of counts/second.

The polarisation-resolved Raman spectra from the DPPC monolayer was much less intense than the signals from Zn arachidate monolayer in the previous section (intensity lower by a factor of ~2.1 taking into consideration that the Zn arachidate spectra were acquired with 200 mW laser power and that of DPPC were acquired with 300 mW laser power). As explained in section 4.3 of chapter 4, this lower intensity was primarily due to higher area per molecule for DPPC monolayer and also due to lower surface coverage on the silica surface. In similarity to the zinc arachidate spectra, the DPPC spectra also show that the intensities of the Sx and Sy spectra attain maxima and the Px and Py spectra attain minima very close to the critical angle (~43.2º) which can be explained by the Fresnel coefficient plots in figure 2.2.6 in chapter 2. In addition to that, the Py spectra resemble the Sx spectra and the Px spectra resemble the Sy spectra above and below the critical angle, which is expected from the symmetry considerations explained in section 5.1.1. At the critical angle the Px and Py spectra are identical which indicates the isotropic nature of the LB monolayer of DPPC deposited on fused silica surface. However, in contrast to the zinc arachidate spectra in the previous section, the Px and Py spectral intensity from DPPC monolayers deposited on silica surface are found to be almost zero at critical angle of incidence. In principle, this indicates that the DPPC molecules in the monolayer are upright or perpendicular to the surface of the fused silica hemisphere. In 1987 Helm *et al.* found that acyl chain tilts in the liquid condensed (LC) phase of DPPC monolayer at the air/water interface is 30º from X-ray reflectivity [5]. Sun *et al.* in 1996 reported the acyl chains of DPPC bilayers in gel phase to have a tilt angle of 31.6º [6]. Our results from DPPC monolayers at a silica/air interface therefore show a sharp contrast to the results obtained from DPPC monolayer at air/water interface or DPPC bilayer in gel phase.

5.2 *In-situ* experiments to probe monolayers at solid-solid interface

The *in-situ* experiments as shown in figure 5.2.1 involved collecting both S-unpolarised spectra and polarisation-resolved spectra from Zn arachidate monolayers and DPPC monolayers sandwiched between SF10 hemisphere on top and fused silica hemisphere on the bottom.

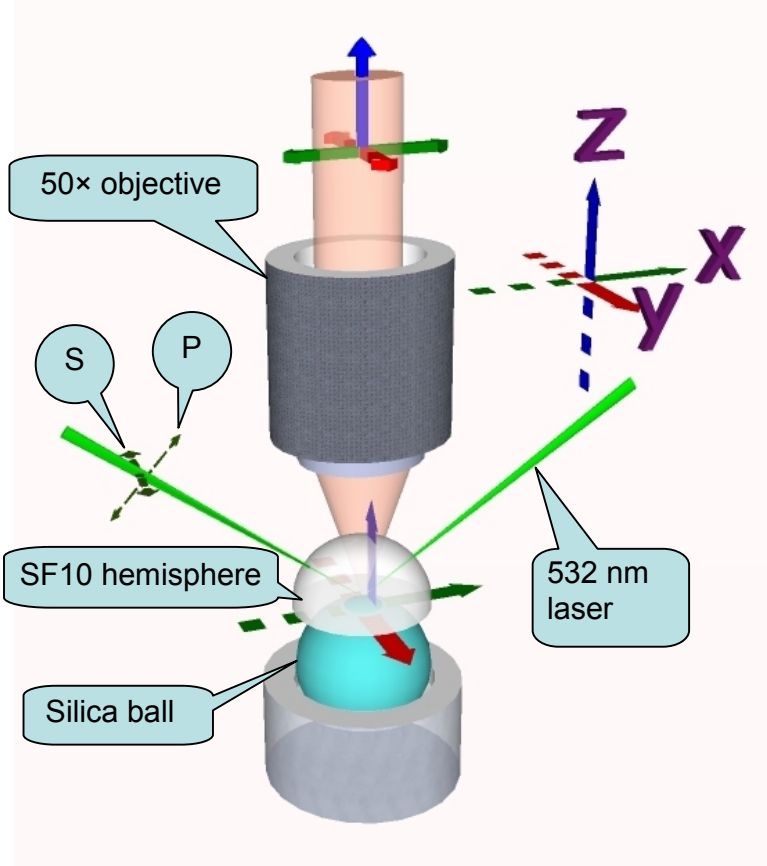

Figure 5.2.1: 3D schematic diagram of TIR geometry for *in-situ* studies of LB monolayers

Both the SF10 hemisphere and the fused silica sphere were deposited with LB monolayers of Zn arachidate or DPPC, and mounted to respective holders. The hemisphere holder was mounted onto a computer-controlled (controller: Newport MotionMaster 2000) motion stage with 0.1-μm resolution (Newport model UTMCC.1DD), which moved the hemisphere in and out of the contact sphere. This stage was in turn mounted onto a set of manual micrometer motion stages, which allowed

movement of the hemisphere in all directions parallel to the Raman bench. The sphere holder was mounted onto one 1-μm resolution (Newport model UTMCC1DD), computer-controlled micromotion stage moving the sphere perpendicularly in and out of contact, which in turn was mounted on a set of another computer-controlled micromotion stages and a manually controlled micromotion stage which controlled the movement of the sphere parallel to the Raman bench. In our experiments, the micron-resolution stages allowed positioning of the optics and pressing them against each other to obtain desired pressures. The computer controlled stages were equipped with DC servo drives, built-in tachometers, and linear encoders for position information to ensure accurate and precise motion.

In the *in-situ* contact experiments, the coated SF10 hemisphere on the top was pressed against a coated silica sphere on the bottom, and pressures as high as ~750 MPa was reached. We were limited to attaining even higher pressures by the chances of damaging the optics. The pressure was calculated using the Hertz equations of contact mechanics measuring the diameter of the central dark spot (fig.2.5.1, chapter 2) in the produced Newton's rings. Direct measurement of force was also obtained from a digital force sensor (Omegadyne Inc., LC204-25) being placed below the sphere holder as described in section 3.1.5 in chapter 3. There were small differences in the pressure reading obtained from digital reading and Hertz equation calculations which can be attributed to the fact that the Hertz equation does not take into consideration the adhesive forces and also due to the possible inaccuracy of measurement of the central dark spot in the Newton's rings (the diameter of the central dark spot was measured omitting the peripheral blur circle, the distance measured in μm calibrating with a standard graticule).

The laser beam (300 mW power at source) was focused at the solid-solid interface at an angle of incidence 57.6° just above the critical angle (θ_c = 57.25°). Spectra were obtained with acquisition times of 10 minutes.

5.2.1 Zinc arachidate monolayers at SF10/silica interface

Figure 5.2.2 shows the S-unpolarised TIR Raman spectra from Zn arachidate monolayers coated on both SF10 hemisphere and silica sphere and sandwiched in the interface at different pressures. Pressure 0 MPa corresponds to the out-of-contact spectrum i.e. without any application of pressure, so the Raman signal collected at 0 MPa pressure is from a single monolayer of Zn arachidate deposited on the SF10 hemisphere. In all the other spectra at higher pressures, the signal collected is from two monolayers of Zn arachidate, one on SF10 hemisphere and the other on silica sphere. As a natural consequence, the intensity of spectra in the SF10/silica contact is at least double the intensity of the out-of-contact spectra. In fact the in-contact spectra are about three times more intense than the out-of-contact spectra. The angle of incidence of 57.6° is far away from the critical angle for SF10/air interface (θ_c = 35.26°), therefore the electric field acting in the SF10/air interface is much weaker.

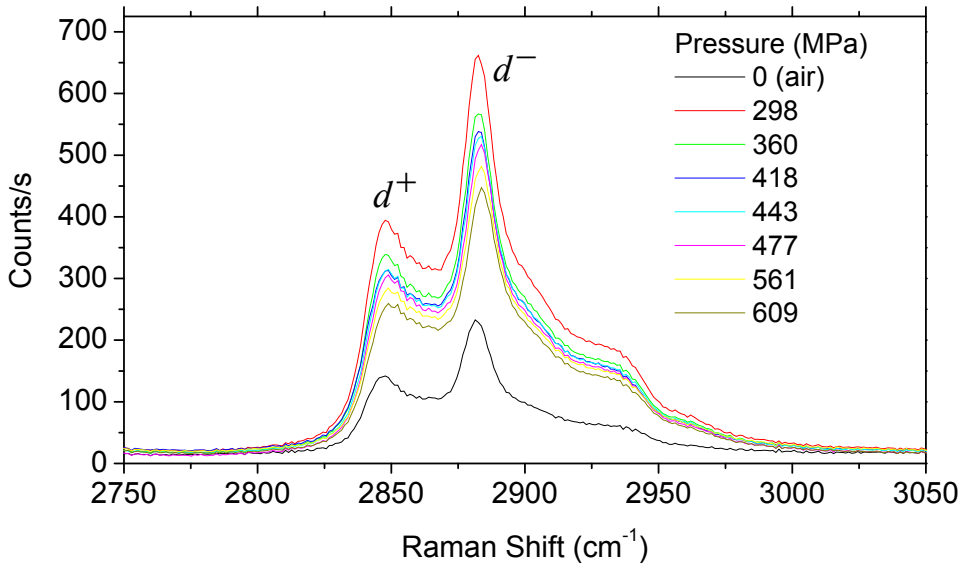

Figure 5.2.2: TIR Raman spectra from Zn arachidate at SF10/silica interface; S-polarisation, 300 mW, 600 s acquisition, θ_i = 57.6°, at different pressures indicated in the figure.

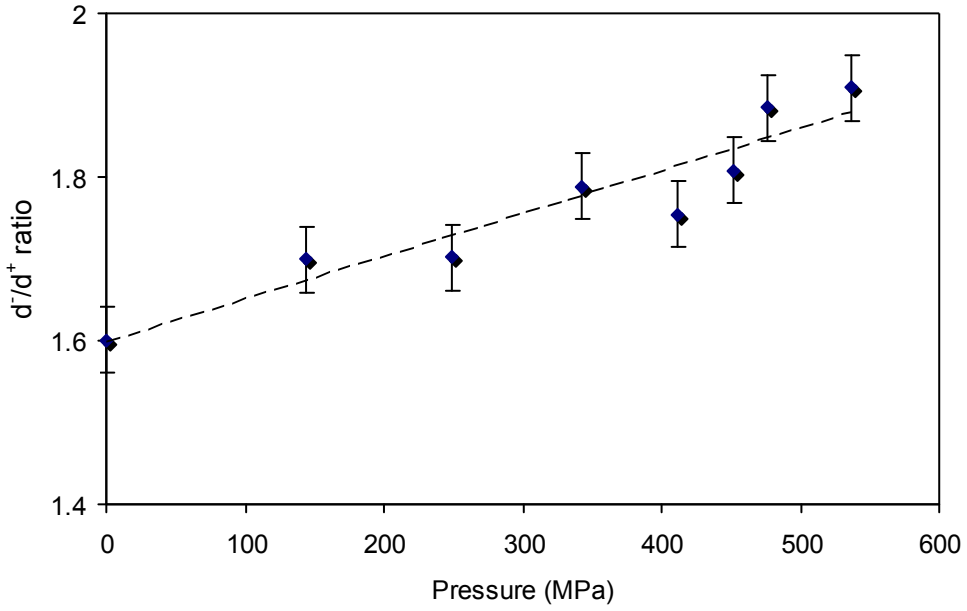

Figure 5.2.3: Plot of d^-/d^+ ratio against applied load showing increase in orderliness with increase in pressure (obtained from curve-fitted data in S-unpolarised spectra in figure 5.2.2)

In figure 5.2.2, the peaks at 2881.5 cm^{-1} arise from asymmetric CH_2 stretching, denoted as d^- and the peaks at 2846 cm^{-1} arise from symmetric CH_2 stretching, denoted as d^+. The intensity ratio d^-/d^+ is a measure of the orderliness of the monolayer packing [7]. d^-/d^+ ratio higher than 1.6 indicated well-ordered packing with few gauche defects.

In the S-unpolarised spectra of Zn arachidate at SF10/silica interface (fig**.** 5.2.2**)**, the intensity of the spectra goes much higher in the spectra obtained at first contact at 298 MPa, than the out of contact spectrum, the reason being explained beforehand. Besides that, the intensity of the spectra gradually decreases as higher pressures are reached. This reduction in intensity of spectra at higher pressures may be related to the tilting of the molecular chains of the aliphatic hydrocarbons away from the surface normal. A closer observation of the molecular chain tilt can be obtained from the obtained polarisation-resolved spectra discussed below. It can also be observed here that the d^-/d^+ ratio gradually increases with increase of pressure, indicating the monolayers of Zn arachidate getting more and more ordered at higher pressures, reducing the amount of defects in

molecular packing. In figure 5.2.3, a plot of d^-/d^+ ratio against applied pressure shows a roughly linear increase in orderliness with applied pressure, the ratio ranging from 1.6 at out of contact to 1.8 at around 550 MPa pressure.

Figures 5.2.4a, 5.2.4b, 5.2.4c & 5.2.4d show the polarisation-resolved spectra Sx, Sy, Px and Py respectively obtained from Zn arachidate sandwiched at the SF10/silica interface, at gradually increased applied pressures. As discussed in chapter 2, if the aliphatic hydrocarbon chains of Zn arachidate were perfectly perpendicular to the surface normal, and if the laser beam is focussed at the critical angle for the pair of dielectrics concerned, the spectral intensity of the Px and Py spectrum should be almost zero (with some small contribution from the $\langle \alpha'_{zz} \rangle$ component). An increase in the spectral intensity in the Px and Py spectra (due to increasing contributions from Raman tensors $\langle \alpha'_{xz} \rangle$ and $\langle \alpha'_{yz} \rangle$, which are nonzero for d^- in the P-polarised spectra if the alkyl chains are tilted away from the surface normal), and a simultaneous decrease in the spectral intensity in the Sx and Sy spectra with increasing pressures at the SF10/silica interface indicated that the aliphatic hydrocarbon chains of Zn arachidate gradually tilted further away from the surface normal with higher pressures. The spectral shape and intensity of the Px and Py spectra were almost identical for the set of different pressures applied, which confirmed that the laser beam was focused very close to the critical angle (θ_c = 57.25°), and that the alignment was stable throughout the complete set of experiments. Also the Px and Py spectrum remaining similar throughout the whole set of experiments meant that the molecular layer continued to be isotropic in spite of all other molecular perturbations, or at least it was isotropic when averaged over the laser spot.

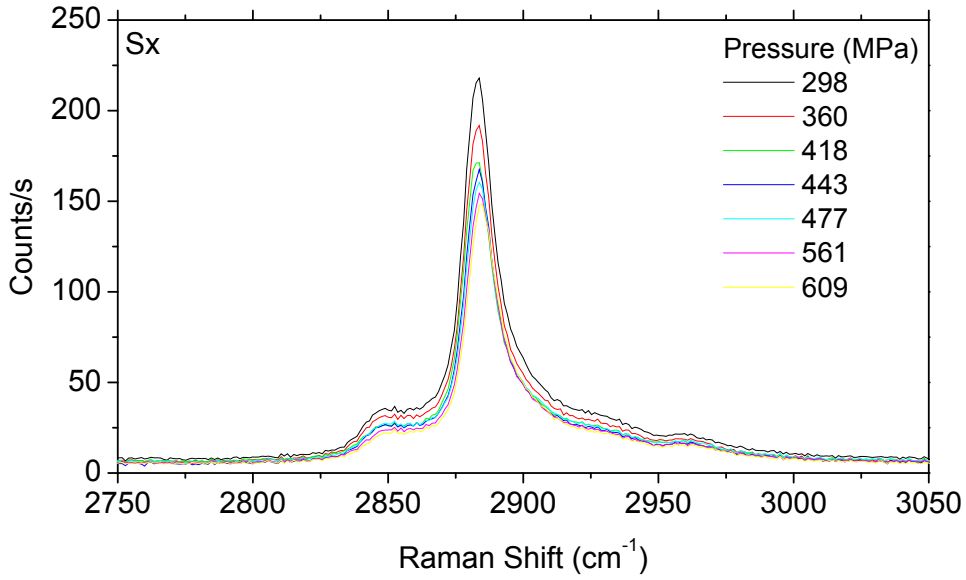

Figure 5.2.4a: Sx polarisation-resolved TIR Raman spectra from Zn arachidate at SF10/silica interface; 300 mW, 600 s acquisition, θ_i = 57.6°, at pressures indicated in the figure.

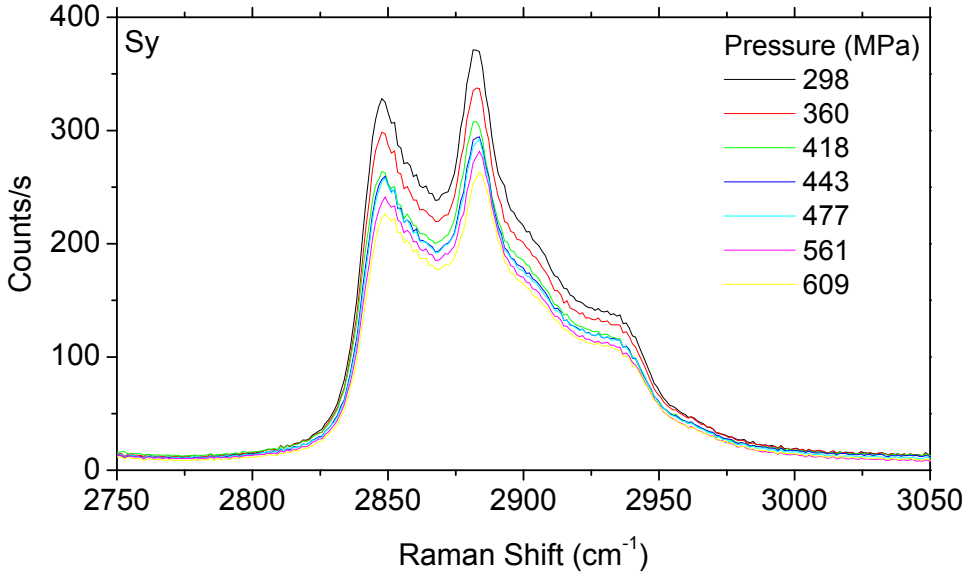

Figure 5.2.4b: Sy polarisation-resolved TIR Raman spectra from Zn arachidate at SF10/silica interface; 300 mW, 600 s acquisition, θ_i = 57.6°, at pressures indicated in the figure.

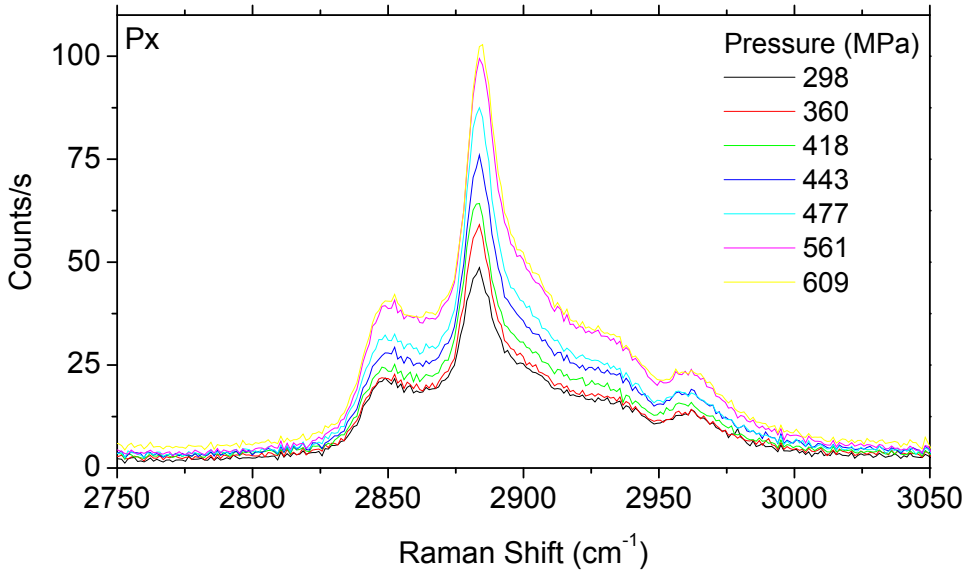

Figure 5.2.4c: Px polarisation-resolved TIR Raman spectra from Zn arachidate at SF10/silica interface; 300 mW, 600 s acquisition, θ_i = 57.6°, at pressures indicated in the figure.

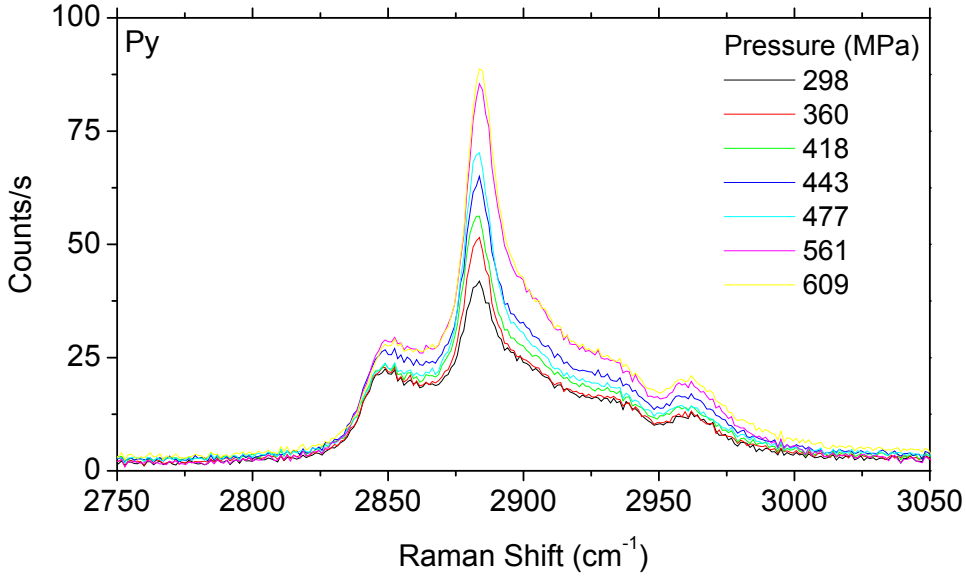

Figure 5.2.4d: Py polarisation-resolved TIR Raman spectra from Zn arachidate at SF10/silica interface; 300 mW, 600 s acquisition, θ_i = 57.6°, at pressures indicated in the figure.

The ratio of the intensities of the S-polarised spectra and the P-polarised spectra was plotted against applied pressure, and a reduction in Is/Ip ratio with increasing pressures

indicated tilting away of the aliphatic chains from the surface normal. Figure 5.2.5 shows the intensity ratio Sx/Px decreased from ~5 to ~2 and that of Sy/Py decreased from ~10 to ~4 for a pressure increase from ~130 MPa to ~680 MPa. So the order of tilt with increasing pressure was the same as derived from both the ratios, which once again supports our inference about the chain tilts. A quantitative treatment of the alkyl chain tilt with applied pressure can be modelled based on the fact that different Raman cross sections are probed while collecting spectra from Sx, Sy, Px and Py polarisations and the Raman scattering intensity for each polarisation can be calculated by integrating the contributions from the appropriate Raman tensors (section 2.4, chapter 2) over the collection cone of the objective. However, the difficulties in this alkyl-chain-tilt-modelling involve:

(1) Determination of the molecular axis, as all the saturated C-atoms are sp^3 hybridised with corresponding bond angles 109°28′, and therefore not linear. This makes the determination of the Raman cross sections at different molecular tilts further difficult.

(2) Making assumptions about the twist of the chain as well as its tilt.

(3) Knowing the aniosotropy of the Raman tensor in the coordinates of the bond (i.e. the perpendicular to parallel component of $\langle \alpha' \rangle$)

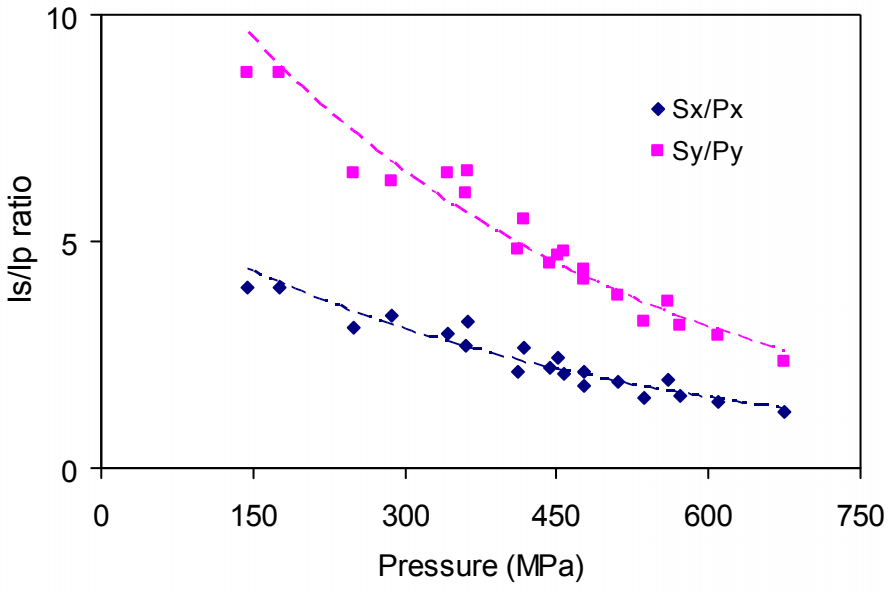

Figure 5.2.5: Plot of Is/Ip ratio against applied pressure for zinc arachidate monolayer

In general vibrational spectroscopy, a red shift or lowering of the wave number is expected with higher molecular ordering of the monolayer, however when the hydrocarbon chains come closer to each other under higher pressures, the vibration of the molecular bonds require more energy, hence an increase in wave number is expected. In our experiments, these two aforesaid factors compete against each other and an overall blue shift is manifested (figure 5.2.6). The S-unpolarised spectra and Sx, Sy spectra were suitably curve fitted (curve fitting of C-H stretching spectral region in LB monolayers of Zn arachidate is discussed in section 5.3) and the peak positions of the d^- peaks were plotted against increasing pressures. A blue shift of 0.1 cm^{-1} was observed on an average for 31 MPa increase in pressure [8].

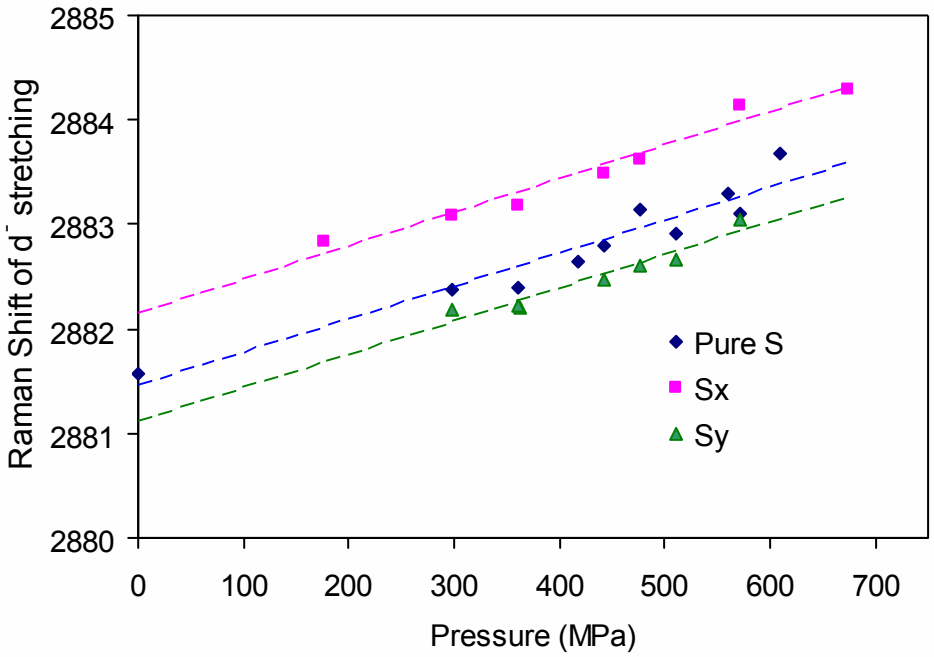

Figure 5.2.6: Plot showing the blue shift of CH_2 asymmetric stretching with higher applied pressures for zinc arachidate monolayer. Dotted lines show a wavenumber increase of 0.1 cm^{-1} per 31 MPa increase in pressure

5.2.1a. Is the tilting of aliphatic hydrocarbon chains under applied pressures a reversible effect?

Different sets of experiments were performed under reciprocating pressures. The changes in tilt of the hydrocarbon chains and molecular ordering were almost reversible i.e. the spectra collected while reducing the pressure gradually in the aforesaid setup suggested that the aliphatic hydrocarbon chains begun to move towards the surface normal and the molecular orderliness began to reduce. Though the out-of-contact spectra before and after the experiments were of similar intensity, the d^{-}/d^{+} ratio was slightly lower in the post-contact spectrum which suggested that the monolayer order gradually reduces as a result of the contact experiments and associated pressure and shear involved.

5.2.1b. Is there any transfer of material between the LB monolayers deposited on the two solids during the contact?

To check if there is any transfer of material between the zinc arachidate coated surfaces under high pressure contact, an SF10 hemisphere coated with LB monolayer of deuterated zinc arachidate was pressed against a fused silica sphere coated with a monolayer of protonated zinc arachidate and pre-contact, in-contact and post-contact TIR Raman spectra were acquired (figure 5.2.7) and analysed. The angle of incidence of the laser beam was set to 57.6° just above the critical angle for SF10/silica interface (θ_c = 57.25°). Spectra were obtained with S-polarised incident radiation and acquisition times of 400 seconds.

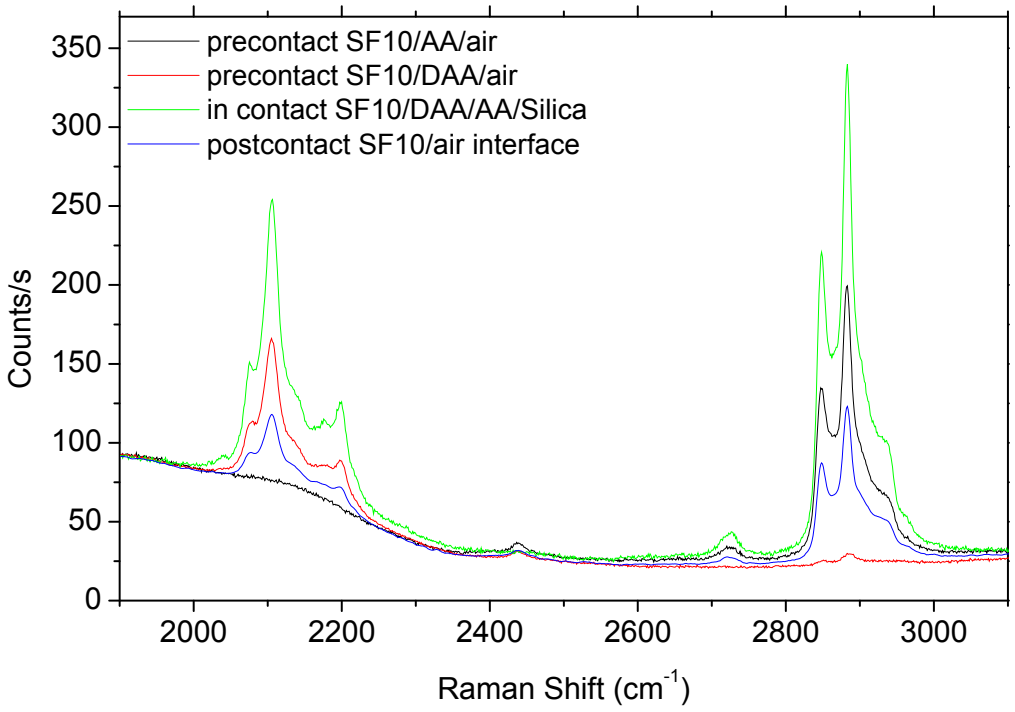

Figure 5.2.7: TIR Raman spectra from protonated Zn arachidate and deuterated Zn arachidate at SF10/air and SF10/silica interfaces; pure S, 300 mW, 400 s acquisition, θ_i = 57.6°.

In figure 5.2.7, the plot labelled 'precontact SF10/AA/air' is a spectrum obtained from a monolayer of protonated zinc arachidate deposited on an SF10 hemisphere from SF10/air interface. The spectral intensity in the 2900 cm^{-1} region corresponds to the Raman signal from the C-H stretching vibrations from a monolayer of zinc arachidate molecules. The plot labelled 'precontact SF10/DAA/air' is a spectrum obtained from a monolayer of deuterated zinc arachidate (LB deposition done with deuterated arachidic acid (Aldrich, 99% D atoms) with $ZnSO_4$ solution as subphase) deposited on an SF10 hemisphere from SF10/air interface. The spectral intensity in the 2100 cm^{-1} region corresponds to the Raman signal from the C-D stretching vibrations from a deuterated zinc arachidate monolayer. The spectra labelled 'in contact SF10/DAA/AA/silica' is a spectra obtained from SF10/silica interface where a SF10 hemisphere coated with deuterated zinc arachidate monolayer was pressing against a silica sphere coated with a monolayer of protonated zinc arachidate at ~300

MPa pressure. The spectral intensity at both 2100 cm^{-1} and 2900 cm^{-1} region for the described in contact spectrum increased by a factor of ~ 1.7 compared to the intensities for the corresponding monolayers when spectra were acquired at SF10/air interface. This is due to the fact that in the out of contact spectra, the angle of incidence 57.6° is far away from the critical angle for SF10/air interface ($\theta_c = 35.26°$) and therefore the electric field, E acting in the interface is weaker for S-polarised incident light. After the pressure was withdrawn and the contact between the coated hemisphere and sphere was removed, a post contact spectrum was acquired from the same spot on the hemisphere where the contact was made, and is labelled as 'post contact SF10/air interface' in figure 5.2.7. From the post contact spectrum it is clearly evident that there was significant exchange of materials between the SF10 and silica surfaces during contact. The spectral intensity in the 2100 cm^{-1} region due to C-D stretching reduced to roughly half compared to the intensity obtained from a deuterated zinc arachidate monolayer coated SF10 hemisphere. Simultaneously appearance of strong Raman bands at 2900 cm^{-1} region on the SF10 hemisphere which was initially coated with deuterated zinc arachidate (99% D atoms) reveal that significant amount of protonated zinc arachidate molecules was transferred to the SF10 hemisphere surface from the fused silica sphere during contact. From the spectral intensities at 2100 cm^{-1} and 2900 cm^{-1} region we can estimate the transfer of the molecular layer was roughly in 1:1 ratio at the area of contact, and the total amount of molecular material was about the same.

5.2.2 DPPC monolayers at SF10/silica interface

Figure 5.2.8 shows the S-unpolarised TIR Raman spectra from DPPC monolayers coated on both SF10 hemisphere and silica sphere and sandwiched in the interface at different pressures. Similar to the zinc arachidate experiments under static contact in section 5.2.1, pressure 0 MPa corresponds to the out of contact spectrum i.e. without any application of pressure, so the Raman signal collected at 0 MPa pressure was from a single monolayer of DPPC deposited on the SF10 hemisphere. In all the other spectra at higher pressures, the signal collected was from two monolayers of DPPC, one on SF10 hemisphere and the

other on silica sphere. As a result the intensity of spectra in the SF10/silica contact is at least double the intensity of the out-of-contact spectra. In fact the in-contact spectra were about six times more intense than the ou-of-contact spectra. This is due to the alignment of the laser beam at AOI = 57.6° was far away from the critical angle for SF10/air interface (θ_c = 35.26°), therefore the electric field acting in the SF10/air interface was also much weaker. Additionally, the transfer ratio of DPPC monolayer on the optics during the LB deposition was much better on fused silica surface than on SF10 surface which accounts for the inconsistency in the rise in spectral intensity from the out-of-contact spectra to the in-contact spectra in the zinc arachidate experiments (section 5.2.1) and the DPPC experiments.

In figure 5.2.8, the peaks at 2883.3 cm^{-1} arise from asymmetric CH_2 stretching, denoted as d^- and the peaks at 2848 cm^{-1} arise form symmetric CH_2 stretching, denoted as d^+. The other major peak in this region is the Fermi resonance of the CH_2 symmetric stretch with an overtone of CH_2 scissors mode at 2934.5 cm^{-1} which appears as a shoulder on the d^- peak. It is observed in the S-unpolarised spectra of DPPC at SF10/silica interface (fig**.** 5.2.8**)**, that the intensity of the spectra goes much higher in the spectra obtained at first contact at 266 MPa, than the out-of-contact spectra. Besides that, the intensity of the spectra gradually decreases as higher pressures are reached. This reduction in intensity of spectra at higher pressures can be related to the tilting of the acyl chains of DPPC away from the surface normal. A closer observation of the molecular chain tilting away from the surface normal can be obtained from the polarisation-resolved spectra obtained from the same setup. It can also be observed here that the d^-/d^+ ratio gradually increases with increase of pressure, indicating the monolayers of DPPC getting more and more ordered at higher pressures, reducing the amount of defects in molecular packing. In figure 5.2.9, a plot of d^-/d^+ ratio against applied pressure is plotted, where d^-/d^+ ratio ~1.34 in the pre contact spectrum at SF10/air interface indicated relatively disordered packing with significant gauche defects. However, the in-contact spectra from DPPC monolayers under higher applied pressures yielded a d^-/d^+ ratio greater than 1.6 which indicated well ordered packing with fewer gauche defects. The d^-/d^+ ratio was as high as 1.77 under 515 MPa applied pressure.

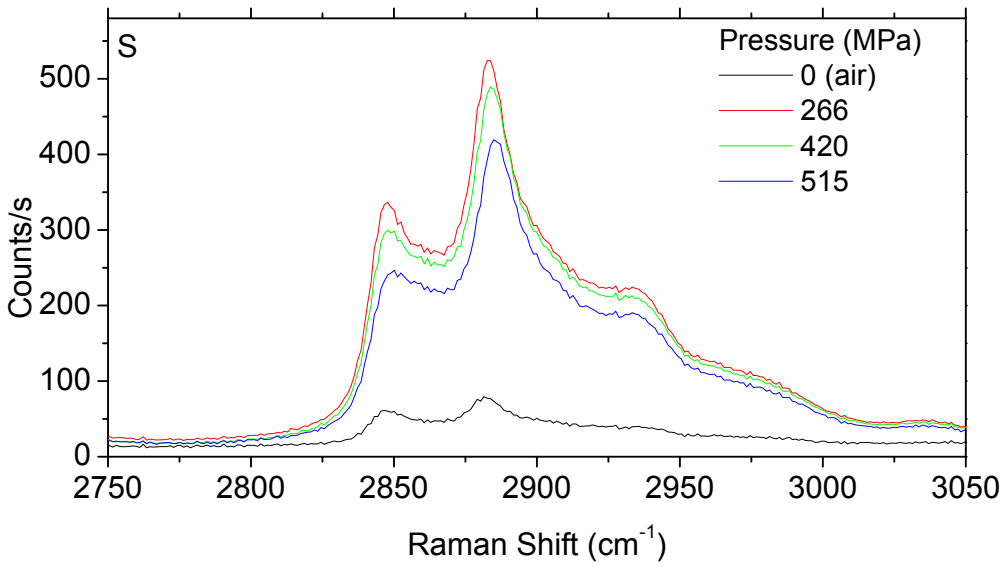

Figure 5.2.8: TIR Raman spectra from DPPC at SF10/silica interface; pure S, 300 mW, 600 s acquisition, θ_i = 57.6°, at pressures indicated in the figure.

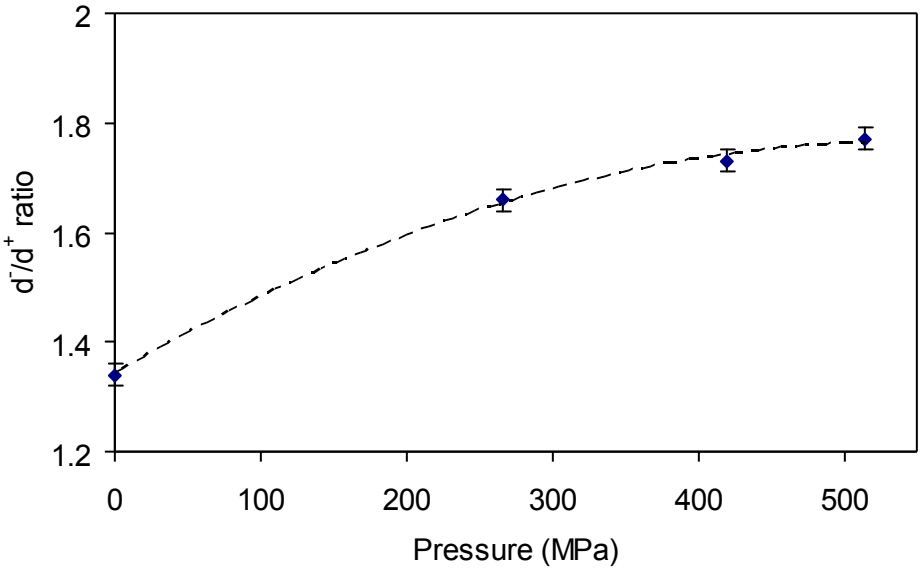

Figure 5.2.9: Plot of d^-/d^+ ratio against applied load showing increase in orderliness with increase in pressure (obtained from curve-fitted data of S-unpolarised spectra in fig. 5.2.8).

Apparently from figure 5.2.9, the DPPC monolayer being more disordered than zinc arachidate monolayer (figure 5.2.3) without application of external pressure, the increase in orderliness in molecular packing with applied pressures is a more pronounced effect in

DPPC monolayer than zinc arachidate. However, on further increasing the pressure, the rate of increase of monolayer orderliness and molecular packing reduces.

Figures 5.2.10a, 5.2.10b, 5.2.10c & 5.2.10d show the polarisation-resolved spectra Sx, Sy, Px and Py respectively obtained from DPPC sandwiched at the SF10/silica interface, at gradually increased applied pressures. As discussed in chapter 2, if the acyl chains of DPPC were perfectly perpendicular to the surface normal, and if the laser beam is focussed at the critical angle for the pair of dielectrics concerned, the spectral intensity of the Px and Py spectra should be almost zero (with some small contribution from the $\langle \alpha'_{zz} \rangle$ component). The Sx spectra hardly had any measurable d^+ peak, while the Sy spectra had strong d^+ and d^- peaks.

An increase in the spectral intensity in the Px and Py spectra (due to increasing contributions from Raman tensors $\langle \alpha'_{xz} \rangle$ and $\langle \alpha'_{yz} \rangle$, which are nonzero for d^- in the P-polarised spectra if the acyl chains are tilted away from the surface normal), and a simultaneous decrease in the spectral intensity in the Sx and Sy spectra with increasing pressures at the SF10/silica interface indicated that the acyl chains of DPPC gradually tilted further away from the surface normal with higher pressures. The spectral shape and intensity of the Px and Py spectra were almost identical for the set of different pressures applied, which confirmed that the laser beam was focused very close to the critical angle (θ_c = 57.25°), and that the alignment was stable throughout the complete set of experiments. Also the Px and Py spectra remaining similar throughout the whole set of experiments meant that the DPPC molecular layers continued to be isotropic in spite of all other molecular perturbations.

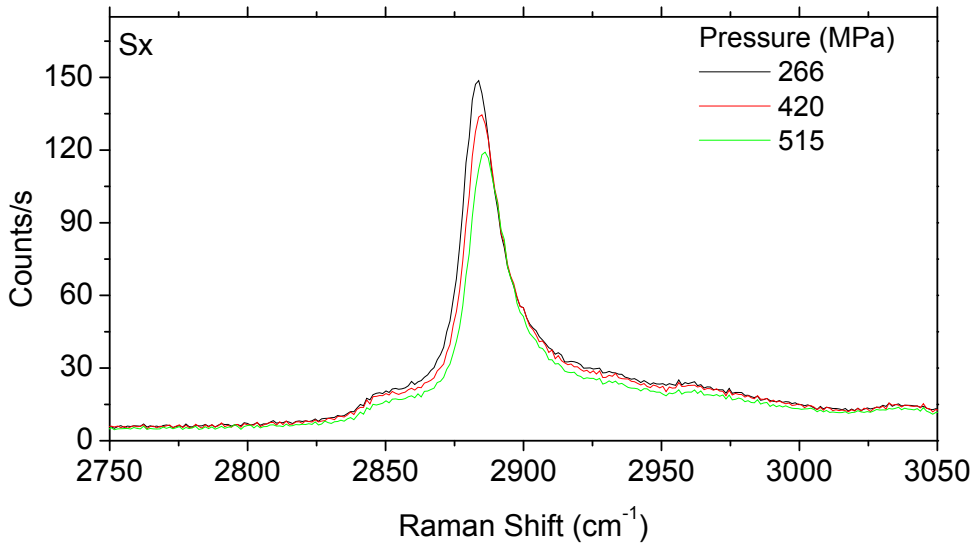

Figure 5.2.10a: Sx polarisation-resolved TIR Raman spectra from DPPC at SF10/silica interface; 300 mW, 600 s acquisition, θ_i = 57.6°, at pressures indicated in the figure.

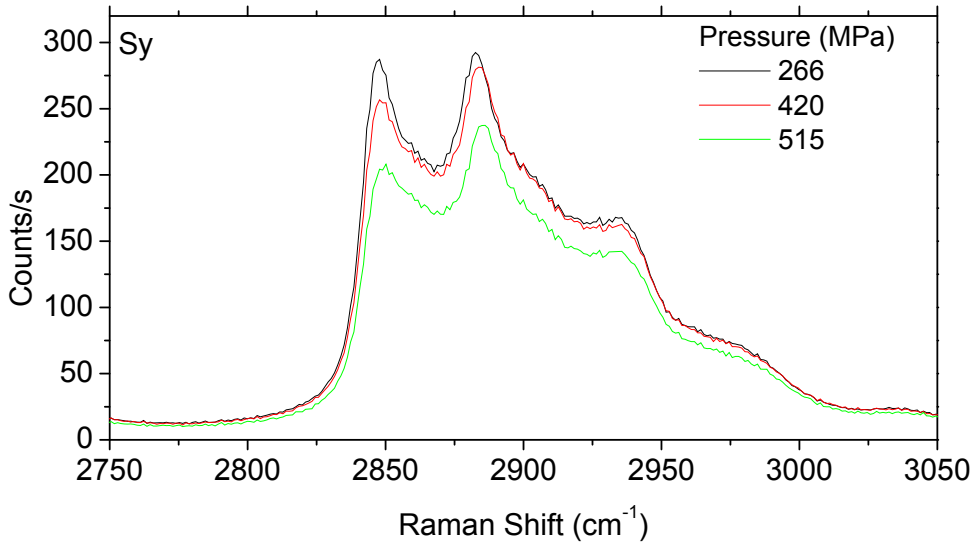

Figure 5.2.10b: Sy polarisation-resolved TIR Raman spectra from DPPC at SF10/silica interface; 300 mW, 600 s acquisition, θ_i = 57.6°, at pressures indicated in the figure.

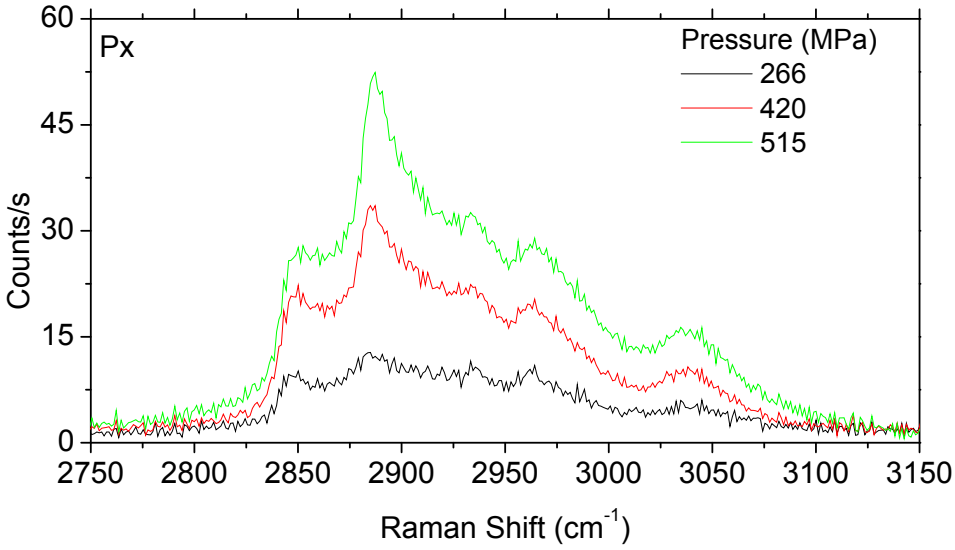

Figure 5.2.10c: Px polarisation-resolved TIR Raman spectra from DPPC at SF10/silica interface; 300 mW, 600 s acquisition, θ_i = 57.6°, at pressures indicated in the figure.

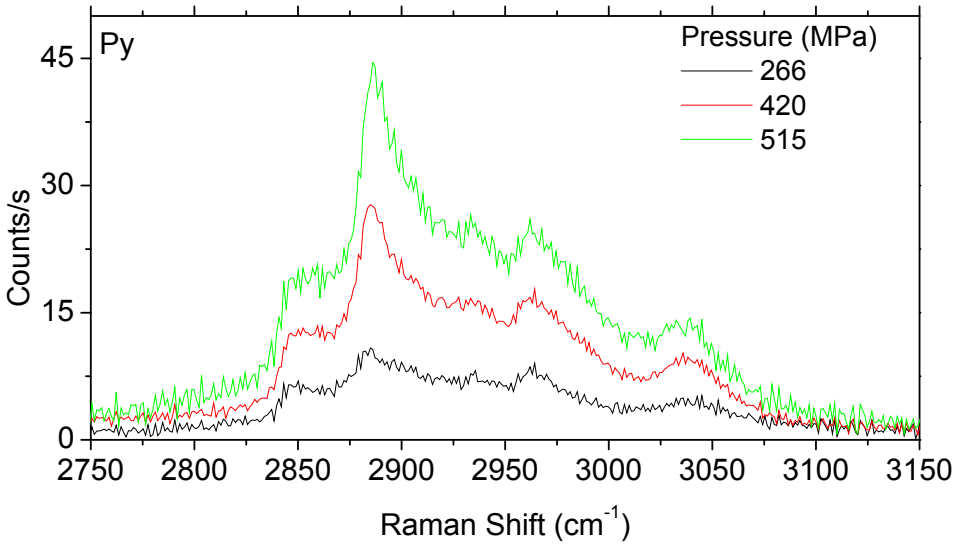

Figure 5.2.10d: Py polarisation-resolved TIR Raman spectra from DPPC at SF10/silica interface; 300 mW, 600 s acquisition, θ_i = 57.6°, at pressures indicated in the figure.

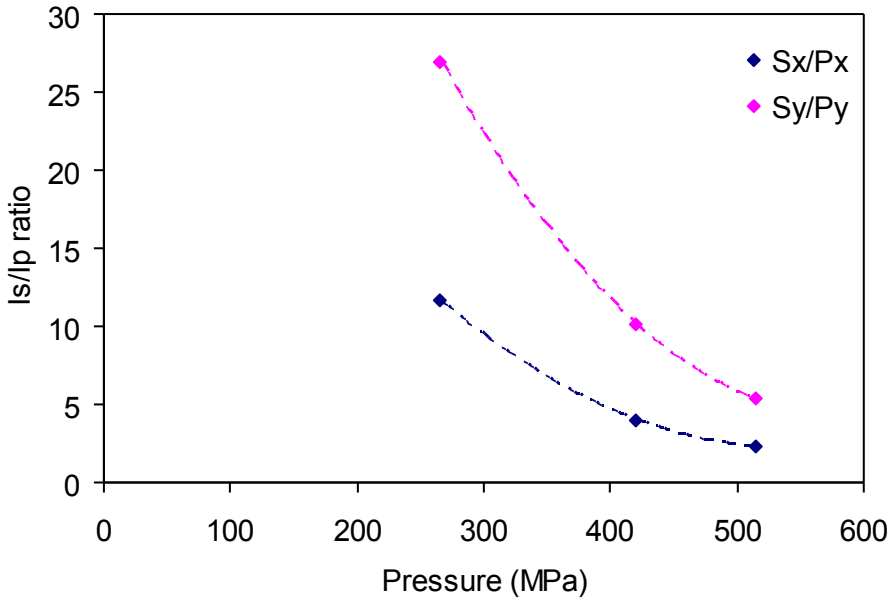

Figure 5.2.11: Plot of Is/Ip ratio against applied pressure for DPPC monolayer

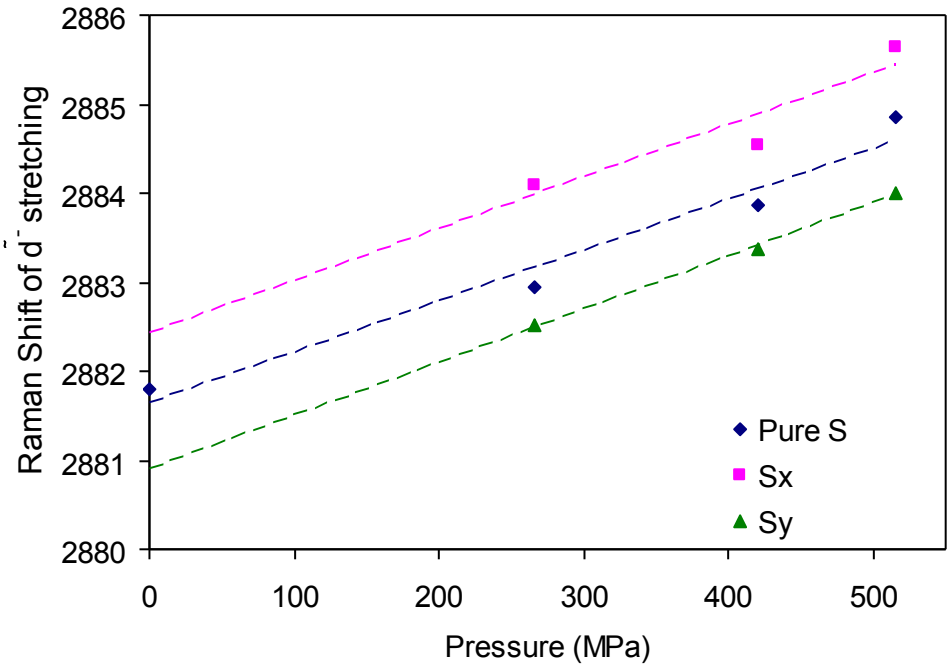

Figure 5.2.12: Plot showing the blue shift of CH_2 asymmetric stretching with higher applied pressures for DPPC monolayer. Dotted lines show a wavenumber increase of 0.1 cm^{-1} per ~17 MPa increase in pressure.

The ratio of the intensities of the S-polarised spectra and the P-polarised spectra for DPPC was plotted against applied pressures, and a reduction in Is/Ip ratio with increasing pressures indicated tilting away of the acyl chains from the surface normal. Figure 5.2.11 shows the intensity ratio Sx/Px decreased from 11.6 to 2.3 and that of Sy/Py decreased from 26.9 to 5.3 for a pressure increase from 266 MPa to 515 MPa. So the order of tilt with increasing pressure was the same as derived from both the ratios, which once again supports our inference about the chain tilts. It can also be noted here that in comparison to zinc arachidate monolayers (figure 5.2.5), the rate of molecular tilt of the acyl chains of DPPC with applied pressures are much higher, resulting in a much steeper Is/Ip curves. The reason is probably because the availability of more lateral space for molecular chain tilts in DPPC than zinc arachidate, as during LB deposition, the zinc arachidate monolayers at deposition pressure (35 mN/m) were much more densely packed (18 $Å^2$/molecule) than DPPC molecules (~46 $Å^2$/molecule) at its deposition pressure (35 mN/m). However, each DPPC molecule has two alkyl chains, therefore the packing density of the chains in the DPPC monolayers were ~23 $Å^2$/chain. This is also evident from the degree of blue shift of the spectra with applied pressures. In figure 5.2.12 the peak positions of the d^- peaks were plotted against increasing pressures. The S-unpolarised spectra and Sx, Sy spectra from DPPC monolayers at SF10/slica interface were suitably curve fitted (curve fitting of C-H stretching spectral region in LB monolayers of Zn arachidate/DPPC is discussed in section 5.3) to locate the exact peak position if the d^- band, and a blue shift of 0.1 cm^{-1} was observed on an average of 17 MPa increase in pressure [8]. On a related note, a blue shift of 0.1 cm^{-1} was observed on an average of 31 MPa increase in pressure for zinc arachidate monolayers, which indicates that the molecules of DPPC on application of same amount of pressure comes closer to each other than zinc arachidate molecules.

5.3 Curve fitting of the C-H stretching spectral region of the Raman bands from Zinc arachidate and DPPC monolayers

The Raman spectra of the C-H stretching bands (obtained with S, Sx and Sy polarisations) in the region 2800 cm^{-1} – 3000 cm^{-1} obtained from zinc arachidate

monolayers and DPPC monolayers at SF10/silica interface were curve fitted for further analysis of d^-/d^+ ratios and blue shifts of the d^- peaks (section 5.2). Table 5.3.1 shows the curve fitting parameters [9] used for our analysis and figures 5.3.1, 5.3.2 & 5.3.3 show the representative curve fits for S-unpolarised (pure S), Sx and Sy spectra respectively from zinc arachidate monolayers at SF10/silica interface.

Peak number	Peak label in curve fit	Raman bands	Centre (cm^{-1})	Width (cm^{-1})	% Gaussian
1	—	CH_2 symmetric stretching	2842 – 2852	14 – 25	50 – 100
2	—	CH_3 symmetric stretching	2855 – 2872	25	50 – 100
3	—	CH_2 antisymmetric stretching	2875 – 2890	14 – 25	50 – 100
4	—	Fermi resonance	2890 – 2906	31.5	100
5	—	Fermi resonance	2928 – 2938	31.5	100
6	—	CH_3 antisymmetric stretching	2950 – 2980	30	100

Table 5.3.1: Curve-fitting parameters for the 2800 cm^{-1} – 3000 cm^{-1} region for TIR Raman spectra from zinc arachidate and DPPC monolayers at SF10/silica interface

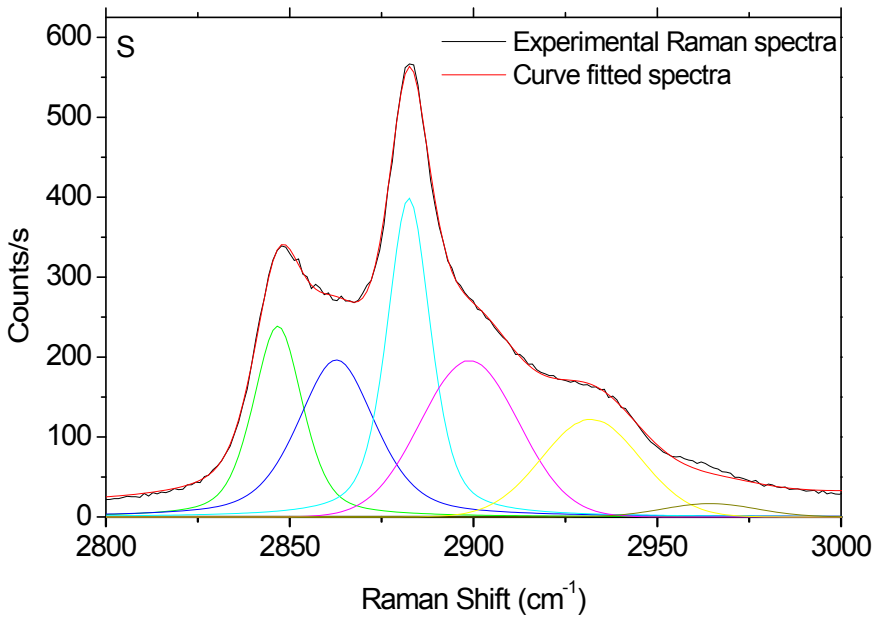

Figure 5.3.1: Curve fitting of pure S spectra in the C-H stretching Raman bands of zinc arachidate

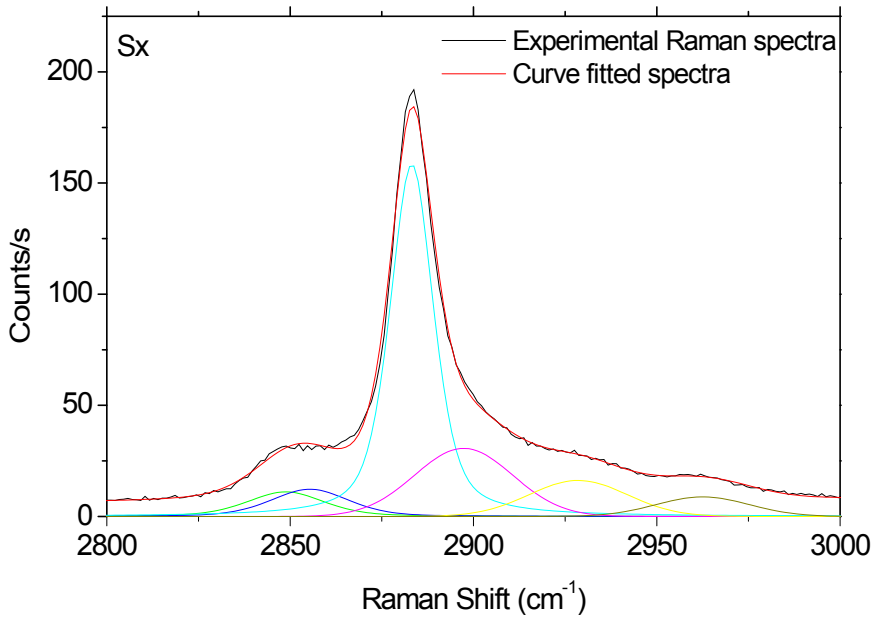

Figure 5.3.2: Curve fitting of Sx pol. spectra in the C-H stretching Raman bands of zinc arachidate.

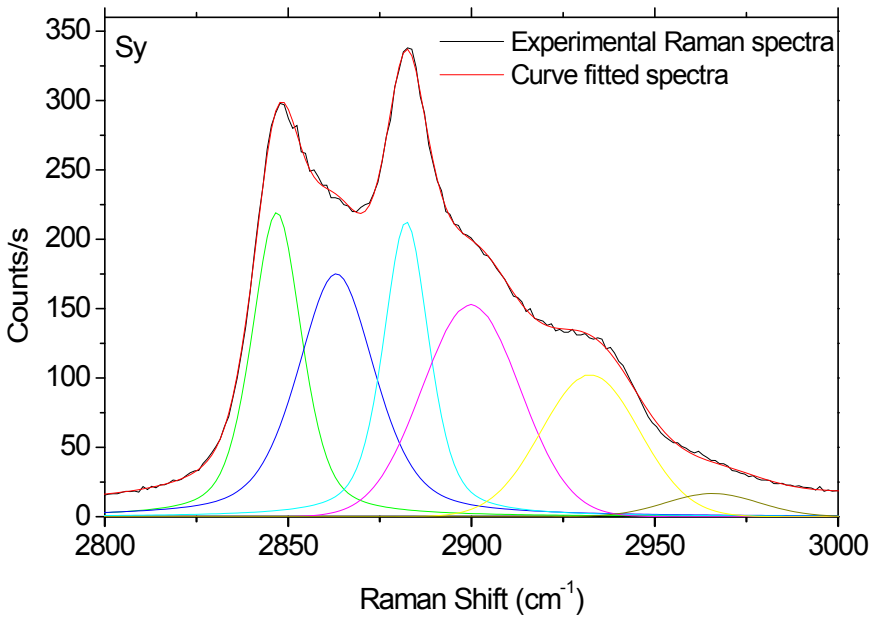

Figure 5.3.3: Curve fitting of Sy pol. spectra in the C-H stretching Raman bands of zinc arachidate.

As evident from previous sections, both zinc arachidate and DPPC monolayers showed C-H Raman stretching bands in the same spectral windows, hence same curve fitting parameters were used for analysis of both the spectra. For both zinc arachidate and DPPC, the bands around 2847 cm^{-1} and 2882 cm^{-1} are associated with symmetric and antisymmetric CH_2 vibration stretching modes [9]. The bands around 2895 cm^{-1} and 2930 cm^{-1} are associated with a broad contribution due to Fermi resonance involving the chain terminal CH_3 symmetric stretching mode and binary combinations or overtones of CH_2 deformation modes. The band around 2865 cm^{-1} is associated to the terminal CH_3 symmetric stretching mode and the band around 2962 cm^{-1} is probably due to terminal CH_3 antisymmetric stretching mode. There is a possibility of a few other weaker bands in the same region; however these bands could not be attributed unambiguously from the literature, hence omitted from our analysis. Curve-fitting of the region 2800 cm^{-1} – 3000 cm^{-1} is attempted for only the S-unpolarised, Sx and Sy spectra and not for the Px and Py spectra as the spectra obtained with P-polarised incident light in the contact experiments were far weaker than the S-polarised spectra as expected from symmetry considerations,

and hence the signal to noise ratio was not suitable for a convincing curve-fitting. The Wire 2.0 software from Renishaw was used to carry out the mathematical curve-fitting on all the spectra, using six bands described in table 5.3.1 as mixtures of Gaussian and Lorentzian functions. For reproducible results and to limit the occurrence of mathematical solutions that are not reasonable from a spectroscopic point of view, some parameters were fixed or allowed to vary within a limited range. The limitations imposed on the parameters are displayed in table 5.3.1. The width of the peaks 1 and 3 associated with the CH_2 symmetric and asymmetric stretching modes were our prime interest and were varied within and range 14 cm^{-1} to 25 cm^{-1}, the rest of the peaks were fixed to a reasonable width. The percentage Gaussian or the peaks 1, 2 and 3 were varied within 50 to 100 while the peaks 4, 5 and 6 were 100% Gaussian [9]. The parameters were so imposed as small changes in peaks 4 and 6 influenced the area of the peak 5 at 2930 cm^{-1} to a significant extent.

Bandwidth of the CH_2 stretch modes, which directly correlates with the rotational and translational motion in alkyl chains, is an important indication of the packing density of the alkyl chains [10, 11]. A decrease in the 'full width at half maxima' (FWHM) or simply 'width' as described in table 5.3.1, of the d^- stretching band indicates more ordered packing of alkyl chains and lesser gauche defects. Conversely, an increase in the FWHM of the d^+ stretching band indicates higher ordering in the packing of alkyl chains.

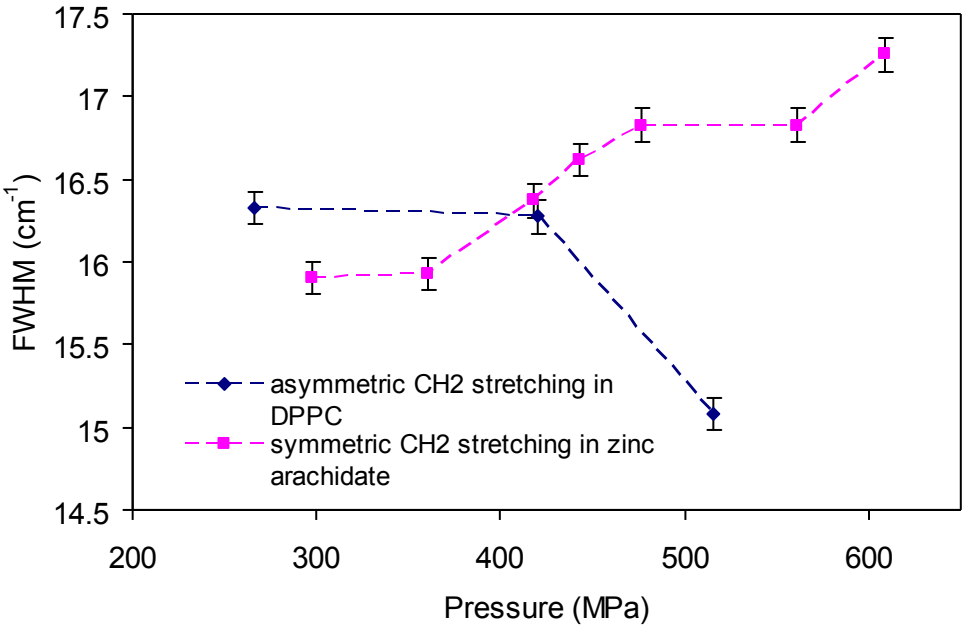

Figure 5.3.4: Plot showing FHWM vs. pressure in the CH_2 stretching modes of Raman bands of zinc arachidate and DPPC.

For DPPC spectra obtained under increasing pressures, the reduction in FWHM from 16.3 cm^{-1} at 266 MPa to 15.1 cm^{-1} at 515 MPa in figure 5.3.4 clearly indicated the increase in packing density of the acyl chain under higher pressures and supports the conclusion arrived from the blue shift of the d^- stretching with applied pressure in section 5.2.2. For zinc arachidate monolayers, which were more densely packed to begin with even without application of external pressure, the restriction of a minimum 14 cm^{-1} bandwidth imposed in the curve fitting parameters (table 5.3.1) did not allow the FWHM to move below that limit. So the increase in the FWHM of the d^+ stretching bands in zinc arachidate spectra were considered as a reconfirmation of the increasing packing density of the alkyl chains with increasing applied pressures. As evident from figure 5.3.4, the FWHM for the d^+ stretching mode in zinc arachidate increased from 15.9 cm^{-1} at 298 MPa to 17.2 cm^{-1} at 609 MPa.

5.4 Discussion

The Langmuir-Blodgett monolayers of both zinc arachidate and DPPC were deposited on SF10 and silica optics by transferring monolayers from a phase where are alkyl chains are supposed to be upright (section 4.2.3). However, the alkyl chains in the transferred monolayers of zinc arachidate were found to be tilted from the surface normal, while the alkyl chains in the DPPC monolayers were upright after transfer as observed from our *ex-situ* TIR Raman experiments (section 5.1).

Khatri *et al.* reported from their ball on disk experiments performed on alkylsilane SAM on aluminium surface [12] that the dynamic friction coefficient, μ_d increased with increasing load and this effect was more prominent when the monolayer was conformationally disordered. A less ordered monolayer resulted in higher friction coefficient. Earlier Salmeron on the basis of their LFM studies [13] suggested load induced changes in molecular conformations as a reason for change in friction. However, in our static experiments we found that with application of higher pressures, the monolayers of both zinc arachidate and DPPC continued to be isotropic with gradually increasing order in the molecular packing. This indicates a possibility that the static friction coefficient, μ_s in our experiments could actually decrease with increase in applied pressure, although the actual measurement of the friction coefficient was beyond the scope of our static experimental setup. This is because, in principle we can not measure the friction force till the first sliding occurs. The sliding experiments to be described in chapter 6 and chapter 7 will have potentially better scope for measuring friction force directly; however the initial sliding may appear to be good enough to initiate disorderliness in the monolayers. Kohno *et al.* [14] reported that in case of a monolayer the friction coefficient is independent of load unless the load is very small in which case it decreases with increasing load. Similar conclusion about decrease in friction coefficient with increasing load was also reported by Xue *et al.* [15] multilayer LB films of MoS_2-behenic acid mixture. In partial contrast to Kohno *et al.* our results predict a decrease in friction coefficient at least till a significant pressure (~700 MPa) applied. Although on a related note, our contact experiments were effectively done on zinc arachidate or DPPC bilayers as both the SF10 and silica surfaces were coated with LB monolayers, hence our

results can somehow relate to reports from Xue *et al.* FFM experiments carried out by Fujiwara *et al.* [16] revealed that friction coefficient of the LB films were decreased if the alkyl chains were tilted which they explained by the increase in the limiting area of the adhering molecule. Our results clearly suggested that the alkyl/acyl chain tilts increased for zinc arachidate and DPPC monolayers with increasing pressures and may contribute to our prediction that the static friction coefficient, μ_s of LB monolayers reduces with increasing pressure.

Reference:

1. Berman, A.D., W.A. Ducker, and J.N. Israelachvili, Langmuir, 1996. **12**(19): p. 4559-4563.
2. Bordarier, P., Schoen, M., and Fuchs, A.H., Physical Review E, 1998. **57**(2): p. 1621-1635.
3. Israelachvili, J.N., Surface Science Reports, 1992. **14**: p. 109.
4. Oncins, G., Torrent-Burgues, J., and Sanz, F, Journal of Physical Chemistry C, 2008. **112**: p. 1967-1974.
5. Helm, C.A., Mohwald, H., Kjaer, K. and Als-Nielsen, J., Europhysics Letters, 1987. **4**(6): p. 697-703.
6. Sun, W.-J., Tristam-Nagle, S., Suter, R.M., and Nagle, J.F., Biophysical Journal, 1996. **71**: p. 885-891.
7. Ho, M., and Pemberton, J.E., Analytical Chemistry, 1998. **70**: p. 4915.
8. Coulon, S., Jabault, I., Lubrecht, A.A., Ville, F., and Vergne, P., Tribology International, 2004. **37**: p. 111-117.
9. Percot, A., and Lafleur, M., Biophysical Journal, 2001. **81**: p. 2144-2153.
10. Evans, S.D., Berrarducci, K.E.G., Urankar, E., Gerenser, L.J., Ulman, A. and Synder, R.G., Langmuir, 1991. **7**: p. 2700.
11. Wood, K.A., Synder, R.G., Strauss, H.L., Journal of Chemical Physics, 1989. **91**: p. 5255.
12. Khatri, O.P., and Biswas, S.K., Surface Science, 2006. **600**: p. 4399-4404.
13. Salmeron, M., Tribology Letters, 2001. **10**: p. 69.

14. Kohno, A., Sugiura, M., Mori, M., Journal of Japanese Society of Lubrication Engineers, 1987. **32**: p. 225.
15. Xue, Q., Zhang, PY., Zhang ZJ., Liu, WM.,Du, ZL., Ma, GH., Thin Solid films, 1999. **346**: p. 234-237.
16. Fujiwara, I., Kamei, T., Seto, J., Japanese Journal of Applied Physics, 1995. **34**: p. 4932.

6. Development of Raman Tribometer

6.1 Purpose of a Raman Tribometer

Changes in the environment e.g. global warming, decrease in total oil resources etc. have greatly influenced the automobile industry in the recent past. To improve the fuel consumption of the automobiles, it is required for the sliding products of the vehicles to move with lower friction resistance with smaller amount of lubricant. To meet these requirements it is essential to design a better friction surface, to develop low friction multifunctional lubricant oil with sufficient thermal and chemical stability, etc. To meet these targets, attempts were made to understand the essential features of the friction phenomenon between a pair of sliding surfaces by various analytical methods [1, 2]. In most of these conventional techniques, mostly *ex-situ* measurements of the tribological surfaces were carried out using suitable analytical equipments and comparisons were made with pre-sliding friction surfaces. However, while these tribological surfaces are being removed to set into the analytical equipment for further testing, there is a significant chance of the surface getting modified due to oxidation, pollution, etc. The problem therefore calls for the conduction of *in-situ* investigations of the sliding surfaces to examine the stress state on the metal surface and the friction environment while sliding, as well as the molecular state of the lubricant.

Many researches have been reported on the sliding friction surface on the basis of time-resolved measurements of X-ray photoelectron spectroscopy (XPS) [3-5], infrared spectroscopy [6-17], Raman Spectroscopy [18-22], but these studies did not necessarily measure the surface under friction or sliding contact but measured the surfaces between and after sliding contacts. Apart from that, Auger and XPS techniques require high vacuum atmosphere which limits the detection of the volatile lubricant molecules in a ‘wet’ atmosphere. A synchrotron X-ray source may be used for obtaining extended X-ray absorption fine structures to study the change in surface state, but it can not give direct information about the interaction of the lubricant molecules with the sliding surface. Vibrational spectroscopy e.g. infrared and Raman can be potentially more useful

techniques compared to the X-ray techniques depending on their implementations in a sense that it can detect changes in orientation, chemical structure and thermal motion of the lubricant molecules directly in terms of vibrational frequencies and absorption/scattering intensities of the characteristic bands.

Piras *et al.* [16] studied the sliding motion of a metal ball in contact with an iron coated Ge element with a sandwiched lubricating agent using infrared attenuated total reflection (ATR-IR) spectroscopy. In their experiment, however, it was not possible to obtain a 2D image of the lubricant molecules distributed on the sliding metal surface as the spectrum included in-contact and out-of-contact areas. Sasaki *et al.* [23] have recently conducted experiments where they have combined Fourier-transform infrared (FTIR)-ATR method with the fast-image FTIR spectrometer to observe in-situ friction over an area of 35 × 35 μm^2 at once. This technique can be quite useful for tracing the change in the 2D image of the lubricant molecules during friction. For their friction experiments, Sasaki *et al.* used an aluminium test ball in a reciprocating motion in contact with the ATR element, a Ge hemisphere in the atmosphere of test oil. The IR beam was incident on the ATR element and the totally reflected beam was detected by a 2D detector to get an infrared spectral image of the contact surface. A reciprocating point of contact, however, meant that a time resolved spectra at every 0.134 seconds in a fast scan mode would acquire spectra from both from in-contact and out-of-contact region depending on the sliding speed of the Al ball (0.05 mm/s) and the total stroke (2 mm). In other words, one spectrum was measured at a timing of every 6.7 μm shift of the ball. The friction force (F) during sliding motion was monitored by a load cell connected directly to the test ball. Another load cell was placed below the test ball to measure the perpendicular force/load (L) applied to the Ge surface. The two forces F and L were used to evaluate the friction coefficient, μ at a particular time using the relation $F = \mu L$.

A Raman experiment was reported by Scharf and Singer [22] where they irradiated the laser beam onto the frictional contact area between a sapphire hemisphere and a diamond like nanocomposite (DLN) coated sliding ball to measure the orientational changes in lubricant molecules and monitor transfer film thickness. However, in most of these

vibrational spectroscopy based tribometric tests [22, 23], the friction tests were carried out by reciprocating movements of one sliding surface over against the other and this kind of setup is generally capable of producing good reproducible results when the sliding speed is relatively lower (less than 1 mm/second). Beattie *et al.* [24-26] applied more surface sensitive techniques, the total internal reflection (TIR) Raman spectroscopy and sum-frequency spectroscopy (SFS) to the prism-lens contacts and studied the LB monolayers and organic films confined at the interfaces under higher pressures. However, those experiments were carried out under static contacts and no shear or lateral friction was involved. Sarah Amanda Haydock in her DPhil thesis [27] reported her attempts to use the TIR Raman experiments at prism-lens systems to study frictional responses from Zn arachidate LB monolayers confined at the interface by reciprocating motion of the prism.

As explained in chapter 3: section 3.1.4, due to the advantages of using hemispherical prisms (hemispheres in case of static experiments) over triangular prisms i.e. ease of laser alignment and eliminated astigmatism, a modification of Sarah Haydock's friction experiments could be using a lens and a hemicylinder system (fig. 6.1.1) where the flat hemicylinder surface can be slid by reciprocating motion against the curved lens surface with a suitable lubricating agent being confined at the interface.

TIR Raman spectroscopy can measure thickness as low as 1–10 nm, hence has a potential applicability in measuring boundary lubrication. To carry out a comprehensive study of the absorption and breakdown of lubricating additives at the sliding interface, development of an in situ Raman tribometer rig was aimed. A rolling ball driven by a DC motor in contact with a fixed optically transparent surface was preferred ahead of reciprocating shear which gave the tribometer a flexibility to study friction at much higher sliding speeds (more than 25 mm/second) if required, and therefore capability of studying hydrodynamic lubrication besides boundary lubrication.

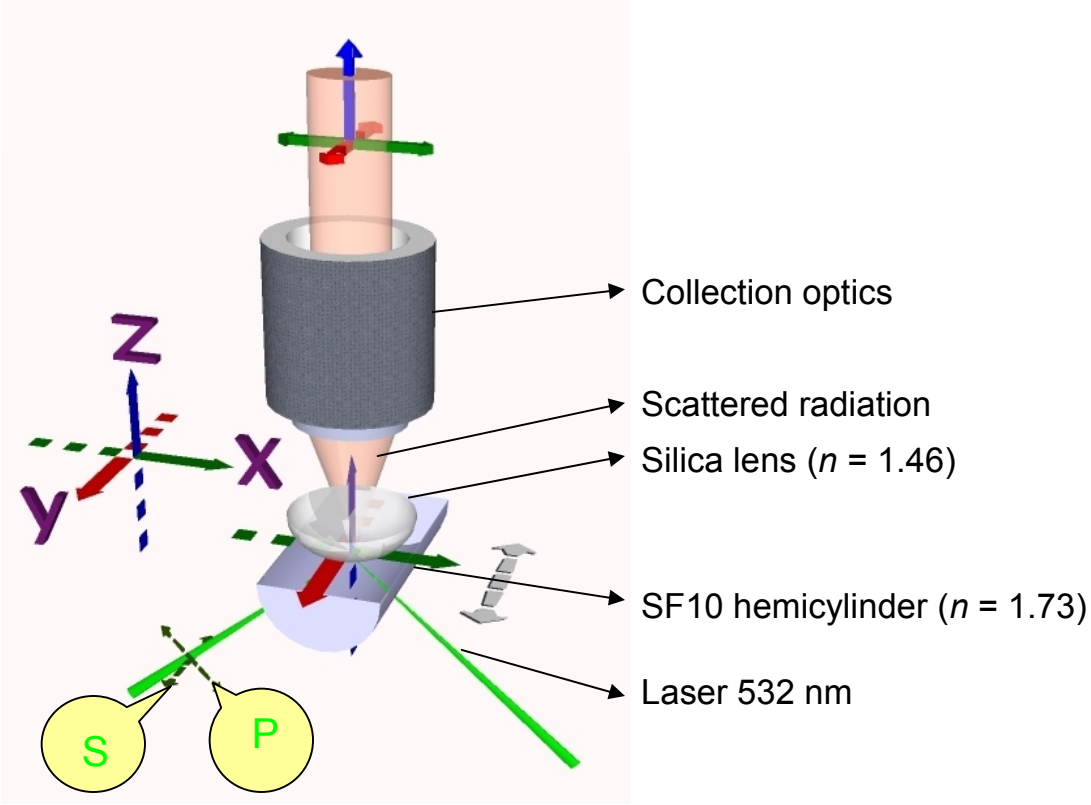

Figure 6.1.1: Schematic diagram of a possible *in-situ* Raman friction test setup where a hemicylinder undergoes a reciprocating motion along the *y*-axis in contact with a fixed optical lens on top and a lubricating agent confined in the interface.

In terms of industrial applications and most of the real world problems, studying the tribology of a steel/metal surface was important. However due to a major potential difficulty in studying a metal/dielectric interface by vibrational spectroscopy, i.e. cancellation of the electric fields at the interface due to formation of image dipoles, provisions were made in the tribometer to replace a steel ball with a glass ball. The difficulty in studying a metal/dielectric interface by TIR Raman spectroscopy will be explained mathematically later in his chapter. In the following sections I will describe the development of two Raman tribometers used during my PhD, their features and associated advantages and disadvantages.

6.2 Experimental set-up & *in-situ* Raman tribometers

The initial challenge was to design and build a tribology rig that would not only allow boundary film lubrication, but would also be compatible with a TIR Raman spectroscopy set-up. Figure 6.2.1 shows a schematic representation of the experimental geometry used in the resultant tribology rig where the laser beam was focused externally into the sliding contact between a rolling ball and the flat surface of a hemispherical SF10 optics.

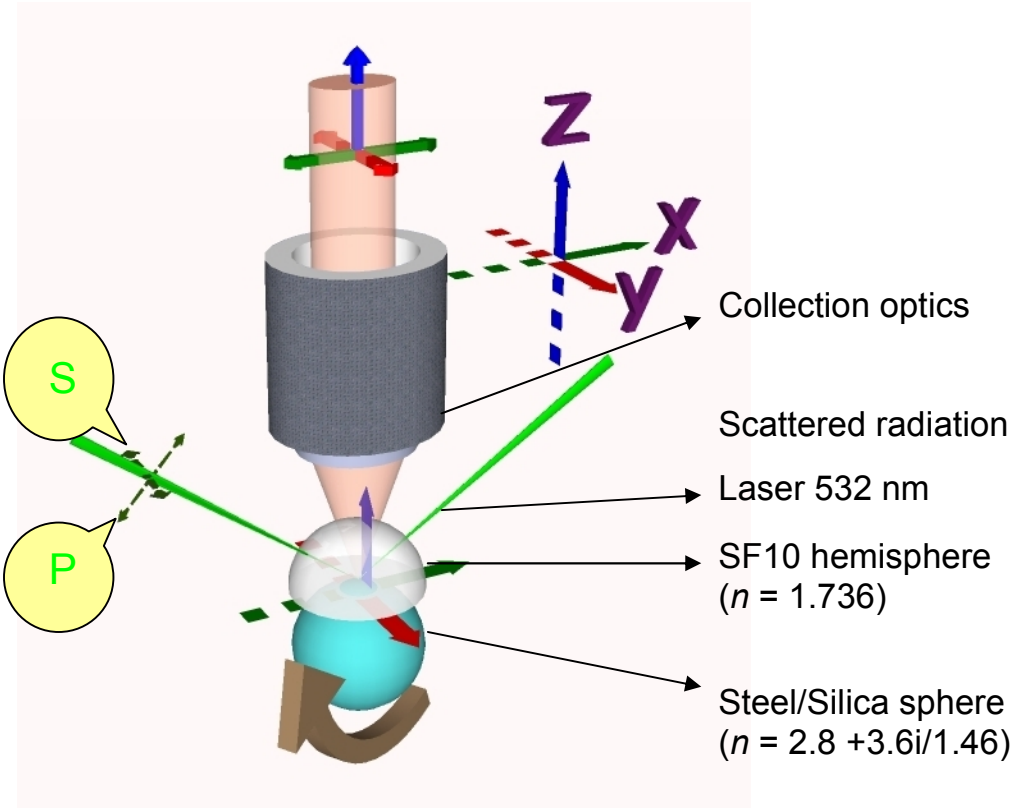

Figure 6.2.1: Schematic diagram of the *in-situ* Raman friction test/tribometer setup where a rotating ball slides against a rigid flat optical surface.

The Raman tribometer shown in figure 6.2.2 was built in collaboration with Prof. Colin Bain group (Department of Chemistry, Durham University) and Prof. S.K, Biswas group (Mechanical Engineering Department, IISc Bangalore) and the Raman tribometer shown in figure 6.2.3 was initially designed and built by Alan McNicol (ICI) and John Putson (Cordell Group Ltd) and later modified and developed by Bain group at Durham

University. The resultant design in both the tribometers used an SF10 hemisphere (10 mm dia.) held in a rigid frame with a steel/fused silica ball (8 mm dia.) underneath. The laser was directed onto the curved surface of the hemispherical SF10 and focused in the hemisphere-ball contact.

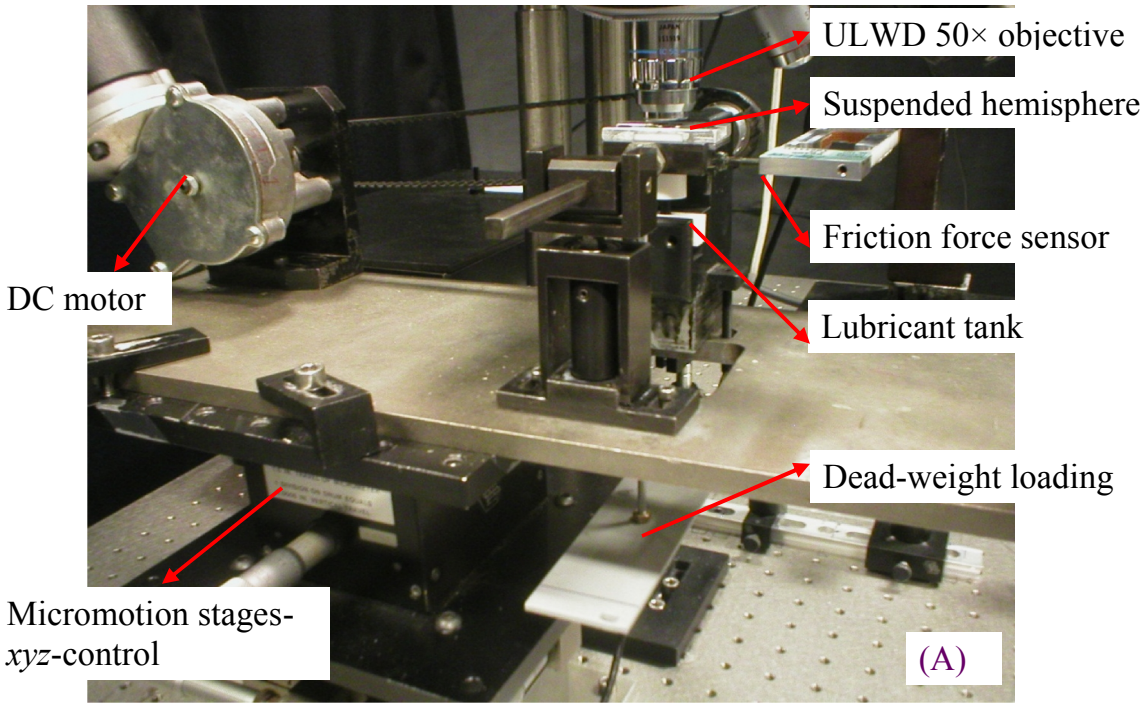

Figure 6.2.2: *In-situ* Raman tribometer setup developed in Durham University-IISc Bangalore collaboration. Special features: dead weight loading, friction force sensor for direct measurement of friction force, etc.

For both the tribometers, the external beam path alignment was set-up so that the point of laser bouncing during total internal reflection (TIR) coincided with the point where the ball meets the flat surface of the SF10 hemisphere (Figure 6.2.1). The angle of incidence at the interface was set to 60º, which corresponded to a penetration depth of 215.8 nm and 234.4 nm at SF10/silica and SF10/PAO interface respectively (fig. 6.2.4). As evident from the figure 6.2.4, the penetration depths of the generated electric field sharply decrease near the critical angle ~57.5º for the SF10/silica and SF10/PAO interfaces. The green line in the figure marks the 60º angle of incidence which was the working angle of incidence for our tribometer experiments.

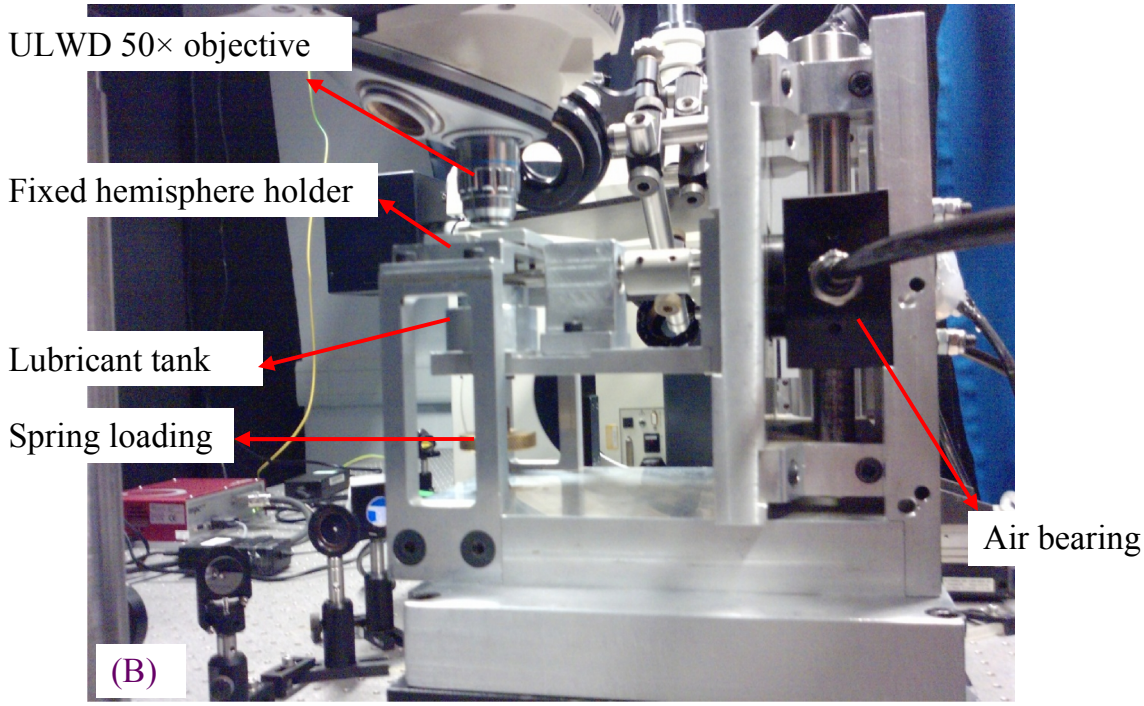

Figure 6.2.3: *In-situ* Raman tribometer setup developed at Durham University. Special features: spring loading, air bearing to balance the run-out of the rotating ball, etc.

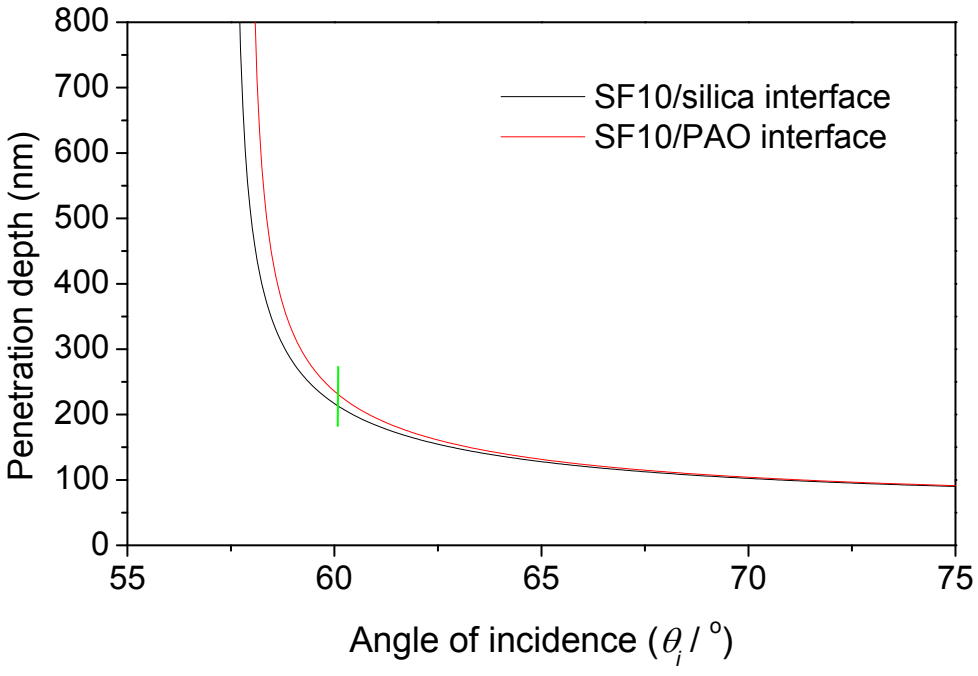

Figure 6.2.4: Variation of penetration depth of the electric field generated by a 532 nm laser focused at SF10/silica and SF10/PAO interface.

The beam expander (fig. 3.1.3) which was removed for the static *in-situ* experiments described in chapter 5, was replaced in the external beam path to obtain a smaller focus at the sliding interface. The working angle of incidence being a few degrees higher than the critical angle for SF10/silica pair there was sufficient margin of error due to run-out of the rotating ball which could move the point of contact by tens of microns and thereby affect the actual angle of incidences. For SF10/steel pair there was no critical angle as such, but the external alignments of the laser beam were kept the same due to ease of comparison of the data obtained from both the pairs, if required. The penetration depth calculation for SF10/silica interface (fig.6.2.4) is effective only when there is a molecular layer of lubricant (less than 10 nm thick, say monolayers of Zn arachidate on the both the surfaces) sandwiched at the interface. For thicker films of the order of ~100 nm, as in the case of poly-alpha olefin (PAO) experiments in chapter 7, the penetration depth calculation at SF10/PAO interface (fig. 6.2.4) is effective.

The steel/silica ball was attached to a shaft driven by a DC motor, which enabled the ball to rotate at various speeds. The tribometer (A) in figure 6.2.2 had a rubber belt attached to the motor which drove the shaft while in tribometer (B) in figure 6.2.3 the shaft was directly attached to the motor by an aluminium coupling. An oil bath was placed underneath the ball. As the semi-emersed ball in oil/lubricant rotated a constant flow of lubricant was supplied to the interface region. Heating cartridges were also embedded in the oil bath for temperature control.

6.2.1 Special features in Raman tribometer (A)

The Raman tribometer (A) built in Durham-Bangalore collaboration as a part of the UKERI project was equipped with dead weight loading mechanism where standard weights were loaded on a hanger suspended from the arm of the hemisphere holder while the hemisphere rested on top of the rotating ball. The advantage in this setup was the possibility of direct reading of the normal load and therefore the pressure calculation at the contact region was easier. The associated disadvantage was that the run-out of the rotating ball due to non-centric axis (+/– 25 μm) could cause the hemisphere to move perpendicularly to the plane of contact and therefore the actual angle of incidence might

have varied within a range (+/– 1º) throughout the experiment. This range of variation in the angle of incidence can be significant as both the electric fields (fig. 6.3.6) and penetration depth (fig. 6.2.5) for SF10/silica interface show sharp changes near the critical angle (θ_c = 57.25°). However the flexibility in perpendicular movement of the hemisphere ensured a constant applied pressure at the interface throughout a rotating ball experiment which can be counted as an advantage in using this tribometer.

There was also a nominal flexibility in the lateral movement of the hemisphere holder which connected to a rigidly fixed force sensor. The force sensor was capable of direct measurement of the friction force from the initial lateral movement or 'jerk' in the hemisphere holder whenever there was any change in lateral force or speed of the rotating ball. The hemisphere was in turn kept in position while the ball rotated by positioning a screw attached to the rigidly fixed force sensor.

6.2.2 Special features in Raman tribometer (B)

The tribometer (B) developed at Durham University has a rigidly fixed hemisphere with a rotating steel/silica ball beneath glued to a shaft and coupled with a DC motor. The rigidly fixed hemisphere made the direct measurement of friction force much more complicated and the force sensor did not form a component in tribometer (B). However, the advantage with a rigidly fixed hemisphere was that the laser alignment and the working angle of incidence remained almost constant throughout the rotating ball experiment; hence negligible changes occur in the electric fields at the interface during the experiment.

The complete mechanism of the hemisphere with a rotating ball beneath it with the DC motor and the oil tank was held in a secondary frame which could also move up and down, via air bearings and a screw mechanism, which enabled different loads to be applied at the contact region. The air bearing mechanism was introduced to negotiate the run-out of the rotating ball which could cause a variation in pressure at the lubricated interface under study. However, the response time of the air bearing was good enough to balance only a fraction of the vertical run-out (minimised to +/– 10 μm) while the

horizontal run-out continued to be a concern; the problem calls for devising a better mechanism of fixing the ball to the shaft with maximisation of the centricity.

The sliding experiments with this tribometer required measurement of the normal applied load by measuring the diameter of the central dark spot of the Newton's rings observed in the microscope in focussing white light to the contact area, as discussed in chapter 2, section 2.5. This procedure was relatively straightforward in dry contacts as the Newton's rings were prominently visible, however as PAO or other lubricating oils were introduced observing the Newton's rings became difficult due to the similarity in refractive indices of PAO and silica. Hence changing the pressure while maintaining a constant speed of rotation of the ball was avoided; rather the speed of the rotating ball was varied with a constant applied pressure.

6.3 Working parameters of the Raman tribometer rig

Determination of certain working parameters of the rig was important to carry out the friction experiments on the Raman tribometer e.g. effect of rotating ball speed and load on the film thickness of the fluid lubricant film at the sliding interface, corresponding pressure in the point of contact, electric field variations at the SF10/lubricant (PAO) and SF10/silica interfaces.

6.3.1 Calculation of film thickness

The Reynolds equation (6.3.1) was used to calculate theoretically the film thicknesses (h_{min}) achieved in the *in-situ* tribology rig experiments [28].

$$\frac{h_{\min}}{R} = 3.63U^{0.68}G^{0.49}W^{-0.073}\left(1-e^{-0.68k}\right) \qquad (6.3.1)$$

$$U = \frac{\eta_0 \bar{u}}{ER} \qquad (6.3.2)$$

where η_0 is the lubricant viscosity at ambient pressure and constant temperature, $\bar{u}$ is the average speed of the surface of rolling ball, E is the reduced modulus of the surfaces and R is the radius of the ball (steel/silica ball used is 8 mm diameter, R = 4×10^{-3} m).

E can be calculated using: $\frac{1}{E} = \frac{1-V_1^2}{E_1} + \frac{1-V_2^2}{E_2}$ (6.3.3)

where E_1 and E_2 are the Young's modulus of the two solid materials used and V_1 and V_2 their corresponding Poisson's ratios.

For the steel ball E_1 = 207 GPa and V_1 = 0.3 [29], while for the fused silica ball E_1 = 75.8 GPa and V_1 = 0.26; for the SF10 hemisphere E_2 = 64 GPa and V_2 = 0.232. Therefore the reduced modulus for the set-up SF10/steel interface was E = 50.16 GPa and for the set-up SF10/silica interface was E = 36.92 GPa.

$$G = \alpha E \quad (6.3.4)$$

where α is the viscosity-pressure coefficient (dependent on the oil used). For PAO at 22 ºC the value of α used for film thickness calculations was 1.34×10^{-8} (data supplied by the manufacturer, Chemtura Corporation Petroleum Additives).

$$W = \frac{Wz}{ER^2} \quad (6.3.5)$$

where Wz is the applied load.

$$k = \frac{Ry}{Rx} \quad (6.3.6)$$

where Ry and Rx are radii in the y- and x-directions (x-direction being the sliding direction). For the steel/silica ball on SF10 hemisphere k = 1

6.3.2 Pressure calculations

Raman tribometer (A) is equipped with a dead weight loading mechanism. Hence the applied normal load could be directly measured by the sum of the standard weight of the discs suspended on the hanger plus corrections due to the weight of the hanger.

The average pressure, P_m in the contact area was calculated by the Hertz equations [30]

$$P_m = \frac{F}{\pi a^2} = \frac{1}{\pi}\left[\frac{16FE^2}{9R^2}\right]^{1/3} \quad (6.3.7)$$

where F denotes the total force exerted, a denotes the radius of the contact area, R denotes the radius of curvature of the sphere, and E denotes the reduced Young's

modulus of the pair of substrates (6.3.3). The focus of the laser beam at the interface was positioned at the centre of the contact area where the maximum pressure was exerted. The maximum pressure, P_0 at the centre of the contact area was calculated by

$$P_0 = 1.5P_m = \frac{1.5}{\pi}\left[\frac{16FE^2}{9R^2}\right]^{1/3} \qquad (6.3.8)$$

A spring loading mechanism was executed in the experiments carried out by the Raman tribometer (B) and indirect measures had to be adapted for the estimation of interfacial pressures. At the beginning of the contact/sliding experiments, white light was focussed onto the contact area from the curved side of the SF10 hemisphere and the radius, a of the contact area was estimated from the central dark spot of the newtons rings [31]. The average pressure, P_m and maximum pressure, P_0 at the contact area were then calculated using Hertz equations (6.3.9) and (6.3.10) respectively.

$$P_m = \frac{4Ea}{3\pi R} \qquad (6.3.9)$$

$$P_0 = 1.5P_m = \frac{3}{2}\left(\frac{4Ea}{3\pi R}\right) \qquad (6.3.10)$$

6.3.3 Fresnel coefficients and phases of electric fields at SF10/steel and SF10/silica interfaces

The interfacial electric fields in terms of Fresnel K-factors were plotted for SF10/steel interface (figure 6.3.1) and SF10/silica interface (figure 6.3.2) against different angle of incidence for a laser beam of wavelength 532 nm as described in chapter 2, section 2.2.3. This required the refractive indices and absorption coefficients for each material. While these values were readily available for the SF10 hemisphere (n = 1.73) and fused silica ball (n = 1.46), the refractive index and absorption coefficient for the steel ball and PAO had to be determined by ellipsometry. For a steel ball these values were calculated to be n = 2.8 and k = 3.6 for λ =532 nm by ellipsometry experiments carried out by Rob Jacobs at the Physical and Theoretical Chemistry Laboratory, University of Oxford. The Brewster angle, θ_B was determined for air/PAO interface (θ_B = 55.7°) using an ellipsometry test and the refractive index of PAO was calculated using the equation (6.3.11).

$$\theta_B = \arctan\frac{n_t}{n_i} = \arctan n_{ti} \qquad (6.3.11)$$

$$\text{where } n_{ti} = \frac{n_t}{n_i} \qquad (6.3.12)$$

where n_i and n_t denotes the refractive indices of the incident medium (air) and the transmitted medium (PAO) respectively. The refractive index of PAO was calculated to be n = 1.466. Since the refractive index of PAO was about the same as fused silica, hence not much difference was expected in the behaviour of the electric fields at the SF10/PAO interface and SF10/silica interface. Therefore Fresnel coefficients at both the interfaces are expected to be similar except very near the critical angle.

We considered the refractive index, n of the monolayer to be ~1.5 for our calculations. However, as the zinc arachidate molecular layer at the interface was very thin compared to the wavelength of radiation, the critical angles, θ_c at the SF10/monolayer/silica interface was effectively the critical angle at SF10/silica respectively. The critical angle, θ_c for the SF10/silica interface is 57.2°. At the SF10/steel interface total internal reflection was not observed as steel being an opaque conducting material, does not have a critical angle.

Figure 6.3.1 shows that at our working angle of incidence, θ_i = 60°, the electric field at the SF10/steel interface due to S-polarised light (Fresnel factor K_{sy}) is weaker than the electric field due to P-polarised light (Fresnel factors K_{px} and K_{pz}). Figure 6.3.2 shows that at the critical angle of the SF10/silica pair, there are not only maximum interfacial fields (as K_{sy} and K_{pz} attain maximum values) and therefore the strongest spectra, but the spectra also gets simplified as a P-polarised incident beam generates an electric field at the interface which oscillates only in the z-direction (K_{px} reduces to 0 at θ_c). However, at our working angle of incidence (θ_i = 60°) for the tribometer experiments (the margin of error in angle of incidence above the critical angle was maintained to cover up for the variation in angle of incidences during the friction experiment due to the run-out of the rotating ball), there were a possibility of significant contributions from the K_{px} factor in the P-polarised spectra.

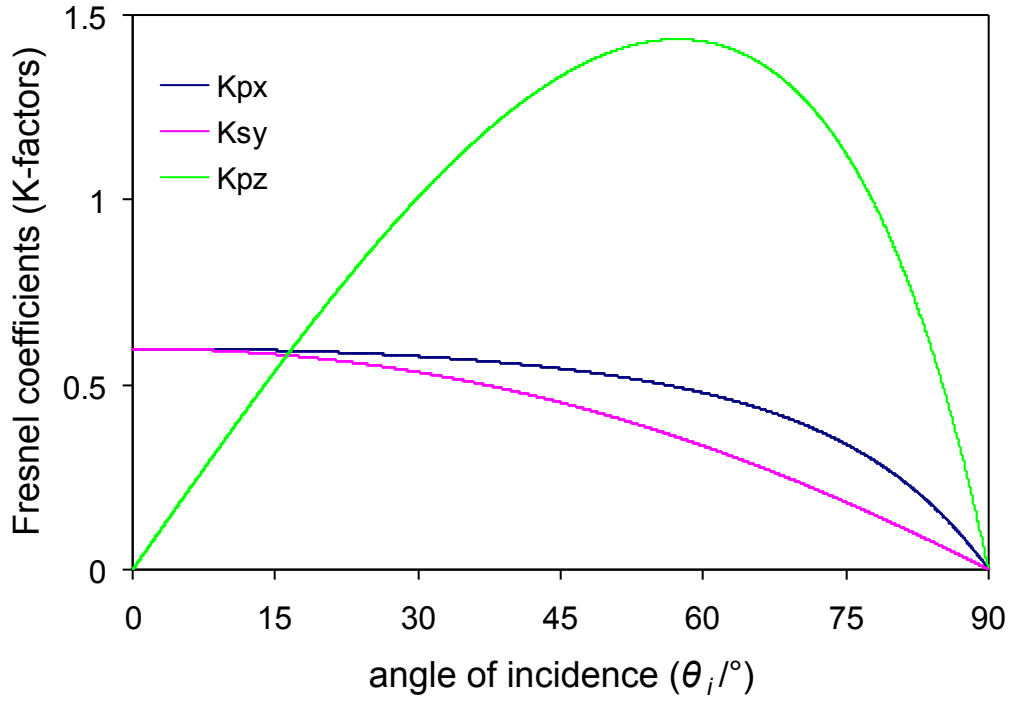

Figure 6.3.1: Plots of K-factors vs angle of incidence for electromagnetic radiation (λ = 532 nm) at SF10/monolayer/steel interface; n_{SF10} = 1.737, $n_{monolayer}$ ~ 1.5 and n_{steel} = 2.8 + 3.6i.

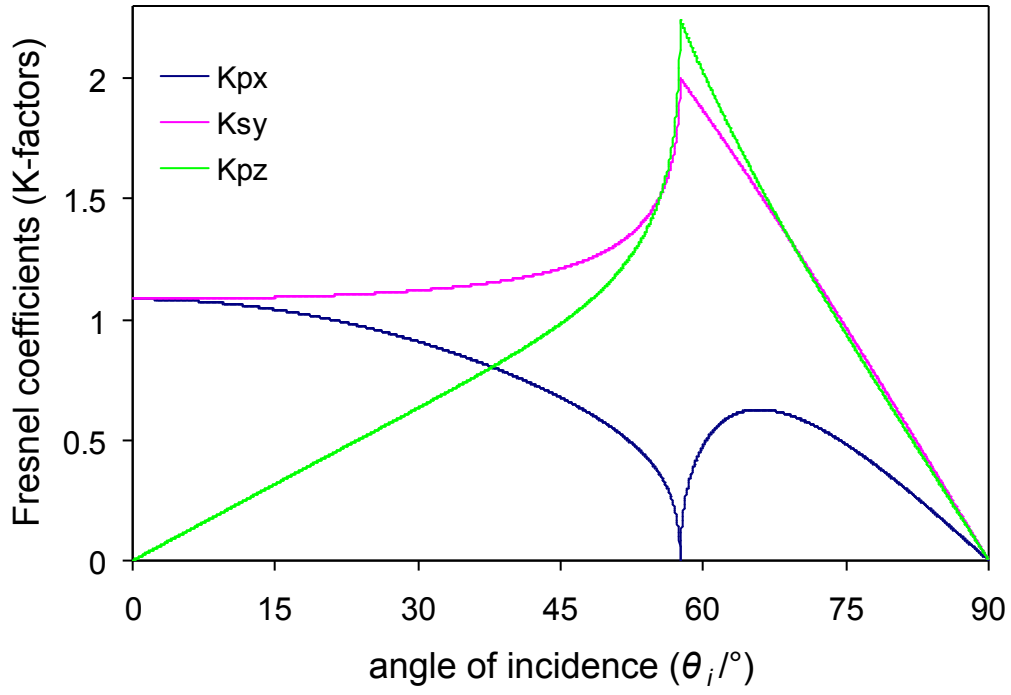

Figure 6.3.2: Plots of K-factors vs angle of incidence for electromagnetic radiation (λ = 532 nm) at SF10/monolayer/steel interface; n_{SF10} = 1.737, $n_{monolayer}$ ~ 1.5 and n_{silica} = 1.461.

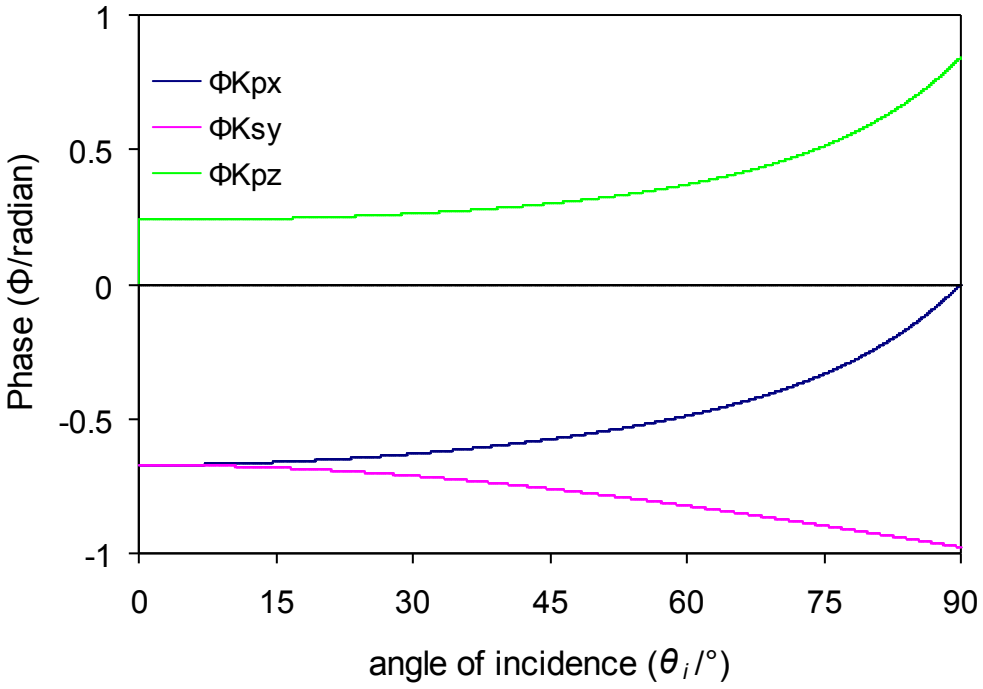

Figure 6.3.3: Plots of phases of the electric fields vs angle of incidence for electromagnetic radiation (λ = 532 nm) at SF10/monolayer/steel interface; n_{SF10} = 1.737, $n_{monolayer}$ ~ 1.5 and n_{steel} = 2.8 + 3.6i.

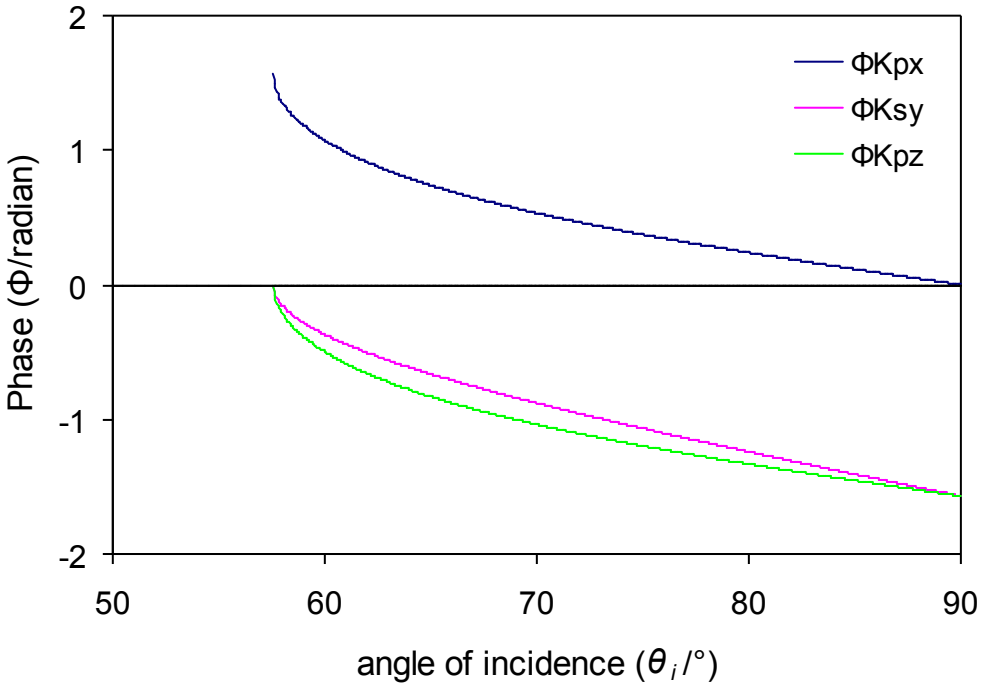

Figure 6.3.4: Plots of phases of the electric fields vs angle of incidence for electromagnetic radiation (λ = 532 nm) at SF10/monolayer/steel interface; n_{SF10} = 1.737, $n_{monolayer}$ ~ 1.5 and n_{silica} = 1.461.

The variation of phases in the different electric field vectors with variation of angle of incidences were plotted for the SF10/steel interface (figure 6.3.3) and SF10/silica interface (figure 6.3.4) to check if there were any major phase shifts or discontinuity arising out the reflection of the laser beam at the respective interfaces which could potentially contribute to cancelling of the effective electric fields at the interfaces. However as the plots show, no change in sign of the phases, neither any discontinuity or major phase shifts were observed at either of the interfaces near the working angle of incidence, $\theta_i = 60°$.

6.4 Image dipole formation at dielectric/metal interface

In chapter 2 we have already discussed (figure 2.4.2) the problem associated with collection of scattered radiation from an induced dipole in the *z*-plane as most of the electric field generated, and hence the scattered radiation, is along the *xy*-plane which a vertically placed 50× microscope objective is unable to collect. In addition to, while studying a dielectric/metal interface such as SF10/steel or oil/steel by TIR Raman spectroscopy, even the electric dipole induced in the *xy*-plane is not good enough to yield Raman signals intense enough for precise analytical measurements. This can be due to the formation of image dipoles that are present in systems when a metal is close to the interface being excited. Image dipoles can be thought of as an imaginary dipole that exists within the metal with a size and direction that is dependent on the material's properties, i.e. absorption and refractive index [32]. In many cases the image dipole oscillates in the same direction as the induced dipole and actually acts to enhance the signal. However, in some cases, if the image dipole is equal and opposite of the induced dipole it can actually cancel out the dipole.

Figure 6.4.1 shows the a possible mode of formation of an image dipole on steel at the vicinity of SF10/steel interface when an induced electric dipole is present on the SF10 in the *xy*-plane due to the reflection of 532 nm laser at the interface.

For the induced dipole in the *xz*-plane as described in figure 6.4.1, the magnitude of electric field, **E** can be expressed by equation (6.4.1)

$$\mathbf{E} = \mu_0 \mathbf{H} \times \hat{\mathbf{n}} \qquad (6.4.1)$$

where μ_0 denotes the impedance in free space, $\mathbf{H}$ the magnitude of induced magnetic field and $\hat{\mathbf{n}}$ a unit vector in the direction of propagation of the electromagnetic radiation. The magnitude of the induced magnetic field, $\mathbf{H}$ can be further expressed by

$$\mathbf{H} = \frac{ck^2}{4\pi}(\mathbf{r} \times \mathbf{p})\frac{e^{i\mathbf{k}.\mathbf{r}}}{r} \qquad (6.4.2)$$

where c denotes the velocity of the electromagnetic wave, $\mathbf{k}$ the wavevector the radiation, $\mathbf{p}$ the induced polarisation, and $\mathbf{r}$ the distance vector from an arbitrary point, O, to the point where the electric field is being measured (bold notations have been used for vector quantities while regular italic notations have been used for scalar quantities e.g. $\mathbf{r}$ denotes distance vector while r denotes the scalar distance).

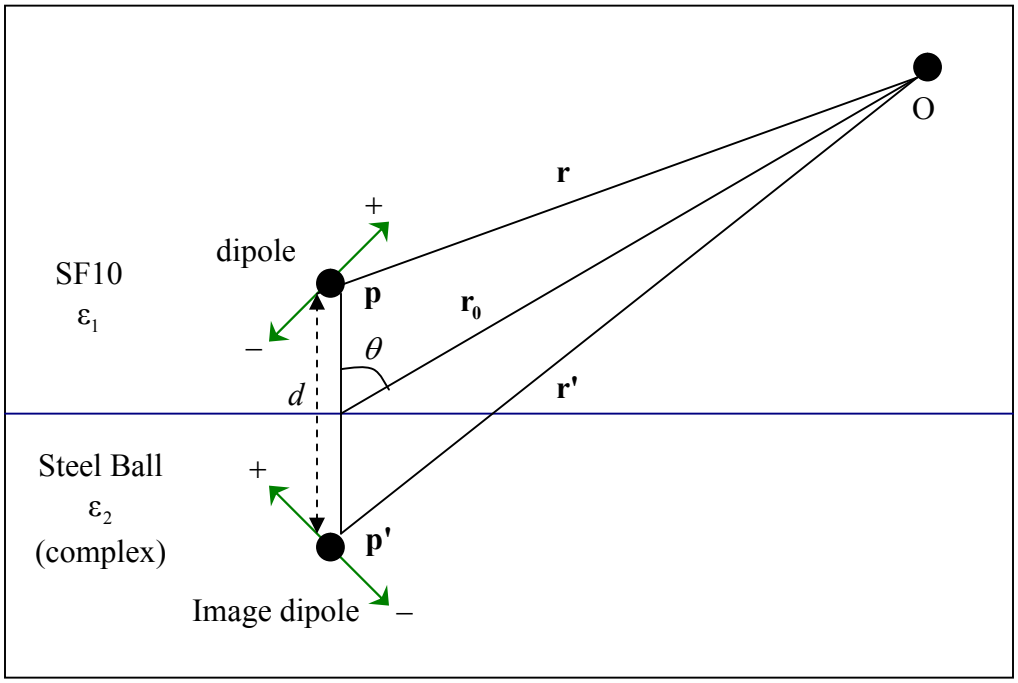

Figure 6.4.1: Figure showing the image dipole formation on steel near the SF10/steel interface due to an electric dipole induced in the *xz*-plane on SF10 due to reflection of a 532 nm wavelength laser beam.

Combining equation (6.4.1) and (6.4.2), we arrive at equation

$$\mathbf{E} = \frac{\mu_0 ck^2}{4\pi}\frac{e^{i\mathbf{k}.\mathbf{r}}}{r}(\mathbf{r} \times \mathbf{p}) \times \hat{\mathbf{n}} \qquad (6.4.3)$$

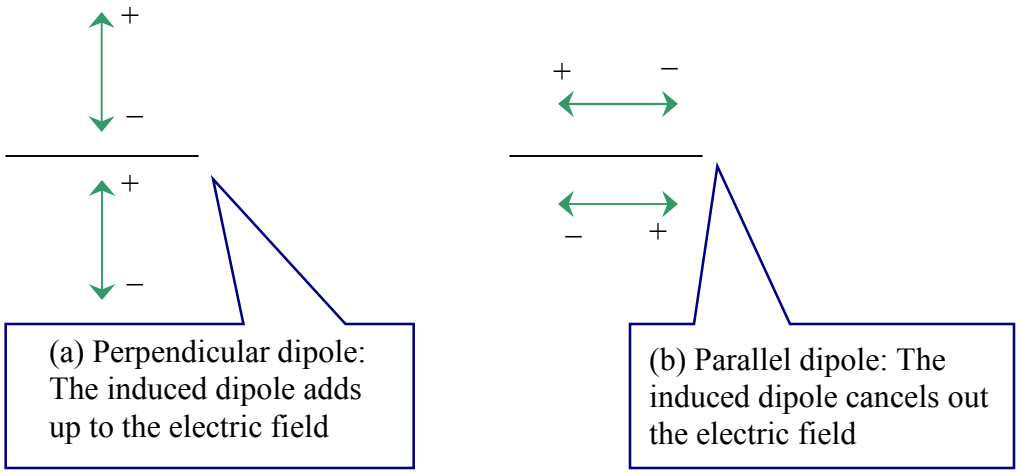

Figure 6.4.2: Orientations of the electric dipoles near the SF10/steel interface leading to differences in total electric field

The induced polarisation, $\mathbf{p'}$ of the image dipole formed on the steel surface can be expressed by

$$\mathbf{p'} = \beta\mathbf{p} \qquad (6.4.4)$$

for perpendicular dipole as shown in figure 6.4.2(a) and for parallel dipole as in figure 6.4.2(b), the induced polarisation, $\mathbf{p'}$ of the image dipole formed on the steel surface can be expressed by

$$\mathbf{p'} = -\beta\mathbf{p} \qquad (6.4.5)$$

where β is given by

$$\beta = \left(\frac{\varepsilon_2 - \varepsilon_1}{\varepsilon_2 + \varepsilon_1}\right) \qquad (6.4.6)$$

and the –ve sign is indicative of the opposite polarity being induced in the image dipole along the direction of the applied electric dipole. Here ε_1 and ε_2 are the dielectric constants or electric permittivities for SF10 and steel respectively. Combining equations (6.4.4) and (6.4.5) with equation (6.4.6), we arrive at equations

$$\mathbf{p'} = \left(\frac{\varepsilon_2 - \varepsilon_1}{\varepsilon_2 + \varepsilon_1}\right)\mathbf{p} \qquad (6.4.7)$$

and $$\mathbf{p'} = -\left(\frac{\varepsilon_2 - \varepsilon_1}{\varepsilon_2 + \varepsilon_1}\right)\mathbf{p} \qquad (6.4.8)$$

for perpendicular dipole and parallel dipole respectively.

The total electric field, $\mathbf{E_{total}}$ due to the combined effect of the induced dipole at the SF10 surface and image dipole at the steel surface, as measured from an arbitrary point, O can be expressed by equation (6.4.9)

$$\mathbf{E_{total}} = \frac{\mu_0 c k^2}{4\pi}\left[\mathbf{r}\times\mathbf{p}\frac{e^{i\mathbf{k}.\mathbf{r}}}{r} + \mathbf{r'}\times\mathbf{p'}\frac{e^{i\mathbf{k}.\mathbf{r'}}}{r'}\right]\times\hat{\mathbf{n}} \qquad (6.4.9)$$

As the induced dipole is formed on the SF10 surface just above the SF10/steel interface and the image dipole is formed just below the same interface, we can imagine the distance between the two dipoles, d to be very small compared to the wavelength of the laser beam and hence negligibly small compared to the distance, r_0 between the interface and the point of observation, particularly in case of far field optical microscopy.

$$d \ll \lambda \ll r_0 \qquad (6.4.10)$$

Additionally, in case of far field microscopy we can consider the distance vectors

$$\mathbf{r} \simeq \mathbf{r_0} \simeq \mathbf{r'} \qquad (6.4.11)$$

$$\text{hence } r \simeq r_0 \simeq r' \qquad (6.4.12)$$

Applying the approximations (6.4.10), (6.4.11), and (6.4.12) and combining the equations (6.4.4), (6.4.5), and (6.4.9) we arrive at equations

$$\mathbf{E_{total}} \simeq \frac{\mu_0 c k^2}{4\pi}\mathbf{r_0}\times\mathbf{p}\left[\frac{e^{i\mathbf{k}.\mathbf{r_0}}}{r_0}\right]\left[1+\beta\right]\times\hat{\mathbf{n}} \qquad (6.4.13)$$

and $$\mathbf{E_{total}} \simeq \frac{\mu_0 c k^2}{4\pi}\mathbf{r_0}\times\mathbf{p}\left[\frac{e^{i\mathbf{k}.\mathbf{r_0}}}{r_0}\right]\left[1-\beta\right]\times\hat{\mathbf{n}} \qquad (6.4.14)$$

for perpendicular and parallel dipoles respectively.

It is evident from equations (6.4.3), (6.4.13) and (6.4.14) that the total electric field at the SF10/steel interface gets modified by a factor of $\left[1+\beta\right]$ for perpendicular dipole and $\left[1-\beta\right]$ for parallel dipole due to the presence of image dipoles in the system. As the Raman scattering intensity varies as the square of the induced electric field, the Raman

scattering intensity in this case gets modified by a factor of $|1+\beta|^2$ and $|1-\beta|^2$ for perpendicular and parallel dipoles, respectively. ε_1 = 3.01 and ε_2 = $-5.12 + 20.16i$ can be calculated by squaring the refractive indices of SF10 and steel respectively. In case of S-polarised incident radiation, the electric dipole oscillates parallel to the interface, in which case a value of $|1-\beta|^2$ = 0.09 for SF10/steel interface corresponds to only 9 % of the dipole intensity being actually shown in the Raman spectra. On the other hand a similar parallel image dipole formation on an SF10/silica interface with dielectric constants ε_1 = 3.01 and ε_2 = 2.13 respectively corresponds to a value of $|1-\beta|^2$ = 1.37, which indicates that the Raman scattering intensity is further enhanced by 37% in comparison to the induced dipole intensity in the absence of the SF10/silica interface. In the case where the incident laser beam is P-polarised, the electric dipole oscillates at an angle equal to the angle of incidence of the laser radiation at the interface and has both perpendicular and parallel components. The parallel component behaves similar to the electric dipole of the S-polarised incident radiation and only 9% of the dipole component intensity is shown in the Raman spectra at SF10/steel interface. In case of the perpendicular component of the electric dipole originating from P-polarised radiation, however, a value of $|1+\beta|^2$ = 4.2 indicates ~4 times enhancement in the electric field. Hence for SF10/steel interface, at the working angle of incidence (60°) the Raman signal in the P-polarised spectra is expected to be much stronger than the S-polarised spectra provided the scattering due to the electric field dipole along the *z*-direction can be efficiently collected. On the other hand, for the perpendicular component of the electric field originating from P-polarised incident radiation at SF10/silica interface, a value of $|1+\beta|^2$ = 0.69 mean that the P-polarised spectra will be weaker than the S-polarised spectra at the same working angle of incidence (60°).

Reference:

1. Numatta, T., Nanao, H., Mori, S., and Miyake, S., Tribology International, 2003. **36**: p. 305.
2. Varlot, K., Martin, J.M., Grossiord, C., Vargiolu, R., Vacher, B., and Inoue, K., Tribology Letters, 1999. **6**: p. 181.
3. Ferrari, E.S., Roberte, K.J., Sansone, M., and Adams, D., Wear, 1999. **236**: p. 259.
4. Liang, H., Mongne, T.L., and Martin, J.M., Journal of Electronic Materials, 2002. **31**: p. 872.
5. Liang, H., Mongne, T.L., and Martin, J.M., Acta Materialia, 2003. **51**: p. 2639.
6. Cann, P.M., and Spikes, H.A., Tribology Transactions, 1989. **32**: p. 414.
7. Cann, P.M., and Spikes, H.A., Tribology Transactions, 1991. **34**: p. 248.
8. Hoglund, E., Wear, 1999. **232**: p. 176.
9. Hoshi, Y., Minami, I., and Mori, S., Journal of Japanese Society of Tribologists, 2004. **49**: p. 878.
10. King, V.W., and Lauer, J.L., Journal of Lubrication Technology , 1981. **103**: p. 65.
11. Lauer, J.L., and Peterkin, M.E., ASLE Transactions, 1978. **21**: p. 250.
12. Lauer, J.L., Mechanical Engineering (American Society of Mechanical Engineers), 1979. **101**: p. 95.
13. Lauer, J.L., and Ahu, Y.J., Tribology Transactions, 1988. **31**: p. 120.
14. Muratov, V.A., Olsen, J.E., Gallois, B.M., Fischer, T.E., and Bean, J.C., Journal of Electrochemical Society, 1998. **145**: p. 2465.
15. Olsen, J.E., Fischer, T.E., and Gallois, B., Wear, 1996. **200**: p. 233.
16. Piras, F.M., Rossi, A., and Spencer, N.D., Langmuir, 2002. **18**: p. 6606.
17. Rossi, A., Eglin, M., Piras, F.M., Matsumoto, K., and Spencer, N.D., Wear, 2004. **256**: p. 578.
18. Cheng, C., and Stair, P.C., Tribology Letters, 1998. **4**: p. 163.
19. Dvorak, S.D., Wahl, K.J., and Singer, I.L., Tribology Transactions, 2002. **45**: p. 354.

20. Hutchinson, E.J., Shu, D., Laplamt, F., and Benamotz, D., Applied Spectroscopy, 1995. **49**: p. 1275.
21. Jubault, I., Mansot, J.L., Vergne, P., and Mazuyer, D., Tribology Transactions, 2002. **124**: p. 114.
22. Scharf, T.W., and Singer, I.L., Tribology Letters, 2003. **14**: p. 3.
23. Sasaki, K., Inayoshi, N., and Tashiro, K., Review of Scientific Instruments, 2008. **79**: p. 123702.
24. Beattie, D., Haydock, S., and Bain, CD., Vibrational Spectroscopy, 2000. **24**(1): p. 109-123.
25. Beattie, D.A., Fraenkel, R., Winget, S.A., Peterson, A., & Bain, C.D., Journal of Physical Chemistry B, 2006. **110**: p. 2278-2292.
26. Beattie, D.A., Winget, S.A., and Bain, C.D., Tribology Letters, 2007. **27**: p. 159.
27. Haydock, S.A., in *D.Phil thesis, Oxford University*. 2002.
28. Bansal, R.K., *A Textbook of Fluid Mechanics* Paperback First ed. 2005: Laxmi Publisher.
29. http://www.sas.org/engineerByMaterial.html. [cited.
30. Johnson, K.L., *Contact Mechanics.* Cambridge University Press, 1985.
31. Heavens, O., and Ditchburn, R., *Insight into optics*. 1991: Wiley: Chichester.
32. Wu, C., Mei Ye, and Hunian Ye, Optik, 2005. **116**: p. 277-280.

7. Tribometer studies of fluid film and boundary lubrication

Throughout the developmental stage of the Raman tribometers described in chapter 6, TIR Raman spectra were acquired from the fluid lubricant poly Synton PAO 100 and LB monolayers of Zn arachidate using both tribometers A & B. The spectra were compared with the calculated Raman intensities for different film thicknesses at different applied pressures and rotation speeds of the ball to validate the accuracy and reproducibility of results for both the tribometer designs. Synton PAO 100 is a high viscosity poly-alpha olefin designed for use as a base oil in a wide range of engine and industrial oil lubricating applications. Langmuir-Blodgett monolayers of Zn arachidate, on the other hand, are good model boundary lubricants for dry-state lubrication as described in chapter 4 & 5.

7.1 Elastohydrodynamic lubrication studies with Raman tribometer

7.1.1 TIR Raman spectra from Synton PAO 100 at SF10/silica interface (Tribometer A)

The first set of TIR Raman spectra were acquired from the tribometer A equipped with dead weight loading (section 6.2.1), built in collaboration with Indian Institute of Science, Bangalore. TIR Raman spectra were obtained from PAO at the sliding SF10/silica interface. This section of the tribometer experiments were carried out together with Praveena Manimunda, a doctoral student from IISc Bangalore.

An 8 mm-diameter fused silica ball was rotated in contact with the flat surface of a 10 mm-diameter SF10 hemisphere. The oil tank in the tribometer was filled with Synton PAO 100 so that on rotation of the silica ball, the fluid PAO was entrained into the SF10/silica contact region. TIR Raman spectra were acquired from the lubricated contact region with 200 mW, S-polarised incident laser probe and with 2 minutes acquisition times at different loads and rotation speeds of silica ball. Figures 7.1.1, 7.1.2 and 7.1.3 are the TIR Raman spectra in the C-H stretching region with applied loads 0.5 N, 1.0 N and 2.0 N, respectively, which corresponded to maximum pressures of 198 MPa, 250 MPa and 315 MPa, respectively, at varied sliding speeds as labeled in the figures.

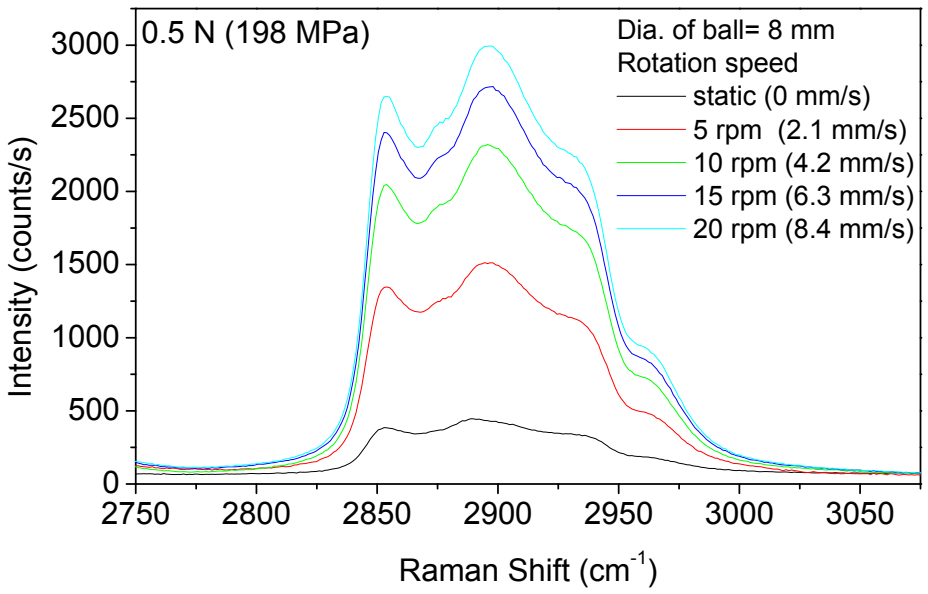

Figure 7.1.1: TIR Raman spectra from Synton PAO 100 at SF10/silica sliding interface using Raman tribometer A; S-pol., 200 mW, 120 s acquisition, θ_i = 60°, 0.5 N load (central pressure = 198 MPa)

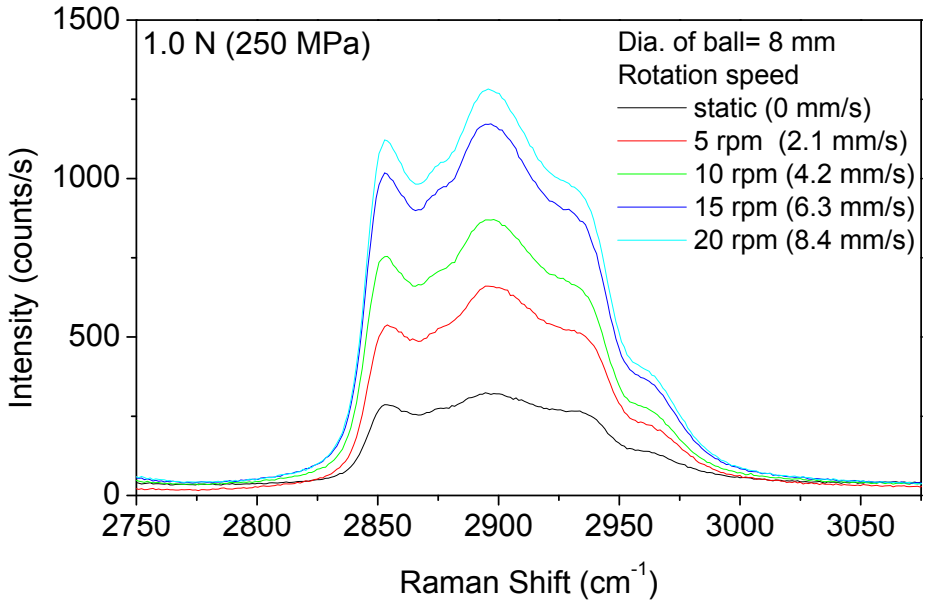

Figure 7.1.2: TIR Raman spectra from Synton PAO 100 at SF10/silica sliding interface using Raman tribometer A; S-pol., 200 mW, 120 s acquisition, θ_i = 60°, 1.0 N load (central pressure = 250 MPa)

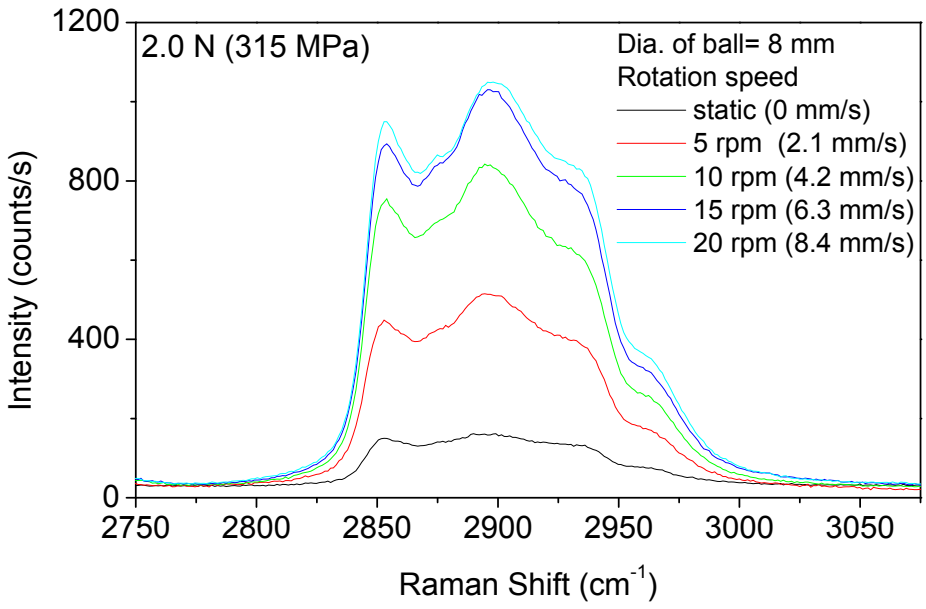

Figure 7.1.3: TIR Raman spectra from Synton PAO 100 at SF10/silica sliding interface using Raman tribometer A; S-pol., 200 mW, 120 s acquisition., θ_i = 60°, 2.0 N load (central pressure = 315 MPa)

The Raman spectral intensities at different applied loads are not directly comparable because with the dead weight loading mechanism in tribometer A, application of higher loads resulted in displacement of the SF10/silica contact area below the focal plane of the objective. Adjustments were made with the *z*-positioning of the *xyz*-micromotion stages to bring back the contact interface to the initial position below the objective. However, unlike the first set of experiments (0.5 N load) where the focusing and alignments were performed with dry contact surfaces, for the other two set of experiments (1.0 N & 2.0 N loads) the contact surfaces were already wet with the PAO (after initial set of rotation experiments when PAO was entrained into the sliding interface) which made the observation of Newton's rings and a contrasting focus very difficult. The full set of experiments was carried out at room temperature ~22° C. At this temperature, the viscosity of the Synton PAO 100 was measured to be 6.05 Pa-s by rheometer measurements (TA Instruments AR2000 rheometer with parallel plate geometry) carried out by Ms. Vicky Bird.

From relative Raman spectral intensities in the figures 7.1.1, 7.1.2 and 7.1.3, it was evident that for constant applied loads, higher speed of rotation of the ball entrained more fluid lubricant at the contact area thereby forming a thicker film. Conversely, for the same rotation speed of the ball, application of higher load squeezed out more lubricant from the contact region forming thinner films (although the absolute intensities for different loads are not directly comparable in the figures). Table 7.1.1 shows the calculated values of PAO film thicknesses at given applied loads and rotation speeds of the silica ball at the SF10/silica interface using the Reynold's equation discussed in section 6.3.1 in chapter 6.

Dia. of silica ball used = 8 mm; dead weight loading mechanism	0.5 N load	1.0 N load	2.0 N load
Static	0 nm	0 nm	0 nm
2.1 mm/s (5 rpm)	59 nm	56 nm	53 nm
4.2 mm/s (10 rpm)	95 nm	90 nm	85 nm
6.3 mm/s (15 rpm)	125 nm	119 nm	113 nm
8.4 mm/s (20 rpm)	152 nm	144 nm	137 nm

Table 7.1.1: Table showing theoretical calculations of PAO film thickness under different load and sliding speeds

According to the Reynold's equation calculations under static contacts lubricated with fluid lubricant, e.g. PAO in this case, all the lubricant should squeeze out of the contact area to yield Raman spectral intensity close to zero. In our experiments, however we found that even on arrest of the rotating ball, TIR Raman spectra from the SF10/silica interface produced signals which corresponded to film of PAO a few molecules thick (apparently ~2 nm thick from figure 7.1.7). The Raman intensity from the PAO film reduced on application of higher loads under similar static contacts which meant that the PAO film further squeezed out of the SF10/silica contact. This Raman signal from the PAO at static contact interface might have originated from a uniform film or liquid trapped in defects of the optical surfaces.

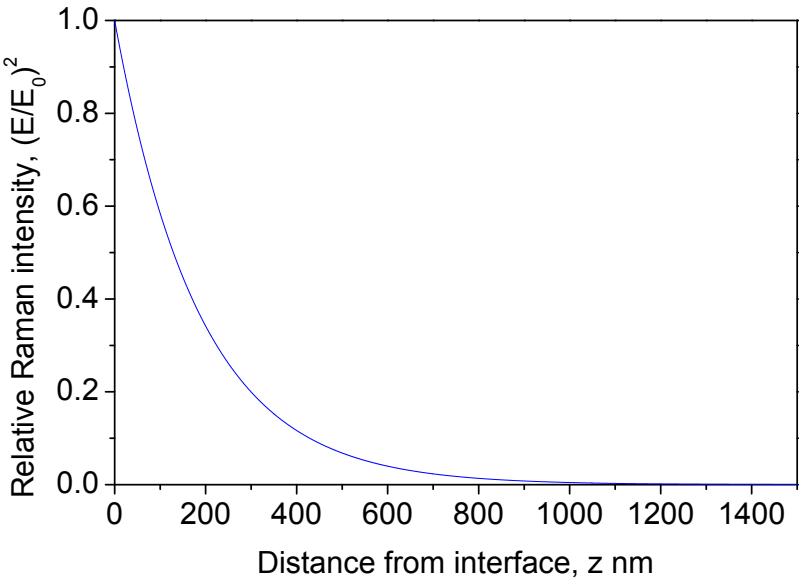

Figure 7.1.4: Plot of calculated relative Raman intensity at a point z nm from the interface with respect to the Raman intensity at the interface, z = 0 nm at the point of laser probing; 532 nm laser, θ_i = 60°.

As described in section 2.2.1 in chapter 2, the Raman intensity decays exponentially away from the interface. Figure 7.1.4 shows the decay of the relative Raman intensity with increasing distance in the silica medium from the SF10/silica interface when the interface is probed by a 532 nm laser at a TIR geometry with angle of incidence, θ_i=60°. At 60° angle of incidence, the penetration depth of the evanescent wave generated by the 532 nm laser at SF10/PAO interface is 234 nm (fig. 6.2.4), which is greater than the maximum thickness of the PAO films calculated by the Reynold's equation for our experimental parameters i.e. 152 nm for a load of 0.5 N and a rotation speed of 20 rpm. Therefore the full thickness of the PAO film in our experiments came under the coverage of the generated evanescent wave and contributed to the Raman signal.

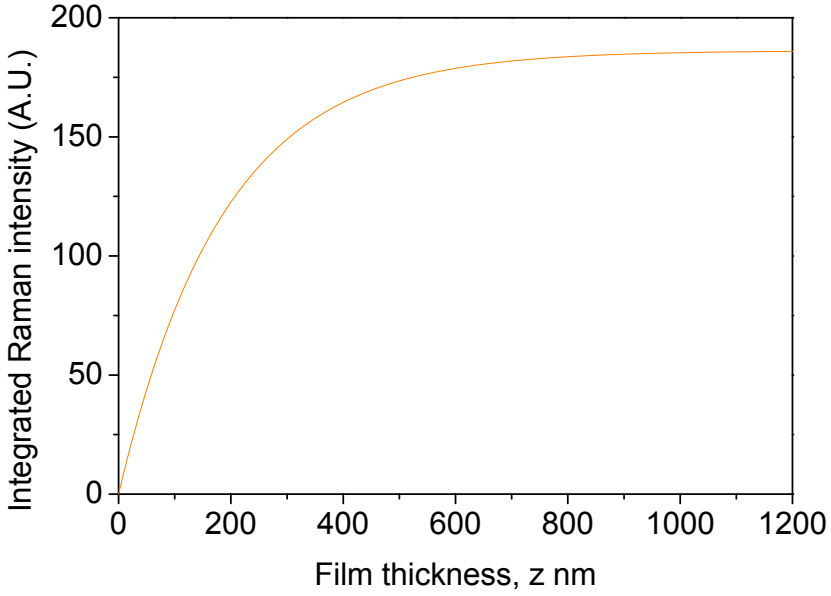

Figure 7.1.5: Plot of calculated integrated Raman intensity from a film z nm thick.

The integrated Raman intensity from a lubricant film of thickness z nm can be calculated and is given by the equation 7.1.1

$$\int_0^z \left(\frac{E}{E_0}\right)^2 dz = \int_0^z \exp(-2\beta z)dz = \frac{1-\exp(-2\beta z)}{2\beta} \qquad (7.1.1)$$

where,
$$\beta = \frac{2\pi n_{ti}}{\lambda}\left(\frac{\sin^2\theta_i}{n_{ti}^2} - 1\right)^{\frac{1}{2}} \qquad (7.1.2)$$

β is the electric field amplitude decay coefficient, θ_i is the angle of incidence, λ is the wavelength of incident light and E_0 is the electric field at z = 0, n_{ti} is the refractive index for the pair of media concerned. Refractive index, *n* for PAO is 1.466 which is very close to the refractive index, *n* for fused silica 1.461 and were approximated to be the same at the SF10/PAO/silica interface, otherwise a much more complicated equation would be required. A plot of the integrated Raman intensity with increasing thickness of the lubricant film is shown in figure 7.1.5. In figure 7.1.6 the spectral intensities for different PAO film thicknesses obtained with the Raman tribometer A at different applied loads

and varied rotation speeds of the ball were plotted against PAO film thicknesses and a good match was obtained with the calculated Raman intensity plot.

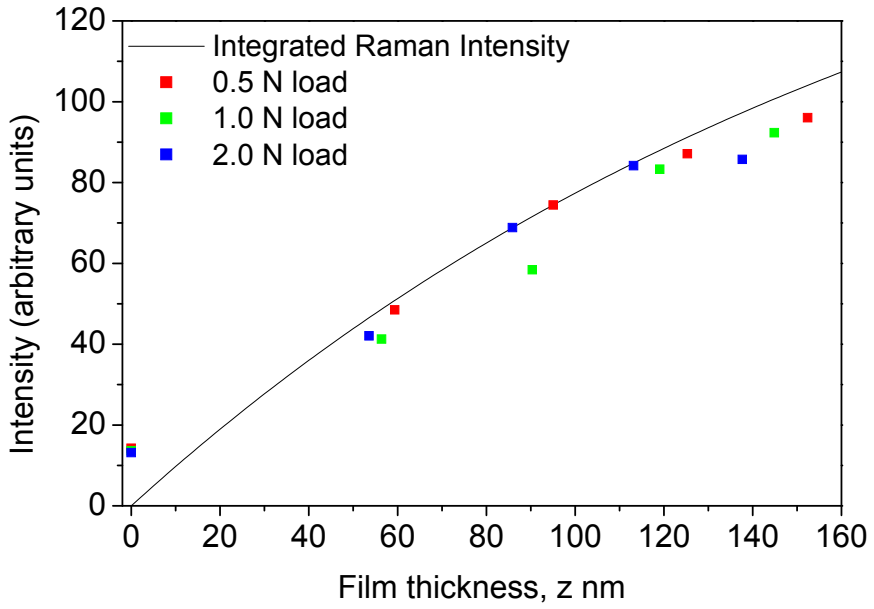

Figure 7.1.6: Plot showing the calculated integrated Raman intensity from a film z nm thick in comparison with the experimentally obtained relative Raman spectral intensities from different PAO film thicknesses at different loads and sliding speeds.

It may be noted here that in figure 7.1.6, that different scaling factors were used for the Raman spectral data sets obtained with different applied loads to account for the intensity variations due to defocusing of the sliding interface on application of higher loads as explained before. The spectral data sets obtained with 0.5 N and 2.0 N loads were scaled such that the film thickness of PAO that corresponded to a rotation speed of 10 rpm (sliding speed = 4.2 mm/s), which was the mean speed of the obtained data sets, yielded a spectral intensity that matched the theoretically calculated integrated Raman intensity plot in figure 7.1.5. These scaling factors resulted in scaled intensities of 14.2 and 13.1 for static contacts (sliding speed = 0 mm/s) with applied loads of 0.5 N and 2.0 N, respectively. The same scaling pattern to fit the experimentally obtained Raman intensity with the theoretically calculated integrated Raman intensity for the PAO film thickness corresponding to the mean rotation speed, 10 rpm and 1.0 N applied load would result in

a scaled intensity at static contact (sliding speed = 0 mm/s) higher than the scaled intensities for the same speed of rotation at 0.5 N and 2.0 N applied loads, which does not make any scientific sense. Hence the spectral data set at 1.0 N applied load were scaled such that the scaled intensity for static contact with 1.0 N applied load lies between the scaled intensities for the static contact with 0.5 N and 2.0 N applied loads. Therefore the spectral intensity at static contact with 1.0 N load was scaled to 13.6 and the spectral intensities with the other sliding speeds with the same applied load were scaled accordingly with the same scaling factor.

To study the mechanism of tribofilm functioning at boundary lubrication regime i.e. at higher pressure and lower shear rate, the SF10 hemisphere was deposited with a monolayer of deuterated zinc arachidate by Langmuir-Blodgett deposition technique described in section 4.2.2 of chapter 4 at a deposition pressure of 35 mN/m. The silica ball in the tribometer was allowed to rotate in sliding contact with the coated hemisphere, entraining PAO from the lubricant tank as usual. TIR Raman spectra were obtained from static contact at SF10/silica interface at an applied load of 0.5 N (198 MPa), both before the PAO was entrained in the contact region i.e. with deuterated zinc arachidate monolayer at SF10/silica interface, and after the PAO was entrained at the contact area at the same SF10/silica interface. The spectra were acquired for 2 minutes with 200 mW S-polarised 532 nm incident laser (figure 7.1.7).

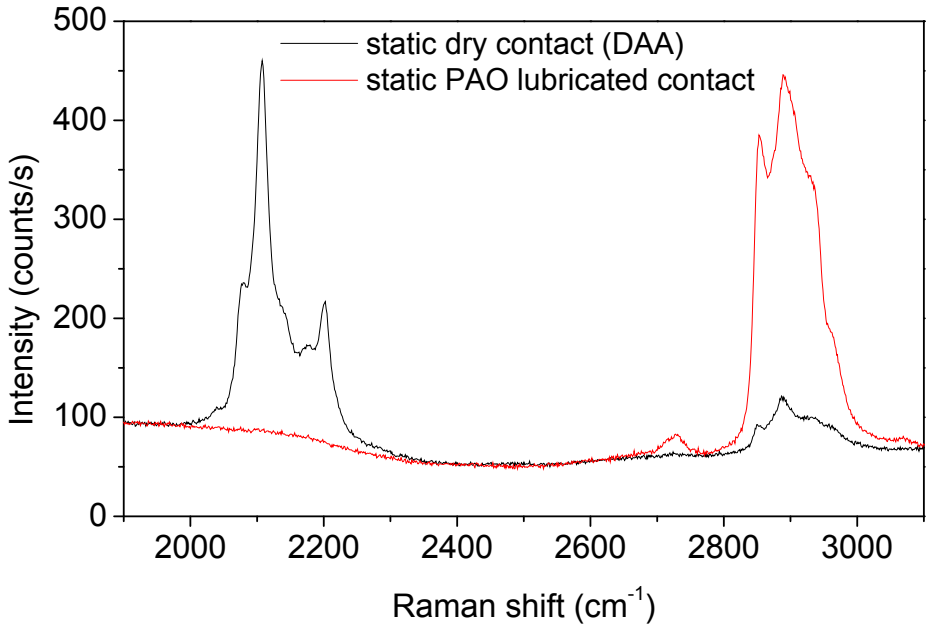

Figure 7.1.7: TIR Raman spectra from LB monolayer of deuterated arachidic acid deposited SF10 hemisphere in static contact with a 8-mm dia. silica ball before and after lubrication of the contact area with Synton PAO 100; S-pol., 200 mW, 120 s acquisition, θ_i = 60°, 0.5 N load.

At static dry contact (i.e. before the PAO was entrained in the SF10/silica contact) the spectral intensity at the 2100 cm^{-1} region corresponded to the C-D stretching vibrations in the deuterated zinc arachidate monolayer and the bands around 2900 cm^{-1} region were from the C-H stretching vibrations in the LB monolayer from the nominal impurities in the deuterated arachidic acid together with Raman bands from the atmospheric contamination on the SF10 hemisphere. After the silica ball was rotated for a 1 minute with PAO entraining in the SF10/silica contact area, the rotation was stopped and the post-rotation spectra at static lubricated contact showed no C-D stretching bands at 2100 cm^{-1} region, which meant that the monolayer was completely removed by the fluid lubricant PAO. The C-H stretching bands at 2900 cm^{-1} in the post-rotation spectra was intensified due to the presence film of PAO a few molecules thick that still existed at the SF10/silica interface at the applied load 0.5 N. Comparing the C-D stretching spectral intensity from deuterated zinc arachidate and C-H stretching spectral intensity from PAO in figure 7.1.7 suggests the thickness of the PAO film at static contact to be ~2 nm, yet

the Raman spectral intensity in the C-H stretching region of the PAO film was similar to a ~13 nm-thick (as scaled in figure 7.1.6) film of PAO in figure 7.1.1. This inconsistency is due to the fact that the scaling operation was performed on the spectral data in figure 7.1.1, 7.1.2, and 7.1.3 to fit the theoretically integrated Raman intensity with the experimentally obtained Raman signal from the film thickness corresponding to the mid-rotation speed (10 rpm) with different applied loads as described before. The objective of the scaling was to compare the relative increment of the Raman intensity with increasing film thickness of PAO under increasing shear rates at different applied loads and therefore the film thickness ~13–14 nm under static contacts with different loads, as apparent from figure 7.1.6 is not an absolute value.

7.1.2 TIR Raman spectra from Synton PAO 100 containing deuterated arachidic acid at SF10/silica sliding interface (Tribometer B)

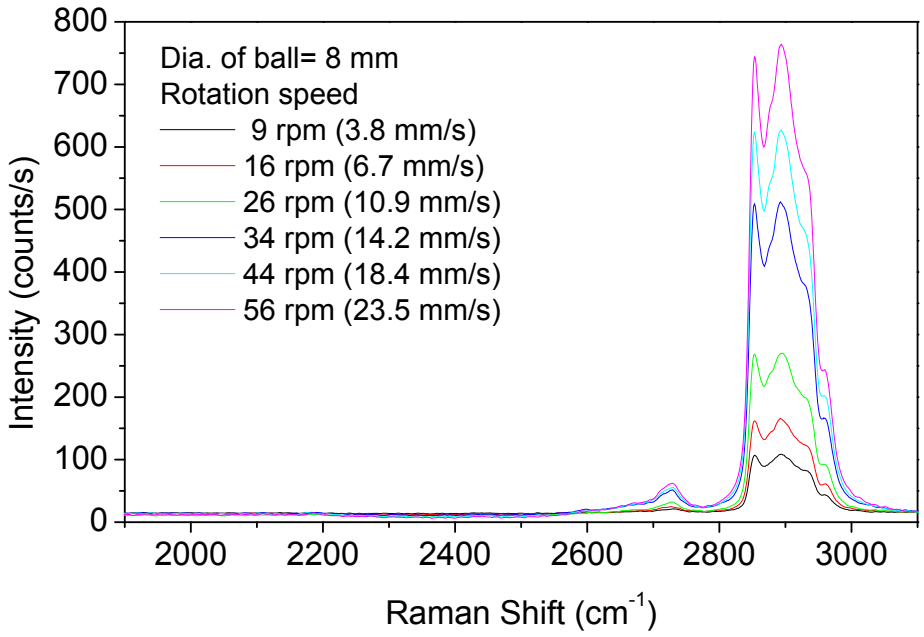

Figure 7.1.8: TIR Raman spectra from Synton PAO 100 containing deuterated arachidic acid at SF10/silica sliding interface using Raman tribometer B; S-pol., 200 mW, 30 s acquisition, θ_i = 60°, ~360 MPa pressure; rotation speeds and sliding rates shown in the figure.

Raman tribometer B, developed at Durham University, was used to study if there was any natural tribofilm formation at the solid-solid interface in the boundary regime i.e. at higher loads and lower sliding speeds (however, we could not really reach the boundary regime under sliding contacts with PAO due to high viscosity). The lubricant in the oil tank of the tribometer contained ~0.1 % by weight of deuterated arachidic acid in Synton PAO 100 (specific gravity = 0.86 at 22 °C). The lubricant mixture was prepared by adding 5 mg of deuterated arachidic acid in ~6 ml Synton PAO 100 and mixing it by a magnetic stirrer at 70 °C for 30 minutes and allowing to cool down to the room temperature 22 °C. The rotating silica ball (dia. 8 mm) entrained the lubricant mixture at the SF10/silica contact region pressed at ~360 MPa (determined by estimation of the central dark spot of the Newton's rings and using the Hertz equation described in chapter 2) and TIR Raman spectra were acquired using S-polarised incident laser beam of 200 mW power with acquisition time of 30 seconds (figure 7.1.8).

As shown in figure 7.1.8, with reduction in rotation speed of the silica ball from 56 rpm to 9 rpm, the thickness of the lubricant mixture film reduced and the spectral intensity at 2900 cm^{-1} dropped to lower counts per second. However, even with lower rotation/sliding speeds (PAO film thickness ~78 nm at 360 MPa pressure/ 3N load and 9 rpm/ 3.8 mm/s sliding speed) there was no indication of any tribofilm formation as no Raman signal was obtained from the 2100 cm^{-1} region corresponding to the C-D stretching vibrations from the deuterated arachidic acid molecules. Reaching lower rotation speeds were not possible as the rotation of the ball was totally arrested at lower voltages of the DC motor at the given load.

7.1.3 TIR Raman spectra from Synton PAO 100 at SF10/steel sliding interface (Tribometer B)

The silica ball in the Raman tribometer B was replaced with a 8 mm-diameter steel ball and the lubricant tank was filled up with Synton PAO 100 to study the elasto-hydrodynamic lubrication regime at SF10/steel interface. As the design of the Raman tribometers were aimed at, the rotating steel ball entrained the fluid PAO at the SF10/steel interface pressed at 560 MPa pressure by spring loading mechanism and TIR

Raman spectra were acquired from the sliding contact area with 200 mW power, 532 nm, S-polarised (figure 7.1.9) and P-polarised (figure 7.1.10) incident laser beam with acquisition times of 30 seconds. The acquisition times of the Raman spectra were shortened to obtain maximum possible data points at different rotation speed of the steel ball before the SF10 hemisphere became scratched; as a result the quality of the spectra was compromised. As faster rotation of the steel ball was expected to entrain a thicker film of lubricant, and therefore higher protection against damage of optics, the set of experiments was initiated at a higher rotation speed of the steel ball and then gradually the speed of rotation was reduced.

Figures 7.1.9 and 7.1.10 show that with both S- and P-polarised incident laser beam, the spectral intensity of the TIR Raman signal at the C-H stretching region decreased with reducing rotation speed of the steel ball. This indicated a reduction in PAO film thickness at the sliding contact with reduction in sliding speeds.

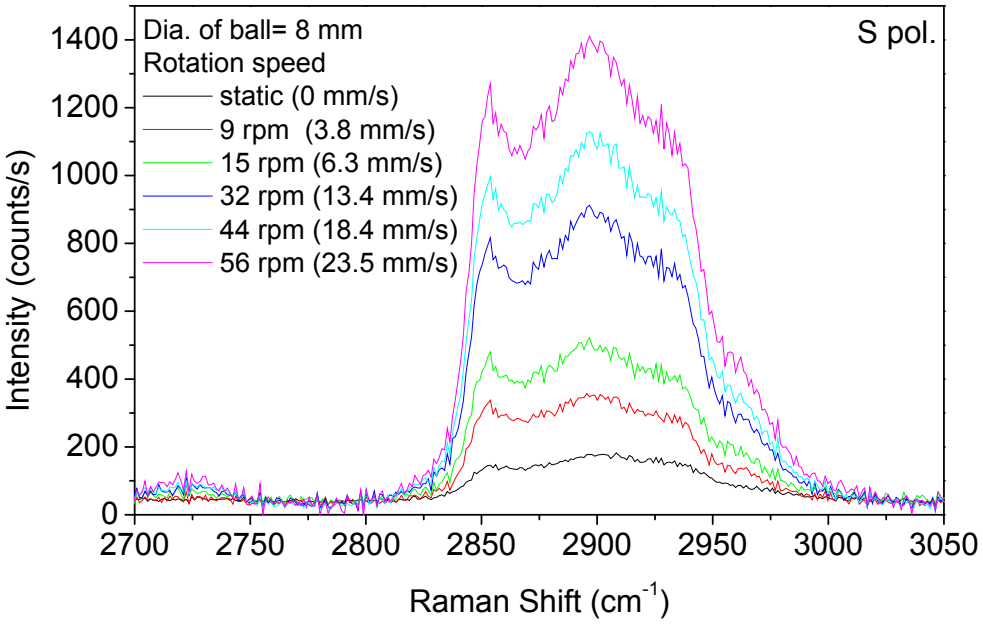

Figure 7.1.9: TIR Raman spectra from Synton PAO 100 at SF10/steel sliding interface using Raman tribometer B; S-pol., 200 mW, 30 s acquisition, θ_i = 60°, central pressure = 560 MPa.

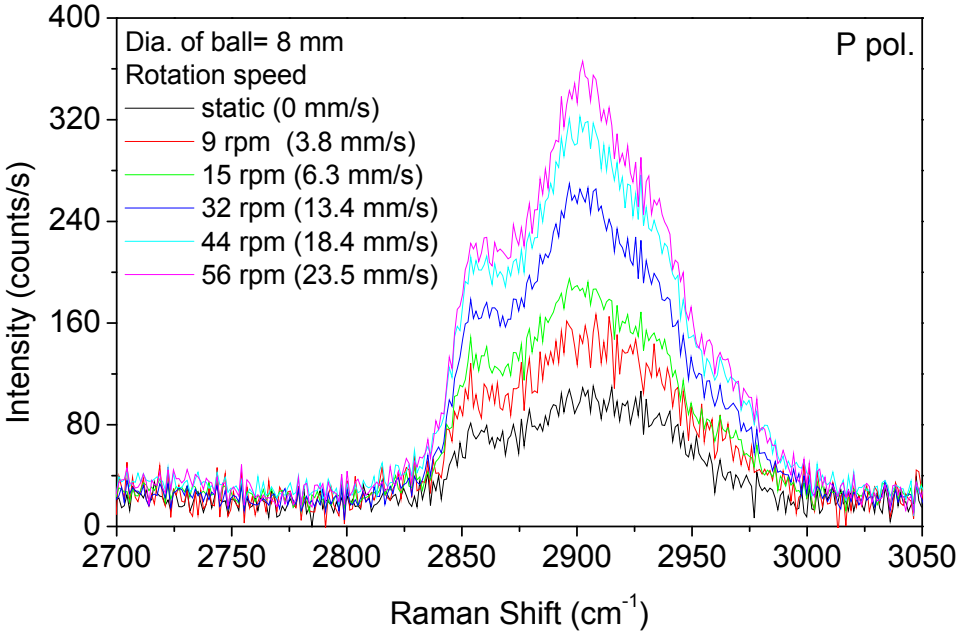

Figure 7.1.10: TIR Raman spectra from Synton PAO 100 at SF10/steel sliding interface using Raman tribometer B; P-pol., 200 mW, 30 s acquisition, θ_i = 60°, central pressure = 560 MPa.

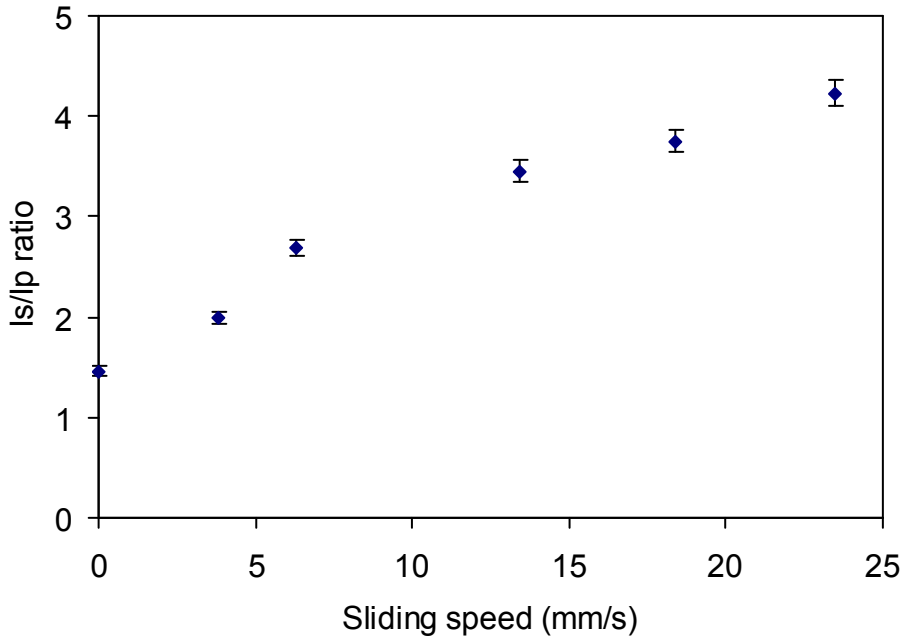

Figure 7.1.11: Plot of Is/Ip ratio in Synton PAO 100 film against increasing rotation speed of the ball/ increased sliding speed at fixed central pressure 560 MPa.

However, a closer look at the Raman spectral intensities at the C-H stretching region in figures 7.1.9 and 7.1.10 suggested that the ratio of the spectral intensity with S-polarised laser radiation to the spectral intensity with P-polarised laser radiation gradually reduced with lower rotation speeds of the steel ball i.e. lower sliding speeds as shown in figure 7.1.11. At 560 MPa pressure at SF10/steel interface, 56 rpm rotation speed of the steel ball entrained a 253 nm-thick PAO film at the interface which reduced to a 73 nm-thick PAO film at 9 rpm rotation speed of the steel ball according to the Reynold's equation (section 6.3.1). At 60° angle of incidence, the penetration depth of the evanescent wave generated by the 532 nm laser at SF10/PAO interface is 234 nm. Therefore for higher speeds of rotation of the steel and for thicker films of PAO at the SF10/silica interface, the electric field at the SF10/PAO interface behaves similar to the SF10/silica interface (refractive index, *n* for PAO is 1.466 which is very close to the refractive index, *n* for fused silica 1.461). However, as the thickness of the PAO film gets reduced with lower rotation speed of the steel ball, the electric field at the SF10/PAO interface starts behaving in a complex manner as the image dipole considerations at SF10/steel interface or dielectric/metal interface come into action (section 6.4 in chapter 6). The plot of the Fresnel coefficients against the angle of incidences in figure 6.3.5 in chapter 6 shows that at 60° angle of incidence, the electric field generated at the SF10/steel interface is much stronger for the P-polarised incident radiation compared to the S-polarised incident radiation. Therefore, as the thickness of the PAO film reduced, the spectral intensity from the P-polarised incident laser pump became relatively stronger compared to the spectral intensity obtained with S-polarised incident laser pump (fig. 7.1.11). Therefore, estimation of the lubricant film thickness on the basis of S- and P-polarised spectral intensities at the SF10/steel interface was not straight-forward.

7.2 Boundary lubrication studies with Raman tribometer (Triobometer A)

Dry boundary lubrication studies under applied pressure and shear were carried out with the Bangalore-built tribometer A equipped with dead weight loading. Langmuir-Blodgett monolayers of zinc arachidate were deposited on an SF10 hemisphere (dia. = 10 mm) and

a fused silica sphere (dia. = 8 mm) glued to a shaft beforehand. The LB deposition was carried out at 35 mN/m surface pressure following the procedures described in section 4.2.2 in chapter 4. The lubricant tank of the tribometer was kept dry to allow dry sliding contact at the SF10/silica interface with the zinc arachidate molecules acting as a model boundary lubricant. The laser beam was focused at the sliding contact area at 60° angle of incidence, and TIR Raman spectra were obtained from the sliding contact area with applied load 0.5 N (198 MPa pressure) at rotation speeds of the silica ball 5 rpm and 10 rpm with S-polarised (figure 7.2.1) and P-polarised (figure 7.2.2) laser pump of power 200 mW and with acquisition times of 150 seconds.

Figures 7.2.1 and 7.2.2 show that both in S-unpolarised spectra and P-unpolarised spectra, the spectral intensity in the C-H stretching region around 2900 cm^{-1} reduced with higher rotation speeds which indicated an erosion of the zinc arachidate monolayer material from the sliding contact region. However, the lower intensity at 5 rpm with both S-unpolarised spectra and P-unpolarised spectra as compared to the spectra obtained from static contacts was more due to the ball run-out (+/– 12 μm) rather than the loss of fatty acid material at the contact. The d^-/d^+ ratio in the S-unpolarised spectra did not change significantly with increasing sliding speeds (d^-/d^+ ratio ~1.66 for static contact; d^-/d^+ ratio ~1.7 at 10 rpm rotation speed of silica ball), indicating no deterioration in the chain packing [1] despite the removal of material from the sliding contact.

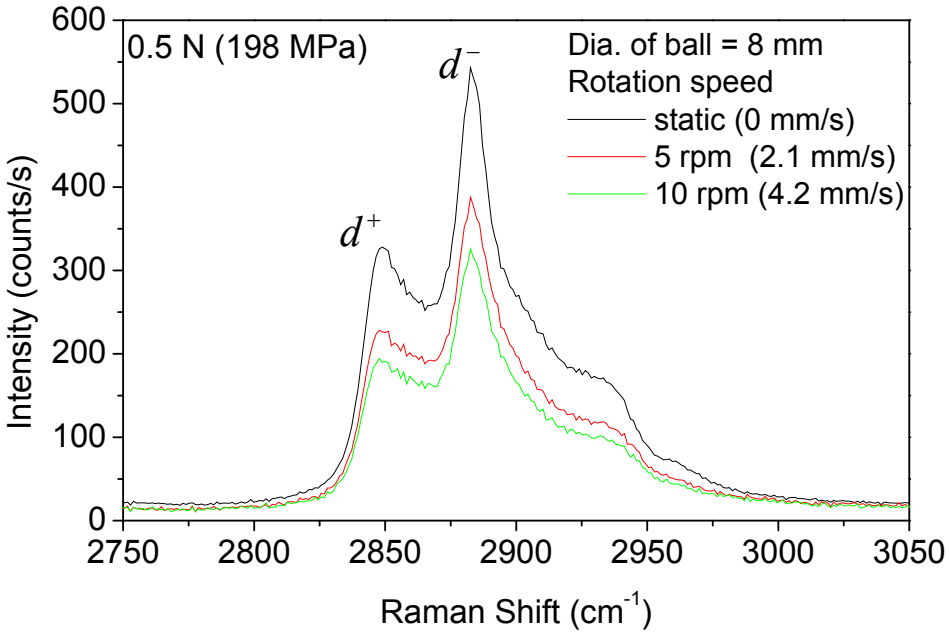

Figure 7.2.1: TIR Raman spectra from Zn arachidate LB monolayers at SF10/silica sliding interface using Raman tribometer A; S-polarised laser, 200 mW, 150 s acquisition, θ_i = 60°, 0.5 N load.

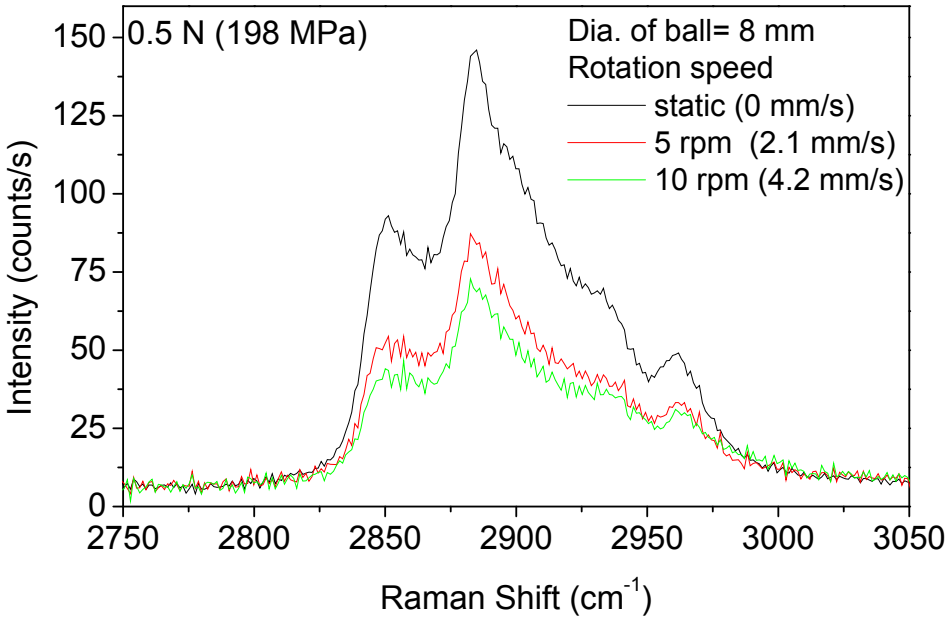

Figure 7.2.2: TIR Raman spectra from Zn arachidate LB monolayers at SF10/silica sliding interface using Raman tribometer A; P-polarised laser, 200 mW, 150 s acquisition, θ_i = 60°, 0.5 N load.

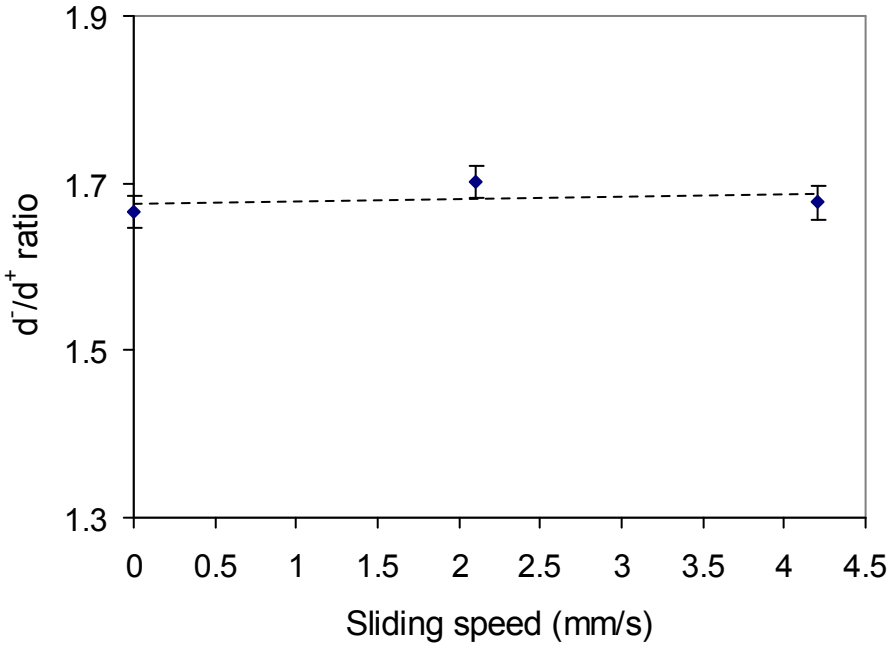

Figure 7.2.3: Plot of d^-/d^+ ratio in Zn arachidate monolayers at SF10/silica interface against increasing sliding speed of the silica ball at fixed load 0.5 N. This indicated that the packing or orderliness in the Zn arachidate monolayers are not significantly affected by variation in sliding speeds, however the monolayers were found to erode away with time.

Figure 7.2.3 shows a plot of the d^-/d^+ ratio against increasing sliding speeds from TIR Raman spectra of zinc arachidate monolayers at SF10/silica interface.

A set of four polarisation-resolved spectra were also acquired using S- and P-polarised incident laser radiation of 200 mW power and collecting the scattered radiation in two mutually perpendicular directions *x* and *y* along the plane of the sliding contact in the above setup from zinc arachidate molecules. Figures 7.2.4, 7.2.5, 7.2.6 and 7.2.7 show the Sx, Sy, Px and Py polarised spectra respectively. All the spectra were acquired with acquisition time of 150 seconds.

In all the polarization-resolved spectra Sx, Sy, Px and Py, the Raman spectral intensities were found to decrease in sliding contact compared to static contact and that the intensity further decreased on increasing the rotation/sliding speeds. The Px polarised spectra and Py polarised spectra under static contact and even at 5 rpm rotation speed of the silica

ball were identical to each other, which indicated that the molecular layer continued to be isotropic at a lower sliding speed. As the Px and Py spectra started to be noisy in the 10 rpm rotation speed of the silica ball (the spectra in fig. 7.2.6 & fig. 7.2.7 were background-subtracted and the increased noise originated form increased background at 10 rpm), most probably due to the onset of scratching of the optics surfaces, not much could be concluded from the spectra. However, apparently with higher rotation/sliding speeds the anisotropicity crept in the zinc arachidate monolayer as the Px and Py spectra started to look different (besides, in the Px spectra the spectral intensity at 10 rpm is lower than that of 5 rpm, while in the Py spectra the spectral intensity at 10 rpm is similar to that of 5 rpm). This is because close to the critical angle, in the Px and Py spectra, the signal obtained is due to the Raman tensor element $\langle \alpha'_{xz} \rangle$ and $\langle \alpha'_{yz} \rangle$, respectively, and in-plane isotropicity leads to $\langle \alpha'_{xz} \rangle = \langle \alpha'_{yz} \rangle$. Therefore an in-plane isotropic monolayer of zinc arachidate would produce similar Raman spectra in Px and Py polarisations (close to the critical angle of incidence) and conversely an in-plane anisotropic alignment would lead to dissimilar spectra in Px and Py polarisations.

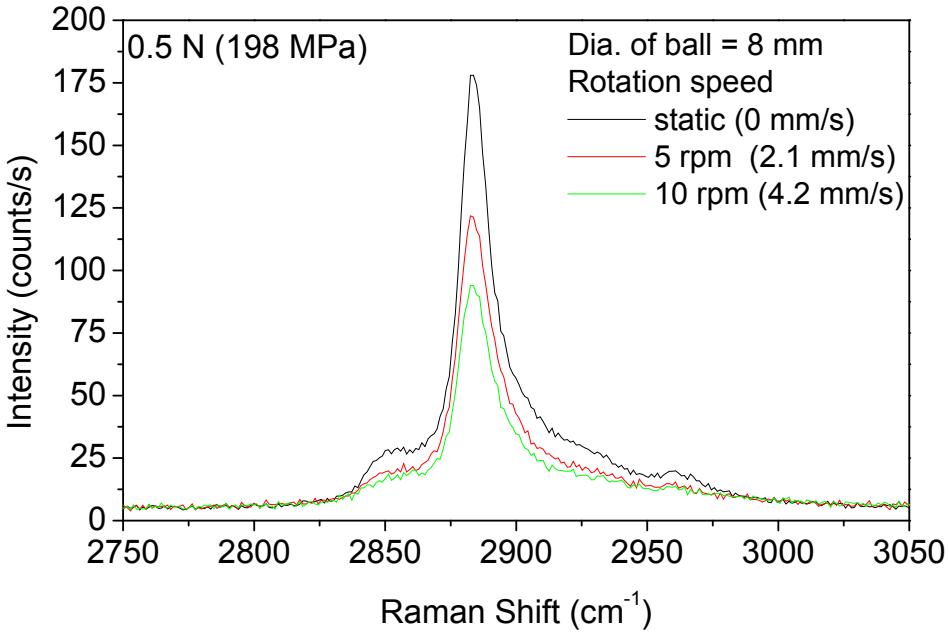

Figure 7.2.4: Sx pol. TIR Raman spectra from Zn arachidate LB monolayers at SF10/silica sliding interface using Raman tribometer A; 200 mW, 150 s acquisition, θ_i = 60°, 0.5 N load (198 MPa).

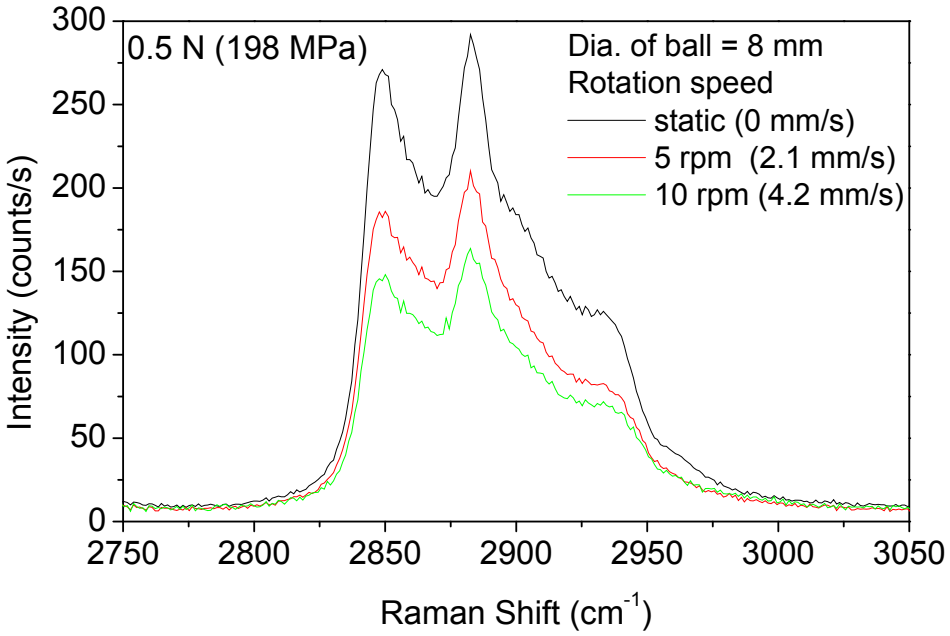

Figure 7.2.5: Sy pol. TIR Raman spectra from Zn arachidate LB monolayers at SF10/silica sliding interface using Raman tribometer A; 200 mW, 150 s acquisition, θ_i = 60°, 0.5 N load (198 MPa).

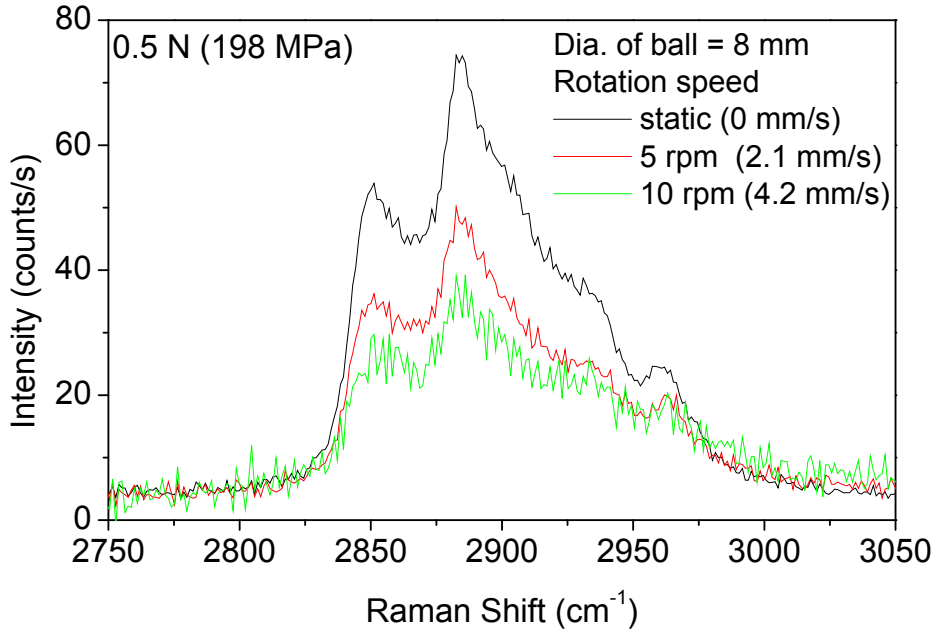

Figure 7.2.6: Px pol. TIR Raman spectra from Zn arachidate LB monolayers at SF10/silica sliding interface using Raman tribometer A; 200 mW, 150 s acquisition, θ_i = 60°, 0.5 N load (198 MPa).

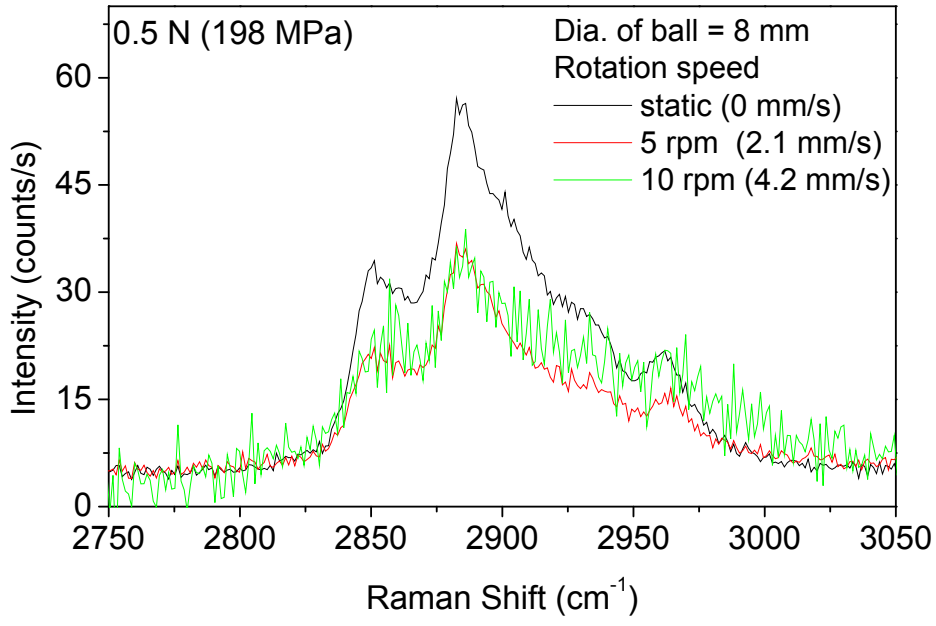

Figure 7.2.7: Py pol. TIR Raman spectra from Zn arachidate LB monolayers at SF10/silica sliding interface using Raman tribometer A; 200 mW, 150 s acquisition, θ_i = 60°, 0.5 N load (198 MPa).

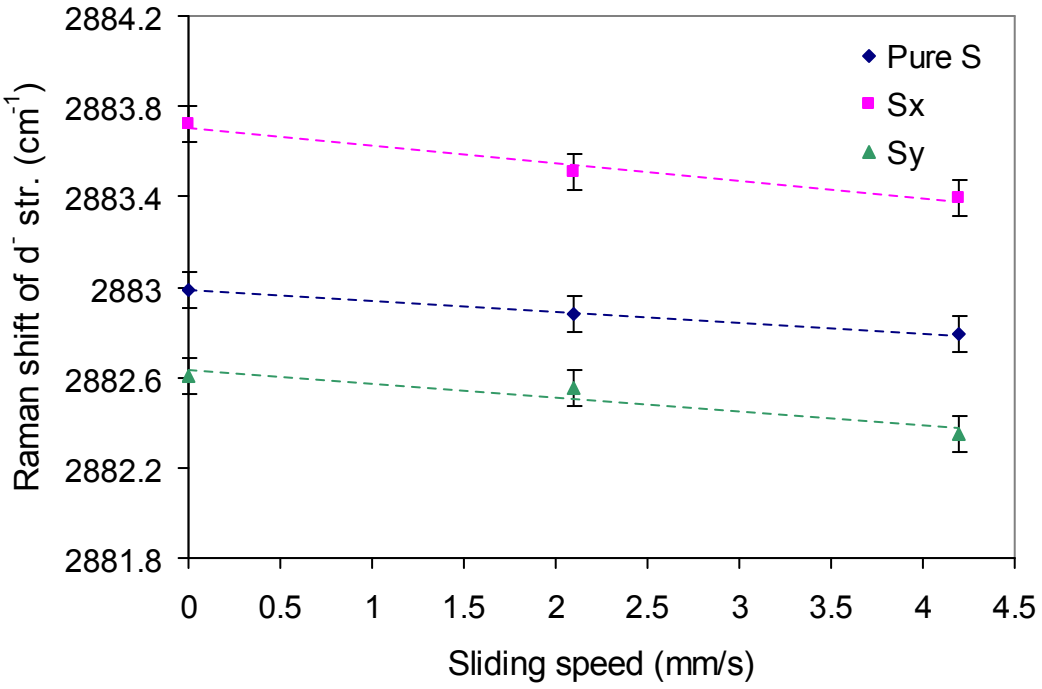

Figure 7.2.8: Plot showing red shift in the d^- and d^+ peaks in Raman spectra from Zn arachidate monolayers with higher rotation/sliding speeds (obtained from curve fitted data in S-unpolarised spectra). Average slope = - 0.062 (+/– 0.001) corresponding to ~ 0.1 cm^{-1} red shift per 1.6 mm/s increase in sliding speed.

The S-unpolarised spectra (fig. 7.2.1), Sx spectra (fig. 7.2.4) and Sy spectra (fig. 7.2.5) were curve fitted using the parameters described in section 5.3 of chapter 5, and the Raman shifts of the d^- stretching in all the spectra were plotted against increasing sliding speeds at the SF10/silica interface loaded with 0.5 N (198 MPa pressure). The plot showed an insignificant red shift in the d^- stretching frequencies for all the S-unpolarised, Sx and Sy spectra (figure 7.2.8). An average slope of - 0.062 corresponded to ~ 0.1 cm^{-1} red shift in the d^- stretching for every 1.6 mm/s increase in sliding speed. This indicated that the zinc arachidate molecular layer at the sliding interface did not have any significant effect (tended to get more ordered marginally) with increasing sliding speeds and this matched the conclusion obtained from the d^-/d^+ ratio plot in figure 7.2.3.

A plot of the ratio of spectral intensities in the S- and P-polarised spectra (including Sx.Px and Sy/Py) in figure 7.2.9 suggested that the rotation/sliding speed of the silica ball

did not have any marked effect in the alkyl chain tilts of the zinc arachidate molecular layer as the intensity ratio of the S-polarised spectra to the P-polarised spectra remained about the same for the range of sliding speeds studied at the given central pressure 198 MPa.

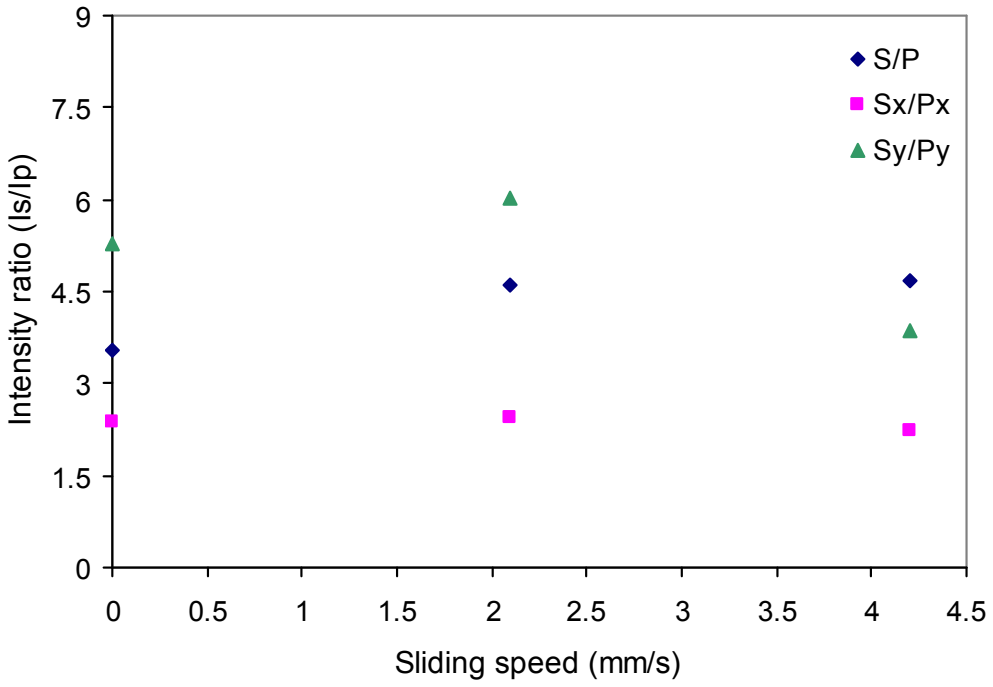

Figure 7.2.9: Plot of Is/Ip ratio in Zn arachidate monolayers against increasing rotation speed of the ball/ increased sliding speed at fixed load 0.5 N. This indicated that the alkyl chain tilts are not significantly affected by variation in sliding speeds.

7.3 Discussion

TIR Raman experiments were carried out with tribomters A & B with Synton PAO 100 at the SF10/silica (section 7.1.1) and SF10/steel (section 7.1.2) sliding interfaces with an objective to study the hydrodynamic/elasto-hydrodynamic regime of lubrication and in the process develop a Raman tribometer capable of accurate in-situ friction measurements together with precise Raman spectroscopic measurements. We were successful to a significant extent in reducing the run-out of the rotating ball and therefore to obtain reproducible TIR Raman spectra from PAO at SF10/silica and SF10/steel

sliding interfaces. The spectral intensities corresponding to different PAO film thicknesses showed a good match with the theoretically calculated integrated Raman intensities (fig. 7.1.6). However, as we wanted to approach the boundary regime with fluid lubricant PAO, we were limited by the minimum rotation speed of the ball. Under a minimum applied load of 0.5 N (central pressure 198 MPa), the rotation of the silica/steel ball was arrested below a rotation speed of 5 rpm, therefore the minimum PAO film thicknesses at the SF10/silica and SF10/steel sliding interfaces obtained were ~52 nm and ~60 nm, respectively, which were significantly above the boundary regime. Therefore no boundary lubrication studies could be performed with PAO at sliding interfaces; however on static contacts the boundary lubrication regime was attained (fig. 7.1.7).

As discussed in section 7.2, the alkyl chains in the zinc arachidate molecules did not tilt any further with increasing sliding speeds within a range of 0 rpm to 10 rpm for a given pressure 198 MPa (fig. 7.2.9), the zinc arachidate molecules did not come any closer during the sliding. As a result the weak and insignificant effect of higher molecular ordering under higher sliding speeds was manifested in a weak red shift of the d^- stretching bands in the C-H stretching region. In comparison to the results obtained in chapter 5, where in spite of higher molecular ordering with higher applied loads, the alkyl chain tilting at higher pressure brought the zinc arachidate molecules closer to each other therefore required higher energy for a C-H bond vibration. As a result, an overall blue shift of the d^- stretching bands in the C-H stretching region were observed for zinc arachidate monolayer pressed at static SF10/silica contact with increasing pressures. According to Fujiwara *et al.*, tilted alkyl chains reduce friction coefficient due to increased limiting area of the adhering molecules [2]. In our boundary lubrication experiments, however, we did not find any sliding induced alkyl chain tilts, even though as described in chapter 5, the alkyl chains in zinc arachidate molecules had a pressure induced tilt for the given pressure 198 MPa. Our experiments suggested that there was no significant molecular chain tilt in the zinc arachidate monolayer at SF10/silica interface with increasing sliding speeds (fig. 7.2.9) and relating this to the observation of Fujiwara *et al.* we can predict that the dynamic friction at the SF10/silica interface did not have significant change with increasing sliding speeds, although the static friction might have

reduced with increasing loads (in principle the Bangalore-built tribometer A could potentially measure friction *in-situ* with simultaneous acquisition of Raman spectra, however the lateral force sensor was not installed during the early days of the development of tribometer A when these zinc arachidate experiments were carried out; later on the tribometer A moved to IISc Bangalore and rest of the experiments were carried out with the Durham based tribometer B). In our boundary lubrication experiments with zinc arachidate monolayers we found that at a higher rotation speed of the silica ball, with increase in time of the sliding contact, the optics started to get scratched and that started to reflect in the Px and Py polarised spectra with a noisy Raman signal (originating from a stronger background). With erosion of the boundary lubricant from the contact area and debris being formed, this probably increased the friction force that resulted in a rapid degradation of the optical surfaces. On a related note Fridmen and Levesque [3] earlier reported that friction force as a function of time and that with increased duration of the sliding contact, the friction force increases.

Reference:

1. Ho, M., & Pemberton, J.E., Analytical Chemistry, 1998. **70**: p. 4915.
2. Fujiwara, I., Kamei, T., Seto, J., Japanese Journal of Applied Physics, 1995. **34**: p. 4932.
3. Fridman, H.D., and Levesque, P., Journal of Applied Physics , 1959. **30**: p. 1572-1575.

8. Tribology of phospholipid bilayers

8.1 Background of phospholipids in tribology

Phospholipids and proteins form the major components of biological membranes and play important roles in many biological processes. Phospholipid layers in particular, are found in synovial fluids and apparently they play a key role in bone joint lubrication by controlling and reducing frictional forces between biological surfaces [1-4]. Lipids are also observed to act as lubricants in other physiological sites like pleura, pericardium, ocular surface and the gut where sliding occurs during gastric motility [5]. Increasing number of osteo-articular diseases have led to the development of joint implants, whose lifetimes depend on their tribological performances [6]. However the *ex-vivo* tribological test conditions being insufficiently realistic as compared to the mechanical and physicochemical conditions of biological environments, development of new biomaterials that would extend the *in-vivo* lifetime of joint implants has been limited.

Phospholipid multilayers can play an important role in the boundary lubrication regime [1, 4, 6]. Phospholipid bilayers adsorbed to a planar solid support are commonly termed as 'supported phospholipid bilayers'. These supported phospholipid bilayers are widely used as model membranes to study the properties of the biological membranes e.g. pleura, pericardium, etc. [7] and for other applications e.g. ligand-receptor interactions, viral attacks and cellular signaling events [8]. AFM is the most commonly used technique to study the structure and stability of supported phospholipid bilayers. AFM has been used to measure the interaction between the bilayers and the tips [9] as well as to measure the nature of bilayer defects [10]. Effects of different physicochemical parameters e.g. pH [11], deposition pressure of outer lipid layer [12], temperature [13] on supported phospholipid bilayer integrity had been studied with AFM. Recently Trunfio-Sfarghiu *et al.* used AFM force spectroscopy to observe a correlation between membrane resistance to indentation and tribological properties of lipid bilayers [14]. They developed a biotribometer (with accessible sliding rates 0.1-1 mm/s and applied pressures 0.2-1 MPa) which allowed them simultaneous measurement of the friction coefficients and visualization of surface degradation by fluorescence microscopy (using lipids labelled

with a fluorophore) [6]. With the friction measurements and fluorescence microscopy images the role of phospholipid bilayers in maintaining a very low friction coefficient was confirmed. They found that the friction coefficient of bare hydrophilic surfaces reduced by nearly 2 orders of magnitude ($\mu = 0.002$) when both surfaces were coated with dipalmitoyl phosphatidylcholine (DPPC) bilayers in the solid phase. However with one bilayer in the contact region, the friction coefficient was much higher than with two bilayers. The friction coefficient gradually increased with prolonged friction while the lipid bilayer degraded as evaluated by fluorescence microscopy.

Scomparin *et al.* studied the diffusion law of DMPC and DPPC in supported lipid bilayers [15] on different substrates and showed that depending on the nature of substrate used and method of bilayer preparation adapted, completely different behaviours can be observed. The same dynamics was observed in both the layers of an LB lipid bilayer on a glass substrate, while on a mica substrate the dynamics of the proximal layer was slower than the dynamics of the distal layer even though the transition temperature is the same for both the layers. Lipid bilayers prepared by vesicle fusion method lead to random behaviours and shifted transition temperatures. Oncins *et al.* with AFM studies [16] found that a more compact supported DMPC bilayer which they obtained with increasing the salinity of media with 0.1 M NaCl has a reduced friction coefficient than the supported DMPC bilayer with lower salinity. Additionally the lipid bilayers with lower salinity recovered more quickly due to lower cohesion between the phospholipid molecules.

Even though AFM and AFM force spectroscopy can yield valuable information about the interaction forces and mechanical behaviour of the studied systems with nanometric and nanonewton resolution [17, 18], to obtain any chemical/molecule specific information from the lipid bilayers under tribological confinement, we have to resort to vibrational spectroscopy, as discussed in chapter 1. The problem associated with the presence of strong water stretching and bending modes around 3200 – 3700 cm^{-1} and 1600 – 1630 cm^{-1}, respectively, which dominates the infrared (IR) spectra of any dilute biological sample, gives Raman spectroscopy a natural advantage over IR. This difficulty in using

IR spectroscopy to study biological samples can be partly overcome by using highly concentrated specimens, short sample path lengths, and/or use of D_2O [19]. However, in context to our work, to observe the C-H stretching region 2800 – 3000 cm^{-1}, the strong water bands in the IR spectra are non-overlapping and should not cause any serious concern. In this chapter I will describe the use of total internal reflection (TIR) Raman spectroscopy to study the tribological confinement of a phospholipid bilayer under applied pressures in aqueous environments.

8.2 Materials and methods

8.2.1 Materials

All lipids/chemicals used in our experiments were of analytical grade and were used without further purification. Powdered products of 1,2-dimyristoyl-sn-glycero-3-phosphocholine (DMPC) and 1,2-dipalmitoyl-sn-glycero-3-phosphocholine (DPPC) were purchased from Avanti Polar Lipids. The lipid bilayer fusion and tribological contact experiments were conducted in Tris buffer solution (15 mM Tris-HCl pH 7.2, Sigma-Aldrich) made up in MilliQ water.

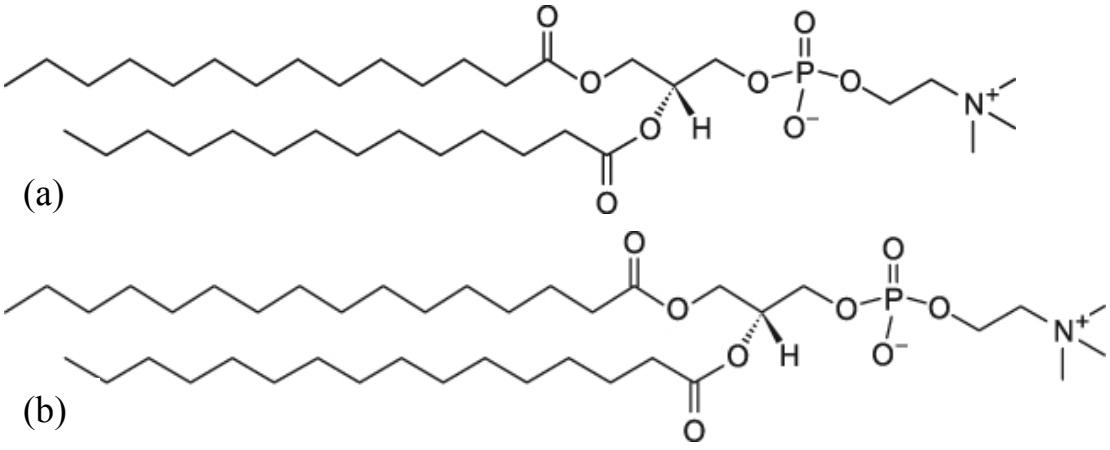

Figure 8.2.1: Chemical structures of lipids used: (a) DMPC and (b) DPPC

Lipid	DMPC, or 1,2-dimyristoyl-sn-glycero-3-phosphocholine, or 1,2-ditetradecanoyl-sn-glycero-3-phosphocholine	DPPC, or 1,2-dipalmitoyl-sn-glycero-3-phosphocholine, or 1,2-dihexadecanoyl-sn-glycero-3-phosphocholine
Molecular formula	$C_{36}H_{72}NO_8P$	$C_{40}H_{80}NO_8P$
Molecular weight	677.933	734.039
Transition temperature	23 °C	41 °C
CMC	6 nM	0.46 nM

Table 8.2.1: Chart showing chemical information of lipids used [20].

8.2.2 Preparation of supported phospholipid bilayers

Supported phospholipid bilayers of DMPC/DPPC were deposited on hydrophilic surfaces of 10 mm diameter fused silica sphere and 10 mm diameter SF10 hemisphere (flat surface) [21]. 5 mg of powdered lipid sample (DMPC/DPPC) was weighed and transferred to a 25 ml beaker containing 5 ml of 15 mM Tris buffer solution (pH 7.2) and left for 30 minutes to be hydrated after proper mixing. The resultant lipid solution was approximately 1.4 mM in Tris buffer solution which was much higher than the critical micelle concentration (CMC) of both the lipids DMPC and DPPC in pure water. The beaker along with its contents was then sonicated in an ultrasonic bath for one hour at temperatures higher than the phase transition temperature (as shown in table 8.2.1) for the respective lipids DMPC (30 °C) and DPPC (50 °C) to form phospholipid vesicles in Tris buffer solution.

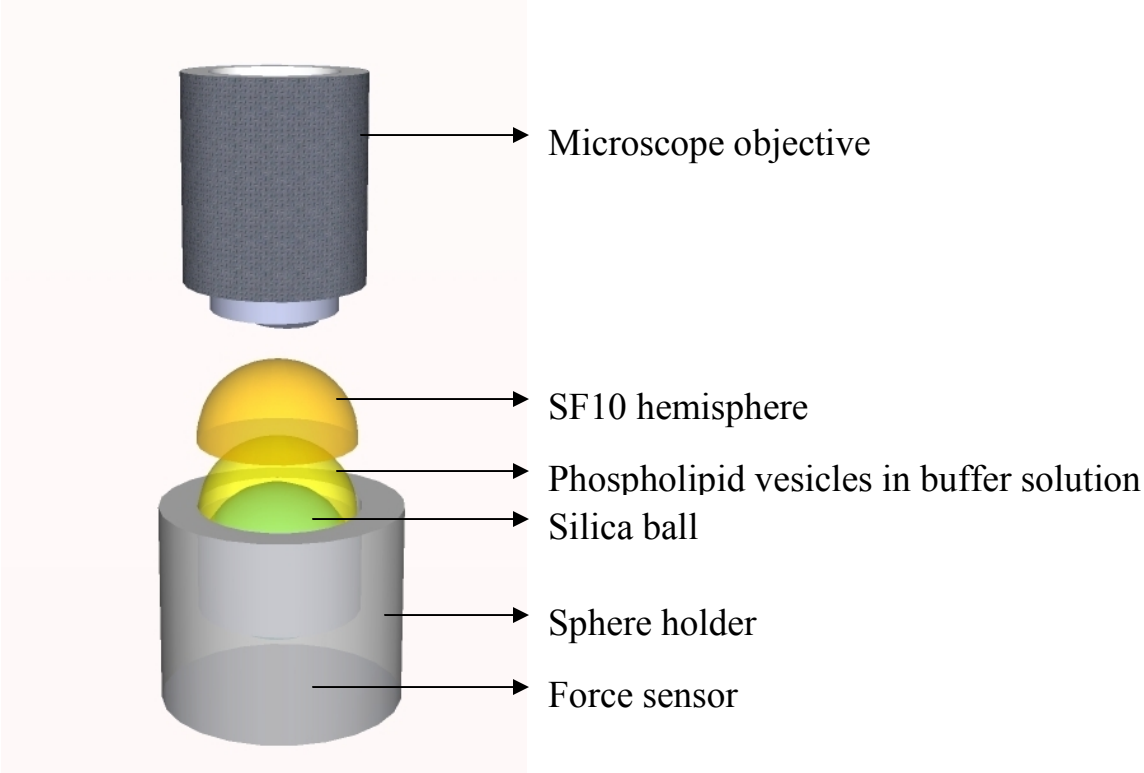

Figure 8.2.2: Schematic diagram showing lipid bilayer fusion on hydrophilic surfaces in progress

A cleaned fused silica hemisphere and an SF10 hemisphere were put into the respective holders and the phospholipid vesicle solution in Tris buffer was poured onto the sphere holder as shown in figure 8.2.2. The hemisphere holder holding the hemisphere was moved into position on top of the sphere holder by the micromotion stages used for positioning, and then gradually lowered such that the meniscus of the phospholipid vesicle solution was in contact with the lower flat surface of the hemisphere (without contact between the silica sphere and SF10 hemisphere). The setup was left undisturbed for another one hour [21] allowing the phospholipid vesicles to rupture and fuse on the hydrophilic surfaces of fused silica and SF10, resulting in *in-situ* deposition of phospholid bilayers. A heat gun was used to maintain steady temperatures at 30 °C during DMPC fusion and at 50 °C during DPPC fusion by clamping it at a suitable distance from the vesicle fusion setup (fig. 8.2.2). The phospholipid vesicle solution was then flushed from the site of deposition by milliQ water using a disposable syringe and pure Tris buffer solution (15 mM) was poured onto the sphere holder covering the fused silica sphere to maintain an aqueous environment throughout the contact experiments (the

buffer solution was replenished at 20 minutes interval using a disposable syringe during the TIR Raman experiments). The heat gun was then removed and external heating was stopped after one hour. The flat surface of the SF10 hemisphere coated with an adsorbed phospholipid bilayer was then brought into contact with the silica sphere which was also coated with the same phospholipid bilyer. The tribological contact experiments were carried out at the room temperature ~22 °C.

8.2.3 Raman experiments on phospholipid bilayers at solid-solid confinement

Supported phospholipid bilayers of DMPC/DPPC were deposited on SF10 hemisphere and fused silica sphere and were confined under applied pressures at SF10/silica interface. The laser beam was focused within the contact region at the SF10/silica interface; the angle of incidence was set to 60°. An aqueous environment was maintained at the contact region by 15 mM Tris buffer solution (figure 8.2.3), which was replenished at regular intervals to prevent drying up of the buffer solution during the Raman experiments. TIR Raman spectra were acquired from the supported phospholipid bilayers under confinement using similar procedures described in chapter 3, while a force sensor placed below the sphere holder gave direct readings for force measurements.

The incident 532 nm laser beam was either S- or P-polarised (figure 8.2.3). Fixed window spectra ranging between 2600 cm^{-1} to 3200 cm^{-1} were obtained to monitor the C-H stretching region of the phospholipid bilayers while extended scans ranging between 2600 cm^{-1} to 4000 cm^{-1} were obtained to monitor the hydration level/water molecules associated with the head group in the supported phospholipid bilayers under applied pressure, together with the C-H stretching region of the phospholipids.

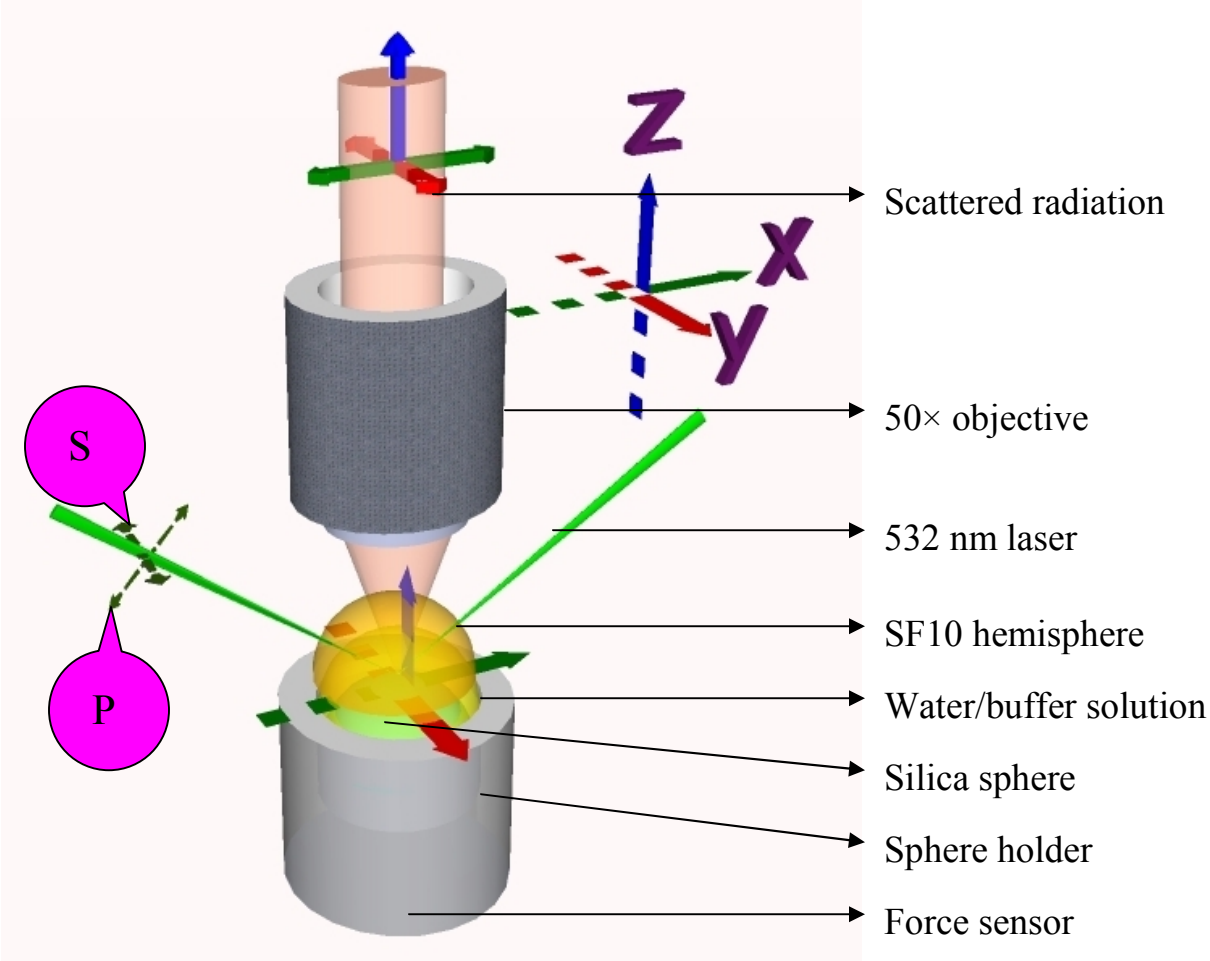

Figure 8.2.3: Schematic diagram showing TIR Raman experimental geometry for lipid bilayer experiments in static tribological contact

During the TIR Raman experiments on the supported phospholipid bilayers, there was a recurring problem of laser damage to the sample in contact (average life span of the sample with 300 mW laser power was ~30 minutes). Therefore each spectrum was acquired with shorter acquisition time of 3 minutes to acquire spectral data from four different loads with both S- and P-polarisation of the incident beam.

8.3 TIR Raman spectra from DMPC and DPPC bilayers

Figures 8.3.1 and 8.3.2 show the S-unpolarised and P- unpolarised TIR Raman spectra respectively from DMPC bilayers deposited on both SF10 hemisphere and silica sphere and sandwiched at the interface in aqueous environment at different pressures.

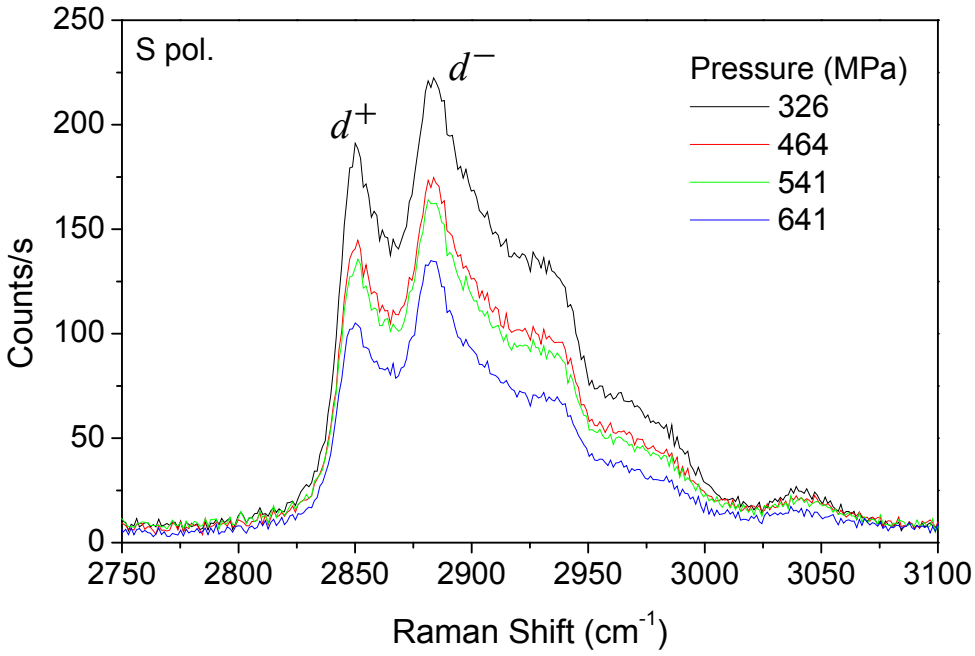

Figure 8.3.1: TIR Raman spectra from DMPC bilayers at SF10/silica interface; S-polarised incident beam, 300 mW, 180 s acquisition, θ_i = 60°, at different pressures.

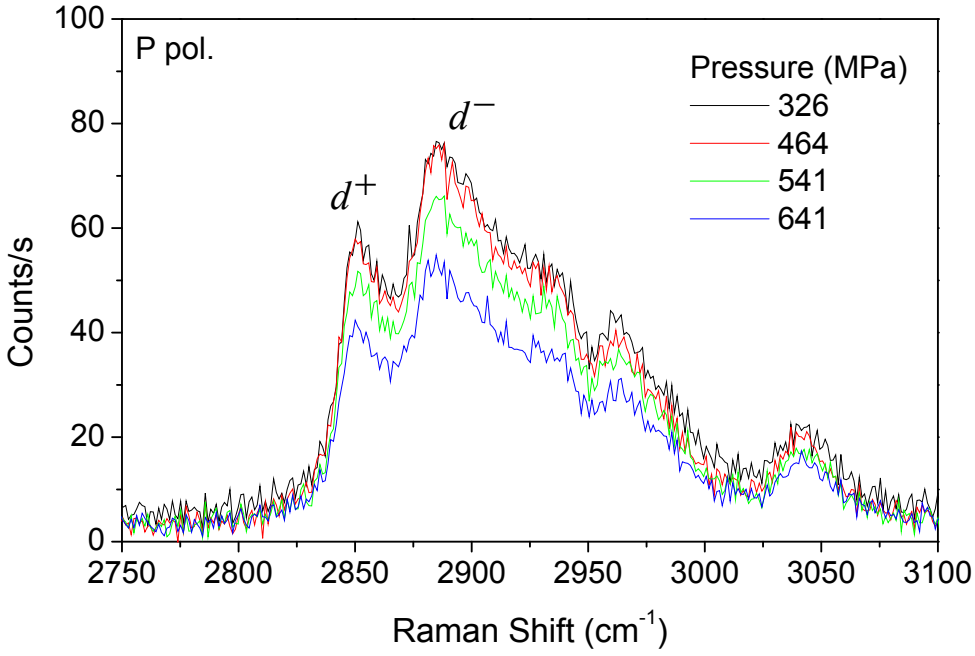

Figure 8.3.2: TIR Raman spectra from DMPC bilayers at SF10/silica interface; P-polarised incident beam, 300 mW, 180 s acquisition, θ_i = 60°, at different pressures.

In figure 8.3.1, the peaks at ~2882 cm^{-1} arise from asymmetric CH_2 stretching, denoted as d^- and the peaks at ~2850 cm^{-1} arise form symmetric CH_2 stretching, denoted as d^+. The intensity ratio d^-/d^+ is a measure of the orderliness of the monolayer packing [22]. d^-/d^+ ratio ranging between 1.1 to 1.4 indicated disordered packing with many gauche defects. Figure 8.3.3 shows a gradual increase in orderliness with increased pressures in the DMPC bilayers in aqueous environment as indicated by the increasing values of the d^-/d^+ ratio with increasing pressures.

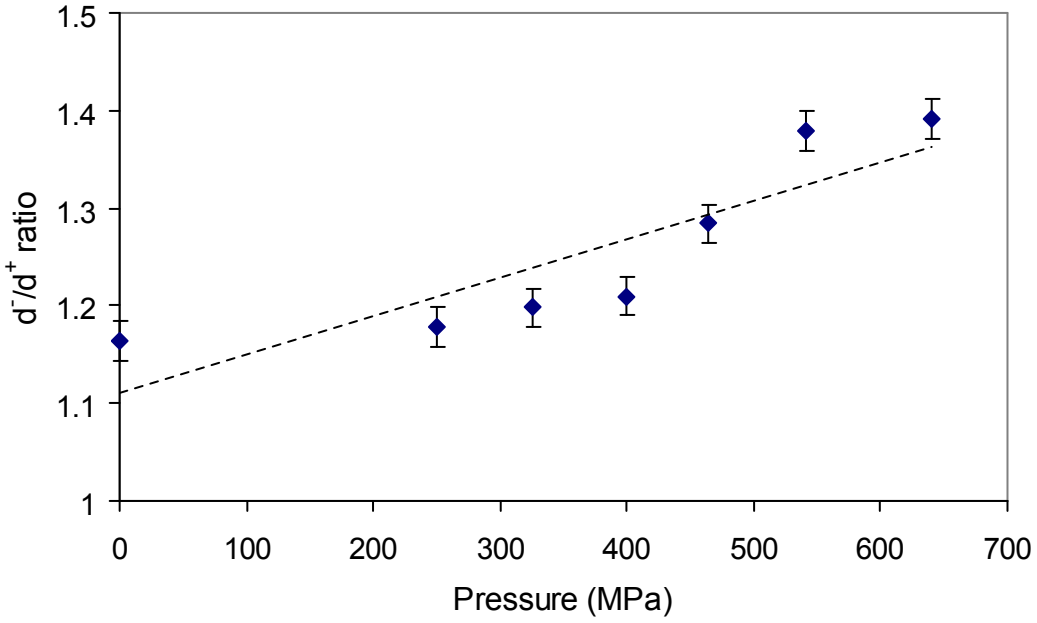

Figure 8.3.3: Plot of d^-/d^+ ratio in DMPC bilayers against applied pressures showing increase in orderliness with increase in pressure (obtained from curve fitted data in S-unpolarised spectra in fig. 8.3.1)

From fig. 8.3.1 and fig. 8.3.2, intensities in the Raman spectra from the DMPC bilayers in aqueous environment sandwiched at SF10/silica interface decreased with increasing pressure both when spectra were acquired with S-polarised and P-polarised incident radiation respectively. This indicated that unlike the LB monolayers of Zn arachidate confined at solid-solid interface described in chapter 5, the DMPC bilayers in aqueous environment under applied pressure tends to squeeze out of the contact region. This phenomenon was observed to be partly reversible (~70 %) in a sense that on reducing the

applied pressure the intensities of the Raman spectra increased but not to the extent when the contact pressure was increased. This partial reversibility was not due to laser damage to the sample in contact as the same difference in Raman signal was observed after and before the contact if the laser was turned off during the contact period. However, on plotting the spectral intensity ratios, Is/Ip at different pressures (fig. 8.3.4) we found the ratio to gradually decrease with increasing pressures which may indicate an increase in the alkyl chain tilt in the DMPC bilayers at higher pressures. The argument for an increasing alkyl chain tilt with decreasing Is/Ip ratio close to the critical angle of incidence can be arrived from symmetry considerations as previously described in chapter 2. The magnitude of decrease in the Is/Ip ratio with increasing pressures is much less in DMPC bilayers in aqueous environment compared to that of LB monalayers of Zn arachidate described in section 5.2.1 of chapter 5; with the increase in pressure, lipid bilayer material is squeezed out of contact region while the LB monolayer of Zn arachidate is firmly adhered to the optic surfaces in the region of contact. To confirm this conclusion, however, further data would be required.

The Wire 2.0 software from Renishaw was used to carry out the mathematical curve-fitting on all the spectra obtained with S polarised incident radiation, using six bands described in table 5.3.1 in chapter 5 as mixtures of Gaussian and Lorentzian functions. The obtained curve fitting data were used to calculate the d^-/d^+ ratios in the spectral intensities of the S-unpolarised spectra (fig. 8.3.3) and plot the red shift of the Raman intensities in the d^- and d^+ stretches with increasing pressures (figure 8.3.5).

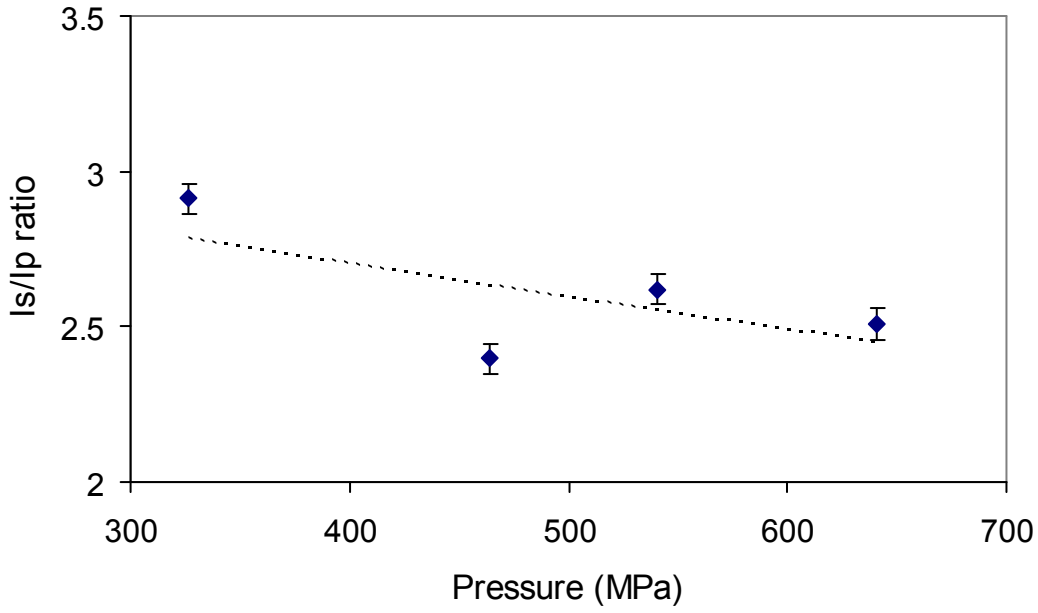

Figure 8.3.4: Plot of Is/Ip ratio in DMPC bilayers against applied pressures showing increase in alkyl chain tilt with increase in pressure.

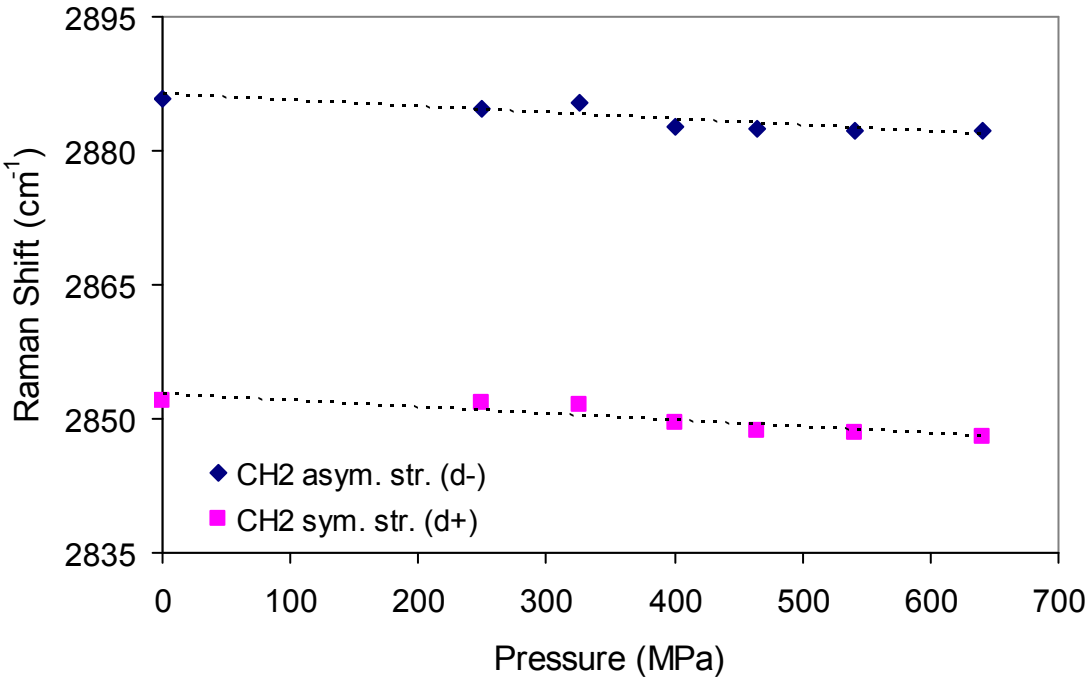

Figure 8.3.5: Plot showing red shift in the d^- and d^+ peaks in Raman spectra from DMPC bilayers with higher pressures (obtained from curve-fitted data in S-unpolarised spectra). Average slope = –0.0007 corresponding to ~0.1 cm^{-1} red shift per 14 MPa increase in pressure.

A red shift in the d^- and the d^+ bands are expected if the lipid bilayers get more ordered with higher applied pressures. On the other hand, as the molecules come closer to each other, more energy is required for the stretching vibrations of the molecular bonds and a blue shift of the Raman bands are expected [23]. In this case, with higher pressures, the DMPC bilayers get more ordered (fig. 8.3.3) and as the DMPC bilayers tend to squeeze out of the contact region, the effect of alkyl chain tilt with higher pressure is much lesser (fig. 8.3.4). Hence in competition of the two opposing factors contributing to shift of Raman bands at CH_2 stretching region, an overall red shift is observed (fig. 8.3.5) with increasing pressures. An average slope of the red shift = – 0.0007 corresponded to ~0.1 cm^{-1} red shift for every 14 MPa increase in pressure.

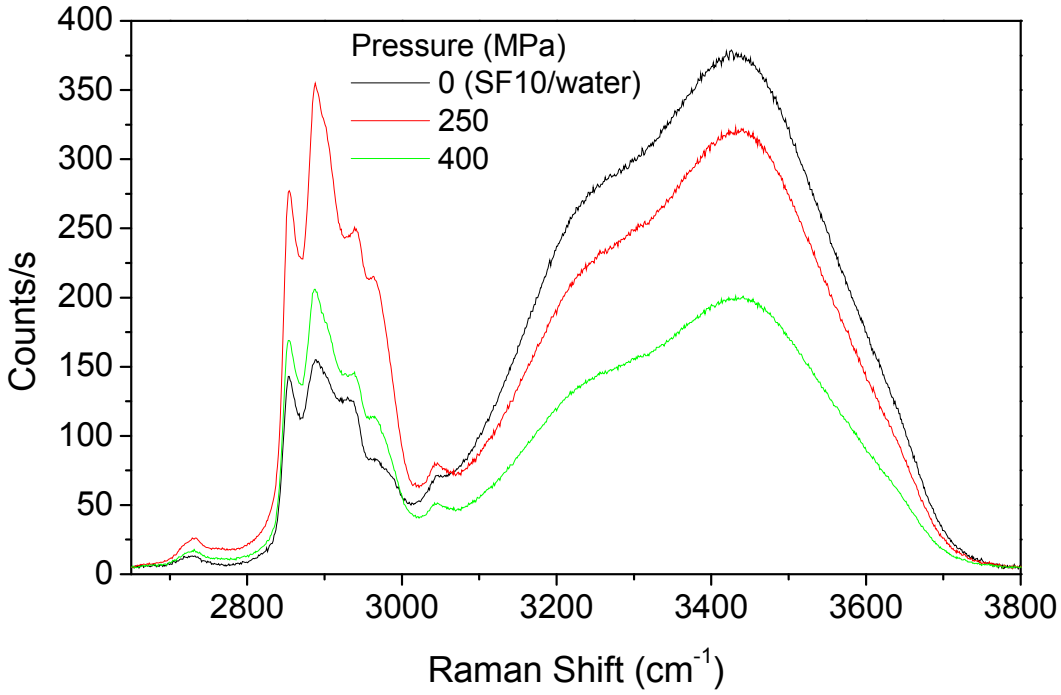

Figure 8.3.6: TIR Raman spectra from DMPC bilayers at SF10/silica interface; S-polarised incident beam, 200 mW, 200 s acquisition, θ_i = 60°, at pressures indicated in the figure.

Extended window spectra were acquired with S-polarised 200 mW laser power and 200 s acquisition time, both at solid-solid confinement in aqueous environment and out of contact solid-water interface from both DMPC bilayers (fig. 8.3.6) and DPPC bilayers

(fig. 8.3.7) to cover the spectral region of the Raman bands from water at ~3400 cm^{-1}. In both the figures, the out of contact spectra from the lipid bilayers corresponded to 0 MPa pressure (SF10/water interface) and a strong water band was observed in the TIR Raman spectra together with the CH_2 stretching bands from the DMPC and DPPC bilayers respectively. At solid-solid confinement of the lipid bilayers in the SF10/silica interface, the bulk water squeezed out of contact and TIR Raman spectra were acquired from lipid bilayers deposited on both SF10 and silica surfaces. Due to the presence of a double bilayer at the SF10/silica interface the spectral intensities from both DMPC bilayers and DPPC bilayers were expected to be $2\times(1.83/1.69)^2 = 2.35$ times the spectral intensity than that recorded at SF10/water interface. This was taking into consideration that the angle of incidence, 60° was further away from the critical angle at the SF10/water interface, 50.2° than the critical angle at SF10/silica interface, 57.2° and therefore at the SF10/silica interface (fig.2.2.7) the electric field generated with S-polarised incident beam was stronger than the electric field at the SF10/water interface (fig. 8.3.8). The actual spectral intensity from DMPC bilayers at SF10/silica interface at 250 MPa (fig. 8.3.6) was ~2.4 times the spectral intensity at 0 MPA while the actual spectral intensity from DPPC bilayers at SF10/silica interface at 298 MPa (fig. 8.3.7) was ~3.3 times the spectral intensity at 0 MPa. This observation suggests that the DPPC bilayers had a higher coverage at the fused silica surface than at the SF10 surface (further discussed in section 8.4). On further increasing of the applied pressure the spectral intensity of the CH_2 stretching bands from both DMPC bilayers and DPPC bilayers decreased which indicated a squeezing out of the lipid bilayer membrane from the contact region accompanied by a decrease in the spectral intensity from the water bands as well. The relative peak intensities of the water bands and the CH_2 stretching bands from the DMPC bilayer at 250 MPa and 400 MPa (fig. 8.3.6) and that from the DPPC bilayer at 298 MPa and 582 MPa (fig.8.3.7) remained the same. This indicated that the Raman signal of the water bands obtained at SF10/silica confinements at higher pressures originated from the water molecules associated with the phosphate head groups of the lipid bilayers and that they squeezed out with the squeezing bilayer lipid membranes with higher pressures.

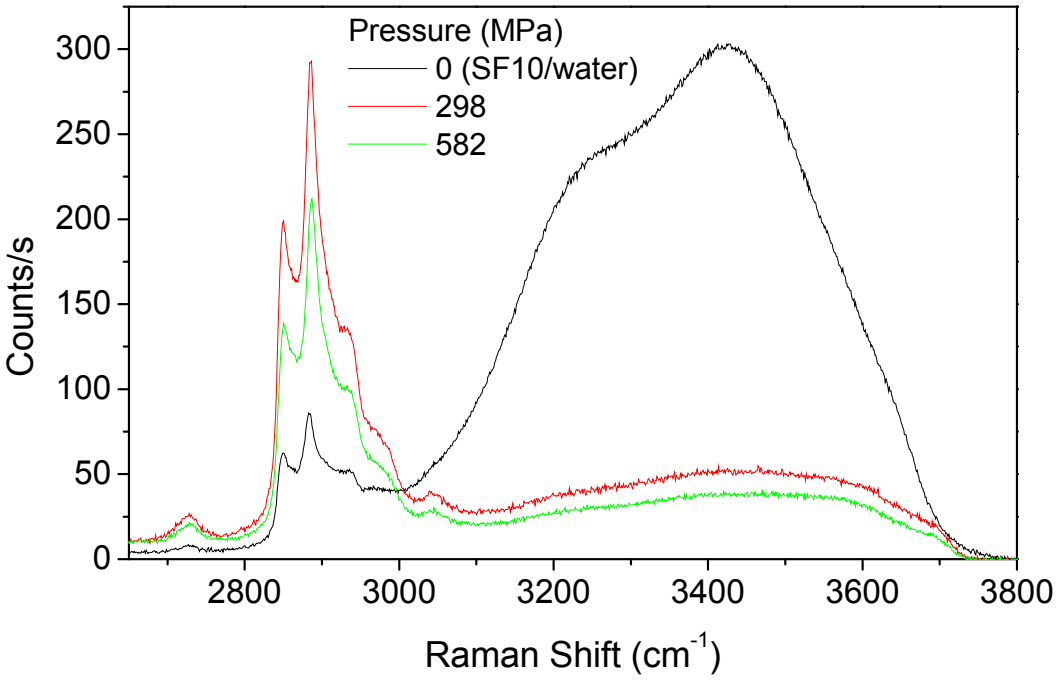

Figure 8.3.7: TIR Raman spectra from DPPC bilayers at SF10/silica interface; S-polarised incident beam, 200 mW, 200 s acquisition, θ_i = 60°, at pressures indicated in the figure.

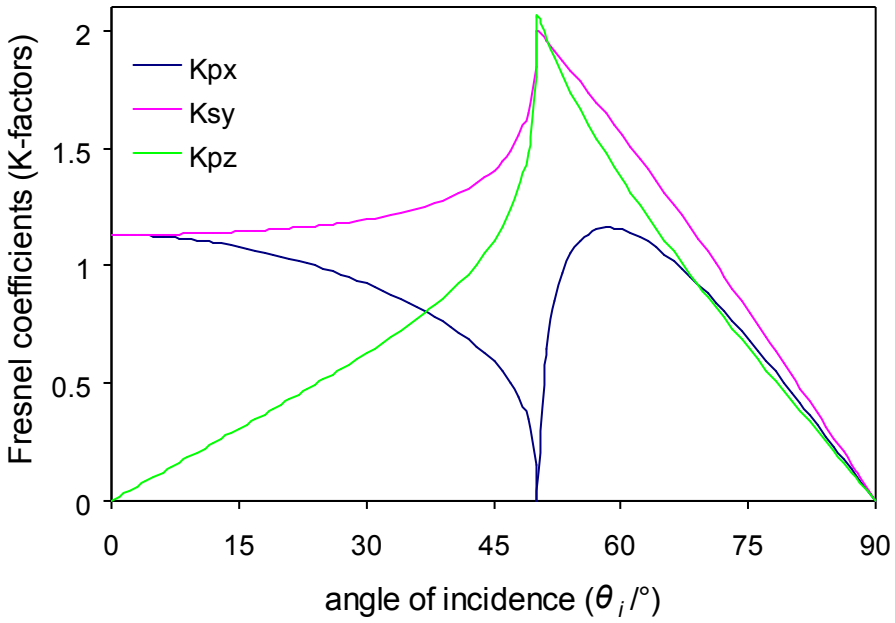

Figure 8.3.8: Fresnel coefficients plotted against different angle of incidences at the SF10/water interface at λ = 532 nm. n_{SF10} = 1.737 and n_{water} = 1.333; n of the deposited lipid bilayer ~1.5.

8.4 Discussion

It was observed that at SF10/water interface, the lipid signal from DMPC bilayers (fig. 8.3.6) was much stronger than for DPPC (fig. 8.3.7), while the water signals were fairly similar. This suggested that we had only a partial bilayer of DPPC on the SF10 surface, since it was expected for DPPC to produce more lipid signal than DMPC if similar bilayers were formed of both the lipids (DPPC has total 28 CH_2- groups and 2 CH_3- groups in two chains, while DMPC has 24 CH_2- groups and 2 CH_3- groups in two chains). The increment in the DPPC signal by ~3.3 times rather than ~2.35 times (as calculated on the basis of Fresnel coefficients at SF10/water and SF10/silica interfaces in section 8.3) in acquiring spectra from a single bilayer at SF10/water interface to acquiring spectra from a double bilayer at SF10/silica interface indicated that the DPPC vesicle fusion was much better on a silica surface than an SF10 surface (fig. 8.3.7). The penetration depth of the evanescent wave generated with a 532 nm laser at SF10/water interface with 60° angle of incidence is ~106 nm, therefore it can be said that in the out-of-contact spectra from DMPC and DPPC bilayers at SF10/water interface, the water signal is coming from a ~106 nm thick film of water. The thickness of the water layer in-contact can therefore be estimated from the ratio of the water intensities in and out of contact, corrected for the Fresnel coefficients (water film thickness remaining constant, the in-contact spectra should be more intense than the out-of-contact spectra by a factor of $(1.83/1.69)^2 = 1.17$). Analysis of the water intensities in figure 8.3.6, shows that the water film thickness in the in-contact spectra at 250 MPa pressure was ~75 nm and that at 400 MPa pressure was ~43 nm. The thickness of a double bilayer of DMPC or DPPC is ~8 nm. Therefore the excess volume of water, as indicated by the spectra must have been trapped in the imperfections in the optical surface. Increasing the pressure to 400 MPa from 250 MPa, the both the lipid signal and the water signal reduced by a factor of ~0.57. In case of DPPC (fig. 8.3.7) the water signal in the in-contact spectra at 298 MPa and 582 MPa originated from 15 nm and 11 nm thick film of water, respectively. The lower thickness in the film of water at contact, as compared to the DMPC spectra is probably due to a relatively new set of optics that was used (with less imperfections/scratches to trap water). However, similar to the DMPC bilayers, on increase of the pressure from 298 MPa to 582 MPa, both the lipid signal and the water signal reduced to similar extents by

a factor of ~0.7. As the level of hydration in the polar head groups of the lipid bilayers remained constant over the range of studied pressures, it can be concluded that the level of hydration or water content in the supported lipid bilayers do not have any significant effect on the lipid bilayer tribology or static friction at varied pressures. There can be two possible situations of the lipid bilayers when higher pressure is applied. The first situation is that one bilayer is obtained from two bilayers, in which case we still expect to have two water layers next to the optics surfaces, but lose any water between the bilayers. The second possibility is that both the bilayers are squeezed out and eventually leave an SF10/silica contact with some different amount of bound water. From our experiments the relative rate of drop in the lipid signal and the water signal with increase in applied pressure supports the second possibility more than the first.

Increasing pressures induced increased order (fig. 8.3.3) and higher alkyl chain tilts (fig. 8.3.4) in the supported DMPC bilayers and hence more compactness. This can contribute to reduced friction coefficients under static contacts. The d^{-}/d^{+} ratios and the peak frequency variation with pressure were not plotted for DPPC bilayers due to the lack of sufficient data (mostly due to laser damage to the sample) that is required to study a trend. The laser damage to the lipid bilayers was found to be more severe in contact than out of contact. There was no obvious reason for this from an optical perspective, but a solid-solid contact excluded oxygen (a radical scavenger) and prevented any reactive species from diffusing away from the surface. A study of the lipid bilayers in aqueous environment with the tribometers described in chapter 6 was also aimed for. In the tribometers, a rolling ball would have carried the reactive species away from the sliding contact and therefore could have avoided laser damage to the lipid bilayers. However, besides the run-out of the rolling ball described in chapter 6, the problems associated with deposition of the lipid bilayers onto the optics (procedure of bilayer deposition in section 8.2.2 does not apply for the tribometer experiments as the ball was glued to a shaft) and fitting/aligning them in the tribometer while keeping them wet was a serious threat to the chances to succeed. Attempts were made to carry out the tribometer experiments with a single lipid bilayer deposited on the SF10 hemisphere, but the lipids were eroded from

the sliding contact within a few minutes, even before single spectra could be acquired successfully and damaged the optics.

References:

1. Hills, B.A., Journal of Rheumatology, 1989. **16**: p. 82-91.
2. Hills, B.A., Annals of Biomedical Engineering, 1995. **23**: p. 112-115.
3. Johnston, S.A., Veterinary Clinics of North America Small Animal Practice, 1997. **27**: p. 699-723.
4. Schwarz, I.M., and Hills, B.A., British Journal of Rheumatology, 1998. **37**: p. 21-26.
5. Hills, B.A., Proceedings of the Institute of Mechanical Engineers, Part H: Journal of Engineering in Medicine, 2000. **214**: p. 83-94.
6. Trunfio-Sfarghiu, A.-M., Berthier, Y., Meurisse, M.-H., and Rieu, J.P., Tribology International, 2007. **40**: p. 1500-1515.
7. Sackmann, E., Science, 1996. **271**: p. 43-48.
8. Castellana, E.T., and Cremer, P.S., Surface Science Reports, 2006. **61**: p. 429-444.
9. Garcia-Manyes, S., and Sanz, F., Biochimica et Biophysica Acta 1798, 2010. **4**: p. 741-749.
10. Dufrene, Y.F., and Lee, G.U., Biochimica et Biophysica Acta 1509, 2000. **1-2**: p. 14-41.
11. Hui, S.W., Vishwanathan, R., Zasadzinski, J.A., and Israelachvili, J.N., Biophysical Journal, 1995. **68**: p. 171-178.
12. Benz, M., Gutsmann, T., Chen, N., Tadmor, R., and Israelachvili, J.N., Biophysical Journal, 2004. **86**: p. 870-879.
13. Fang, Y., and Yang, J., Biochimica et Biophysica Acta (BBA) Biomembranes, 1997. **1324**: p. 309-319.
14. Trunfio-Sfarghiu, A.-M., Berthier, Y., Meurisse, M.-H., and Rieu, J.P., Langmuir, 2008. **24**: p. 8765-8771.

15. Scomparin, C., Lecuyer, S., Ferreira, M., Charitat, T., and Tinland, B., European Physical Journal E, 2009. **28**(2): p. 211-220.
16. Oncins, G., Garcia-Manyes, S., and Sanz, F., Langmuir, 2005. **21**(16): p. 7373-7379.
17. Garcia-Manyes, S., Oncins, G., and Sanz, F., Biophysical Journal, 2005. **89**: p. 1812-1826.
18. Loi, S., Sun, G., Franz, V., and Butt, H.J., Physical Review E, 2002. **66**(031602): p. 1-7.
19. Arkin, I.T., Current Opinion in Chemical Biology, 2006. **10**(5): p. 394-401.
20. http://www.avantilipids.com/. [cited.
21. Lee, C. and Bain, C.D., Biochimica et Biophysica Acta (BBA) - Biomembranes, 2005. **1711**(1): p. 59-71.
22. Ho, M., & Pemberton, J.E., Analytical Chemistry, 1998. **70**: p. 4915.
23. Coulon, S., Jabault, I., Lubrecht, A.A., Ville, F., and Vergne, P., Tribology International, 2004. **37**: p. 111-117.

9. Conclusion

Tribology has emerged as an interdisciplinary science in the past few years. While much empirical evidence is shown in these studies, there is no basic understanding why one molecule is a better lubricant than the other. As a consequence the chemical techniques are now being used in conjunction with the more conventional engineering techniques in order to gain a better understanding of questions related to molecular tribology (chapter 1).

Raman spectroscopy gives information on vibration of molecules and with the change in local conditions of the molecules, the Raman signal changes as well. The Raman signal is sensitive to temperature, pressure and shear, therefore the molecular changes at the tribological contact due to change in temperature, pressure, and shear reflects in the Raman signal. Total Internal reflection (TIR) Raman spectroscopy is a non-invasive variant of Raman spectroscopy which is surface sensitive (~100 nm), with enhancement the Raman intensity at the critical angle of incidence and allows for orientational analysis of substrate molecules by obtaining polarization-resolved spectra (chapter 2).

In this project a TIR geometry (earlier developed by Sarah Haydock from Prof. Colin Bain group at Oxford University) for the tribology studies with Raman spectroscopy have been developed with assistance from Dr. Eric Tyrode during the initial part of this project. In moving from prism-lens contact geometry to hemisphere-sphere contact geometry, the laser alignments were made easier and astigmatism-corrected (chapter 3). The *ex-situ* experiments carried out with obtaining TIR Raman spectra from LB monolayer of zinc arachidate on silica surface confirmed that the alkyl chains were tilted to the surface normal (section 5.1). Similar experiments carried out with DPPC monolayer on silica surface surprisingly revealed that the alkyl chains were aligned with the surface normal, even though the LB monolayer of DPPC was much more disordered than the zinc arachidate monolayer, as revealed from the d^-/d^+ ratios. The static contact experiments with LB monolayers of both zinc arachidate and DPPC at the SF10/silica interface revealed that the monolayers get more ordered with increasing pressures and

simultaneously the alkyl chains tilt further from the surface normal (section 5.2). A blue shift in the peak frequencies confirmed that the molecules in the monolayers come closer to each other with application of higher pressures. We found that with static contact, both the LB monolayers of zinc arachidate and DPPC continue to have in-plane isotropicity. The degree of tilt of the alkyl chains and ordering of the monolayer molecules with increasing pressures was more prominent in DPPC monolayers than in zinc arachidate monolayers. This is probably due to the fact that the DPPC monolayers were more disordered to begin with hence had a higher degree of freedom to rearrange them under pressure. Transfer of material between the surfaces in contact was observed, however the total amount of molecular material at the contact apparently remained the same. Static contact experiments carried out with supported phospholipid bilayers of DMPC and DPPC at SF10/silica interface in an aqueous environment revealed that the lipid molecules squeeze out of the contact with increasing pressures (chapter 8). In this case the lipid molecules do not come closer to each other significantly enough and a higher ordering of the lipid bilayers with increasing pressures were reflected both the d^{-}/d^{+} ratio as well as a red shift in the peak frequencies.

Development of a multi-purpose Raman tribometer capable of measuring lateral and normal forces at a sliding interface besides acquiring TIR Raman and/or normal incidence Raman spectra from lubricant molecules at the sliding interface were aimed as a part of the PhD project (chapter 6). In spite of a number of engineering difficulties faced related to the run-out of the rotating ball and insufficient sensitivity due to weaker collection efficiency at a metal/dielectric interface which hindered us from studying the tribology of a steel ball, for example, significant progress was made in getting the Raman tribometer ready to be used for the study of fluid film lubrication in the hydrodynamic and elesto-hydrodynamic regime. At the sliding interface of SF10/silica, the fluid lubricant Synton PAO 100 was tested in the elasto-hydrodynamic regime of lubrication (chapter 7). It was found that the fluid PAO forms a thicker film at the sliding interface with higher rotation speed of the ball and with application of higher loads/pressure, the PAO film gets thinner. The calculated film thickness using Reynold's equation matched up with the experimentally obtained Raman spectral intensities to a good extent (figure

7.1.6). This confirmed the Raman tribometer to be in a good working state. The boundary regime of lubrication could not be reached with the fluid lubricant PAO because of its high viscosity and also due to the fact that the minimum rotation speed of the ball ~5 rpm (below which the rotation of the ball stopped) was not low enough. A calculated blending of PAO with hexadecane and measurement of the viscosity of the PAO-hexadecane mixture should be useful in reaching the boundary lubrication regime with fluid lubricant if being used as a lubricant. Dry boundary lubrication experiments were carried out with zinc arachidate monolayers on SF10 hemisphere and silica ball and TIR Raman spectra were acquired from the sliding interface (section 7.2). But as the molecular material at the sliding interface here was much lesser than the fluid PAO film material, the run-out of the rotating ball emerged as a threat again and the spectral intensity in sliding contact was weaker than the static contact under same load. On successive increase in the rotation speed of the ball the monolayer material tended to erode away after a certain time and cause damage to the optics. The sliding experiments were however stopped at the onset of the material erosion at the sliding contact which reflected in the Raman spectra with a higher noise level due to stronger background, and therefore no time dependent spectra of material erosion was not presented in the thesis. While working on the static contact experiments with the supported lipid bilayer in aqueous environment, a recurring problem of laser damage to the sample was encountered, therefore sufficient number of datasets could not be obtained at different pressures to our satisfaction before the bilayer was damaged. Therefore some of the conclusions drawn in chapter 8 would require further data for confirmation (section 8.3). As discussed in chapter 8, the laser damage was much more severe in contact than out of contact as the contact excluded oxygen, a radical scavenger, and prevented any reactive species from diffusing away from the surface. It was expected that shear experiments on the supported lipid bilayers using Raman tribometers should allow the reactive species from the sliding contact to diffuse away and therefore reduce the chances of laser damage. However, other problems associated with the run-out of the rotating ball, difficulties in *in-situ* deposition of lipid bilayers onto the aligned optics, held up the experiments.

With the current setup of Raman tribometer, it would be possible to reach a pressure of ~750 MPa and a rotation speed of ~40 rpm without damaging the optics in presence of fluid lubricant (with dry boundary lubricants ~250 MPa pressure with a rotation speed of maximum ~10 rpm would be safe for the optics). The Bangalore-built Raman tribometer A (chapter 6) is also capable of measuring the friction force simultaneously while acquiring the Raman spectra. However, the current tribometer setup strikes off the option of studying the tribology of metals, a major interest for the tribologists. This is because at the optics/metal interface the electric field oscillating in the *xy*-plane gets significantly subdued due to the formation of image dipoles on the metal surface (section 6.4). The electric field oscillating along the *z*-axis, however gets enhanced due to the image dipole formation, but the Raman scattering due to the electric field along *z*-axis is mostly horizontal (in the *xy*-plane) and the collection efficiency of the 50× microscope objective was not high enough to collect these horizontal radiations. Possible solutions to this issue are the use of a parabolic mirror to reflect the horizontal radiations along *xy*-plane towards the collection objective or moving to a fiber optic collection mode where the collection fiber optics can be held along the *xy*-plane to maximise the collection due to the electric field along *z*-axis. However, either of these solutions will involve some good amount of modifications to the current tribometer designs.

Further developments on the existing tribometer designs are currently being carried out by Bain's group to facilitate the tribology studies at steel/dielectric interface. Studying the frictional properties of a mixture of lubricating molecules and the associated molecular changes at the interface can be of immense practical interest. It will also be interesting to find out if the composition of the lubricating molecules change at the sliding interface under the given conditions of pressure and shear. For a curved surface pressing against a flat surface (e.g. SF10 hemisphere and silica/steel ball contact), pressure profiling across the contact area for a given normal load and its variation with applied shear can be studied to correlate to the friction force map and the molecular behaviours at different areas within the contact.

Overall, TIR Raman spectroscopy was a very useful tool for the tribological studies, both in the boundary regime and elasto-hydrodynamic regime. In spite of a few challenges yet to overcome, this technique applied on the Raman tribometers will allow a wide range of tribological sampling to be tested with simultaneous molecular and physical measurements and therefore expected to be of immense interest to the tribologists around the globe.